UNIVERSITY OF SOUTHAMPTON

Single Particle Dielectrophoretic Sorting Technologies

by

Rupert Thomas

A thesis submitted for the
degree of Doctor of Philosophy

in the
Faculty of Engineering, Science and Mathematics
School of Electronics and Computer Science

June 2010

UNIVERSITY OF SOUTHAMPTON

ABSTRACT

FACULTY OF ENGINEERING, SCIENCE AND MATHEMATICS
SCHOOL OF ELECTRONICS AND COMPUTER SCIENCE

Doctor of Philosophy

by Rupert Thomas

Cell sorting is an important laboratory process with medical and biotechnological research applications, but a problem common to many current techniques is the contamination of sorted populations with other non-target cells, which limits the usefulness of recovered populations. Microfluidic devices enable new methods of handling minute volumes of biological and chemical samples, including single cells. This work explores techniques for the manipulation of single cells and particles in a microfluidic channel using electrokinetic forces, intended for the isolation of cells from a heterogeneous population and recovery with a high purity.

Real-time image processing techniques have been used with an automated control system to sort fluorescent cells and particles using dielectrophoresis as they flow through a microfluidic channel. The use of image data enabled more complex decision algorithms to be used to distinguish between target and non-target particles. Multiple single cells and particles were tracked simultaneously, and identified by their colour, luminosity, size and shape.

Several novel electrode geometries have been developed for the manipulation of single cells and particles using dielectrophoresis. Ring electrodes have been used for trapping single cells and particles, and are suitable for massively-parallel and arrayed operation. Minority subpopulations have been enriched by using the traps to select single cells from the bulk population, and recovered with 100% purity. This method of sorting cells is advantageous if further processing or analysis is intended within the microfluidic device, as cells are volumetrically concentrated as well as being enriched.

Dielectrophoretic sorting gates have been developed for sorting particles by deflecting them laterally as they flow through a microfluidic channel junction, with up to five spatially separated outputs. Sorting performance has been characterised by measuring the velocity at which synthetic particles break-through the dielectrophoretic barriers, and the maximum rate at which particles can be sorted. The purity of recovered populations is related to the flow velocity and particle concentration during sorting, and 100% purity has been obtained for populations sorted at rates of up to 0.9 particles per second.

Contents

List of Figures

List of Tables

Nomenclature

a	Radius
A	Cross-sectional area
c_p	Specific heat at constant pressure
C_m	Membrane capacitance
C	Concentration
d	Width of the microfluidic channel
D	Electric flux
D	Diffusion coefficient
D_H	Hydraulic diameter
ϵ_0	Permittivity of free space
ϵ_m	Permittivity of the suspending medium
ϵ_p	Permittivity of the particle
ϵ^*	Complex permittivity
ϵ_m^*	Complex permittivity of the suspending medium
ϵ_p^*	Complex permittivity of the particle
ϵ_r	Relative permittivity
E	Electric field
η	Dynamic fluid viscosity
θ	Angle
f	Fluid body force
f_{CM}	Clausius-Mossotti factor
F	Force
F_B	Buoyancy force
F_{DEP}	Dielectrophoretic force
F_g	Gravitational force
F_{HD}	Hydrodynamic drag force
F_L	Hydrodynamic lift force
F_N	Normal surface reaction force
F_{TWDEP}	Travelling wave dielectrophoretic force
F_S	Sedimentation force
g	Gravitational constant
G_m	Membrane conductance per unit area

Γ_{ROT}	Electrorotational torque
h	Height
J	Current density
k	Thermal conductivity
K_s	Surface conductance
κ	Reciprocal of the Debye length
l	Length
λ	Wavelength of the travelling wave field
m	Mass
μ_{DEP}	Dielectrophoretic mobility
ν	Kinematic fluid viscosity
p	Pressure
P	Power dissipation per unit volume
Q	Electric charge
Q	Fluid volumetric flow rate
r	Position vector
R	Sorting rate
ρ	Charge density
ρ_i	Resistivity of the cell interior
ρ_m	Resistivity of the suspending medium
ρ_m	Fluid mass density
ρ_p	Particle mass density
Re	Reynolds number
S	Shear rate
σ	Conductivity
σ_{qo}	Surface charge
T	Temperature
ϕ	Scalar electrical potential
u	Fluid velocity
U	Transmembrane potential
v	Velocity
v_{DEP}	Resultant velocity under the DEP force
V	Mean fluid velocity
ω	Angular frequency
ζ	Zeta potential of the interface
∇	Spatial gradient

Acknowledgements

The completion of this thesis has only been possible with the help and support of many people. First and foremost, I would like to thank Professor Hywel Morgan for introducing me to this fascinating area of science and many subsequent years of mentorship and support. I would also like to thank Dr Nicolas Green for his help and guidance throughout and significant patience in many stimulating discussions.

This work was supported by Philips Research Laboratories, to whom I am most grateful for the receipt of a CASE award and much technological assistance. I am also deeply grateful to Professor Richard Oreffo and Peter Mitchell of the School of Medicine, University of Southampton, in conjunction with whom part of this work was performed.

I would like to thank Nico Kooyman of Philips Research Laboratories and Katie Chamberlain of the Southampton Nanofabrication Centre for the fabrication of many electrodes and microfluidic devices, and all the members of the Morgan Group at the University of Southampton, past and present, for the companionship, camaraderie, coffee and cakes. Finally, I must express my gratitude to my friends and family for their never ending support through this journey, I am indebted to you all.

Chapter 1

Introduction

1.1 Microfluidics and the Lab-on-a-Chip

There has been a trend in analytical chemistry and biochemistry to work with ever decreasing quantities of reagents. Fields of work such as genetics, proteomics and rare cell analysis have now become commonplace, but the analytes involved can often be obtained only in minute quantities without significant expense, and there being no direct benefit in working with larger amounts. With modern laboratory equipment, it is relatively simple to generate sub-microlitre volumes, but containing and processing such volumes in conventional vessels is difficult. Subsequently, there has been significant interest in alternative means for carrying out reactions, and in particular integrated microfluidic systems - or 'Lab-on-a-Chip' (LoC).

Early work that can be categorised as part of the LoC field includes a gas chromatograph developed by Terry (1975). Etched into a silicon wafer, the device included a capillary column, two sample injection valves and a thermal conductivity detector element, and was a step forward in the use of integrated-circuit fabrication techniques for both miniaturisation and integration of non-electronic systems.

Continued integration of electrical, mechanical and thermal elements into silicon (Ruzicka and Hansen, 1984; Shoji et al., 1988; Vanlintel et al., 1988) spawned the idea of micro-total-analysis-systems (μTAS) - a term introduced by Manz et al. (1990) to describe devices incorporating all the components necessary for performing a biological or chemical analysis. A typical system may include components such as pumps (Green et al., 2004), valves (Thorsen et al., 2002), mixers (Sasaki et al., 2006), reaction chambers and heating elements, all of millimetre or sub-millimetre dimensions, so an entire (bio) chemical reaction can take place on the device. Reaction progress can be monitored optically, or sensors can also be incorporated within the device to provide a direct electrical output (Gerardo, 2006). The use of silicon - either as a substrate for bulk

micromachining or by deposition - opens up the possibility of incorporating electronics to control the active elements and process and interpret the sensor data (Manaresi et al., 2003) although this is not common due to the costs involved in prototyping with silicon/CMOS fabrication.

As previously stated, reduction of the size of reactions and the volumes of reagents involved is of great value when reagents are rare or expensive, or as in the case of forensic science, simply unobtainable (Verpoorte, 2002). Thermal cycling, as required for polymerase chain reaction (PCR) DNA amplification, can also be performed more quickly because of the small thermal masses involved and so cycle times as low as 30 seconds can be achieved (Khandurina et al., 2000; Lagally et al., 2001). Miniaturisation of chemical processes also enables analyses to be performed with smaller, sometimes hand-held devices, rather than in a conventional full-scale laboratory. This has been particularly exploited in the medical device sector, where there is both the medical need and the funding available to develop point-of-care (PoC) equipment, to provide real-time or near-real-time measurements (Tdos et al., 2001). Of the range of medical tests commonly available, a small number of monitoring tests represent the bulk of tests carried out. These tests are used to monitor the progress of a patient during the course of a disease, and so frequent or sometimes real time measurements are required. With such tests, the value of the results decreases over time, and so the advantage of fast-turnaround point-of-care equipment (such as a bedside monitor) over conventional laboratory-based equipment is greatest (Lauks, 1998).

A range of techniques exist for the fabrication of micron-sized structures that were originally developed for the silicon integrated circuit industry. The use of photolithography for microfabrication is discussed in more depth in Chapter 4 - Fabrication of Microfluidic Electrokinetic Devices. A number of techniques have been used to enclose these microstructures to form fluidic channels (Agirregabiria et al., 2005; Vulto et al., 2005). Complex systems of interconnections can be produced, in a similar manner to electrical connections on a printed circuit board. Fluidic channels fabricated in this manner have the advantage that they can be produced with a length-scale smaller than is normally possible with conventional machining processes.

Fluid flow in a micro-channel exhibits markedly different characteristics than on a larger length-scale. Viscous forces significantly outweigh inertial forces in the fluid, a condition described as laminar flow - the flow follows streamlines, with a notable absence of turbulent mixing. Diffusive mixing due to Brownian motion occurs, leading to a gradual mixing of fluids, but this process is normally considered slow given the dimensions and fluid velocities typical of micro-channels. An example is two differently coloured dyes flowing in parallel along a straight channel that is many times longer than it is wide: the fluids flow side-by-side, with no turbulent mixing - see Section 2.6 - Flow in Microfluidic Systems.

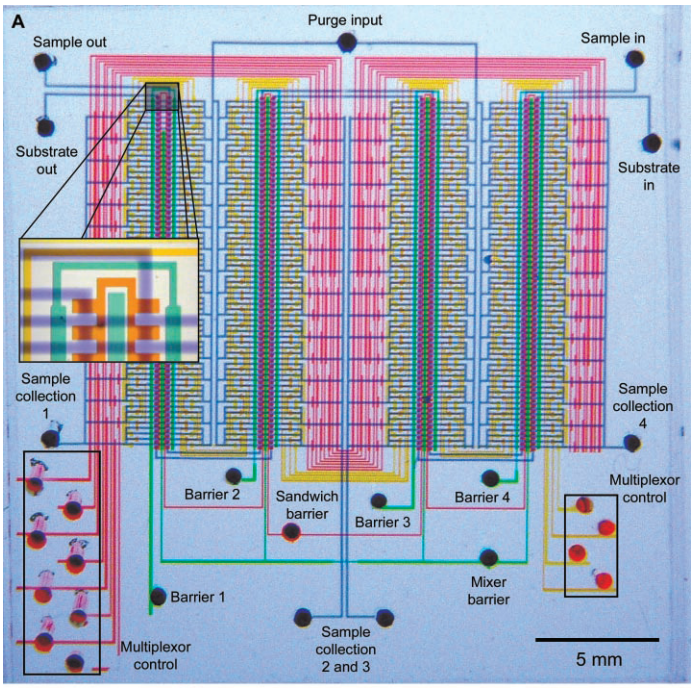

FIGURE 1.1: A highly integrated microfluidic circuit, with microvalves and mixing chambers. Taken from Thorsen et al. (2002).

Application of microfabrication to fluidic components has enabled the large-scale integration of microfluidics (Thorsen et al., 2002), with many thousands of valves and chambers integrated into a fluidic system. Complex sequential mixing operations are possible, producing exponentially increasing numbers of mixtures.

1.2 Electrokinetics

Electrical analysis and manipulation of chemical and bio-chemical processes is widely used on the macroscale, and many processes scale favourably to the microscale. Microelectrodes enable strong electric fields to be created with otherwise comparatively low voltages, and detection and signal processing electronics can be integrated close to their target if there is a requirement to make particularly sensitive measurements.

1.2.1 Electrophoresis

A charged particle in an electric field experiences a Coulomb force (see Section 2.1). If the particle is not otherwise restrained, it will move - either in the direction of the field or against it, depending on the polarity of the charge on the particle. This effect is known as electrophoresis, and has become the basis of a standard laboratory technique for identifying small, charged particles.

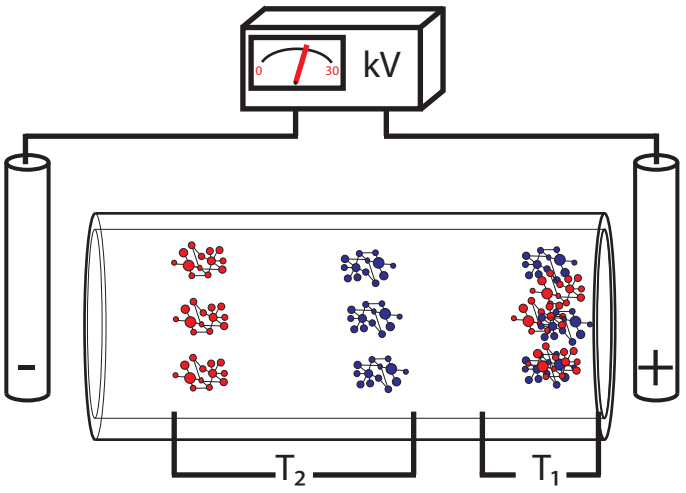

FIGURE 1.2: Overview of a typical equipment configuration used for capillary electrophoresis.

During gel electrophoresis, a thick agarose gel greatly retards the motion of particles. Large particles experience greater drag forces than smaller particles, and so move at slower velocities through the gel. Similarly, particles with greater charge experience a larger force, so move faster through the gel. Species can be identified, and different components of a sample separated and identified, by the distance that they move through the gel in a given time.

Separation and identification of DNA, RNA and protein molecules is commonly performed using electrophoresis. The negative charge on the sugar-phosphate backbone of nucleic acids causes fragments of DNA and RNA to move towards the negative electrode. The complex folding of proteins can strongly influence their migration through the gel, so they are normally denatured in a surfactant. Separation then occurs based almost purely on molecular weight.

Capillary electrophoresis is a similar technique, but separation occurs inside a narrow-bore tube without the stabilising gel (Mikkers et al., 1979; Jorgenson and Lukacs, 1981, 1983). Figure 1.2 shows a typical equipment configuration for performing capillary electrophoresis. Capillary electrophoresis was one of the first separation techniques to be successfully translated into the microscale - Harrison et al. (1992) used a microfabricated device to separate calcein and fluorescein with resolution similar to a conventional device.

Electrophoresis is widely used as a laboratory technique and has been extensively developed in the scientific literature (Kutter, 2000; Monton and Terabe, 2005). While it is not within the scope of this study, it serves as a useful introduction to the field of electrokinetics as the underlying phenomenon can be modelled as a simple physical relationship - discussed in more detail in Chapter 2.

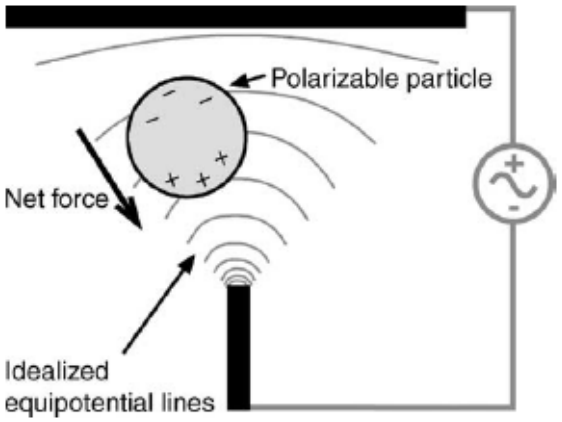

FIGURE 1.3: A particle in a non-uniform electric field experiencing positive DEP. Taken from Gray et al. (2004).

1.2.2 Dielectrophoresis

An uncharged particle in a uniform electric field will polarise, effectively forming a dipole, but will not move as a charged particle does because the Coulomb force on each half of the dipole is equal and opposite. In a spatially non-uniform electric field, however, variations in the electric field strength across the dipole lead to a net force on the particle (see Section 2.3) - an effect known as dielectrophoresis (DEP). Dielectrophoresis potentially has a wide application area, as unlike electrophoresis, it is effective on all particles - charged or uncharged - but has yet to be exploited on the scale of electrophoresis. This is most likely because dielectrophoresis is only really practical on a microscopic scale, whereas electrophoresis as an analysis technique has been developed with simplicity on the macroscale.

The term dielectrophoresis was first introduced by Pohl (1951) after observing the motion of graphite and nickel particles in an electric field between two concentric cylindrical electrodes. The technique was also applied to living cells (*S. cerevisiae*), and its use for monitoring and characterisation was observed (Pohl, 1970; Pohl and Crane, 1971). Pohl noted that age, chemical poisons, or thermal treatment of the cells lead to a clear difference in their motion under DEP, and also refined and reduced the size of the electrodes to produce a stronger DEP force.

More recently, the ability to produce smaller electrodes with micron-sized features has made DEP more practical, as the voltages required to produce useful forces on cells and similarly sized particles is consequently reduced from tens of kilovolts to several volts. Subsequently, DEP has been used in a wide variety of applications, such as characterisation (Markx et al., 1994; Kriegmaier et al., 2001; Holzel, 2002), separation (Becker et al., 1995; Cheng et al., 1998; Morgan et al., 1999; Gascoyne and Vykoukal, 2002), manipulation (Manaresi et al., 2003; Chiou et al., 2005) and trapping of a wide variety of particles, including: cells , bacteria (Markx et al., 1994; Wang et al., 1993;

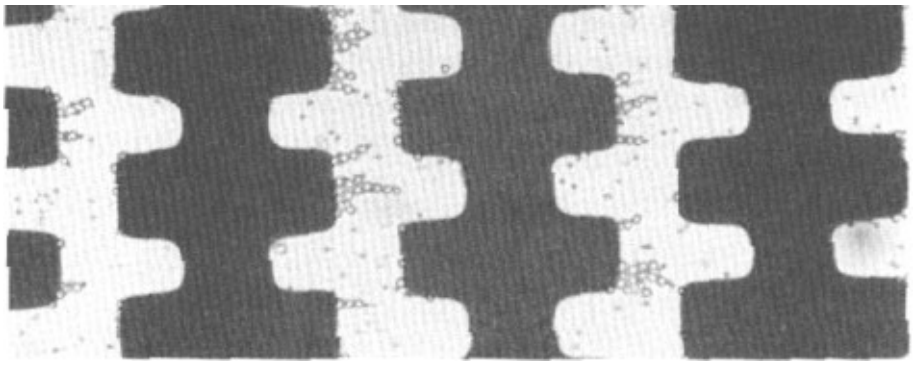

FIGURE 1.4: Becker et al. observed that HL-60 cells (human leukaemia) could be retained on the electrode tips using when an alternating electric field was applied (20-80 kHz) while normal blood cells remained in solution and could be removed with fluid flow. Taken from Becker et al. (1994).

Yang et al., 2002; Markx et al., 1996), viruses (Green et al., 1997; Hughes et al., 1998), and DNA (Tuukkanen et al., 2007).

Numerous electrode designs have been constructed for DEP, some of the most common being the interdigitated (Becker et al., 1994), castellated (Pethig et al., 1992; Price et al., 1988; Wang et al., 1993), and quadrupole types (Schnelle et al., 1999; Voldman et al., 2003). Interdigitated and castellated designs have proved useful for exploiting differential dielectric affinity for the separation of particle mixtures. For example, Becker et al. (1994) separated HL-60 human leukaemia cells from human blood cells by immobilising the HL-60 cells on to the edges of the electrodes using positive dielectrophoresis. Differences in the polarisability of the cells meant that under the conditions chosen, the blood cells were repelled slightly from the electrodes and could be carried away by the fluid flow. Figure 1.4 shows castellated electrodes, with HL-60 cells immobilised on the electrode edges. The use of dielectrophoresis (and other technologies) for cell and particle separation is discussed in more detail in Section 1.4.

The quadrupole design (Figure 1.5) has been studied widely as it can be used to trap and immobilise a particle between the electrodes using negative dielectrophoresis. Huang and Pethig (1991) refined the design to create 'polynomial' quadrupole electrodes with well defined spatial variations in the electric field that could be modelled with an analytical solution. The electrodes have received particular attention as they can levitate a trapped particle above the surface (Hartley et al., 1999). While the hydrodynamic drag forces from fluid motion around the particle do not exceed the DEP force exerted on a particle within the electrodes, the particle will remain trapped (Voldman et al., 2001). The ability to precisely locate a particle (such as a biological cell) and hold it in that position against a steady flow enables many novel methods of handling cells. Additionally, to be able to isolate the particle from others in the medium can permit single particles to be manipulated - a potentially very useful way to conduct characterisation and analysis.

FIGURE 1.5: A quadrupole electrode set (titanium gold electrodes patterned on a glass substrate). Scale bar is 200 μm.

This area is covered in more detail in Section 1.3 - Single Particle Manipulation and Trapping.

While dielectrophoresis has been demonstrated successfully in isolation, it can be more usefully employed when integrated into a microfluidic device (Fiedler et al., 1998; Cummings, 2003; Holmes et al., 2003). Muller et al. (1999) and many others have demonstrated integrated systems that use DEP for focusing, trapping and sorting of particles, with fluid flow carrying particles through the device and between the active elements. Particles are often focused into a narrow stream to facilitate single particle manipulation and analysis, so that they all pass in single file through the same point in a small detection region, or so that they can all be manipulated by the same electrodes. The most common method is hydrodynamic focusing, where the sample stream is surrounded with a sheath flow and is confined into the centre of the channel - Figure 1.6 (a). This requires additional fluidic equipment, however, and it can be difficult to confine the particle stream within 2-dimensions using the planar architecture common in microfluidics. Dielectrophoretic focusing using negative DEP barriers is an attractive alternative as it is relatively simple to confine particles within both the horizontal and vertical axes - Figure 1.6 (b) (Holmes et al., 2006).

1.2.3 Electrorotation

So far only spatially invariant electric fields have been examined, but it is also possible to use three or more out-of-phase alternating electric fields to create a rotating electric field. When a dielectric particle is suspended in a fluid within such a rotating electric field, the interaction between the field and the dipole induced within the particle can produce a torque on the particle, causing it to rotate.

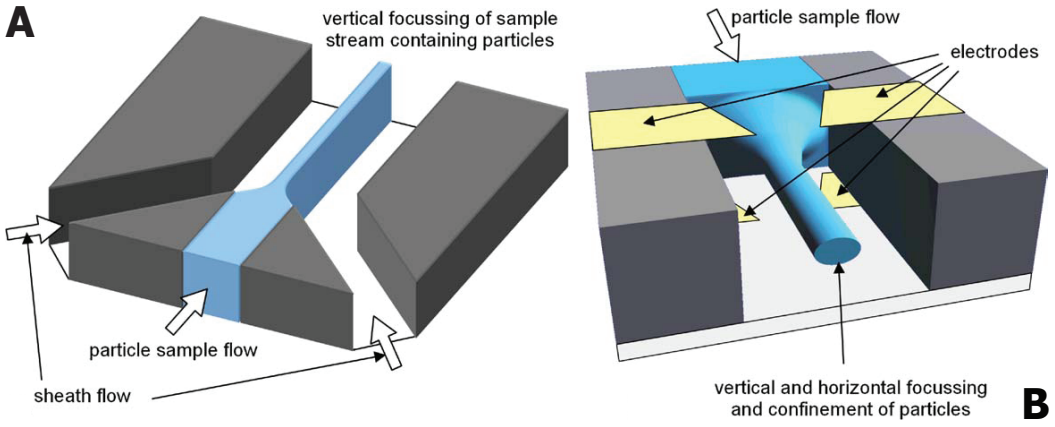

FIGURE 1.6: Focusing of a sample stream within a microfluidic channel. (a) Hydrodynamic focusing confines the stream within the horizontal axis. It is possible to confine within the vertical axis as well, but this requires a more complicated fabrication process. (b) Dielectrophoretic focusing of a particle stream in the horizontal and vertical axes, with no additional fluidic connections. Taken from Holmes et al. (2006).

Electrorotation (ER) has been used widely as a tool for characterisation, because the speed at which the particle rotates is related to the dielectric properties (electrical conductivity and permittivity) of the particle and the medium and the electrical parameters of the rotating electric field. The technique can be used to calculate electrical properties of cells (such as the membrane capacitance) from measurements of its angular velocity within a rotating electric field (Zhou et al., 1996). A solution of cells is prepared with a known electrical conductivity and permittivity, and the rotation of a cell is observed under rotating electric fields over a range of frequencies. Figure 1.7 shows a photograph of the electrorotation of a single cell within quadrupole electrodes. The detail behind the characterisation of particles by electrorotation is discussed in more detail in Section 2.3.1.

Similar experiments could be performed using dielectrophoresis, by measuring the linear velocity of a particle under the DEP force to determine its electrical properties. Electrorotation is the most commonly used method, however, because the inherently constant torque on the particle (under a temporally invariant field) makes measurements far simpler. The dielectrophoretic force on a particle is dependent on the spatial gradient of the electric field, meaning the force changes as the particle is displaced by the force; determining the particle properties from such measurements becomes a complex, convoluted process but nevertheless some attempts have been made (Gimsa, 1999; Holzel, 2002).

The complex structure of biological cells means that each structure, interface or organelle has an influence on the overall polarisation of the cell - the electrical properties of each of these must be resolved if the characteristics of the cell as a whole are to be completely determined. In practice, however, simplified electrical models of the cell as a spherical particle with a number of concentric shells (Huang et al., 1992; Chan et al., 1997) are currently the best that the available mathematical models can determine, and indeed

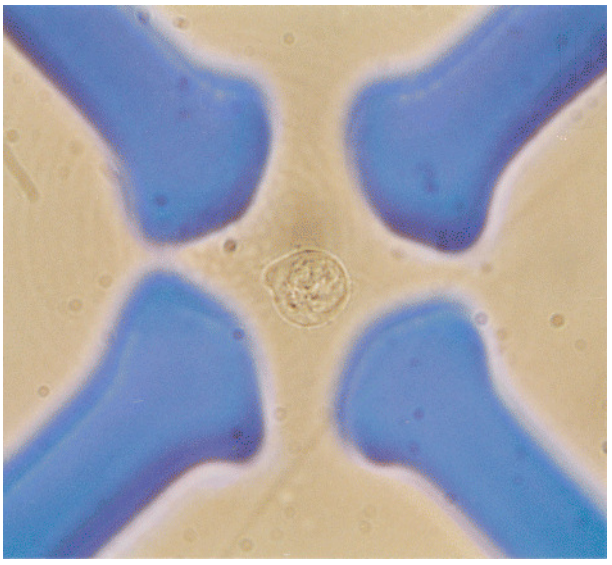

FIGURE 1.7: Image of a human T lymphoma cell (Jurkat) trapped and rotating in a quadrupole electrode set. Taken from Reichle et al. (1999).

are normally sufficient to predict the kinetics of a cell under the electrical conditions found within the lab-on-a-chip environment. Electrical modelling of cells is discussed in more detail in Section 2.5.

1.2.4 Travelling-wave Dielectrophoresis

The phase relationships exploited by electrorotation can also be used to move particles in a linear motion. Figure 1.8 shows three electrodes from a larger set, in which the phase difference between adjacent electrodes is 90° - essentially the electrorotation electrodes have been 'flattened out' and repeated. The electric field travels along the electrode set as a wave, and can produce dielectrophoretic forces both perpendicular and parallel to the surface of the electrode set.

A particle in solution above a travelling-wave electrode set will experience a component of its DEP force that is perpendicular to the surface, which can either draw it towards the electrodes (pDEP) or repel it away (nDEP). Rather than induce rotation in the particle, the travelling-wave effect will also induce a component of the DEP force that is parallel to the surface, pushing the particle along the electrode set.

Travelling-wave DEP is particularly attractive because it opens up the possibility of continuous separation and sorting of particles. Talary et al. (1996) exploited the differences in the dielectrophoretic responses of viable and non-viable yeast cells to separate the two. Viable cells were drawn towards the electrodes by pDEP, while the non-viable cells were repelled by nDEP and pushed along the channel (to the right in Figure 1.9).

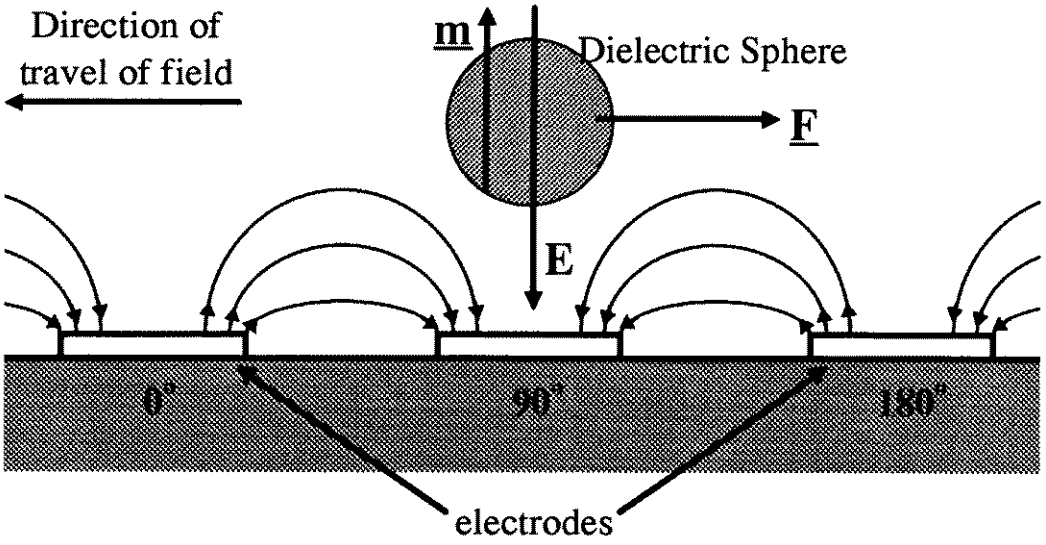

FIGURE 1.8: A travelling DEP wave can have a levitating effect on the particle as well as propelling it along the array. Taken from Morgan et al. (1997).

Morgan et al. (1997) used travelling-wave DEP to separate erythrocytes and leukocytes - both were repelled from the electrodes but the leukocytes experienced a stronger travelling-wave DEP force and so moved faster.

Although some interesting work has been demonstrated using travelling-wave DEP, it has not been widely exploited. Very controlled conditions are required, such as tight control of medium conductivity, to obtain reproducible results. Induced fluid flow can have a more significant effect on particle motion than the particle DEP force itself, complicating the sorting of particles.

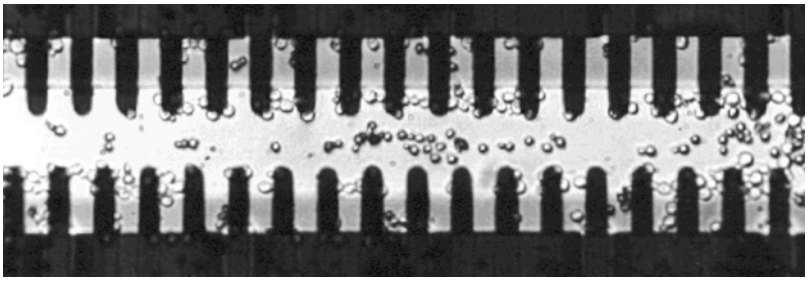

FIGURE 1.9: Continuous separation of viable and non-viable yeast cells. Taken from Talary et al. (1996).

1.3 Single Particle Manipulation and Trapping

As explained above, an analysis technique performed on an entire population of cells simultaneously will return a measurement that is averaged across the entire population. This does not present many problems when a purified sample is being examined, or when the species of interest represents the majority of the population. The effect of

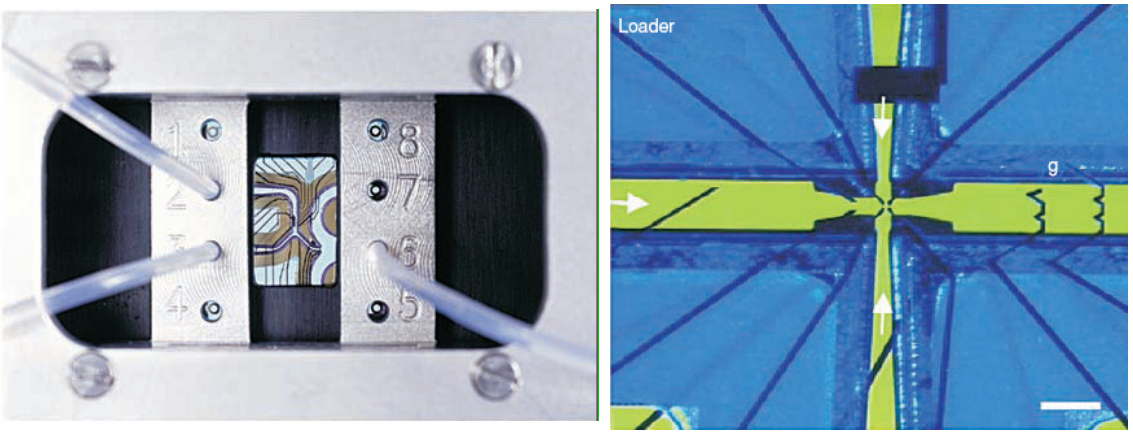

FIGURE 1.10: Overview of a commercial single-cell handling system (Evotec AG). Taken from Muller et al. (2003).

sub-populations will not be observed, however, unless their significance in the measurement output can be amplified - as an example, this is sometimes possible with selective fluorescent stains.

To aid single-cell analysis, it is often advantageous to separate and isolate cells of interest from the bulk cell population. Figure 1.10 shows a commercial single-cell handling system (Cytoman, produced by Evotec AG). A dielectric field cage is created in the quadrupole electrode set (see below), shown in the centre of the second picture, where a single particle can be trapped and isolated from the rest of the particle stream. Such a system has been used to measure the calcium flux through single cells in the presence of an alternating electric field, and to observe the effect of DEP manipulation (Muller et al., 2003).

1.3.1 DEP Trapping

Price et al. (1988) used a castellated electrode geometry to measure the dielectric properties of bacteria, and observed the cells agglomerating at low field minima when subject to nDEP. The concept of trapping cells in suspension is attractive because they can be retained for further analysis with precise control of their spatial position, while maintaining an environment that is conducive to their continued viability. One particular application for the precision positioning of living cells is the manufacturing of cell-based biosensors, and Gray et al. (2004) developed a microelectrode array with this in mind. Using pDEP, cells were drawn to the electrodes, and attached to the surface using patterned fibronectin.

Positive DEP is useful for patterning cells to a substrate, as the electrode geometries and electrical interconnections required are very simple, but it has potential to cause damage to the membranes of viable cells. Under pDEP, cells are drawn towards high field regions - the resulting field distribution can cause a large potential difference across

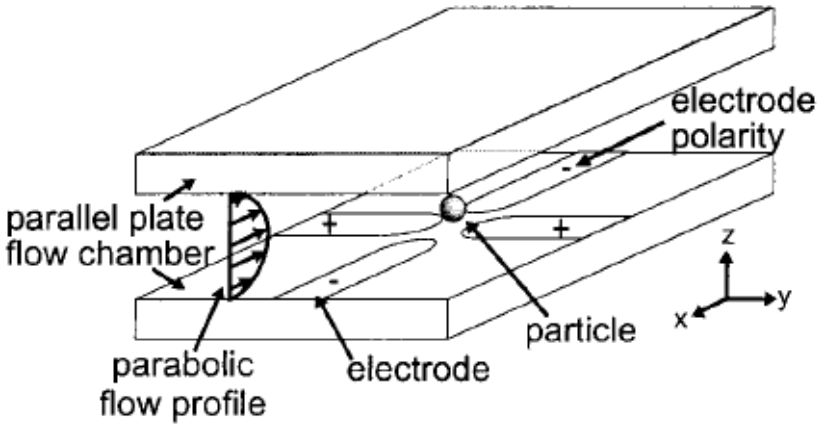

FIGURE 1.11: A single particle immobilised and levitated in a quadrupole DEP trap. Taken from (Voldman et al., 2001).

the insulating cell membrane, large enough to permeate the membrane and cause loss of cell viability. Also, media with a low conductivity (and hence low ionic content) is required to create the electrical condition for cells to experience pDEP. This does not mirror the physiological conditions that are required for extended cell viability, and it creates stress on the cells as ions diffuse out.

The quadrupole electrode configuration (Figure 1.5) is a popular arrangement that is particularly useful as a particle trap. When the four electrodes are energised with alternating voltages so that adjacent electrodes are out of phase, a low-field region is created in the centre of the trap, at a distance above the surface. This can create a stable nDEP trap, levitating a particle above the surface.

Provided the vertical component of the DEP force is sufficiently strong to raise the particle, the particle settles at a point where a force equilibrium exists between gravity and the DEP force. Negative DEP levitation at a stable equilibrium, termed passive levitation by Hartley et al. (1999), has advantages over active pDEP systems (Jones and Kraybill, 1986; Qian et al., 2002) because complicated sensor-feedback systems are not required. Levitating traps are an attractive method of handling particles, as they are inherently non-contact. Surface interactions are reduced, particularly useful for the manipulation of adherent cells.

A potential limitation of the quadrupole design as a trap is that the electric field forms a 'force funnel' rather than a closed dielectrophoretic cage - see Figure 1.12. Particles can be pushed out of the funnel if the DEP force becomes much stronger than the sedimentation force (gravity) or if the particles are less dense than the medium. Such traps also have a tendency to accumulate particles in the presence of a prevailing flux.

Schnelle et al. (1999) developed quadrupole electrode designs into an octopole structure to create closed nDEP cages. Octopole designs have a lengthier fabrication procedure, as electrodes must be fabricated on top and bottom surfaces - see Figure 1.13. The

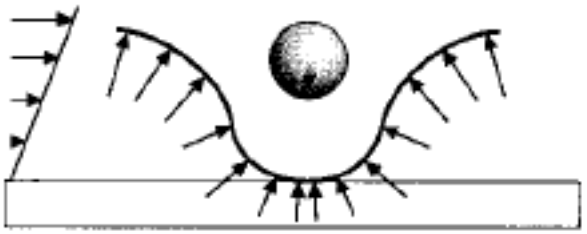

FIGURE 1.12: The quadrupole DEP trap directs a particle to a low-field region above the centre of the trap, but relies on gravity to keep the particle contained. Taken from Voldman et al. (2001).

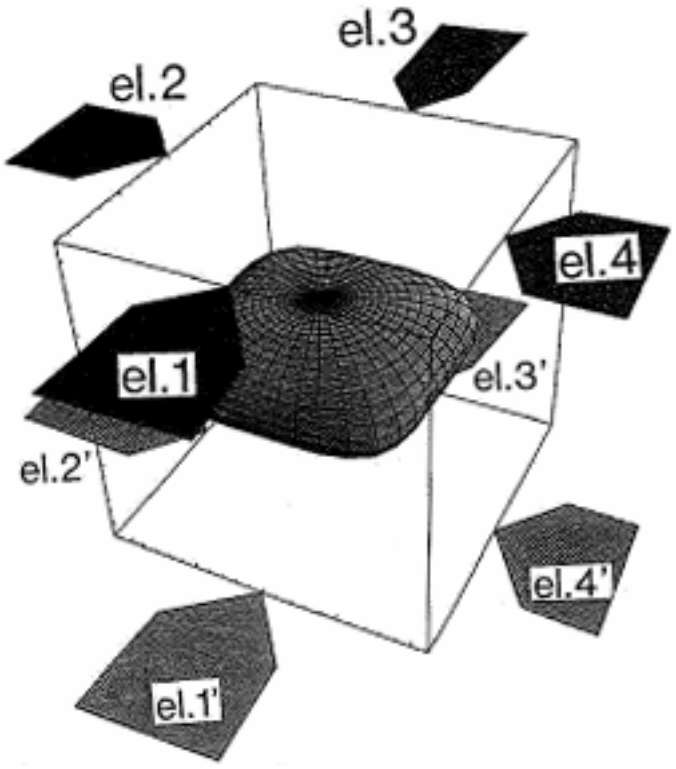

FIGURE 1.13: The octopole configuration requires electrodes on both top and bottom surfaces, but creates a closed well-defined cage. Taken from Schnelle et al. (1993).

packaging requirements are also more complex, as both surfaces must be aligned and mated before use. Micron-scale alignment is required for single-cell traps. Nevertheless, such alignment is well within the reach of modern production techniques, and octopole traps have been implemented in many DEP systems (Muller et al., 1999; Reichle et al., 1999).

Figure 1.14 shows an array of nDEP traps developed by Rosenthal and Voldman (2005) for patterning single particles on a surface. An alternating electric field between the two tracks creates a DEP field cage with a field minima close to the centre of the square region. The shared electrical connections between the traps make obvious the purpose of the design was to trap large numbers of particles, without the need for individually addressing the traps. A similar design could be produced, however, with

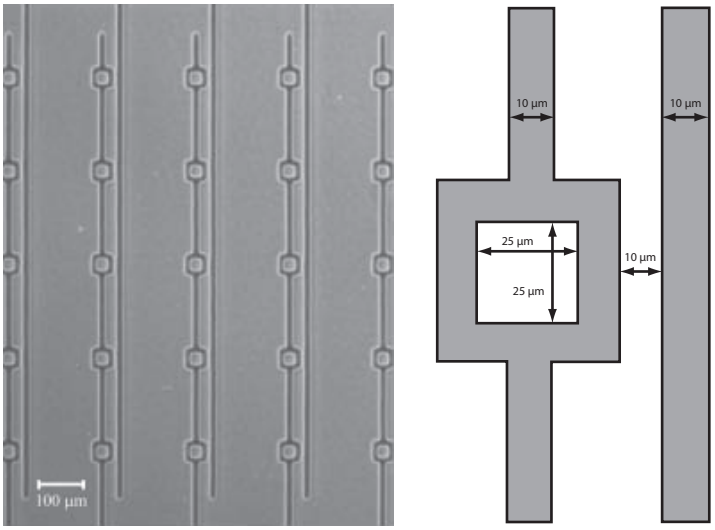

FIGURE 1.14: Negative DEP traps for single-particle patterning. Adapted from Rosenthal and Voldman (2005).

the traps connected individually, and only a single electrical connection per trap would be required - the second, straight electrode can still be shared between many individually addressable traps, as this electrode would typically be grounded. Minimising the number of connections required per trap is a key requirement for parallel operation of multiple traps.

Negative DEP traps have also been developed for a number of specialist purposes - an example being the 'horseshoe' design by Seger et al. (2004) (see Figure 1.15). The trap has an open front, and relies on hydrodynamic pressure from fluid flow to keep the particle contained. The design has the advantage that particles can be immobilised from a flow without a controlling input - while the trap is energised it will remove particles from the flow. This system was used to temporarily hold cells while they were 'dipped' in a medium different from their native culture medium, with potential applications for cell lysis or chemical assays.

1.3.2 Massively-Parallel Control of DEP Traps

Immobilisation of single cells is in itself interesting as a tool for developing analysis techniques, but for useful result it may be required to trap large numbers of cells, with single-cell resolution. With larger numbers of particle traps implemented within a device, it becomes increasingly difficult to provide electrical connectivity while maintaining independent control of each trap. A number of novel techniques have been implemented to address these problems.

Matrix addressing techniques enable traps to be operated by a reduced number of control lines. Row/column addressing is used, so that (m x n) traps can be controlled by (m + n) control lines. The obvious application of this concept has been thin-film transistor

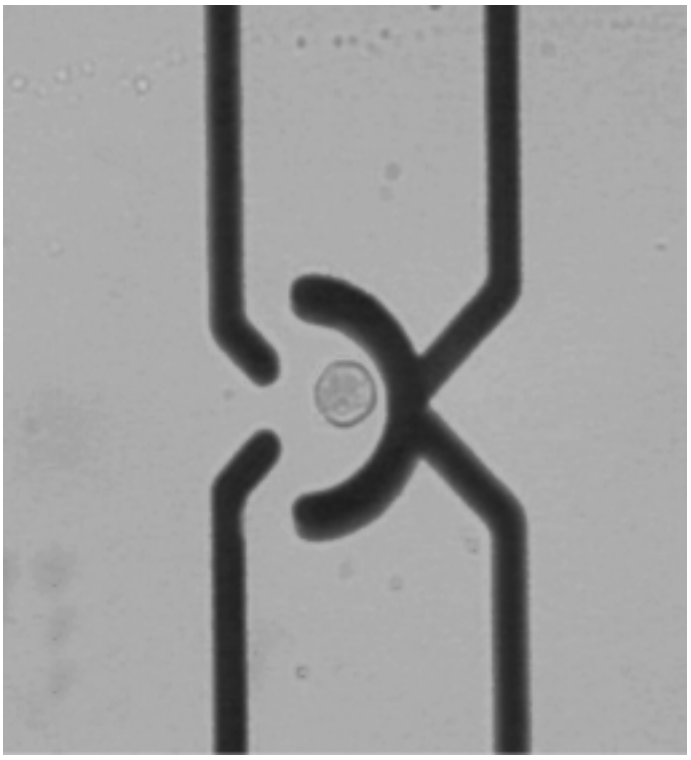

FIGURE 1.15: A single cell held against a fluid flow by a semi-open 'horseshoe' trap. Electrodes are required on both the top and bottom surfaces. Taken from Seger et al. (2004).

(TFT) liquid crystal displays (LCDs), in which a matrix of pixels is controlled by row and column data buses. This requires integration of a transistor into each pixel, however, so that only simultaneous signals from both the row and column inputs will switch the pixel - otherwise it would not be possible to address single pixels.

The dot-ring structures developed by Taff and Voldman (2005) are particularly suitable for matrix addressing. Using pDEP, cells are trapped at the high-field region at the exposed 'dot' in the centre of the traps. The geometry and field plot is shown in Figure 1.16. Trapped cells can be selectively removed from the array by connecting the appropriate control lines to ground (Figure 1.17) in the presence of a fluid flow. Other traps on the same axes are weakened (DEP force reduced by a factor of 4 as the potential difference across the traps is halved), but provided the trapping force exceeds the hydrodynamic drag by at least four times, the other cells will remain trapped.

This mode of operation provides a convenient method to control a large number of traps without resorting to an exorbitant number of parallel control lines, and the strong trapping forces required are not unreasonable when working with pDEP. The limitations of such a system are clear, however, as cells are trapped at high-field regions on the electrodes where they are vulnerable to damage, and the use of pDEP limits the choice of media to low ionic-content solutions rather than physiological media. Without any closed field cages or repulsive effect, there is also little to limit the retention of multiple

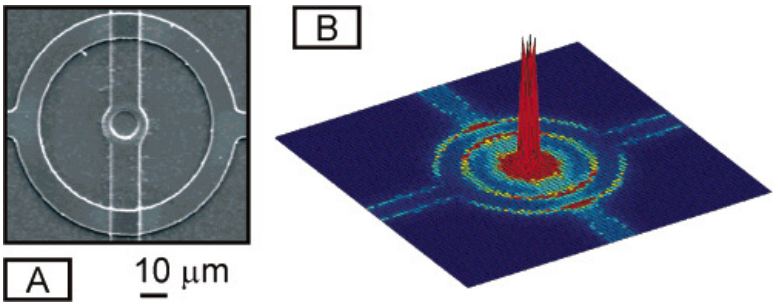

FIGURE 1.16: The dot-ring pDEP trap creates a region of very strong electric field strength directly above the centre of the trap:(a) SEM of the electrode structure and (b) plot of the electric field strength on a plane 1 μm above the surface of the electrodes. Taken from Taff and Voldman (2005).

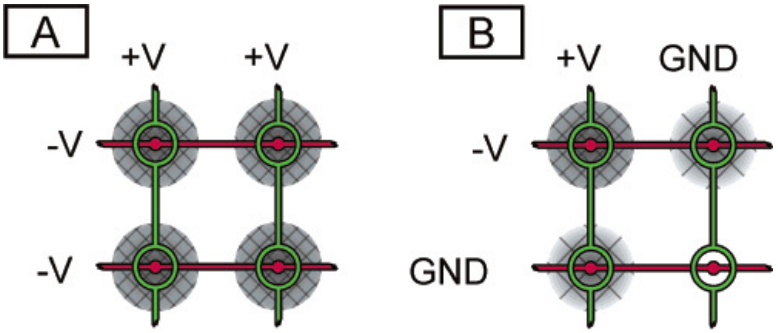

FIGURE 1.17: Operation of the dot-ring particle traps: (a) with all lines energised, the traps are filled. (b) A trap is switched off by its row and column lines being grounded, other traps that share addressing space have their DEP force weakened but not removed. Taken from Taff and Voldman (2005).

cells on a single electrode, although this problem was not evident in the published data. While it is not the ideal choice, however, work has shown that pDEP can be used effectively without catastrophic cellular disruption (Archer et al., 1999).

Voldman et al. (2002) envisage using single particle dielectrophoretic traps as part of a screening cytometer (Figure 1.18), whereby fluorescence measurements can be made repeatedly on each cell, and their response to a particular stimulus observed. Such an arrangement would be a useful component of a highly automated cell-based assay system, for example.

CMOS fabrication techniques have been used to develop a true active matrix of DEP electrodes by Manaresi et al. (2003). Integration of a transistor into each element of the array enables row/column addressing, so that each of the 102,400 elements can be switched individually. Groups of electrode elements have been used to create closed nDEP cages - see Figure 1.19. Optical sensors have also been embedded into each element, for a direct (albeit low resolution) image of particle position.

Compatibility with standard IC fabrication processes is of great advantage for further production, as CMOS is a widely adopted and well understood technology. A silicon substrate enables easy switching and sensor integration, and all the control electronics

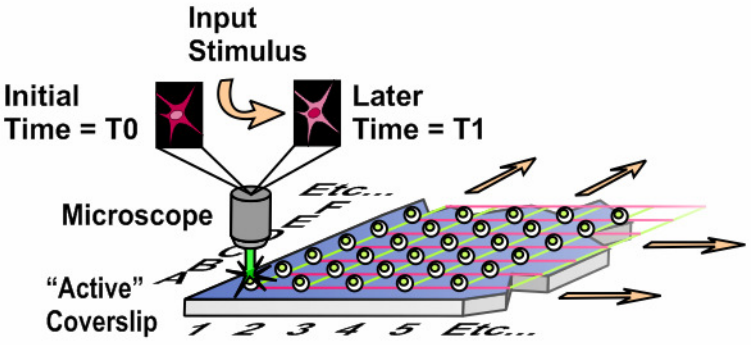

FIGURE 1.18: The concept of a screening cytometer. As the spatial location of each cell is tightly controlled by an array of DEP traps, repeated fluorescence measurements can be made on each cell. Taken from Taff and Voldman (2005).

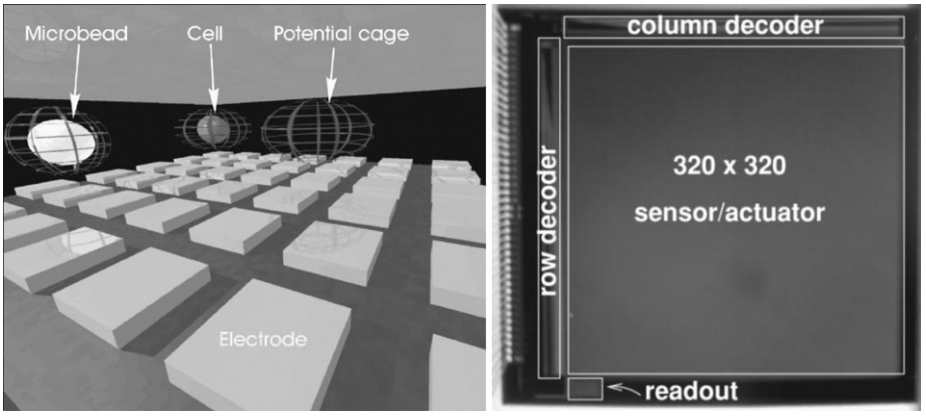

FIGURE 1.19: The CMOS electrode array incorporated 320x320 elements, each with an optical sensor. Taken from Manaresi et al. (2003).

can be packaged on the same chip. Little data has been published on work carried out with the system, but it has numerous applications for cytometry, sorting, cell culture and drug discovery assays. CMOS fabrication is, nevertheless, expensive and time consuming with many sequential steps - probably not suitable for the disposable devices in which there is much recent interest. A silicon substrate also complicates optical measurements, as it is not transparent.

In its present state, the CMOS electrode matrix has an electrode pitch of 20 μm and is composed entirely of square electrode matrix elements. Particles are moved across the matrix by expanding and shifting the dielectric field cages, although this was found to be relatively slow, with particles moving at approximately 20 μm/sec. Development of the technology through reducing the size of the features, and integration of other fluidic/electrokinetic elements, may mean devices of this type are more widely used.

A novel method of trapping particles has been developed using optical images to stimulate a photoconductive layer (Figure 1.20), which overcomes some of the limitations of CMOS-based devices (Chiou et al., 2005). Transparent electrodes (indium tin oxide) on the top and bottom of the microfluidic channel are driven by an alternating voltage

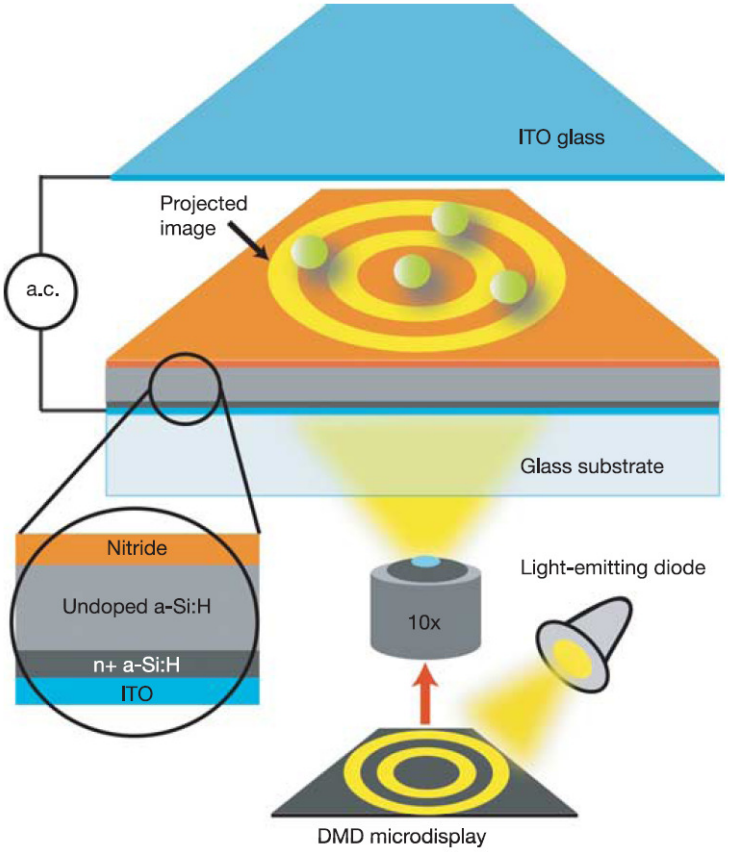

FIGURE 1.20: Manipulation of microparticles using optical images. Taken from Chiou et al. (2005).

source, but the bottom layer is insulated from the fluid by layers of doped and undoped amorphous silicon that present a poor conduction path in their native state. A digital micromirror device (DMD) unit - thousands of tiny microfabricated mirrors that can be individually manipulated - is used to project an image on to the bottom glass substrate, switching the silicon in the illuminated regions into a more conducting state, creating 'virtual electrodes'.

The system has been used to produce and control 15,000 nDEP traps simultaneously, each with a diameter of 4.5 μm. Various trapping and sorting operations have been demonstrated, as well as the controlled movement of particles. Live cells can also be manipulated. The microfluidic portion of the device has relatively simple fabrication requirements, and none of the deposited layers are patterned. This is attractive if disposable fluidic elements are desired, such as single-use sample analysis chips. The use of a digital micromirror device necessitates the presence of an optical system, however, limiting its use in miniaturised or point-of-care-equipment.

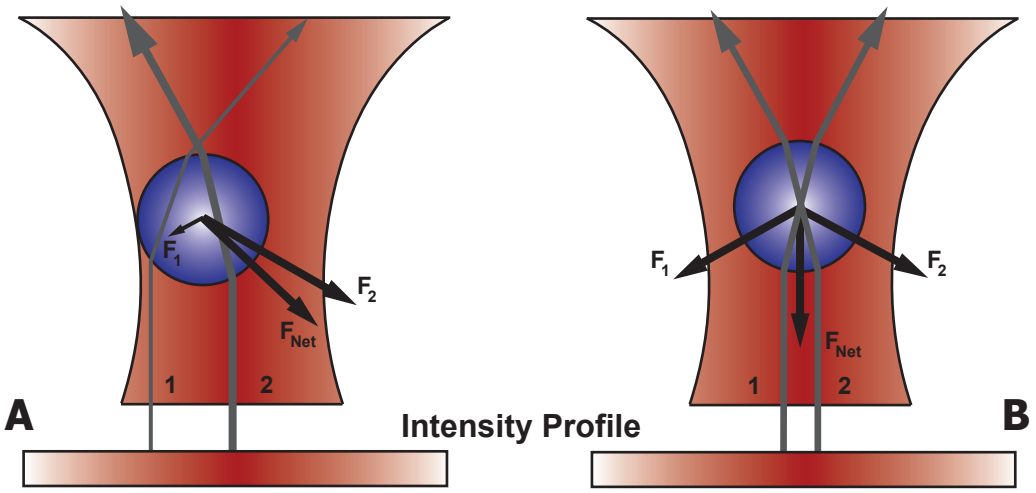

FIGURE 1.21: A particle near to the apex of a tightly focused laser beam (with Gaussian intensity profile) experiences a force due to the imbalance of radiation pressure on each side of the particle (a), directing the particle towards the centre of the beam (b).

1.3.3 Optical Techniques

The use of focused beams of light to manipulate particles was demonstrated by Ashkin (1970), whereby radiation pressure directs a particle towards the apex of a tightly-focused cone of light. Figure 1.21 shows a beam of converging laser light with Gaussian profile passing through a microparticle near to the beam waist. The light is refracted as it crosses into and out of the particle, and a corresponding force is applied to the particle as it affects the momentum of photons passing through. In the case of Figure 1.21 (a) the beam paths 1 and 2 have different intensities due to the intensity profile of the laser beam, and so the corresponding forces are unequal, leading to a net force directing the particle towards the centre of the beam. When in the centre of the beam - Figure 1.21 (b) - the forces are equal. Optical traps have been successfully used to manipulate and analyse a variety of synthetic and biological particles, including cells (Ashkin et al., 1987; Grimbergen et al., 1993), viruses and bacteria (Ashkin and Dziedzic, 1987; Sato and Inaba, 1996).

A development of optical trapping technology is the use of diffractive optical elements (DOE) to create complex 3-dimensional interference patterns that can trap many particles simultaneously, or even be used for sorting. Figure 1.22 shows the equipment used by MacDonald et al. (2003) - the principal element being the DOE that splits the incident beam and is the source of the interference pattern.

Manipulation of optical elements in the light path (cover slips for simple beam steering and neutral density filters for intensity adjustments) was used to create different configurations of interference patterns in a microfluidic channel - Figure 1.23 shows two examples. Particles within the microfluidic channel experience radiation pressure, directing them towards local maxima in the intensity field. The technology has been

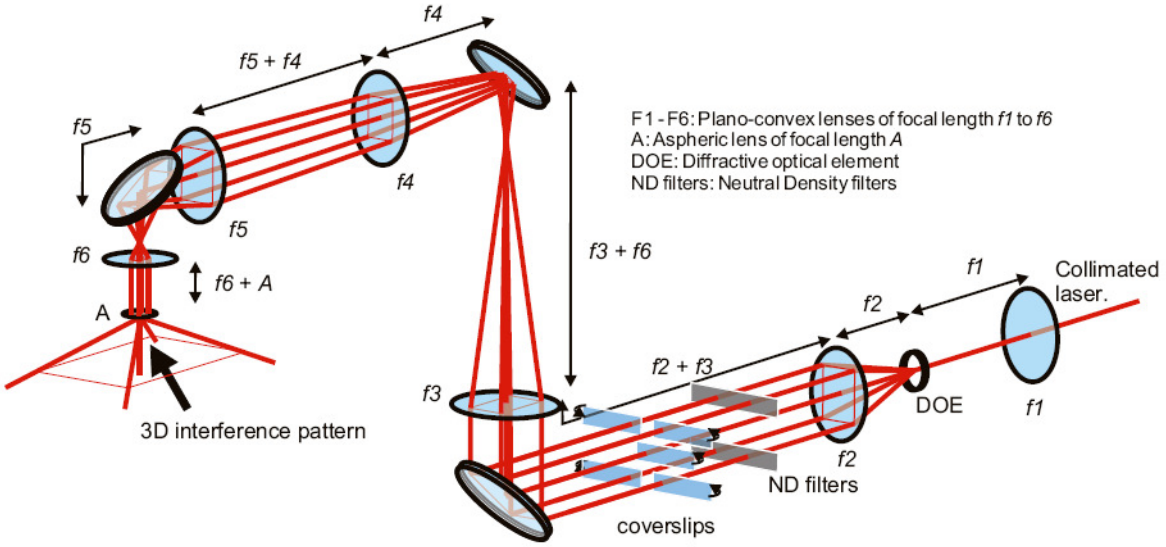

FIGURE 1.22: A diffractive optical element can be used to produce a 3D interference pattern suitable for optical trapping. Taken from MacDonald et al. (2003).

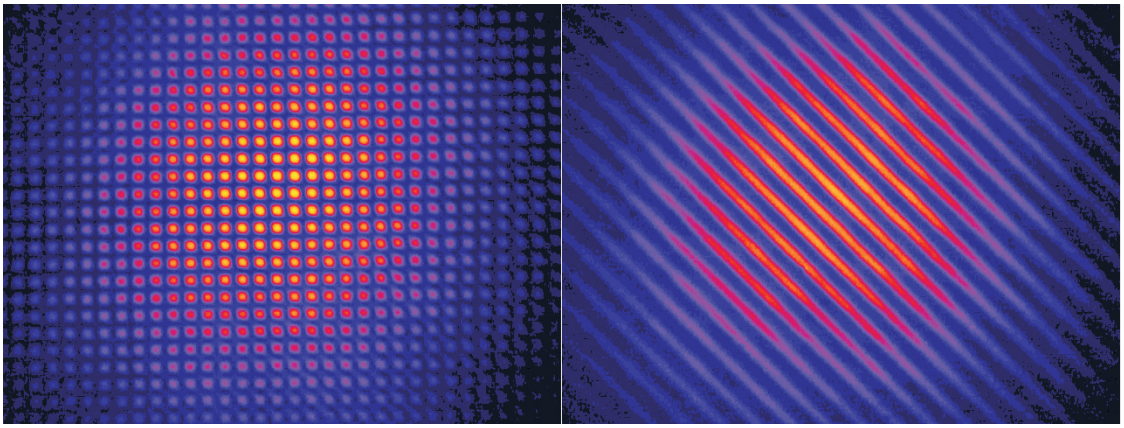

FIGURE 1.23: Intensity maps of the optical lattices produced by manipulation of the interference pattern, (a) isolated maxima produce a lattice of discrete optical trapping locations including and (b) conjoined maxima produce 'extended guides' or paths of equipotent force along which particles can move in conjunction with fluid motion. Taken from MacDonald et al. (2003).

demonstrated as suitable for trapping single particles, as well as sorting particles (including biological particles) by size or refractive index - see Section 1.4.4.3. As a trapping technology, the system is useful as it allows cell patterning on any plain glass substrate, without the need to fabricate electrodes or mechanical traps. Trap locations can be easily reconfigured, and the method could be easily scaled to trap much larger numbers of particles. The inability to address individual traps does place limitations, however, on its usefulness as a platform for single particle manipulation.

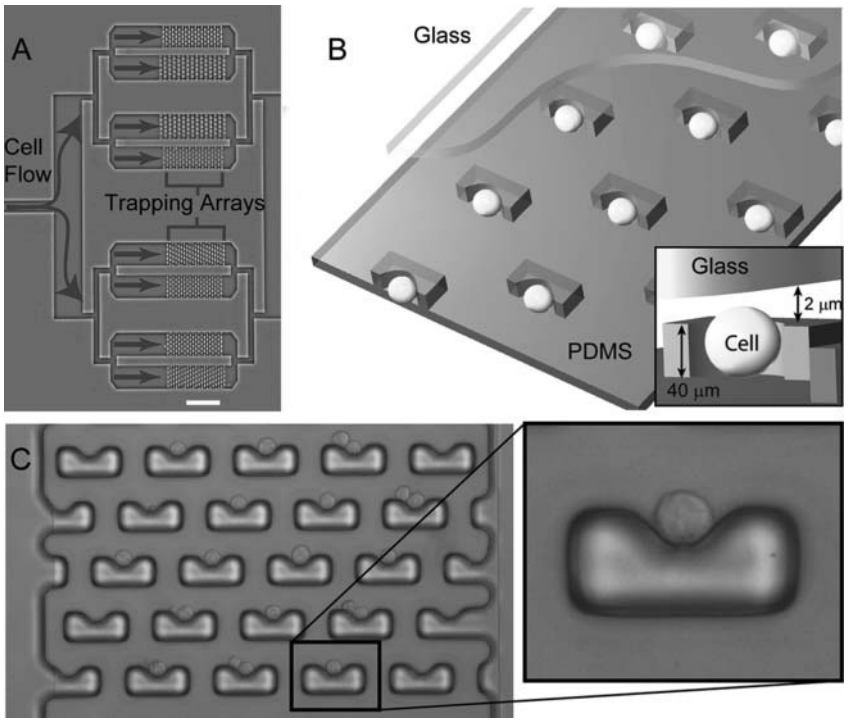

FIGURE 1.24: Hydrodynamic single cell trapping arrays. Taken from Carlo et al. (2006)

1.3.4 Hydrodynamic Techniques

The hydrodynamic trapping arrays developed by Carlo et al. (2006) have the advantage that they are inherently passive - requiring only the continued passing of fluid to locate and hold cells into shaped wells (see Figure 1.24). Small gaps above each trap permit fluid to flow over the trap, guiding cells in. Once located in the trap, hydrodynamic pressure keeps the cell pressed against the well. Accurate sizing of the well to the cells for trapping means that only single cells are trapped. Reliable and repeatable trapping of single cells in precise locations has been demonstrated, as well as cell adherence and proliferation. Traps are, however, not individually addressable. Cells can be released by flow reversal (before adherence), but release of a single cell is not possible.

1.4 Cell and Particle Separation Techniques

Biological cells naturally occur in heterogeneous populations, with multiple specialised cell types in codependence. While study of cells in their natural environment is an important discipline in its own right, it can be difficult to determine the cause-effect relationships within such a system. Hence, the first step in many cell biology experiments is to isolate or purify the cells of interest (Eisenstein, 2006). There is also much interest in cell isolation as a tool for medical therapeutic use. An example is the group of cells known as stem cells, which are pre-cursor cells to all the differentiated cell types found in the human body (and other species). Isolation of stem cells could enable

tissues for transplant to be grown in vitro, with a broad range of subsequent therapies made possible. Mesenchymal stem cells can be obtained from samples of bone marrow, typically obtained from the femur or iliac crest by biopsy, but are typically a minority subpopulation that comprises less than 0.01% of the total number of cells. A method to efficiently isolate the stem cells must be found if they are to be widely used as a theraputic tool. Another example is autologous bone marrow transplants, in which a highly efficient method of separation is required to remove tumour cells from the graft product before it can be returned to the patient (Dainiak et al., 2007).

Orfao and Ruiz-Arguelles (1996) defines laboratory cell separation techniques as having two parts: a classification stage, where cells are identified by one or more discernible parameters, and a sorting/separation stage, in which cells are physically separated. Furthermore, separation techniques can be categorised as either bulk or single-cell techniques, with reference to the manner in which cells are processed.

1.4.1 Bulk Techniques

A wide variety of laboratory processes fall into the category of 'bulk' separation, such as centrifugation, filtration and cell affinity methods. The process of cell separation is applied to all of the cells in the sample simultaneously, and the classification and separation stages usually occur within a single step and exploit a single distinguishing cellular characteristic such as size or density as the mechanism of separation. The development of monoclonal antibodies has seen a rapid increase in the use of immunological methods of cell separation, including MACS (see below) which uses separate classification and separation stages. This category of techniques are often used as the first stage in obtaining a purified cell population as they offer high levels of enrichment and high throughput, in a relatively simple process. As an example, to isolate human bone marrow cells (HBMCs) from an ex vivo sample, the homogenised tissue would be centrifuged through a density gradient medium (such as Ficoll-Paque) to quickly separate the erythrocytes from the mono-nuclear cells. Although this method does not have the specificity to isolate the target cells in one stage, erythrocytes are by far the most numerous cell type present, so this method quickly allows 99% of the cells in the sample to be separated out.

1.4.1.1 Immunomagnetic Sorting

Cell populations that present particular surface antigens can be identified by attachment with antibody-labelled paramagnetic beads, and removed from solution by passage through a magnetic separator. The process is commonly known as magnetic-activated cell separation (MACS) - a trademark name for the separation systems developed by Miltenyi Biotec GmbH (Germany).

In conjunction with a strong magnet around the outside, large gradients in the magnetic field within the separator are created by ferrous obstructions such as steel wire or ball bearings. Cells labelled with the magnetic beads are retained within the separator, and can be subsequently recovered by removing the magnetic field and flushing through with the suspending medium. Cell populations can be purified by positive selection (direct labelling of the target cells expressing a particular antigen), negative selection (removal of cell populations that express a particular antigen), or a combination of both. Enrichment rates of more than 100-fold (positive selection) and depletion rates of several 1,000-fold (negative selection) can be achieved. Typically, 50nm beads are used, which have little effect on further analysis steps (such as FACS) or cell culture. It is difficult to perform further MACS separations on sub-populations once the parent population has been labelled with magnetic beads, however, as the separation is inherently a binary process (Miltenyi et al., 1990).

The throughput of a MACS system can be difficult to define, as a typical sorting operation may take approximately 30 minutes to set up and perform, but virtually all of this time is spent in preparation and incubation stages with the number of cells sorted having little influence. Purity of recovered populations typically exceeds 90%, although this is dependent on the combination of surface antigens that are used to select the population (Willasch et al., 2009). Modern automated immunomagnetic separation systems (autoMACS, Miltenyi Biotec) have throughputs in the region of 10^7 cells per second.

1.4.2 Single-Cell Sorting

The analysis of large numbers of single cells, one after the other, removes the averaging effect that occurs when cells are analysed as a bulk population. It is particularly useful when the cell type of interest is a minority sub-population, whose significance would normally be overshadowed by more numerous cell types. During single-cell based sorting, cells are first categorised by an analysis technique, and then separated by a manipulation technique, so the whole process occurs through two distinct stages.

1.4.2.1 Fluorescence-Activated Cell Sorting

The technique of fluorescence activated cell sorting (FACS) was developed by Herzenberg et al. (1976) as an extension of existing methods of flow cytometry. Becton Dickinson Immunocytometry Systems introduced commercial systems in the 1970s, and it is estimated that there are now approximately 30,000 of the machines in use world-wide (Herzenberg et al., 2002).

Figure 1.25 shows an overview of the equipment used for FACS. The sample (a solution of cells or other particles) is pumped into the flow chamber, confined into a narrow stream

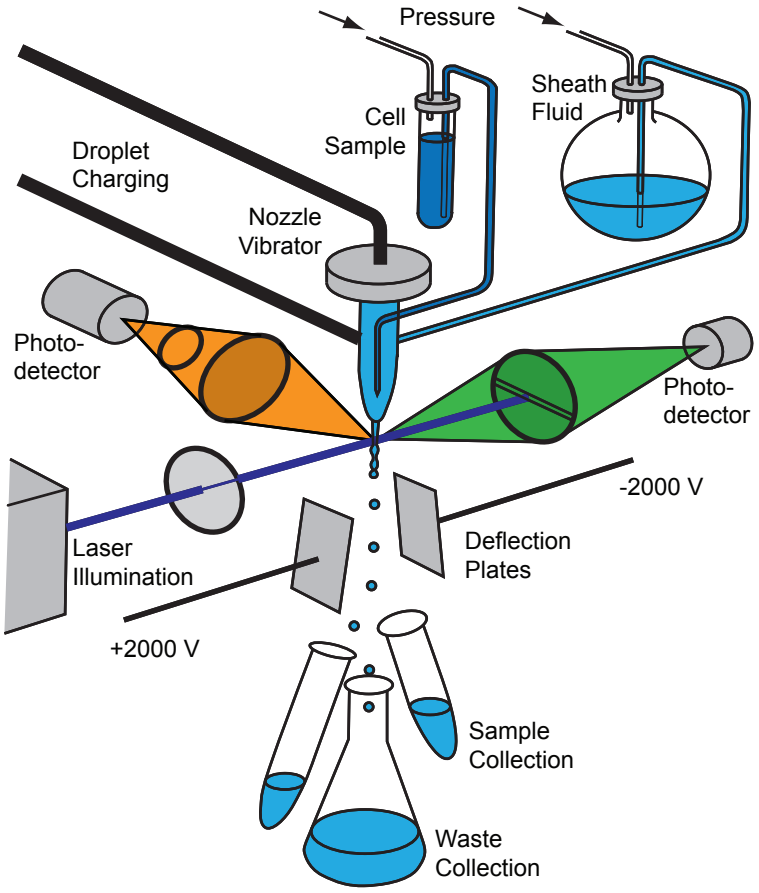

FIGURE 1.25: Overview of an early FACS machine, comprising of a single laser with two optical detectors. Adapted from Herzenberg et al. (1976).

by the sheath flow, and electrically charged by the droplet-charging electrode. The stream is forced through a narrow aperture, and is broken into a stream of droplets by a vibrating nozzle. Each droplet passes through a detection region and is illuminated by one or more laser beams, and emitted fluorescent signals are detected by the surrounding optical sensors. These fluorescent signals are used to switch the polarity on the high-voltage deflection plates, which direct each individual droplet into one or more collection chambers below.

The flow rate is maintained so that the probabilistic distance between each particle is large, to reduce the likelihood of multiple particles being confined within the same droplet. Some machines use software algorithms that can detect 'doublets', so that they can be rejected to a waste output to avoid contaminating the purified sample, although this must be deduced from the fluorescent signals and generally calculations are based on the peak amplitude and width of the fluorescent pulse. Modern FACS machines are able to process and sort many thousand fluorescence events every second, depending on the particle flow rates and concentrations used; specialist machines can operate at up to 70,000 particles per second (Eisenstein, 2006).

While some organisms, such as plankton and marine algae, have sufficient autofluorescence for useful measurements to be made on the cells in their native phenotype, it is more common to detect fluorescent signals from artificial fluorophores such as dyes or labels. Fluorescent dyes attach to particular regions of cells (such as the membrane, or nucleic material) and are useful to track cells as they are reintroduced to a mixed populations. Although dyes are generally not very selective, some can also be used as a means of viability assessment. Fluorescent conjugated antibodies can be used instead to identify particular surface antigens on a cell - the magnitude of the fluorescent signal for a particular cell reflects the number of antibodies bound to its surface.

Green fluorescent protein (GFP) has a single emission peak at 509 nm when excited with a blue light over a broad range of wavelengths. Originally isolated from the jellyfish *Aequorea victoria* by Shimomura et al. (1962), the protein has become a mainstay of biochemical research into gene expression. The GFP gene contains all the information necessary for the post-translational synthesis of the fluorophore, and no jellyfish-specific enzymes are needed (Tsien, 1998). Expression of the gene in other organisms produces fluorescent characteristics and unlike many other small fluorescent molecules (such as FITC) which are highly phototoxic, GFP within live cells can be illuminated without causing significant harm. Transfection of the gene into a particular regulatory sequence causes GFP to be simultaneously expressed with any other proteins that are coded for, so fluorescent measurements can be made on the expression of a whole range of other proteins (Chalfie et al., 1994). Shimomura, Chalfie and Tsien shared the 1998 Nobel Prize for Chemistry for their work on GFP.

Cell isolation is often an early step in the investigation of a particular cell type, so it is important that the phenotype of sorted populations is unchanged as a result of the sorting process. Concern has been raised about the effects of FACS sorting on cell health, particularly with regard to the hydrodynamic shear stresses that the cells experience on passing through the machine and during collection. Seidl et al. (1999) found an immediate decrease in cell viability following sorting (20-25% of population not viable, compared to <10% in control samples) of both N1 fibroblastic cells and BT474 breast carcinoma cells. While the loss of a certain proportion of the cell population can be compensated for by the considerable throughput possible with modern machines, the possibility exists of physiological changes within the remaining population. Disruption of the cellular membrane was detected in the remaining viable cells, possibly caused by the triggering of pressure-dependant ion channels, with membrane polarisation gradually returning to normal over the course of several hours following sorting. Changes in the membrane potential were also observed following MACS sorting, although the viability of recovered populations did not appear to be significantly affected. It was concluded that the majority of changes apparent after FACS and MACS sorting could be attributed to shear stress effects following passage through the sorting nozzle/magnetic separator. There are also safety concerns regarding sample aerosolisation as droplets are ejected

from the FACS flow cell. This is of particular issue if pathogenic organisms are being handled.

A number of alternatives to the electrostatic deflection of droplets used in conventional FACS machines have been developed, with the intention of sorting larger and potentially more fragile particles, with a high viability of recovered populations. An example is the COPAS family of instruments (Union Biometrica, MA, USA) that are designed for separation of cell clusters, embryos, and small organisms such as *C. elegans*. Particles are analysed using conventional flow cytometry, but are sorted into collection chambers by short pulses from jets of compressed air. Sorting rates of 100-300 particles per second are typical (Eisenstein, 2006). It is possible that microfluidic technologies may hold the future for cell processing with minimal disruption to the homeostatic processes of sorted cells, as it is possible to manipulate single cells within a microfluidic environment without producing the jets of high velocity droplets in air that are used in conventional FACS machines.

1.4.3 Microfluidic Techniques

Many classification and separation methods have been mirrored in the microfluidic environment, in particular the detection of fluorescent signals to identify cell types during single-cell sorting. Due to the reduced scaling, processes that have previously been described as *bulk* separation may be better termed *continual* separation when performed within a microfluidic device, as the entire population of cells is generally not sorted simultaneously; an example would be the use of magnetic microparticles by Adams et al. (2008) (see Section 1.4.4.2) that is analogous to MACS. Advantages of moving cell separation process to a microfluidic platform can include more sensitive optical detection (through small detection volumes), smaller devices with lower cost, and innovative sorting methodologies (Fu et al., 1999). It also enables new methods of cell classification that are not possible with macroscale devices, such as single cell impedance spectroscopy (Gawad et al., 2001; Morgan et al., 2007).

1.4.3.1 Flow Manipulation - Electrokinetic

A simple method to control the trajectory of a cell within a microfluidic device is to direct the flow of fluid within the device. Fu et al. (1999) used electroosmotic pumping to carry cells through the device and control their trajectory at a microfluidic junction. Electrodes were inserted into chambers at the inlet and each of the outlets, as shown in Figure 1.26 (a). This required voltages of 150 V to be applied to the electrode, producing a field of approximately 100 V cm^{-1} in the channel. Fluorescent measurements of particles and cells passing through the system were made using laser illumination and optical detection by a photomultiplier tube.

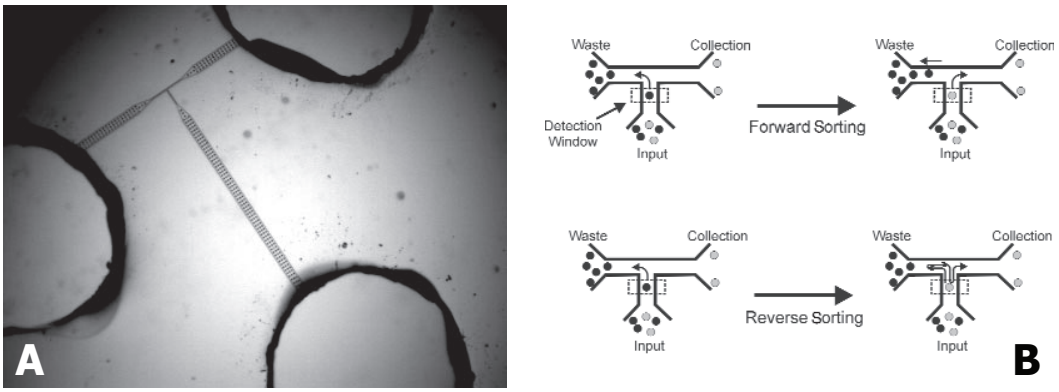

FIGURE 1.26: (a) An overview of the microfluidic channel used for cell sorting using electroosmotic flow. The large circular reservoirs can be seen at each of the inlets and outlets. (b) The use of a microfluidic flow cell enables innovative sorting methodologies to be used. The conventional method (forward sorting) is to direct particles to the appropriate output as they pass through the detection region. An alternative method that offers higher throughput and becomes practical if the target cells represent a small fraction of the total population is reverse sorting. Cells are carried through the device by the fluid flow at high speed towards the waste outlet. If a target cell is detected the flow is reversed to bring the cell back into the detection region at lower speed, and the flow is switched to direct the cell into the collection outlet. This method allows the sorting of cells moving at velocities that exceed the normal operating limit of the device (the switching speed). Taken from Fu et al. (1999).

Direct control of the fluid also enables innovative sorting strategies to be implemented for efficient, high-speed sorting. The 'reverse sorting' strategy - Figure 1.26 (b) - involves flowing cells through the device towards the waste output at speeds greater than at which cells can be reliably sorted. When a target cell is detected passing through the sorting junction, the flow is driven in reverse at a lower speed until the cell has been returned to the junction, at which point the cell is directed towards the collection output. This permits cells to be sorted at a rate that exceeds the normal system constraints imposed by the switching speed. Such strategies are not possible using conventional FACS machines. Red fluorescent beads were enriched by 80x, to a purity of 95.7% at approximately 10 beads per second; GFP E. coli were enriched by 38x, to a purity of 30.7% at approximately 17 cells per second. The use of electroosmosis does impose some limitations on the system, however. The large voltages required necesitate the use of high voltage amplifiers, and it was found that the voltage levels needed to be frequently adjusted to compensate for ion depletion and pressure imbalances within the system (Fu et al., 2002). The viability of recovered populations was approximately 20%; Dittrich and Schwille (2003) observed a similar reduction in cell health at such electric field strengths.

Electroosmosis was also used by Dittrich and Schwille (2003) to sort fluorescent beads and cells within a microfluidic channel, although a cross-channel flow was used to deflect the particles laterally in the main channel (see Figure 1.27). This would have alleviated some of the problems of ion depletion within the media usually encountered when

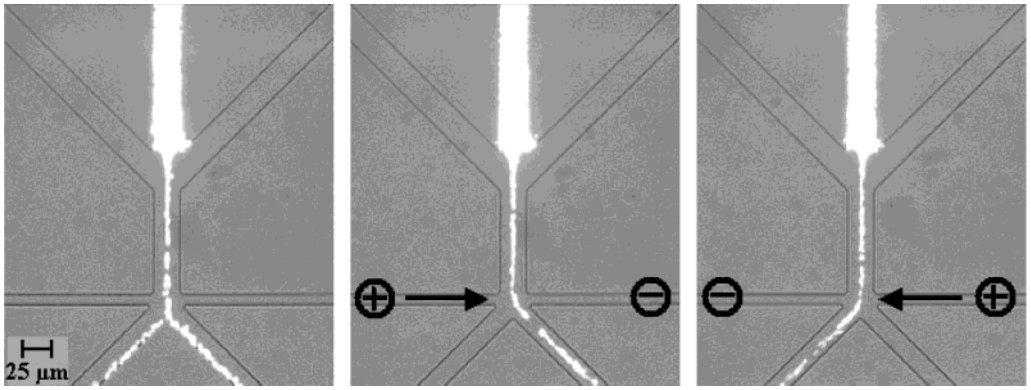

FIGURE 1.27: A sequence of images of a highly concentrated solution of fluorescent beads flowing through the microfluidic channel. Application of the electroosmotic flow produces a small displacement in the particles trajectory, sufficient to deflect them into either the left or right outlet. Taken from Dittrich and Schwille (2003).

electroosmosis is used, as fresh medium (cell suspension) was being continually pumped through the device. Electric field strengths of 100 V cm^{-1} were required. Fluorescent beads were enriched by 4.5x, to a purity of 94.8% at approximately 0.79 beads per second. *E. coli* cells were also sorted with a viability of 80-90% at electric field strengths of 30 V cm^{-1}, although data on the rate or purity was not presented.

1.4.3.2 Flow Manipulation - Valve Control

The fluid flow within a microfluidic device can also be manipulated with flow control valves. Fu et al. (2002) demonstrated an integrated device with valves and peristaltic pumping fabricated on chip in multi-layer PDMS structures, controlled by compressed air through external pneumatic solenoid valves. Fluorescence observations were made as a stream of cells flowed through the device and target particles were selected by momentarily reconfiguring the flow control valves so that the fluid and cell passed through the recovery outlet. By keeping the pumping equipment on-chip, it was possible to quickly reconfigure the direction and velocity of the flow, so innovative 'reverse sorting' methodologies could be implemented - see Figure 1.26. GFP-transfected *E. coli* were sorted from the wild-type using this method, and data was presented on a variety of sorting configurations, most notably cells sorted at 2.16 cells sec^{-1} with a recovered purity of 34% (an enrichment of 13x), and 44 cells sec^{-1} with a recovered purity of 3.6% (an enrichment of 83x).

Wolff et al. (2003) used a similar technique to sort fluorescent latex beads from chicken red blood cells, although the fluid flow was controlled directly by an external fluid solenoid valve. Although the target particle was not a biological cell, the overall throughput was 12,000 cells sec^{-1} with a recovered purity of 0.24% (an enrichment of 100x).

Although the fabricated device was quite complex, as it contained a number of components including an integrated cell culture chamber, this shows that cell populations can be significantly enriched using a commercial microvalve, and that custom built on-chip valves or electrodes are not always required. It is not clear, however, if the use of an external valve restricted the purity of the recovered population that could be achieved. The reported values (0.24%) are quite low, and this could be caused by the switching speed of the valve and its internal volume being such that a large volume of fluid flows into the collection channel each time it is opened, meaning that selection of an individual particle is not possible. Alternatively, the concentration of negative cells within the cell suspension may have been so high that selection of an individual cell was not possible regardless.

1.4.4 Particle Manipulation

An alternative method of particle separation is to manipulate the particles directly, rather than the fluid that suspends them. Many of the manipulation technologies that fall into the category, such as dielectrophoresis, have only been made practical as a result of the development of microfabrication technologies, as the forces that can be produced scale favourably with a reduction in the spacing of the electrodes. A principal advantage of using microelectrodes and dielectrophoresis is the ability to manipulate single cells and particles.

1.4.4.1 Particle Manipulation - Electrokinetic

The potential to use dielectrophoresis to separate mixtures of cells and particles was recognised early on, and many different methods have been attempted. Cells with different sizes or electrical properties exhibit differing electrokinetic responses (also known as dielectric affinity), so it is possible to use dielectrophoresis to separate cell populations based on these properties. Becker et al. (1995) used this method to separate human metastatic breast cancer cells (MDA231) from normal peripheral blood cells using dielectrophoresis and a castellated electrode. By measuring the response of cells to electrokinetic manipulation using electrorotaion (see Section 2.3.1), a frequency window was observed in which the breast cancer cells would experience positive DEP and the peripheral blood cells would experience negative DEP. Hence, the breast cancer cells were drawn towards the edges of the electrodes, and immobilised in the high-field regions, while the normal peripheral blood cells were repelled from the electrodes and could be removed from the device by fluid flow. This technique provides a simple method to separate cells, although as one population is retained on the electrodes there is a practical limit to the number of cells that can be separated before the electrodes become saturated with cells and must be removed.

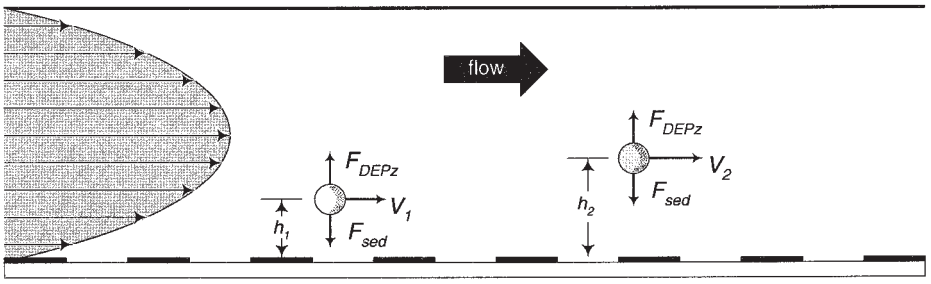

FIGURE 1.28: Cross-sectional view along the central axis of the microfluidic channel used for dielectrophoretic field flow fractionation. Particles above the microelectrode array patterned on the bottom of the channel experience negative DEP, lifting them towards the centre of the channel. At a certain height, a force equilibrium is reached with the sedimentation forces. Particles move through the channel at the local velocity of the fluid, so particles nearer the centre move faster. Taken from Wang et al. (2000).

Morgan et al. (1997) used large arrays of travelling-wave electrodes (see Section 2.3.1) for the continual separation of erythrocytes and leukocytes from human blood samples. Cells were levitated above the electrodes by negative DEP, and transported along the array by travelling-wave forces. Data on throughput or purity is not available, as samples were not recovered from the device for further analysis, but cell types were observed moving in opposite directions, with mean velocities of 32 μm s^{-1} for the erythrocytes and 20 μm s^{-1} for the leukocytes. This method has the advantage that cells are not retained on the electrodes, so providing cells can be correctly transported to the electrode array and sorted cells carried array from its ends, it represents a true continuous sorting process.

Particle separation on the basis of dielectric affinity has been shown capable of differentiating between cell types, and is of interest as it is a label-free technique - requiring no modification of the cells, such as fluorescent labelling. The technique is not widely used, however, as it is necessary to perform the dielectrophoretic manipulation with the cells suspended in a medium of artificially low conductivity in order to create the conditions in which cells can experience both positive and negative DEP. Although the medium can be rendered isotonic by additional sugars, the lack of essential ionic constituents is not conducive to long term cell viability. It is also necessary to accurately map the response of each cell type to electrokinetic manipulation, an involved and laborious process.

Field flow fractionation, described by Giddings et al. (1976), is a family of techniques that uses the parabolic flow velocity profile produced by laminar flow in microfluidic systems to separate particles under the action of a cross field at right-angles to the channel. The cross field distributes particles into different positions across the parabolic flow profile, based on their mobility within the cross field. Particle species separate as they move with the velocity at which the fluid is moving at that position in the flow profile. Particles with a higher mobility in the cross field are distributed closer to the centre of the channel and so travel faster than particles with a lower mobility that are positioned closer to the wall. The cross field can be any phenomenon that exerts a force

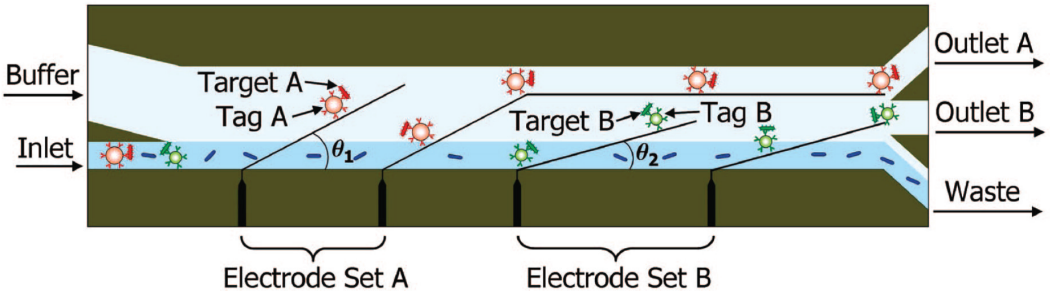

FIGURE 1.29: Overview of the microfluidic channel used for dielectrophoretic separation of *E. coli* cells labelled with polystyrene microparticles. The angle of the DEP barriers meant that only the larger Tag A experienced sufficient force to be deflected by Electrode Set A towards Outlet A. The smaller Tag B was deflected by Electrode Set B towards Outlet B, while the unlabelled bacteria were not deflected and were carried by the flow towards the waste outlet. Taken from Kim et al. (2008).

on particles within the channel, such as electrical, magnetic and gravitational forces, a thermal gradient, or a cross fluid flow. Huang et al. (1997) used dielectrophoresis within a microfluidic channel to induce field flow fractionation, with an interdigitated array of microelectrodes along the bottom surface of the channel to lift cells into the fluid flow, and separate HL-60 cells from peripheral blood mononuclear cells. Wang et al. (2000) used a similar system to separate human breast cancer cells (MDA-435) from normal T-lymphocytes and CD34+ hematopoietic stem cells with purities in excess of 90%. Figure 1.28 shows a cross-sectional view through the microfluidic channel used for field flow fractionation.

The methods described above are useful as they enable cell populations to be separated continuously without complicated external hardware or control systems, but fall down when cell sub-populations cannot be well distinguished by their electrical properties (such as in high conductivity physiological medium, where all cells experience negative DEP). An alternative approach for the continuous separation of cells is to bind differingly-sized synthetic particles on to cells using immunological methods. Kim et al. (2008) used this method to separate three different strains of *E-coli* bacteria, using nDEP barriers at different angles across a microfluidic channel (Figure 1.29). Much stronger DEP forces were produced than would have otherwise occurred if the bacteria alone were processed, as they were attached to large polystyrene particles. Cells were sorted at a rate of approximately 1.5 x 10^7 cells hour^{-1} (about 4.2 x 10^3 cells sec^{-1}, although samples contained a large number of non-target cells (99.559%). The population of 'target A' cells in outlet A increased from an initial population of 0.071% to 66% corresponding to a 930-fold enrichment. Similarly, the 'target B' cell population in outlet B was enriched 260-fold from 0.37% to 96%.

Numerous systems have also been produced for single-cell processing and sorting. Fiedler et al. (1998) describes a system for the cell processing in which particles are focused, trapped and sorted by switching negative DEP barriers. Fluorescent observations were

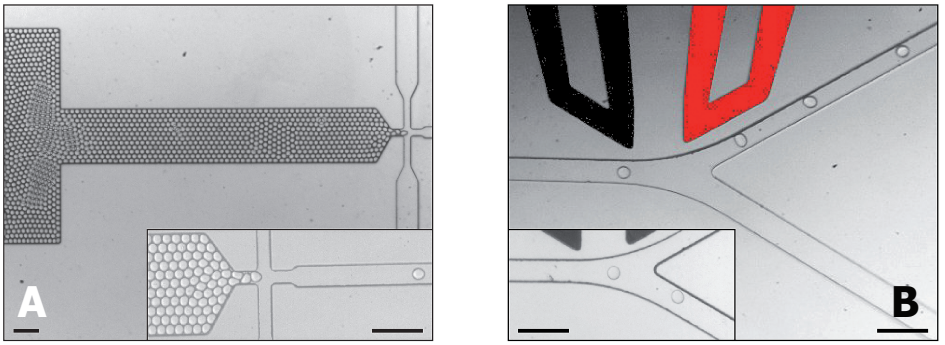

FIGURE 1.30: Preformed droplets were dispensed into the channel within a sheath flow of fluorinated oil and surfactant (a). Droplets naturally flow down the larger waste channel (lower, see inset) unless deflected towards the electrodes (above the channel) by pDEP and into the smaller recovery channel (b). Scale bar 100 μm. Taken from Baret et al. (2009).

made through a microscope system, although these signals were not used to automatically switch the sorting electrodes. Synthetic 15 μm latex particles in low conductivity buffer (100 μS cm^{-1}) were manipulated, as well as L929 mouse cells in RPMI, 5% FCS (σ_m = 1.3 S m^{-1}), although no data on throughput or purity was presented.

Baret et al. (2009) used positive DEP to separate fluorescent aqueous droplets suspended in oil. Figure 1.30 shows an overview of the channel and electrodes used. The electrodes are outside of the channel and hence are insulated from the liquid. This meant that large voltages were required to sufficiently deflect the droplets, 1.4-1.6 kV at 30 kHz. Nevertheless, droplets could be deflected at rates of up to 2000 sec^{-1} under these conditions. Laser illumination with photomultiplier detection was used for fluorescence measurements. The use of droplets as a carrier mechanism for particles helps optimise the sorting process, as droplets arrive at the sorting junction at regular intervals and their spacing can be controlled.

Droplets containing small groups of *E. coli* cells were also sorted, based on the activity of a fluorogenic enzyme, at 300 droplets sec^{-1}. The concentration of cells was reduced to avoid the co-encapsulation of multiple cells within a single droplet, the final ratio being approximately one cell per 50 droplets. Although detailed data on the purity of recovered populations is not presented, the false positive error ratio was estimated at less than 1 in 10,000 (or >99.99% purity). It was noted that the major limit on the efficiency of the operation arose due to co-encapsulation of multiple cells within a single droplet rather than due to the sorting equipment itself. The use of a fluorogenic enzyme aids the detection process, as its action releases fluorescein that causes the entire droplet to fluoresce brightly - an easier target to detect than a single fluorescent bacterial cell.

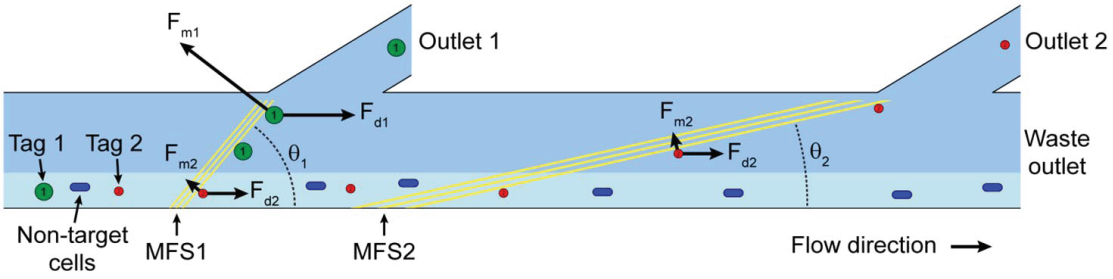

FIGURE 1.31: An overview of the microfluidic channel used for the separation of *E. coli* MC1061 cells bound to 2.8 and 4.5 μm diameter magnetic beads functionalised with monoclonal antibodies. The larger beads (Tag 1) were most affected by the magnetic field gradient, so were deflected by MFS1 which is inclined at a large angle to the flow, and left the device through outlet 1. The smaller beads (Tag 2) passed through the barrier but were deflected by MFS2, which is at a shallower angle to the flow, and left the device through outlet 2. The non-target cells (unattached to magnetic beads) were not affected by the magnetic field gradient, so were carried by the fluid flow to the waste outlet. Taken from Adams et al. (2008)

1.4.4.2 Particle Manipulation - Magnetic

It is also possible to use magnetic microparticles to separate cells within a microfluidic environment. Adams et al. (2008) demonstrated the separation of bacterial strains bound to 2.8 and 4.5 μm diameter magnetic beads functionalised with monoclonal antibodies. Termed 'magnetophoresis', as large gradients in the magnetic field (from an external permanent magnet) are created locally by microfabricated ferromagnetic strips (MFS), the technique has been used to separate bacterial cell types with >90% purity and >500-fold enrichment at a throughput of 10^9 cells per hour, although a large excess of non-target cells made up the bulk of the processed cells. Figure 1.31 shows an overview of the microfluidic system used - MFS barriers are positioned upstream of outlets 1 and 2, first at a large angle to the fluid flow to catch the larger particles that experience a stronger force, and then at a shallow angle for the smaller particles.

The technique is interesting as it permits multiple different cell types to be positively selected (see above) for recovery in a single stage. Although it would require multiple separation cycles to perform this operation with standard (macroscale) MACS, this would still be faster than microfluidic separation, as both methods require lengthy preparation and incubation steps, but the physical cell separation step requires minutes with standard MACS to achieve what may take an hour with the microfluidic system. The commonly used 50 nm diameter MACS beads have been shown to have little effect on subsequent processing such as FACS - the larger particles necessary for the microfluidic system may interfere with some measurements of scattered light. As the microfluidic device is a continuous sorting system, magnetic particles are not retained within the separation device as is the case with conventional MACS. Hence, there is no risk of saturation of the magnetic separator if large numbers of cells are processed.

1.4.4.3 Particle Manipulation - Optical

Detection of fluorescent signals for particle classification is widely used, but optical forces can also be used during the physical separation stage of particle sorting. MacDonald et al. (2004) produced a 3-D interference pattern to create a network of connected optical traps (described in Section 1.3.3), which was used to sort erythrocytes and lymphocytes based on differences in size and refractive index, with efficiencies achieved in excess of 95%. An advantage of optical systems is that the interference pattern can be rapidly reconfigured, and tailored to the particle sizes. If a blockage occurs, the laser can simply be switched off. An optical system is often required around a microfluidic system for observations, so the additional equipment for creating the optical lattice may only require a few additional components.

Wang et al. (2005) used optical forces to drive a microfluidic single-cell sorting platform. Fluorescence measurements were made on a hydrodynamically focused stream of cells as they passed through a detection region. Target cells were selected from the stream by momentarily switching (2-4 ms, by acousto-optical modulation) a focused laser beam on to the channel, slightly offset from the stream. Radiation pressure drew the selected cells towards the centre of the beam, and into a flow streamline that would carry them through to the collection outlet. The system was used to sort GFP-transfected HeLa cells (human cervical carcinoma) from non GFP HeLa cells, with recovered sample purities of 88.6% (105.9 cells sec^{-1}) to 98.5% (22.9 cells sec^{-1}). The transfer of all switching hardware off-chip means that the microfluidic device only comprises a simple three inlet, two outlet channel, and can be constructed from any optically-clear material. Quite significant optical power was necessary to achieve the specified sorting rates - a 20 W ytterbium fibre laser (1070 nm) was the source for the switching element, typically used for engraving or micro-welding.

Kovac and Voldman (2007) used a combination of hydrodynamic, gravitational and optical forces to sort fluorescent cells. An array of microwells was moulded in PDMS, which formed the bottom of a microfluidic channel. A mixture of cells was introduced into the device, and were allowed to settle to the bottom of the channel. Fluid was passed through the device, and cells which had not settled into the bottom of the wells were washed out of the device. The remaining cells were sorted by levitating non-target cells out of their microwells using a focused laser beam so that they were washed out of the device. Figure 1.32 shows an overview of the device. The technique was coined 'image-based' cell sorting, as sorting decisions were based on the interpretation of microscopy images of cells produced by a colour CCD camera, rather than the signals from a photomultiplier tube that are used in most other fluorescence-based cell sorting equipment. This allows a large range of additional data to be collected on each cell, such as size and morphological features, as well as the fluorescent intensity. As cells are immobilised at fixed positions, measurements can be made repeatedly, in a similar manner

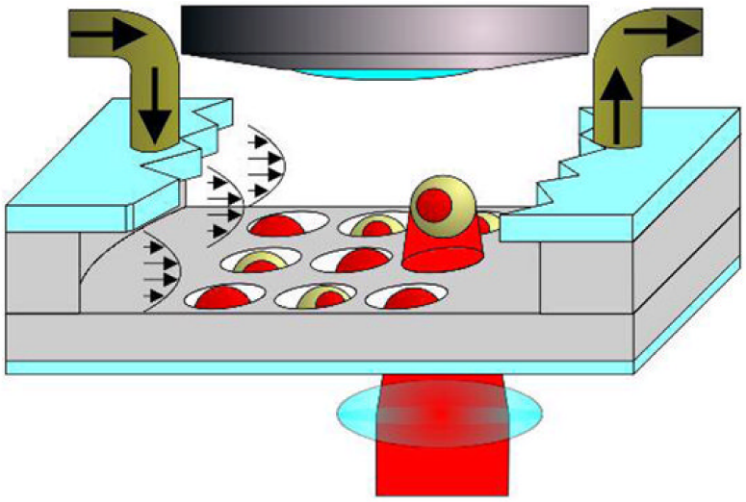

FIGURE 1.32: A cell is removed from a microwell by a focused laser beam during cell sorting. Taken from Kovac and Voldman (2007).

to the screening cytometer, described in Section 1.3.2. As a cell sorting technique, it is markedly slower than most other methods, with approximately 70 cells being sorted per hour, and a purity of 89% being achieved. It was not possible to recover all of the sorted cells from the microfluidic device into culture, with the recovery ratio varying between 26 and 74%.

1.4.5 Summary of Sorting Techniques

Table 1.1 shows a summary of the key parameters of the microfluidic sorting devices discussed above, for which data concerning throughput and the purity of recovered populations is available. As can be seen from the multiple entries present for some devices, there is generally a relationship between sorting rate and the purity of recovered populations. Usually a compromise between the two must be sought, with reference to the intended application for the sorted cells. For example, the impressive throughput achieved by Wolff et al. (2003) of 12,000 cells sec^{-1} must be weighed against the low purity of the recovered population: the particle solution was most likely almost saturated with chicken red blood cells, and every fluorescent particle that was sorted was accompanied by approximately 400 other, non-target cells. Nevertheless, this still represents an enrichment of 100 times, and with multiple sorting stages such a system may represent a practical route to high-throughput, high-purity sorting.

Data from Baret et al. (2009) is not included in Table 1.1 as insufficient data was presented for an accurate comparison. Fluorescent droplets containing *E. coli* bacterial cells were sorted at a rate equivalent to 6 cells per second, however, with a false positive error ratio estimated at less than 1 in 10,000. Such droplets are a very suitable target for fluorescence-activated sorting as they are large, bright, and reasonably uniform in intensity. Droplet technology offers many advantages to microfluidic cell sorting devices,

as it provides a means to control the rate and regularity at which cells arrive at the sorting junction. The droplets can also provide an enclosed microenvironment conducive to cell viability, so that a suspending medium can be chosen that is optimised for DEP manipulation, such as a fluorinated oil that has very low conductivity and permits high voltages to be used without causing significant heating of the medium.

Bulk sorting technologies such as immunomagnetic (Adams et al., 2008) and immunodielectrophoretic (Kim et al., 2008) dominate the table in both the sorting rate and the enrichment possible. The main concern with both of these methods is that the cells are bound to synthetic particles that are larger than the cells themselves, which may complicate further processing and analysis. The most commonly used method to isolate specific cell types with high purity remains a two step process: bulk separation using immunomagnetic techniques, followed by single-cell separation such as FACS.

Originators	Year	Method	Sorting Rate	Max. Purity	Enrichment
Fu et al.	1999	Electroosmosis	20 cells sec^{-1}	30.8%	30x
Fu et al.	2002	Valve Control	2.16 cells sec^{-1}	34%	13x
			44 cells sec^{-1}	3.6%	83x
Dittrich et al.	2003	Electroosmosis	0.68 beads sec^{-1}	99.1%	1.1x
			0.79 beads sec^{-1}	94.8%	4.5x
Wolff et al.	2003	Valve Control	12,000 cells sec^{-1}	0.24%	100x
Wang et al.	2005	Optical	22.9 cells sec^{-1}	98.5%	1.9x
			105.9 cells sec^{-1}	88.6%	8.3x
Kovac et al	2007	Optical	70 cells $hour^{-1}$	89%	155x
Adams et al.	2008	Magnetic	2.7 x 10^6 cells sec^{-1}	93.9%	245x
Kim et al.	2008	DEP	4200 cells sec^{-1}	96%	260x

TABLE 1.1: Performance data for several microfluidic sorting devices published in scientific literature. Where data for multiple combinations of speed/purity existed, the data sets with the highest purity and highest sorting rate are listed.

Chapter 2

Background Theory

2.1 Concepts in Electrostatics and Electrodynamics

An electric charge can be described as an excess (negative charge) or shortage (positive charge) of electrons, in comparison to a body that is electrically neutral. Such a body has equal numbers of positive and negative charges, and so has no overall charge. A charged particle in an electric field experiences a Coulomb force:

$$F = Q\mathbf{E} \tag{2.1}$$

Q is the electric charge on the particle, and $\mathbf{E}$ is the electric field vector. The electric field surrounding a charged particle (point charge) can also be described, using the equation below:

$$\mathbf{E} = \frac{1}{4\pi\epsilon}\frac{Q}{r^2}\hat{i} \tag{2.2}$$

r is the distance from the particle centre to the point of interest, and $\hat{i}$ is the unit vector from the particle centre to the measurement location.

The displacement of charged particles within an electric field is the phenomenon of electrophoresis - and is commonly used as a scientific tool to identify small charged particles, such as proteins or DNA. Particles are identified by the distance that they move through a viscous gel under an electric field in a given time - charge and size of the particles determining the Coulomb and hydrodynamic drag forces on the particle, the sum of these determining the velocity at which the particle moves. A picture of the arrangement inside a typical machine for sample identification using electrophoresis is shown in Section 1.2.1.

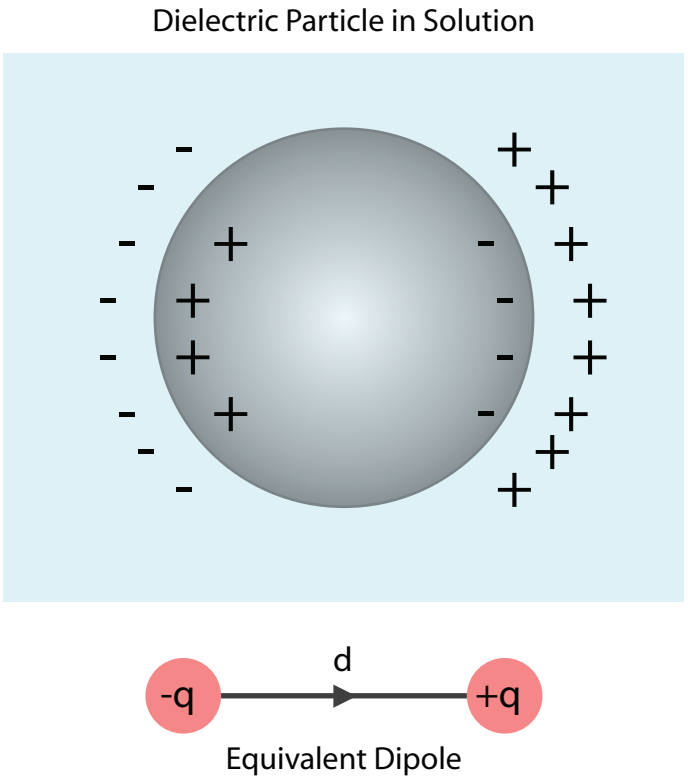

FIGURE 2.1: A dielectric particle in a more polarisable solution: under the influence of an external electric field an equivalent dipole is formed.

A dipole is a pair of opposite charges, separated by a fixed distance d. Dipoles can exist naturally, such as across molecules of water, or can be created by the movement of charges (see below). The net movement of electrons is described as an electric current, and the ease at which electrons move through a material defines it as a conductor, semiconductor or and insulator. Electrons are free to move through the lattice of a metallic conductor relatively unhindered, due to overlapping electron orbits. No such mechanism exists in materials described as insulators, and hence the energy required to drive electrons through such a material is significantly higher. The electrons in an insulating material are described as bound charges, because they are generally bound to an individual atom and are not free to move through the atomic lattice.

2.2 Polarisation of a Dielectric Particle

2.2.1 Electronic Polarisation

Electrons in an insulating material are considered to be bound to their parent atom, and do not readily flow through the material in the presence of an electric field. The electrons will be displaced, however, with the focus of their random orbits shifted by the force of the electric field on the charged particle. The charge in the material is no

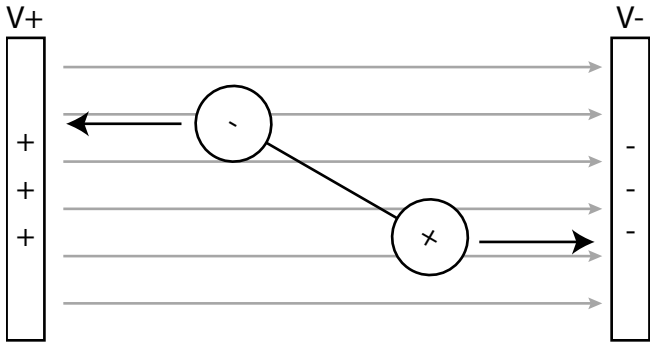

FIGURE 2.2: A dipole in a uniform field experiences a torque that directs it towards alignment with the field, but the net force on the dipole is zero.

longer evenly distributed, with regions of net negative and net positive charge at either ends of the body: the material is polarised. A particle in an electric field will polarise, as charges throughout the material are displaced. The surfaces of the particle will have a net charge, as electrons are displaced either towards or away from the surfaces. This difference in net charge across the particle can be modelled as an equivalent induced dipole, and in the case of a spherical, homogeneous particle in a uniform electric field, this is a valid mathematical model and is frequently used in the numerical analysis of electrokinetic systems. The polarisation of a material by the displacement of electrons is described as the electronic mechanism of polarisation.

2.2.2 Interfacial polarisation

In the case of a particle suspended in a dielectric liquid, the charges at the surface of the particle attract oppositely charged counter-charges from the liquid - this is known as interfacial polarisation. If the effective polarisability of the medium is different to that of the particle, the magnitude of the counter-charge that is developed from the medium will be different to the surface charge on the polarised particle - leading to a difference in the net charge across the particle - see Figure 2.1.

In the case of a spherical, homogeneous particle, this difference in net charge across the particle can be modelled as an equivalent induced dipole. Particles of other geometry or configuration can be modelled by an equivalent induced multi-pole.

2.3 Dielectrophoresis

A dielectric particle placed in an electric field will polarise, forming an induced equivalent dipole. A dipole in a uniform electric field will experience a torque, directing it towards alignment with the field, but as Figure 2.2 shows, the net force on the dipole is zero because an equal and opposite force acts on each half of the dipole.

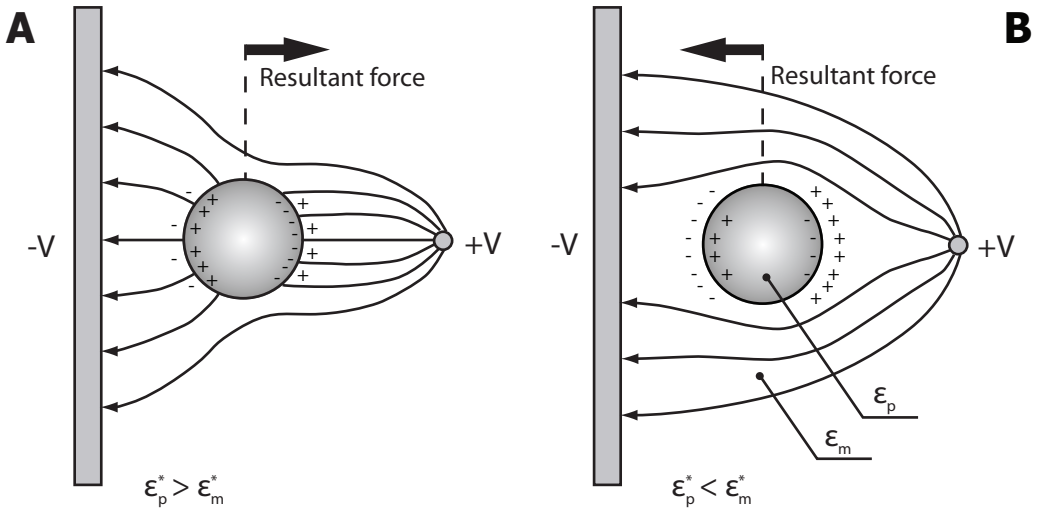

FIGURE 2.3: (a) Positive and (b) negative DEP. Adapted from Medoro et al. (2007).

If the electric field is not uniformly distributed, however, the electrostatic force on each half of the dipole will be different, resulting in a net force on the dipole - this is the dielectrophoresis effect. The direction that the DEP force acts is dependent on the relationship between the polarisability of the particle and the polarisability of the medium, described by the Clausius-Mossotti factor (see below). The time averaged DEP force can be calculated by the equation (Morgan and Green, 2003):

$$\langle F_{DEP} \rangle = \pi \epsilon_m a^3 Re(f_{CM}) \nabla |\mathbf{E}|^2 \tag{2.3}$$

ϵ_m is the permittivity of the suspending medium, $Re(f_{CM})$ represents the real part of the Clausius-Mossotti (CM) factor, and $\mathbf{E}$ is the peak value of the electric field vector. The CM factor is a complex number that describes the polarisability of the system (particle and medium), and for a homogeneous sphere it can be calculated as:

$$f_{CM} = \frac{\epsilon_p^* - \epsilon_m^*}{\epsilon_p^* + 2\epsilon_m^*} \tag{2.4}$$

ϵ_p^* is the complex permittivity of the particle, and ϵ_m^* is the complex permittivity of the medium. The complex permittivity can be calculated from the electrical properties of a material:

$$\epsilon^* = \epsilon - j\frac{\sigma}{\omega} \tag{2.5}$$

ϵ is the bulk permittivity of the material, σ is the conductivity, ω is the angular frequency of the applied electric field and j is the imaginary vector.

The polarisation relationship between the particle and the medium defines the direction of the induced dipole, and hence the DEP force. Figure 2.3 (a) shows the case where the complex permittivity of the particle exceeds that of the medium - Equation 2.4 evaluates to have a positive real part, and the DEP force directs the particle towards regions of high electric field strength. This is called positive DEP. Figure 2.3 (b) shows the case where the complex permittivity of the particle is less than that of the medium - Equation 2.4 evaluates to have a negative real part, and the DEP force vector points towards regions of lower electric field strength. This is called negative DEP.

Figure 2.4 shows the variation in the Clausius-Mossotti factor for a 1 μm latex bead in an aqueous suspension of conductivity 0.1m S/m. As can be seen from Equation 2.5, the frequency is very important in determining the significance of the conductivity or permittivity. The low-frequency effects are dependent on the ratio of the conductivities, whereas the high frequencies are almost solely dependent on the ratio of the permittivities. The crossover frequency (f_{xo}) is the point at which the CM factor is equal to zero, and occurs when (Jones and Kraybill, 1986):

$$f_{xo} = \frac{1}{2\pi}\sqrt{\frac{(\sigma_p - \sigma_m)(\sigma_p + 2\sigma_m)}{(\epsilon_p - \epsilon_m)(\epsilon_p + 2\epsilon_m)}} \tag{2.6}$$

Measurement of the crossover frequency is a quick and simple method to asses the polarisability of a particle in comparison to the medium.

2.3.1 Electrorotation and Travelling-wave DEP

Figure 2.5 shows the waveforms of four alternating sinusoidal voltages, each with a phase-lag of 90° to the previous wave. When applied to the quadrapole electrode array (Section 1.2.3, Figure 1.7), a rotating electric field is produced. This will interact with an induced dipole on a particle within the electrodes to produce a torque on the particle. The torque can be calculated using the equation:

$$\langle \Gamma_{ROT} \rangle = -4\pi\epsilon_m a^3 Im(f_{CM})|\mathbf{E}|^2 \tag{2.7}$$

$Im(f_{CM})$ represents the imaginary part of the CM factor. The particle will rotate either with or against the direction of rotation of the field, depending on if the imaginary part of the CM factor is positive or negative.

Similarly, if the 4-phase electric fields are applied to the travelling-wave array shown in Figure 1.8, the field maxima will appear to move along the array, and will interact with the dipole induced on a particle above the electrodes to produce forces on the particle both perpendicular and parallel to the surface of the array. The travelling wave force

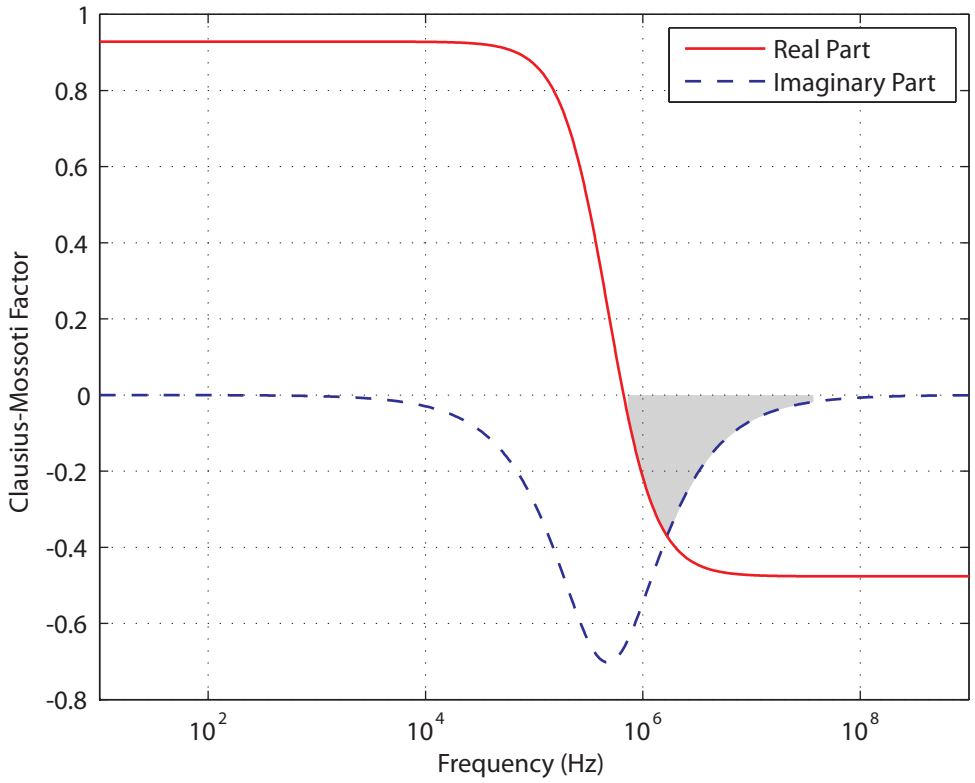

FIGURE 2.4: Plot of the Clausius-Mossotti factor for a 1 μm diameter latex bead in aqueous solution of conductivity 0.1 mS m^{-1}. Travelling wave DEP is feasible in the greyed frequency bands where the CM factor has a negative real part and a non-zero imaginary part.

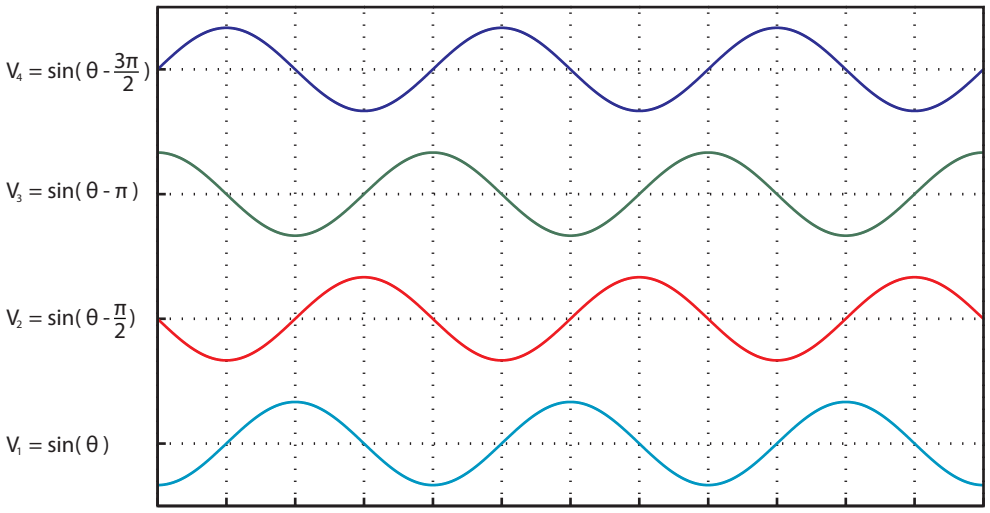

FIGURE 2.5: 4-phase waveforms used to drive an electrorotation array.

developed on a particle can be calculated from (Morgan et al., 1997):

$$F_{TWDEP} = \frac{-4\pi\epsilon_m a^3 Im(f_{CM})|\mathbf{E}|^2}{\lambda} \tag{2.8}$$

λ is the wavelength of the travelling field (determined by the geometry of the electrode array.) A particle will experience a DEP force (proportional to the real part of the CM factor) that attracts/repels the particle from the electrodes in conjunction with a ROT or TW force. In the case of electrorotation, a positive DEP force will destabilise the electrorotation effect as the particle is drawn towards the electrodes. The phase angle of 90° between neighbouring electrodes reduces the gradient of the electric field by a factor of 2, hence reducing the DEP force on the particle by a factor of 4. For the majority of particles (that are more dense than water), a negative DEP force is required for travelling-wave manipulation so that the particle is lifted above the electrode surface. The particle will rise until an equilibrium is reached between gravity and the (vertical) DEP force. Figure 2.4 shows a plot of the Clausius-Mossotti factor for 1 μm diameter polystyrene microparticles. Travelling-wave manipulation is possible in the greyed regions, where the real part of the CM factor is sufficiently negative for the cells to be levitated and the imaginary part is non-zero.

2.4 Interactions between Fluids and Electric Fields

2.4.1 Overview

Electrokinetic effects are not limited to the manipulation of microparticles in suspension, as interactions between the electric field and the fluid itself can also take place. Electric field-induced fluid motion is often produced unintentionally, when electrokinetic manipulation of microparticles was the primary intention. In such cases, it can be of help or hindrance. Electric field-induced fluid motion has also been intentionally exploited, such as its use as a pumping mechanism. Such techniques are useful as they permit pumping hardware to be integrated into microfluidic systems.

2.4.2 The Double Layer

Ionic content in a fluid greatly affects its electrical conductivity, acting as charge carriers. These electrolytic solutions (or electrolytes) are commonly used within microfluidic devices, particularly for the manipulation of cells as a certain level of salts are required to regulate the osmotic pressure. The local field that surrounds an ion in solution draws water molecules towards it due to their permanent dipole. This creates a cloud of water molecules around each ion (Morgan and Green, 2003).

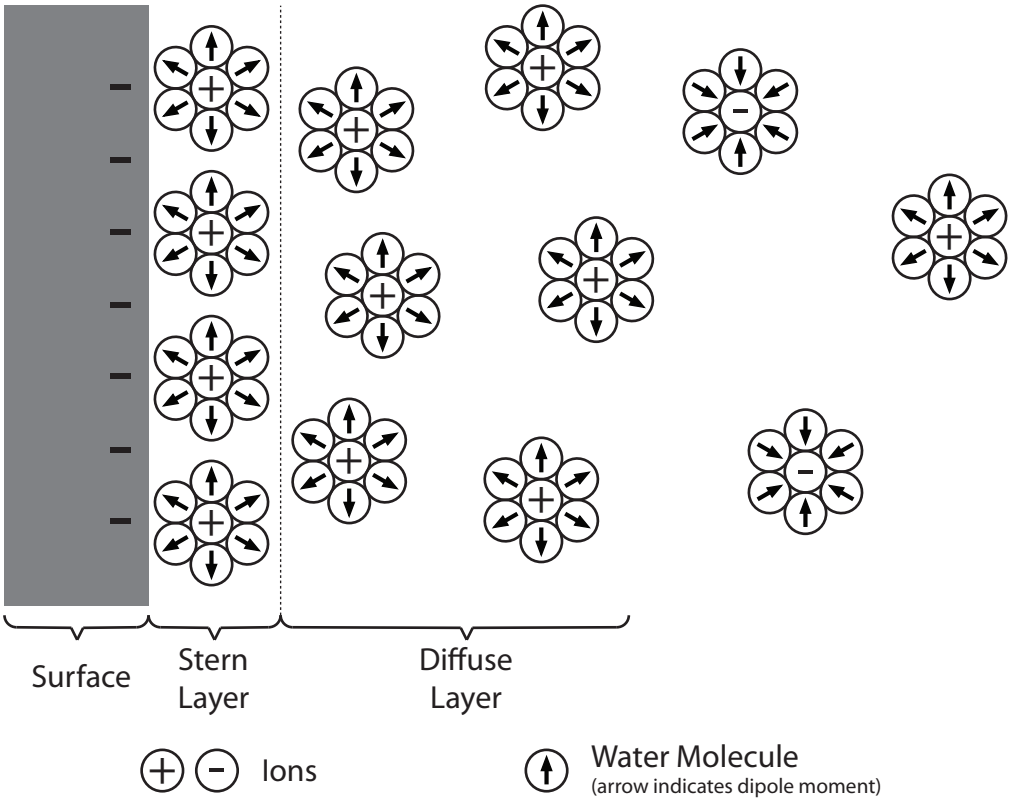

FIGURE 2.6: Counter-ions in aqueous solution are drawn towards a charged surface. Water molecules are drawn to the ions by their local field. An imbalance of ion concentration is created, forming the Stern and diffuse layers around the surface. Adapted from Morgan and Green (2003)

The interface between a solid surface, such as the wall of a channel or a suspended particle, and an electrolyte is strongly affected by surface charge and the presence of ions from the electrolyte. Surfaces can accumulate charge through dissociation of chemical groups on the surface, or adsorption of ions from solution; in the case of electrodes, an applied voltage causes movement of charge carriers through the circuit and a corresponding charge imbalance on the surface of the electrodes.

The electric field surrounding a charged surface draws counter ions from the solution towards the surface, creating a higher than average concentration of counter ions in the area around the electrodes, known as the diffuse layer. Figure 2.6 shows a schematic representation of this. In addition, the ions (with their associated cloud of water molecules) form a very thin layer, bound to the surface, known as the Stern layer.

The presence of counter ions at the surface/water interface acts as a capacitor, with the surface potential dropping over the double layer, so that the potential in the fluid bulk is much lower. In the case of an electrode driven with an alternating voltage, the effect is frequency-dependent. At low frequencies, much of the potential will drop over the counter ions at the electrode surface. With higher frequencies, the counter ions in the solution will not have sufficient time to re-establish polarisation at the electrodes before

the polarity reverses again, and majority of the potential will be applied across the bulk solution.

In hydrodynamic terms, the Stern layer represents a highly viscous, immobile monolayer. The outer surface of the Stern layer is the slip plane, the point at which fluid can move relative to the surface. The potential at this point is known as the zeta potential, and is a function of the charge density in the solution. Disruption of the charges in the double layer can induce fluid motion, known as electroosmosis.

2.4.3 Electroosmosis

An electric field in a direction parallel to a polarised interface will move charges in the double layer, generating a flow. The flow velocity is zero at the fluid/electrolyte interface, rising to its maximum at the slip plane. The velocity is maintained with a flat profile throughout the bulk of the fluid. This phenomenon has been exploited as a pumping technology, by applying a DC potential across the length of a microfluidic channel, such as Fu et al. (1999); Dittrich and Schwille (2003). The electroosmotic fluid velocity can be determined from Equation 2.9 (Morgan and Green, 2003):

$$u_x = -E_x \frac{\epsilon_m \zeta}{\eta} \tag{2.9}$$

ϵ_m is the permittivity of the fluid, η is the dynamic viscosity of the fluid, and ζ is the zeta potential at the interface. Electroosmotic flow is particularly significant as the fluid velocity profile is flat across the bulk of the fluid, very different from the parabolic velocity profile usually found in microfluidic channels. This flat profile avoids the spreading of a small sample that occurs when a parabolic velocity profile causes sample at the centre of the channel to move faster than that at the edges.

2.4.4 AC Electroosmosis

Electroosmosis as described in the previous section is a phenomenon that occurs only under a DC field - reversal of the field would produce a corresponding reversal in flow, and a zero time-averaged net flow. Under a non-uniform electric field, however, displacement of ions in and around the double layer is possible, producing local fluid motion. Figure 2.7 shows a coplanar pair of electrodes producing a non-uniform electric field within a microfluidic channel. The field is normal to the surface as it meets the electrodes, but quickly assumes a tangential component as it curves toward the opposing electrode. The interaction between the electric field and the ions drawn towards the electrode surface produces fluid motion across the surface of the electrode. The key difference with AC electroosmosis is that as the field reverses, oppositely charged ions

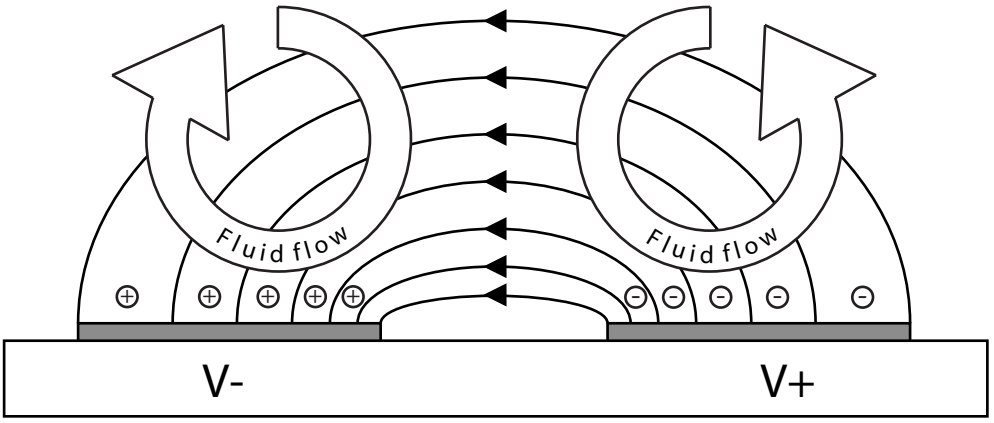

FIGURE 2.7: Electroosmotic flow around an electrode pair. Adapted from Morgan and Green (2003).

are drawn to the surface and displaced in the same direction, so the fluid motion continues unchanged. The effect of AC electroosmosis can be seen while performing pDEP trapping of microparticles. Particles are drawn to the high field regions at the edges of electrodes, but are pushed back, on top of the electrodes by the fluid flow. The fluid flow field can be determined from the equation (Morgan and Green, 2003):

$$\langle u_x \rangle = \frac{1}{2} Re \left[\frac{\sigma_{qo} E_t^*}{\eta \kappa} \right] \tag{2.10}$$

$$\kappa = \sqrt{\frac{\sigma_m}{D \epsilon_m}} \tag{2.11}$$

σ_{qo} is the surface charge, E_t^* is the tangential component of the electric field, D is the diffusion coefficient of the electrolyte and κ is the reciprocal of the Debye length - a length scale that describes the rate at which the electric potential drops off with distance. In the case of Equation 2.11, this is the potential around a single, monovalent ion.

The magnitude of the fluid velocity is frequency dependent, due to the electrode polarisation effects. At higher frequencies, the electrodes do not fully polarise before the field reverses, meaning that there is not the required excess of counter-ions near to the electrodes to be displaced by the tangential component of the electric field. At low frequencies, the electrodes fully polarise each half cycle which blocks the field from the bulk of the electrolyte. It is in the intermediate region that AC electroosmosis can take effect, typically from 10^1 to 10^5 Hz (Morgan and Green, 2003).

The effect of AC electroosmosis around a symmetrical electrode pair is to redistribute the fluid outwards, away from the gap between the electrodes. This has the effect of producing swirls of liquid over each electrode as fluid is brought down between the

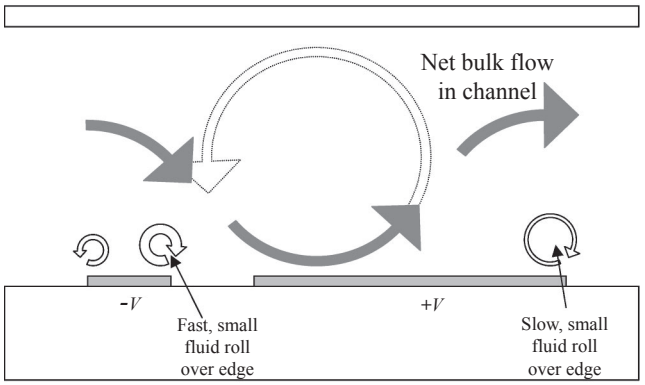

FIGURE 2.8: Asymmetric electroosmotic flow around differently sized electrodes produces a net flow through a microchannel. Taken from Ramos et al. (2003).

electrodes from the top of the channel, and recirculated. Over the system as a whole, this will only lead to local fluid motion, as the circulating flow is mirrored above the opposing electrode. Brown et al. (2000) observed, however, that an asymmetric pair of electrodes would produce differently sized swirls of fluid, leading to a net fluid flow through the channel. Hence, AC electroosmosis could be used to produce an on-chip solid-state pump. An overview of the fluid motion from a cross-section view is shown in Figure 2.8.

2.4.5 Electrothermal Flow

The presence of an electric field within a fluid will give rise to electric current flow if the fluid has a non-zero conductivity. This leads to Joule heating of the fluid, producing a temperature gradient within the system. In the case of electrodes for electrokinetic manipulation, the heat sources can be quite localised, leading to large thermal gradients in the vicinity of the electrodes (Ramos et al., 1998):

$$P = \sigma_m |\mathbf{E}|^2 \tag{2.12}$$

P is the power dissipation per unit volume. Variation in temperature produces a corresponding variation in the conductivity of the fluid, and hence thermal input produces a conductivity gradient in the fluid. In the presence of an electric field these variations give rise to a body force on the fluid, leading to fluid flow as can be seen from Equation 2.20 below in Section 2.6.3. The body force can be determined from (Chen and Du, 2006):

$$\langle f_e \rangle = \frac{1}{2} Re \left[\left(\frac{(\sigma_m \nabla \epsilon_m - \epsilon_m \nabla \sigma_m) \cdot \mathbf{E}}{\sigma_m + i\omega\epsilon_m} \right) \mathbf{E}^* - \frac{1}{2} |\mathbf{E}|^2 \nabla \epsilon_m \right] \tag{2.13}$$

E is the electric field vector, and * represents the complex conjugate. Electrothermal flow is highly dependent on the fluid bulk conductivity, as power dissipation in the

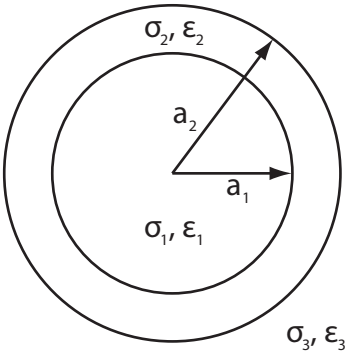

FIGURE 2.9: A single concentric shell model, typically used for modelling a biological cell.

fluid increases with conductivity. Electroosmotic flow (see below) is usually the more dominant effect at electric field frequencies of less than 100 kHz (Morgan and Green, 2003).

2.5 Electrical Characteristics of Biological Cells

The developed internal structure of biological cells means that they have a complicated response to electrical stimulus. The cell membrane is a very thin (approximately 5 nm) and highly insulating bilayer, while the cytosol that comprises the vast majority of the cell volume has a much higher conductivity, of approximately 0.2 S m^{-1}. Polarisation will occur at every internal membrane and discontinuity within the cell, as well as at the exterior interface. The most common approach to simulate the electrical characteristics of cells is to use a concentric shell model. The cell is treated as a spherical particle, with one or more discrete shells, each with uniform electrical parameters - see Figure 2.9.

Shelled models are typically derived from the cells physical structure, the most commonly used has a single shell representing the cell membrane with the rest of the internal volume representing the cytosol and cell interior. The cell wall and membrane of yeast cells (*S. cerevisiae*) have also been successfully represented using a two-shell model by Huang et al. (1992).

The Clausius-Mossotti factor for a single-shell model particle in suspension can be calculated by determining first the Clausius-Mossotti factor for the particle itself (Equation 2.14), calculating the equivalent complex permittivity for the particle (Equation 2.15), and finally calculating the Clausius-Mossotti factor for the particle/medium system together (Equation 2.16), as shown by Huang et al. (1992):

$$f_{CM12} = \frac{\epsilon_2^* - \epsilon_1^*}{\epsilon_2^* + 2\epsilon_1^*} \tag{2.14}$$

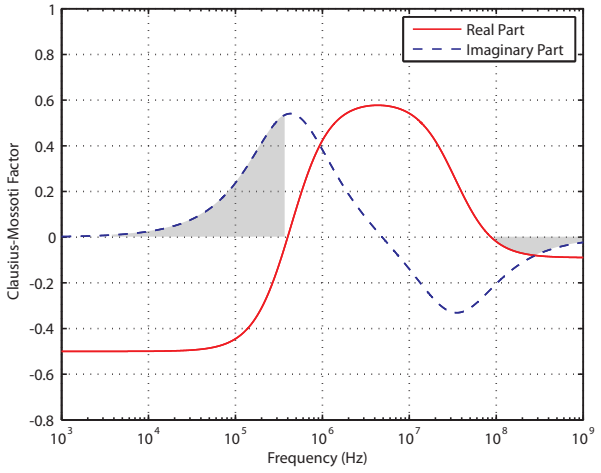

FIGURE 2.10: Plot of the Clausius-Mossotti factor for viable yeast cells in aqueous solution, calculated using a single shell model (σ_m = 50 mS/m, $\sigma_{membrane}$ = 0.25 μS/m, $\sigma_{cytoplasm}$ = 0.3 S/m, $\epsilon_{r,medium}$ =78, $\epsilon_{r,membrane}$= 6, $\epsilon_{r,cytoplasm}$ = 60, a_2 = 4 μm, $a_2 - a_1$ = 8 nm) - travelling wave DEP is feasible in the greyed frequency bands where the CM factor has a negative real part and a non-zero imaginary part.

$$\epsilon^*_{12} = \epsilon^*_2 \frac{(a_1/a_2)^3 + 2f_{CM12}}{(a_1/a_2)^3 - f_{CM12}} \tag{2.15}$$

$$f_{CM123} = \frac{\epsilon^*_{12} - \epsilon^*_3}{\epsilon^*_{12} + 2\epsilon^*_3} \tag{2.16}$$

ϵ^*_3 is the complex permittivity of the medium, and can be calculated from Equation 2.5. The response of more complex particle models (with more shells) can be calculated in the same manner, by sequentially calculating the effective permittivity for pairs of shells (Huang et al., 1992). Figure 2.10 shows a plot of the Clausius-Mossotti factor for a single shell model of *S. Saccharomyces* in aqueous suspension, using a single shell model.

To model the electrical characteristics of cells, a more appropriate model maybe as a thin membrane surrounding a lossy dielectric. Small discrepancies in the value of the cell membrane thickness in a numerical model may cause a significant change in the model output, so it is advantageous to remove this element from a model if possible. By introducing the capacitance of the membrane per unit area, the Clausius-Mossotti factor may be modified accordingly (Kriegmaier et al., 2001):

$$C_m = \frac{\epsilon_2}{d} \tag{2.17}$$

$$f_{CM} = \frac{aC^*_m(\epsilon^*_3 - \epsilon^*_1) - \epsilon^*_1\epsilon^*_3}{aC^*_m(\epsilon^*_3 + 2\epsilon^*_1) + 2\epsilon^*_1\epsilon^*_3} \tag{2.18}$$

2.6 Flow in Microfluidic Systems

2.6.1 Regimes of Flow

Intuitive physical relationships that occur in the macroscopic world, such as fluids flowing with turbulence and mixing easily, are not maintained on smaller length scales. On the micro-scale, viscous forces dominate, and inertia becomes much less important. The Reynolds number of a system describes the ratio between viscous and inertial forces:

$$Re = \frac{\rho_m V D_H}{\eta} = \frac{V D_H}{\nu} = \frac{Q D_H}{\nu A} \tag{2.19}$$

ρ_m is the fluid density, D_H is the characteristic length of the system (or *hydraulic diameter*, equal to the actual diameter in a circular pipe), V is the mean fluid velocity, η is the dynamic fluid viscosity, Q is the fluid volumetric flow rate, A is the cross-sectional area and ν is the kinematic fluid viscosity. As Equation 2.19 shows, decreasing the length scale and the fluid velocity causes the Reynolds number to decrease. Fluid flow in a low Reynolds number system is described as laminar, and has some unique properties.

2.6.2 Laminar Flow

The flow in a microfluidic system is almost always laminar, as the dimensions of the system push the Reynolds number below 1 (flows with Reynolds numbers of 2300 and below are generally considered to be laminar). There is little lateral motion of the fluid, and the primary method of mixing is diffusion. Particles in suspension follow flow streamlines through the channel, so (in the absence of external forces) the particle distribution is the same throughout the length of the channel.

Laminar flow conditions mean that multiple fluids can be carried in the same channel without them mixing. Novel microfluidic devices have been constructed to move particles between different fluids flowing side-by-side in a microchannel, a potential application for this technology is cell lysis: cells from a blood sample are moved laterally across a microfluidic channel by DEP, into a lysis buffer, before being returned to their physiological media. Unwanted erythrocytes are destroyed, leaving the more robust leukocytes intact for further analysis. Such conditions are less than advantageous, however, for performing chemical reactions within a microchannel. Mixing of reagents by diffusion is slow, and hence a number of active and passive mixing devices have been developed to accelerate the process.

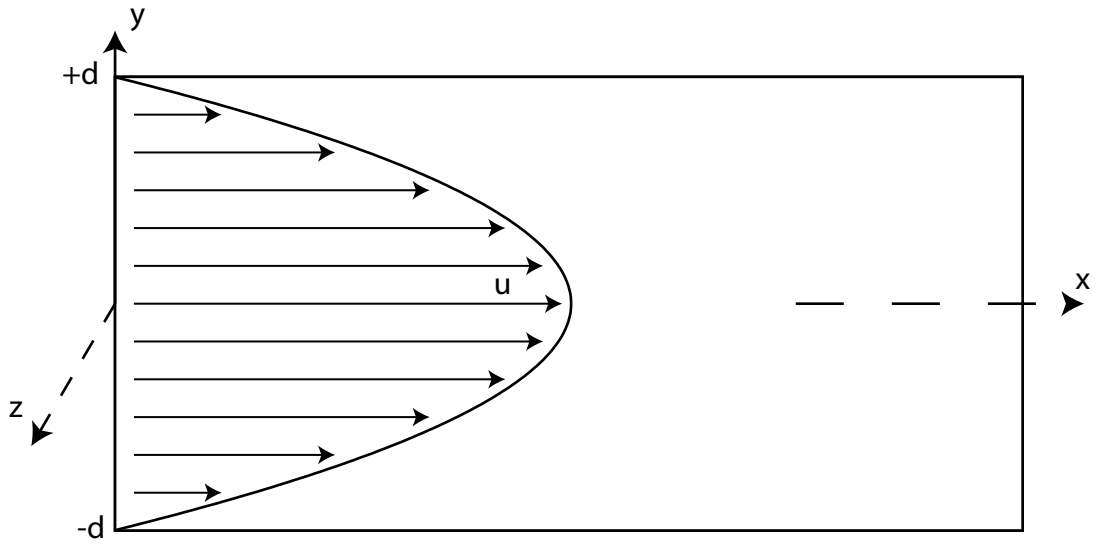

FIGURE 2.11: Fluid velocity (u) profile across the vertical (Y) axis of a channel as it flows in the x-direction.

2.6.3 Flow Velocity Profile

Laminar flows exhibit streamlines, with little lateral movement or turbulence of the fluid. Hydrodynamic drag on the fluid from the walls of the channel reduces the flow rate of the fluid near to the wall, leading to clear and defined gradients in the fluid velocity across the channel. A plot of the fluid velocity over a cross-section through the channel has a parabolic profile, with zero velocity at the channel walls - see Figure 2.11.

The Navier-Stokes equations describe the motion of fluids and gases, and can be used to calculate the velocity profile across a channel if the boundary conditions can be defined. In the case of a continuous Newtonian fluid flowing under low Reynolds number conditions, the governing equation is the Navier-Stokes equation:

$$\rho_m \frac{d\mathbf{u}}{dt} + \rho_m(\mathbf{u} \cdot \nabla)\mathbf{u} = -\nabla p + \eta \nabla^2 \mathbf{u} + f \tag{2.20}$$

∇p represents the pressure drop along the channel, ρ_m is the density of the fluid, $\mathbf{u}$ is the velocity of the fluid, η is the viscosity of the fluid and f is a body force acting on the fluid. For a flow that varies in one dimension only (assuming the channel width along the z-direction is very large), with a steady (time invariant) flow, only along the x-axis - depicted in Figure 2.11 - Equation 2.20 reduces to the form of:

$$\frac{\partial^2 u_x}{\partial y^2} = -\frac{p_0}{\eta l_0} \tag{2.21}$$

p_0 is the pressure drop along the channel, and l_0 is the length of the channel. The differential equation can be solved by integration and using boundary conditions - namely that the fluid velocity is zero at the channel walls (when $y = \pm d$).

$$u_x = \frac{p_0}{2\eta l_0}(d^2 - y^2) \tag{2.22}$$

An alternative method for calculating the flow velocity profile when the volumetric flow rate is known (for example if fluid is pumped using a positive displacement device, such as a syringe pump) is to calculate the pressure drop over the length of the channel from the volumetric flow rate.

$$Q = \int_{-d}^{d} u_x dy = \frac{2}{3}\frac{d^3}{\eta}\frac{p_0}{l_0} \tag{2.23}$$

$$\therefore \frac{p_0}{l_0} = \frac{3\eta Q}{2d^3} \tag{2.24}$$

$$\therefore u_x = \frac{3Q}{2d^3}(d^2 - y^2) \tag{2.25}$$

This method of solving the differential equation is not appropriate if the flow varies in 2-dimensions, however, as the boundary conditions do not sufficiently constrain the solution. This would be the case if the aspect ratio of the channel was near to 1, and hence the flow velocity would be a function of the position in both the y and z axes. A number of methods exist to solve such problems, including numerical simulation by finite element analysis. Alternatively, an analytical method can be used by constraining the solution to a harmonic solution, and introducing a Fourier series. This method is used to calculate the hydrodynamic drag force on a particle within a microfluidic channel in Chapter 5, and a full derivation of the method is given in Appendix A.

2.7 Forces Acting on a Particle Within a Microfluidic System

The motion of a particle is a vector sum of the independent forces acting upon it. This can be used to construct a generalised model of forces in a microfluidic system. A particles mass causes it to experience a gravitational force, which can be expressed in terms of the particle volume:

$$F_g = -mg = -\frac{4}{3}\pi a^3 \rho_p g \tag{2.26}$$

ρ_p is the particle density, g is the gravitational constant. This is opposed by a buoyancy force, equal to the weight of fluid displaced:

$$F_B = \frac{4}{3}\pi a^3 \rho_m g \tag{2.27}$$

ρ_m is the density of the suspending medium. Hence, a net sedimentation force on the particle is proportional to the difference in the densities of the particle and the medium:

$$F_S = \frac{4}{3}\pi a^3 \rho_m g - \frac{4}{3}\pi a^3 \rho_p g = \frac{4}{3}\pi a^3 (\rho_m - \rho_m) g \tag{2.28}$$

As the particle accelerates, hydrodynamic drag forces on the particle will increase until they equal the sedimentation force, and the particle will have reached terminal velocity. Any motion relative to the fluid will be opposed by a drag force, the magnitude of which depends on the particle velocity with reference to the fluid:

$$\mathbf{F}_{HD} = -6\pi a \eta \mathbf{v} \tag{2.29}$$

$\mathbf{v}$ is the velocity vector between the particle and the local fluid. Electrokinetic forces can be applied to particles in solution, the direction and magnitude of which are functions of the electrode and channel geometry, the particle size and composition, the media composition and the frequency and magnitude of the electric field. The governing equations for these phenomenon are covered in the preceding sections. Vector maps of the dielectrophoretic forces within microfluidic devices can be obtained by numerical simulation, and this is discussed in Chapter 3 - Numerical Simulation of Microfluidic and Electrokinetic Devices.

The parabolic flow profile of a fluid under laminar flow means that a particle within a microfluidic channel is likely to be within a shearing flow (unless it is at the centre of the channel, after focusing for example). The shear gradient induces a lift force, directed down the shear gradient and towards the wall. Also, the flow field between the particle and the wall causes asymmetry in the wake of the particle, producing a lift force directed away from the wall. The balance of these two forces produces a lift force on the particle normal to the surface of the wall as a result of fluid flow tangential to the surface of the wall (Carlo et al., 2007; Asmolov, 1999):

$$F_L = \frac{\rho_m \mathbf{u}^2 a^4}{D_h^2} f_c(R_c, x_c) = \frac{\eta^2}{\rho_m} R_p^2 f_c(R_c, x_c) \tag{2.30}$$

$f_c(R_c, x_c)$ is a lift coefficient that is a function of the particle position within the channel cross-section x_c and the channel Reynolds number R_c, R_p is the Reynolds number of the

particle. As Equation 2.30 shows, the lift force is proportional to the square of the fluid velocity (U_m^2) and the channel Reynolds number, which is also a function of the fluid velocity. Hence, the lift forces decrease rapidly in response to any decrease in the fluid velocity. Lift forces have been used to confine particle streams flowing at high velocity - such as 1.8 m s^{-1} used by Carlo et al. (2007) - but at the more modest velocities of several hundred micrometres per second used in this work the lift forces are negligible.

Chapter 3

Numerical Simulation of Microfluidic and Electrokinetic Devices

3.1 Introduction

The dielectrophoretic force developed on a particle can be modelled to allow the electrode geometry to be optimised. Figure 3.1 shows the field in a plane between a point charge and a ring electrode (this could be a section within a 3-dimensional system consisting of a long thin wire inside a hollow cylindrical electrode). The electric field within such a system is accurately described by Equation 3.1, obtained using Gauss's Law. Hence, the dielectrophoretic effect on a particle within the system can be determined from an analytical solution of this equation:

$$\mathbf{E} = \frac{Q}{2\pi \mathbf{r} \epsilon_0} \tag{3.1}$$

Q is the charge on the surfaces of the electrodes, and $\mathbf{r}$ is the vector from the centre of the ring to the point of interest. It is not always possible to find analytical solutions for every system, however. The field within more complex electrode geometries cannot always be described by a single equation, but approximate solutions can be obtained using finite element analysis. A mesh of smaller elements is created through the model space, and partial differential equations (PDE) that govern the electrical relationships are solved iteratively. Real space is not composed of separate elements, of course, but is a continuous space. Hence, finite element models become more representative of real space as the size of mesh elements decreases and the number of mesh elements within the model is increased. Finite element analysis can be applied to any physical relationship that

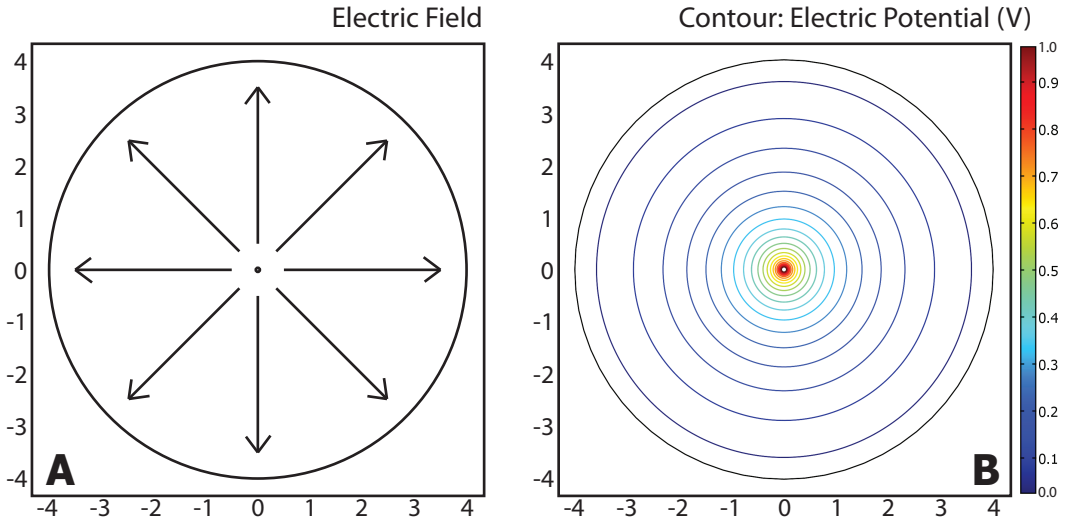

FIGURE 3.1: A 2-dimensional electrode set comprising a point and ring structure, with (a) a schematic representation of the electric field lines, and (b) a contour plot of the electric potential.

can be described by PDEs; examples in this work include calculations of the DEP force developed on a dielectric particle, hydrodynamic laminar flow through a microchannel, and Joule heating of a conductive liquid.

3.2 Modelling Considerations

The computational power required to solve finite element problems is directly proportional to the number of mesh elements within the model. Hence, it is advantageous to avoid unnecessarily complex meshes where possible. Where planes of symmetry exist within a system, only part of a system need be simulated, and results can be extrapolated across unsimulated regions. A system with rotational symmetry can be reduced to a 2-dimensional plane, for example, and the model equations solved in cylindrical geometry without loss of generality.

3.2.1 Electric Fields

One approach to the calculation of electric field distributions is to relate the electric field to the charge density within the system, as described by Maxwell's Equations:

$$\nabla \cdot \mathbf{E} = \frac{\rho}{\epsilon_0} \tag{3.2}$$

∇ represents the gradient function, ρ is the charge density. This leads to complexities, however, as the electric field ($\mathbf{E}$) is a vector quantity. An alternative method is to relate

the electric field to the scalar electric potential (Equation 3.3), leading to Poisson's equation (Equation 3.4).

$$\mathbf{E} = -\nabla\phi \tag{3.3}$$

$$\nabla \cdot \nabla\phi = \nabla^2\phi = \frac{-\rho}{\epsilon_0} \tag{3.4}$$

ϕ is the scalar electric potential, ρ is the charge density within the system. The electric potential throughout the system can be determined by solving Poisson's equation, from which the electric field distribution can be obtained. Boundary conditions are specified at the extents of the simulation space - in this study these were either a fixed electrical potential ($\phi = V_0$) or electrical insulation (no field lines across the boundary - $n \cdot D = 0$). Current flow may be obtained from such a model using a line integral (2-d) or a surface integral (3-d) of the electric field - Equation 3.5. The integral is usually performed across the surface of one of the electrodes. The DEP force can be calculated from $\nabla |\mathbf{E}|^2$ and Equation 2.3.

3.2.2 Electrothermal

Heat is generated within microfluidic devices by resistive (Joule) heating of the electrolyte. While this is often negligible within electrolytes with a low ionic content, it is an important consideration when cells are manipulated in physiological medium. The current density (J) within the electrolyte is related to the electric field ($\mathbf{E}$) by the electrical conductivity (σ) - Equation 3.5, which gives rise to the power dissipation relationship - Equation 3.6.

$$\mathbf{J} = \sigma\mathbf{E} \tag{3.5}$$

$$P = J \cdot \mathbf{E} = \sigma\mathbf{E}^2 \tag{3.6}$$

P is the power dissipated as thermal energy per unit volume within the system. As the temperature in the system changes, thermal energy leaves the system by conduction through the boundaries of the device, and is also carried away by fluid flow. The thermal field is a solution of the energy balance equation (Morgan and Green, 2003):

$$\rho_m c_p \frac{\partial T}{\partial t} + \rho_m c_p \mathbf{u} \cdot \nabla T = k\nabla^2 T + \sigma_m |\mathbf{E}|^2 \tag{3.7}$$

ρ_m is the mass density of the medium, c_p is the specific heat at constant pressure, $\mathbf{u}$ is the fluid velocity vector, T is the temperature of the medium, k is the thermal conductivity and σ_m is the medium conductivity.

Under steady state conditions, the first term of Equation 3.7 can be disregarded. The Grashof number, the ratio of natural convection to heat diffusion, has been shown to be very much less than one when within typical microsystems (Castellanos, 1998), so the natural convection term ($\rho_m c_p \mathbf{u} \cdot \nabla T$) can be disregarded as it is much smaller than the rate of heat diffusion ($k\nabla^2 T$) within the system. Equation 3.7 then reduces to the form:

$$k\nabla^2 T + \sigma \left|\mathbf{E}\right|^2 = 0 \tag{3.8}$$

3.2.3 Hydrodynamics

The Navier-Stokes equation for flow at low Reynolds number (Equation 2.20) accurately describes the flow within a microchannel. Although this can be solved directly for a steady-state solution for 1-dimensional flow (and this can be a reasonable approximation for the flow within channels that have particularly large or small aspect ratios), the boundary conditions do not sufficiently constrain the solution for flow that varies in two dimensions. Under steady-state conditions and a uni-directional flow, the Navier-Stokes equation reduces to the form of:

$$\frac{\partial^2 u_x}{\partial y^2} + \frac{\partial^2 u_x}{\partial z^2} = -\frac{p_0}{\eta l_0} \tag{3.9}$$

p_0 is the pressure drop along the channel, and l_0 is the length of the channel. A number of methods exist for determining the surface of the velocity flow profile for 2-dimensional flow, which include finding a solution by iterative finite element analysis, or assuming a harmonic solution exists (which it does) and solving using a Fourier series. A derivation of the method using Fourier series is given in Appendix A, which produces a solution in the form of:

$$\mathbf{u}_x = \sum_{k=1,3\ldots}^{\infty} \sum_{l=1,3\ldots}^{\infty} a_{kl} sin\left(\frac{k\pi}{d} y\right) sin\left(\frac{l\pi}{h} z\right) \tag{3.10}$$

$$a_{kl} = \frac{-16 \frac{1}{\eta} \frac{\partial p}{\partial x}}{kl\pi^2 \left[\left(\frac{k\pi}{d}\right)^2 + \left(\frac{l\pi}{h}\right)^2\right]} \tag{3.11}$$

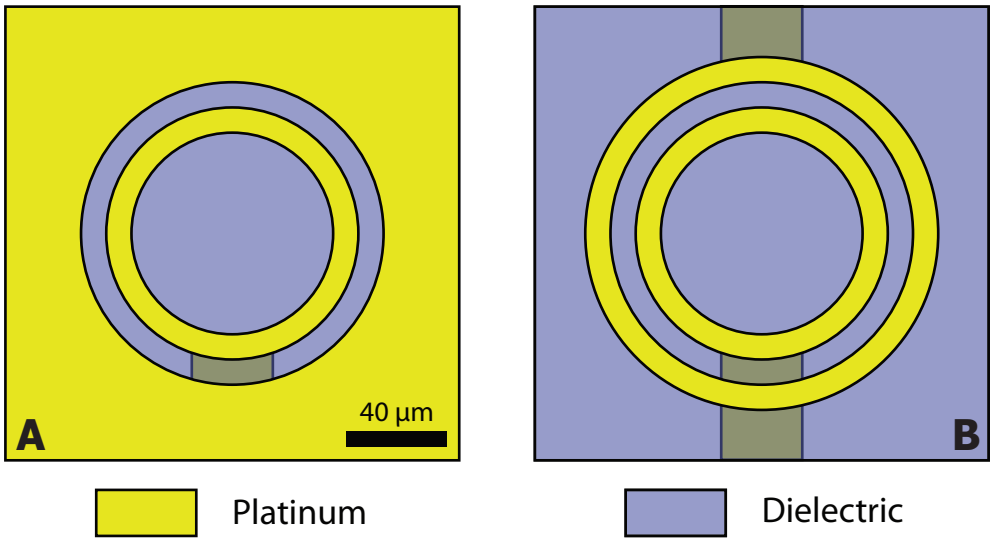

FIGURE 3.2: The Ring Trap electrodes with ground plane (a) or ground ring (b).

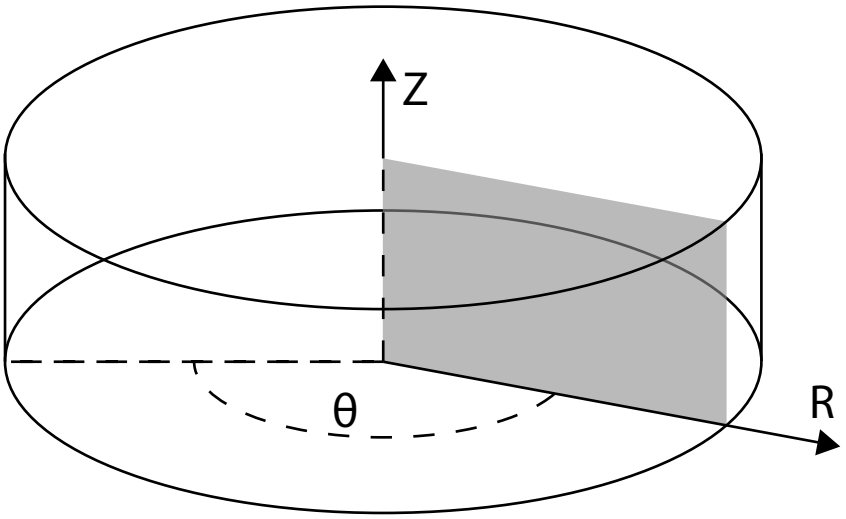

FIGURE 3.3: Rotational symmetry permits the electric field around the electrodes to be analysed as a 2-dimensional plane within cylindrical coordinates without loss of generality.

3.3 Ring Trap Device

The ring trap electrodes - discussed further in Chapter 5 - create a closed nDEP trap to isolate single cells or particles from a flow within a microfluidic channel. They consist of either a metal ring and surrounding ground plane (Figure 3.2 a) or two concentric, coplanar metal rings (Figure 3.2 b). The electrodes produce an electric field that has a gradient minima at their centre, creating a trapping region.

The distribution of the electric field can be simulated on a 2-dimensional plane within a cylindrical coordinate system (Figure 3.3), rather than a full 3-dimensional system,

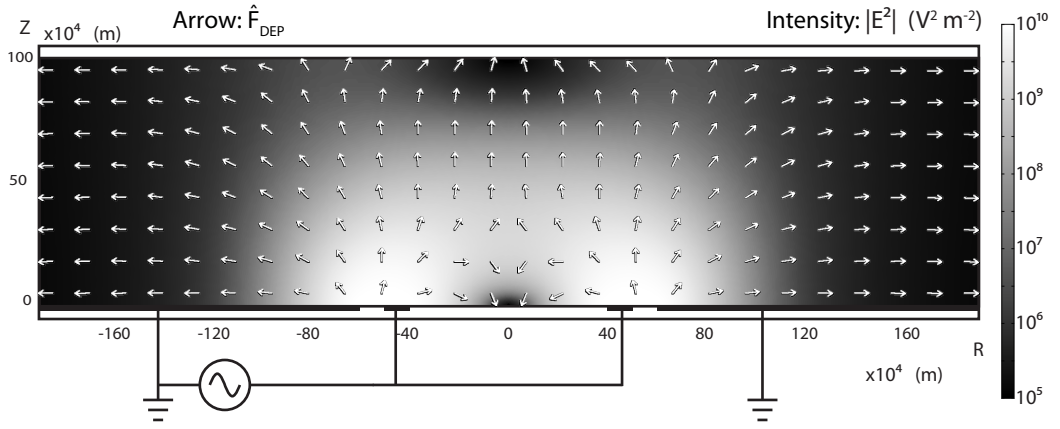

FIGURE 3.4: Plot of the electric field ($|\mathbf{E}|^2$) within the ring-plane electrodes, with an arrow plot (normalised vectors) indicating the direction of the DEP force on a particle experiencing negative DEP. Also shown are the electrical connections to the ground plane and ring electrodes.

because of the rotational symmetry of the electrodes. This dramatically reduces the mesh complexity and correspondingly the number of computational steps required.

3.3.1 Electric Field Distribution

The electric field within the ring trap electrodes was simulated over a plane using a cylindrical geometry. Figure 3.4 shows a plot of the electrostatic simulation of the electric field ($|\mathbf{E}|^2$) as an intensity plot, overlaid with arrows (normalised vectors) indicating the direction of the DEP force (the direction of $\nabla |\mathbf{E}|^2$) on a particle experiencing negative DEP. The plots have been mirrored across the axis of symmetry to show a cross-section across the whole trap. The electric field is assumed to be confined entirely to the region within the microfluidic channel, which contains an aqueous solution (ϵ_m=78). This is a valid approximation below the charge relaxation frequency, which is 300 MHz in physiological medium such as PBS or DMEM. All boundaries are defined as insulators, except the electrodes which are set at fixed potentials of either 0 or 2.5 V - the peak value of the alternating potential.

The two designs of ring trap electrodes operate in a similar manner. Figures 3.5 and 3.6 show plots of an electrostatic simulation of the electric field lines from the ring-plane and ring-ring electrodes respectively. Figures 3.7 and 3.8 show comparison plots of the magnitude of the electric field ($|\mathbf{E}|^2$) for the ring-plane and ring-ring electrodes respectively - similar to that shown in Figure 3.4, although only one half of the device is simulated (the axis $R = 0$ being a line of symmetry). As can be seen from the plots, the magnitudes of the electric field within the ring-plane and ring-ring electrodes are similar, producing similar DEP forces on trapped particles. The DEP force is calculated from the gradient of this value, so the plot shows the potential energy of the DEP field. Under negative DEP, cells and particles are trapped at the region of low electric field

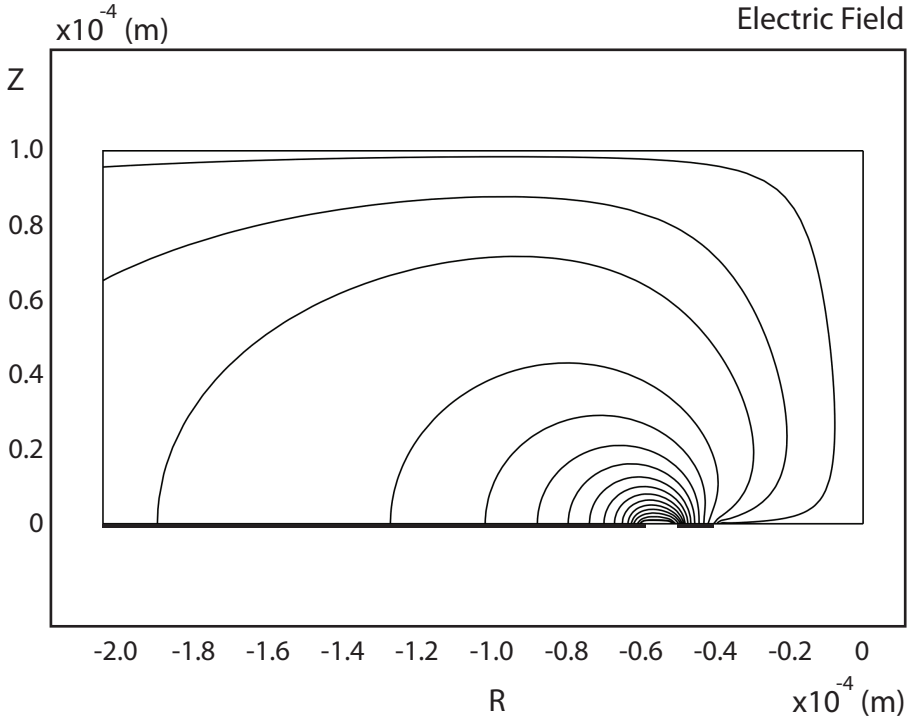

FIGURE 3.5: Plot of the electric field lines within the ring-plane electrodes.

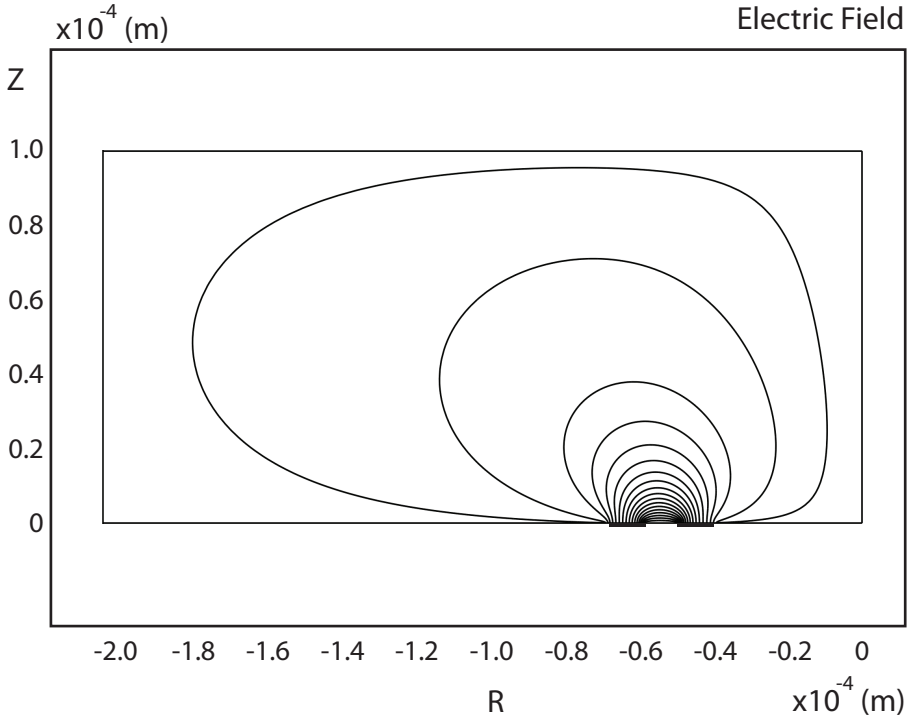

FIGURE 3.6: Plot of the electric field lines within the ring-ring electrodes.

strength at the centre of the trap (the bottom, right-hand corner of the plot). This result is more generalised than the DEP force itself, which is dependent on characteristics of the particle and suspending medium.

3.3.2 Electro-thermal Effects

To accurately model the temperature within the channel, it is necessary to model the heat dissipation out of the system. The water in the channel is bounded by two glass substrates of 700 μm thickness. An overview of the simulation geometry is shown in Figure 3.9. Thermal power dissipation is of most significance when the electrical conductivity of the electrolyte is high, such as physiological medias that contain considerable ionic content. The ring electrodes were used to sort fluorescently labelled cells - see Chapter 6 - suspended in DMEM ($\sigma_m = 1.6$ S m^{-1}), although the device was cooled to 10°C and the electrical conductivity is a function of the temperature of the electrolyte. For the purposes of simulation the electrical conductivity of the electrolyte was set at 0.8 S m^{-1} as this was the electrical conductivity of DMEM measured at 10°C. Figure 3.10 shows the results of simulation as a contour plot.

3.3.3 Hydrodynamic Flow Profile

Figure 3.11 shows the results of calculation of the fluid velocity profile using a Fourier series solution to the Navier-Stokes equation (Equation 3.10), for fluid within the microfluidic channel used in Chapter 5. The channel is much wider than it is deep, so the effect of the top and bottom walls of the channel is much more significant than the effect of the side-walls, and the velocity flow profile has a flat profile throughout the central 95% of the channel width.

The velocity flow profile may also be obtained by solving the partial differential equation through iterative finite element analysis. This method is more suited to complex channel geometries for which an analytical solution cannot be found. An example is the fluid junction of the sorter device, discussed in Section 3.4.

3.3.4 Combined Solutions

The low Reynolds number of microfluidic systems mean that viscous forces dominate over inertial forces, and particles reach terminal velocity almost instantaneously. Hence, it is possible to develop the DEP force equation (Equation 2.3) to determine the particle mobility under a DEP force (Morgan and Green, 2003):

$$\mathbf{v}_{DEP} = \mu_{DEP} \nabla |\mathbf{E}|^2 \tag{3.12}$$

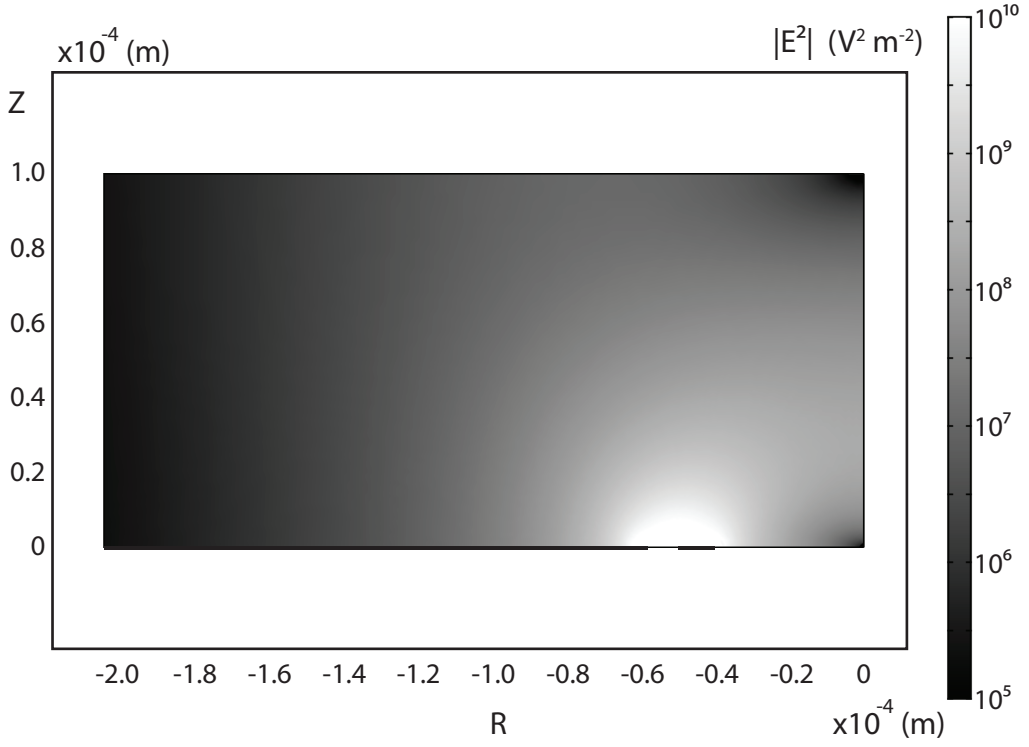

FIGURE 3.7: Plot of the electric field ($|\mathbf{E}|^2$) within the ring-plane electrodes. Electrode voltage is 2.5 V peak, medium relative permittivity (ϵ_m) = 78.

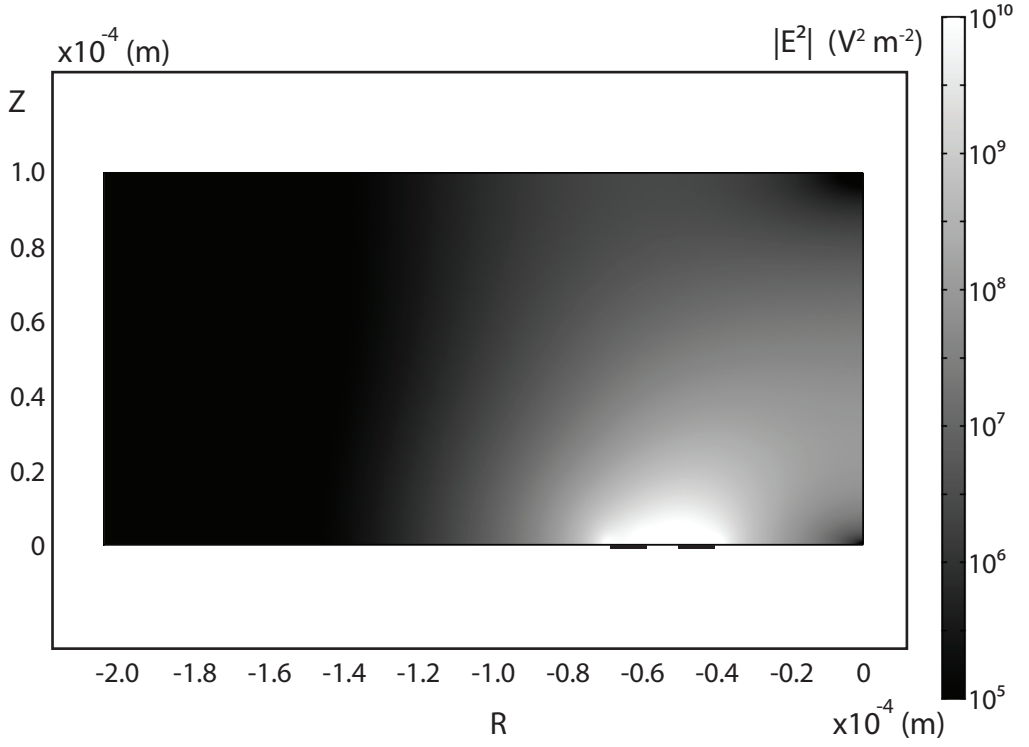

FIGURE 3.8: Plot of the electric field ($|\mathbf{E}|^2$) within the ring-ring electrodes. Electrode voltage is 2.5 V peak, medium relative permittivity (ϵ_m) = 78.

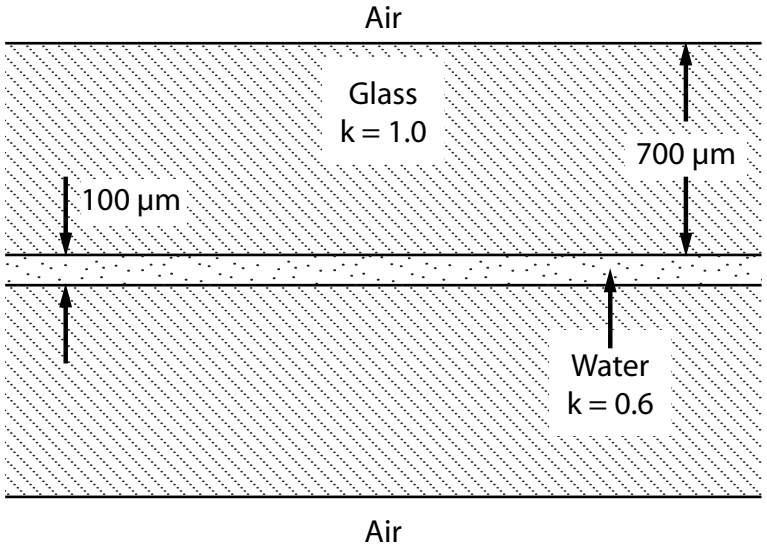

FIGURE 3.9: Schematic of the geometry used for simulation of the thermal environment within the microfluidic channel. The interface between the glass substrates and the air is assumed to be at a constant temperature of 10°C.

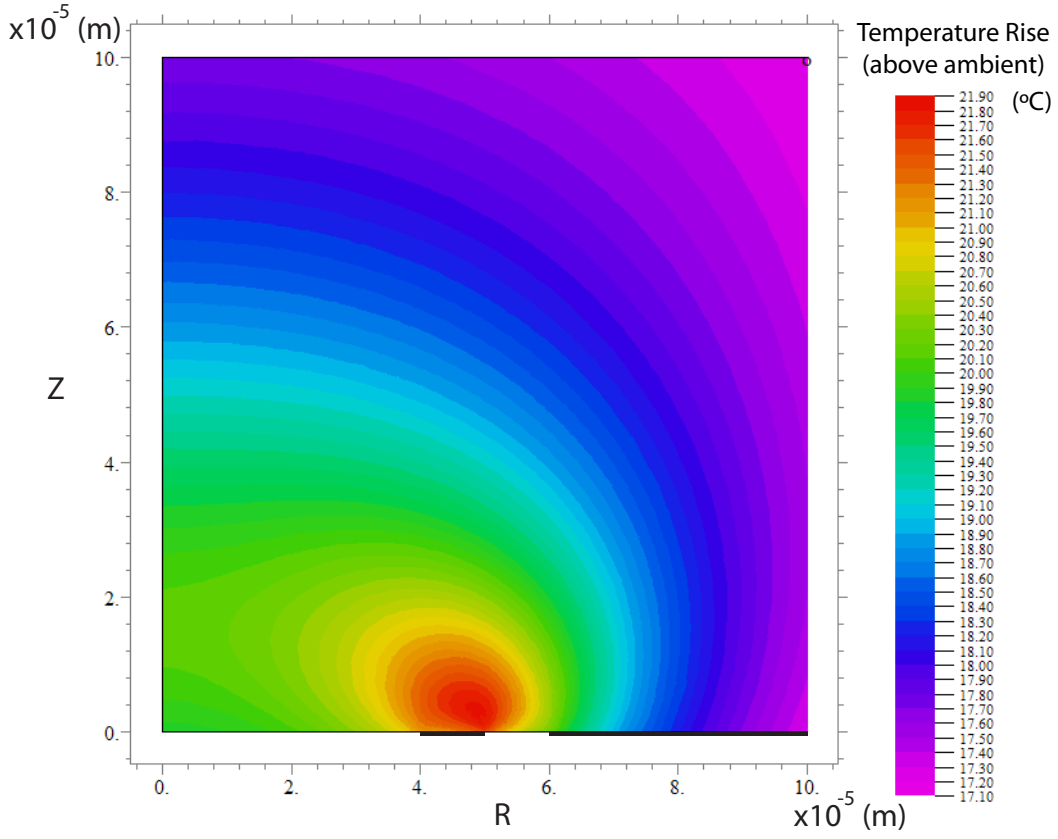

FIGURE 3.10: Simulation of the temperature within the microfluidic channel during trapping of cells in physiological media (device cooled to $10°C$). The origin $R, Z = 0$ is at the centre of the ring electrodes. Applied voltage = 10 Vpp, fluid electrical conductivity = 0.8 S m^{-1}. Simulation produced by N.G. Green (Thomas et al., 2009) supplementary material.

$$\mu_{DEP} = \frac{a^2 \epsilon_m Re\left[f_{CM}\right]}{6\eta} \tag{3.13}$$

$\mathbf{v}_{DEP}$ is the resultant particle velocity under the DEP force, and μ_{DEP} is the particle DEP mobility. In the absence of an external force, particles in suspension move at the local fluid velocity. The vector sum of the DEP mobility and the fluid velocity gives rise to a velocity field that can be used to determine the trajectory of a particle moving through the system (ignoring other effects such as Brownian motion, buoyancy and lift forces). Figure 3.12 shows streamlines through the velocity field that represent the trajectory that a 15 μm polystyrene particle would take as it is carried through the microfluidic channel and deflected by the DEP force produced by the ring electrodes.

3.3.5 Summary of Results for the Ring Trap Device

The electric field within the ring trap electrodes has been simulated, demonstrating how they create a region of low electric field strength at their centre in which particles can be trapped using negative DEP. This data is used in Chapter 5 to model the DEP force on a trapped particle. The electrical power dissipation through the microfluidic device has also been modelled, and used to simulate the temperature rise due to Joule heating. Thermal effects are of prime concern if biological cells are to be manipulated, as a significant increase in temperature will lead to a loss of viability. This data provides some additional validation to the method of sorting cells using the ring electrodes, discussed in Chapter 6. The two designs of ring electrodes have been shown to operate in a similar manner and produce similar forces. The main advantage of the ring-ring electrodes is that they do not block light transmission through the device, permitting diascopic illumination during microscopic observation.

3.4 Sorting Gate Device

The sorting gate is an electrode configuration designed to sort particles as they pass through a fluidic junction. The electrodes deflect particles either to the left or to the right - a small displacement is sufficient to move a particle into a different fluid streamline and change the output through which it leaves the junction. Precise control of the electric field and the hydrodynamic flow is required to accurately sort particles. This technology is discussed in more detail in Chapter 7.

3.4.1 Electric Field Distribution

Each element of the sorting gate is effectively a negative DEP barrier formed from a pair of opposing electrodes on the top and bottom of the channel. Due to the symmetry

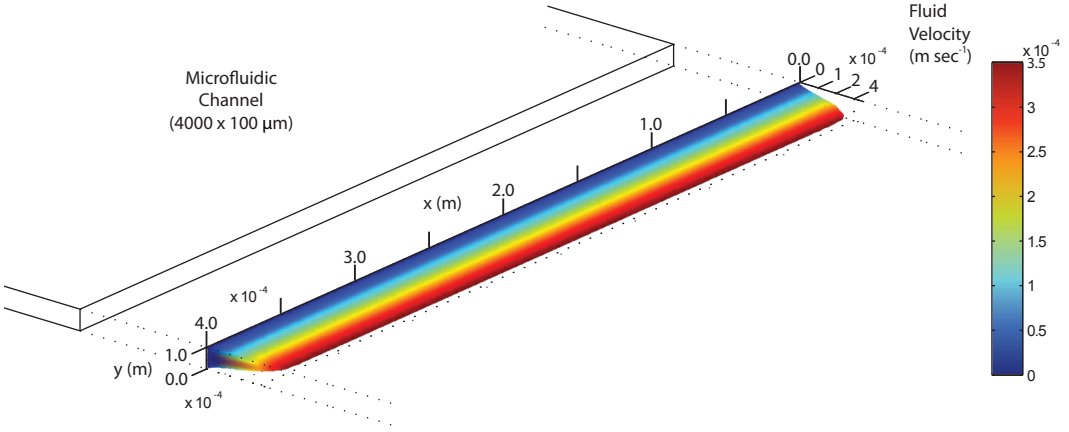

FIGURE 3.11: Plot of the calculated fluid flow velocity through the microchannel used for force characterisation of the ring electrodes (Chapter 5 - 4000 x 100 μm), at a volumetric flow rate of 5.5 μL min^{-1}.

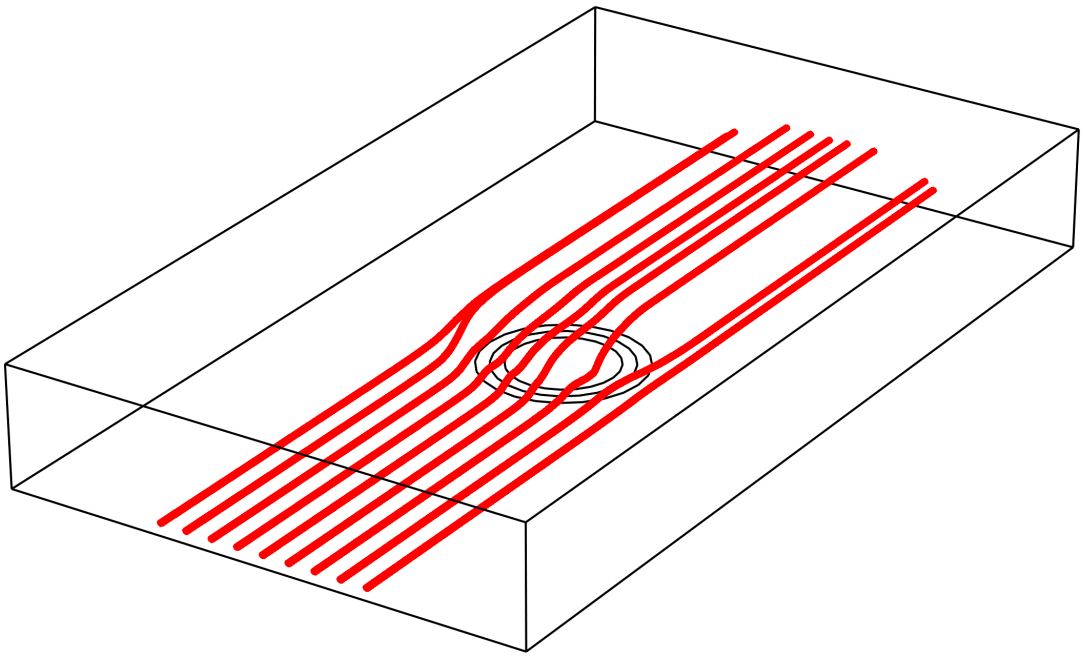

FIGURE 3.12: Plot of the trajectories of 15 μm polystyrene microspheres around a ring trap, modelling the dielectrophoretic and hydrodynamic forces. (σ_m = 0.18 mS m^{-1}, ϵ_m = 78, 2.5 V peak electrode voltage, 1 MHz, flow rate equivalent to 5.5 μL min^{-1} through 4000 x 100 μm.)

present, such a geometry can be accurately simulated in two dimensions, on a cross-sectional plane across the electrodes. Figure 3.13 shows a plot of the field lines between each barrier. The dashed line is a plane equidistant from the two electrodes, along which the magnitude of the electric field is at it lowest value. Particles experiencing negative DEP are repelled from the strong electric field at the edges of the electrodes, and are focused into the centre of the channel. A plot of the magnitude of the electric field ($\mathbf{E}^2$) on the central plane between the electrodes (dashed line) is shown in Figure 3.14. The electric field is at its maximum at a point between the two geometric centres of the two electrodes (a displacement of zero on the x-axis), and decreases in either direction away from the electrodes.

As discussed previously, the DEP force is dependent on the gradient of the electric field, $\nabla |\mathbf{E}|^2$. For the electrode geometry in question, this reaches a maximum (on the equidistant plane) at two points, at displacements approximately ± 50 μm from the centre of the electrodes. A particle in a microfluidic channel that is carried by fluid flow towards the barrier will be repelled from the electrodes, leading to motion relative to the suspending medium and a corresponding hydrodynamic drag force (Equation 5.3). The drag force acts in the opposite direction to the DEP force, so the particle is held at a distance from the electrodes at which the DEP and the hydrodynamic drag forces are equal. If the hydrodynamic drag force exceeds the peak DEP force, the particle will be carried through the point at which the DEP force is at its maximum, and will pass through the barrier.

Schnelle et al. (1999) showed that a DEP barrier at an angle to the direction of fluid flow could be used to laterally displace suspended particles, and that a force equilibrium existed that was dependent on the angle between the electrodes and the direction of fluid flow:

$$F_{HD} = F_{DEP} \sin \theta \tag{3.14}$$

θ is the angle between the electrodes and the direction of fluid flow. Figure 3.15 shows the system of forces on a particle in the vicinity of a negative DEP barrier. Angled DEP barriers are used in the sorter device to focus particles into a narrow stream so that they all pass through the detection region in single-file (see below).

Figure 3.16 is a simulation of the entire sorting gate device showing the electric potential over a series of vertical slices, produced by finite element analysis in 3-dimensions using Comsol Multiphysics 3.4. The sorting gate is comprised of three pairs of electrodes, which form negative DEP barriers. All boundary surfaces are modelled as electrical insulators, except the electrodes which have a fixed electric potential. For the purposes of simulation, these are set at either 0 (ground) or 1 V, although higher voltages may be used in the device if stronger DEP forces are required. Figure 3.17 is a plot of the simulation of the electric field produced within the microfluidic channel. This shows how the four sloping focusing electrodes create a region of low electric field strength at

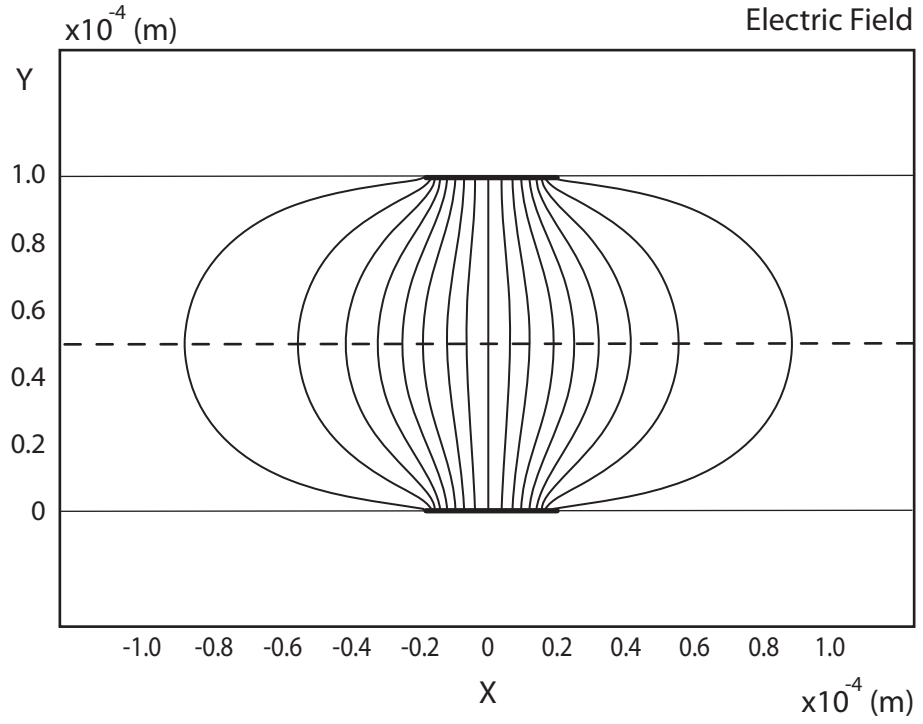

FIGURE 3.13: Plot of the electric field lines between the opposing electrodes of a negative DEP barrier, on a cross-section through the electrodes. The electrodes are shown as black lines at the top and bottom of the channel.

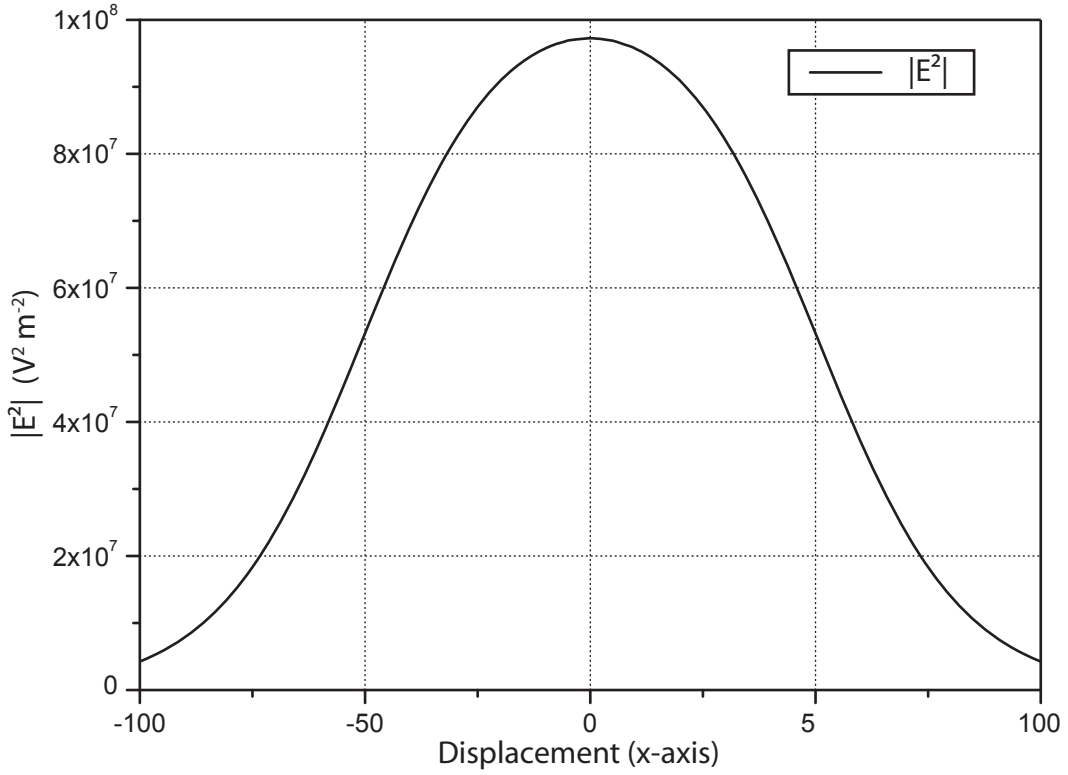

FIGURE 3.14: Plot of the electric field ($\mathbf{E}^2$) between the opposing electrodes of a negative DEP barrier - along the dashed line in Figure 3.13. Potential difference across the electrode pair is 1 V, electrode spacing 100 μm.

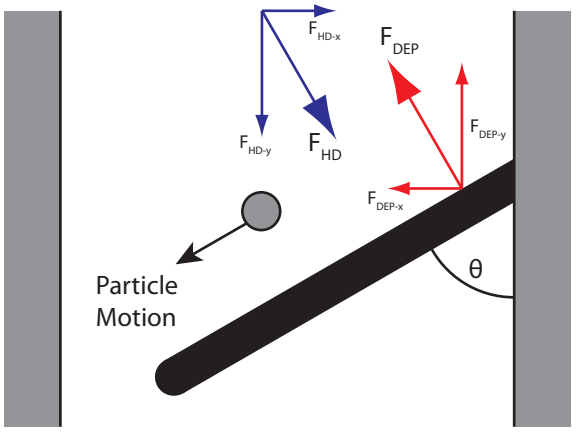

FIGURE 3.15: Schematic of the forces on a particle in the vicinity a nDEP barrier. Provided the hydrodynamic drag does not exceed the peak DEP force, a force equilibrium exists ($F_{HD} = F_{DEP}$) and the particle is carried along the edge of the electrode by the fluid flow and the horizontal component of the DEP force.

the centre of the channel, surrounded by a stronger field nearer the electrodes. Particles are focused by negative DEP into the centre of the channel.

Figure 3.18 shows results of simulation of the electric field ($|\mathbf{E}|^2$) on a horizontal plane through the middle of the electrodes. The plot shows how the electrodes create a negative DEP 'tunnel' through the electrodes, along which the electric field is at a local minimum. Particles experiencing negative DEP are constrained to follow this path as they are carried through the device by fluid flow. Reversal of the electric potential across the central electrode pair reconfigures the electric field to direct particles towards the opposite outlet. Although Figure 3.18 shows the magnitude of the electric field on a plane, it is a vector quantity with components in each of the three axes. On the vertical axis, the most significant effect (under negative DEP) is the focusing of the particles into a narrow stream towards the centre of the channel.

3.4.2 Hydrodynamic Flow Profile

The microfluidic channel geometry of the sorter device is too complex for an analytical solution of the Navier-Stokes equation to be used. The fluid velocity flow profile through the microfluidic junction was modelled by finite element analysis in 3-dimensions using Comsol Multiphysics 3.4. Figure 3.19 shows a plot of the fluid velocity on a mid-plane through the channel. The dimensions of the microfluidic channel ensure the flow is entirely laminar, and so fluid moves along streamlines through the device. A velocity profile exists across the channel, with fluid moving fastest at the centre of the channel. The fluid velocity decreases through the junction as the total cross-sectional area of the outlets is greater than the inlet.

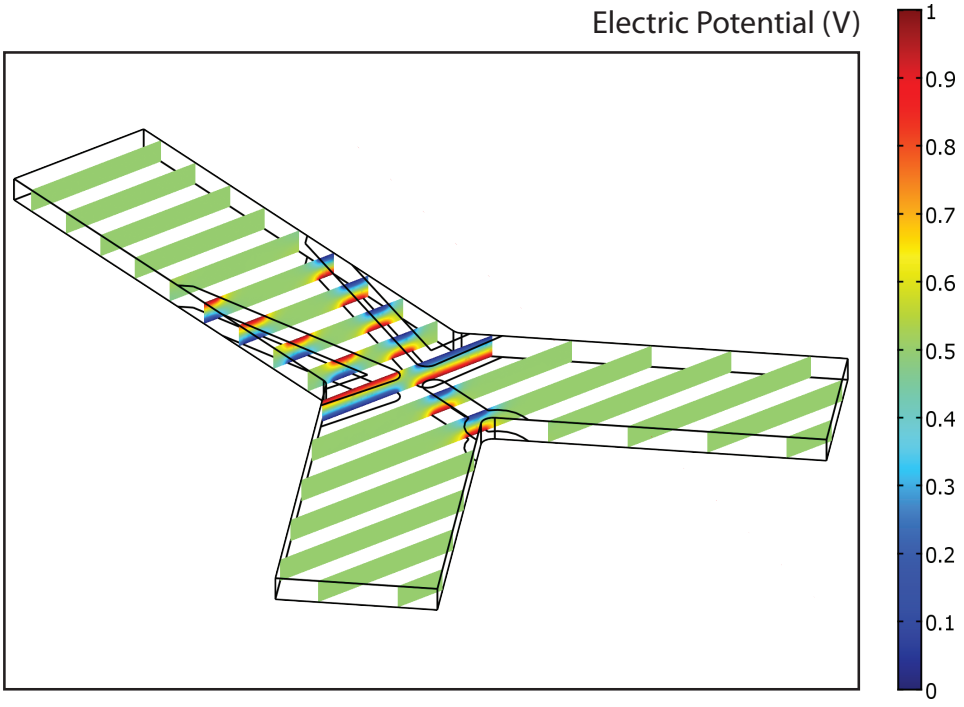

FIGURE 3.16: Plot of the electric potential around the electrodes of the sorter gate, configured to direct particles through the lower outlet. Potential difference across opposing electrode pairs is 1 V.

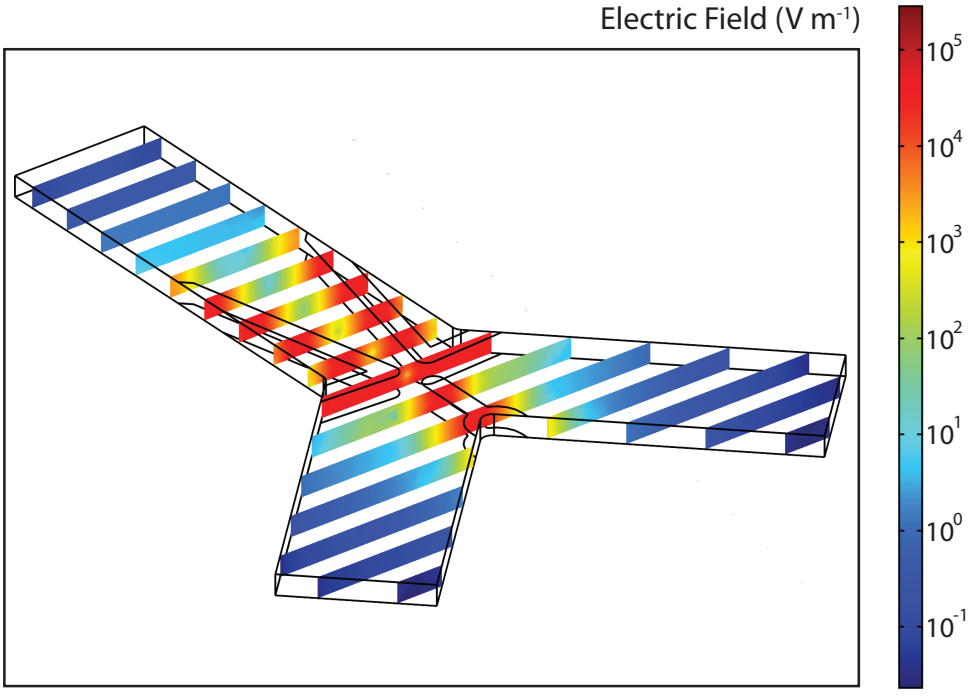

FIGURE 3.17: Plot of the electric field distribution around the electrodes of the sorter gate, configured to direct particles through the lower outlet. Potential difference across opposing electrode pairs is 1 V.

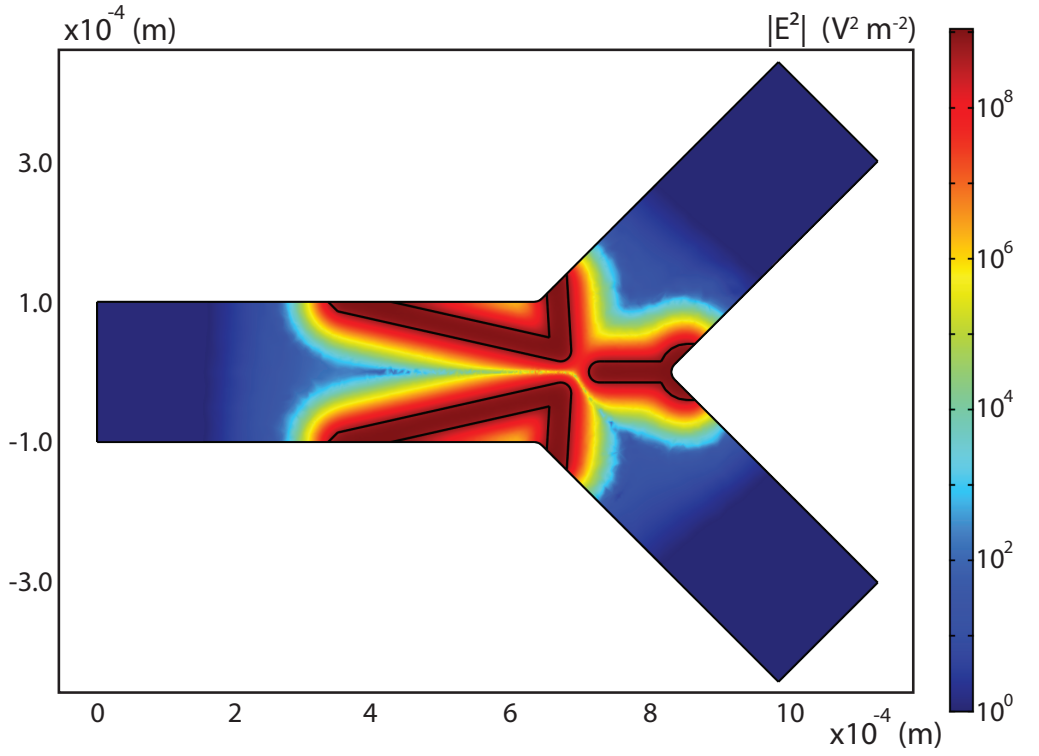

FIGURE 3.18: Plot of the electric field distribution ($|\mathbf{E}|^2$) on a mid-plane through the sorting electrodes, configured to direct particles through the lower outlet. Potential difference across opposing electrode pairs is 1 V.

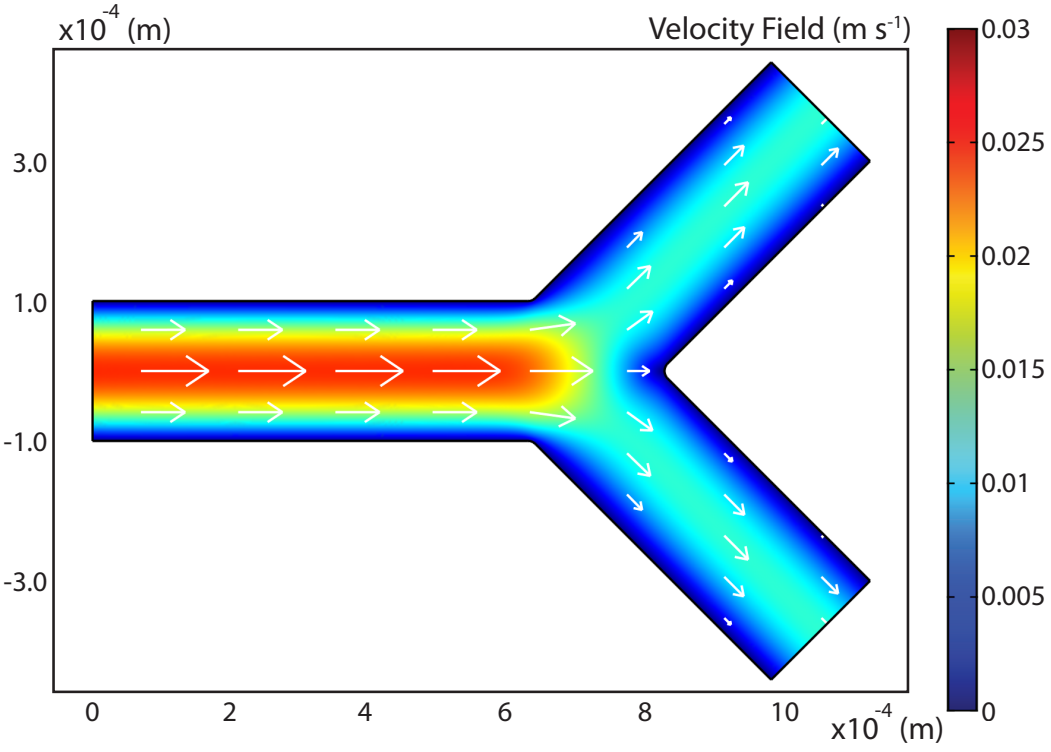

FIGURE 3.19: Plot of the results of simulation (finite element model) of laminar flow in a microchannel dividing at a junction, along a mid-plane through the sorting electrodes (flow of 100 μL min^{-1}, channel depth 26 μm).

3.4.3 Summary of Results for the Sorting Gate Device

Numerical simulation of the electric field within the sorting gate electrodes shows how the device creates a 'tunnel' of low electric field strength through the centre of the electrodes, towards one of the outlets. Particles are focused into this region, and are carried through it by fluid flow towards the selected outlet. Switching the phase relationship of the electric field between the central pair of electrodes changes the outlet that particles are directed towards. In Chapter 7 these simulations of the electric field are used to model the force produced by a negative DEP barrier and hence calculate the fluid velocity required for a particle to break through the barrier.

3.5 Conclusions

Numerical simulation offers a useful tool to analyse the physical relationships within microfluidic devices. Dielectrophoretic forces arise due to spatial inhomogeneity within an electric field, so the electrode geometry is an important consideration when designing electrokinetic devices. As computational power has increased, it has become more practical to use numerical simulation and finite element analysis to solve complex physical interdependencies in multiple dimensions. Calculations are only as good as the model that they are based on, however, and it is not possible to incorporate every parameter that may affect the analysis. As an example, during the simulation of electrothermal heating around the ring electrodes, the electrical conductivity of the electrolyte was assumed to be of a fixed value (adjusted for the ambient temperature) and the temperature dependence as a second-order effect was ignored. This is unlikely to cause a large deviation from the true value as the temperature increase around the electrodes was relatively small, but is nevertheless an additional source of error. As far as is possible, results of numerical analysis should be validated against experimental data to confirm accuracy. This concept is explored further in Chapter 5, where the results of simulation of the DEP force produced on a particle immobilised in the ring electrodes are compared with experimental measurements of the hydrodynamic drag.

Chapter 4

Fabrication of Microfluidic Electrokinetic Devices

4.1 Introduction

MEMs fabrication grew as an offshoot of semiconductor manufacture, so early methods involved the bulk micromachining of silicon wafers. Although silicon has some unique electrical and mechanical properties that can be usefully exploited in MEMs devices, its processing is laborious and expensive. Other materials exist in which microfluidic channels can be more readily fabricated, with more useful properties - such as optical transparency. While all the metallised electrodes used in this work were fabricated by professional staff from a commercial clean-room environment, a number of techniques for the fabrication of microfluidic channels were simple enough for the author to perform using a rudimentary laboratory set-up.

4.2 Microfluidic Channel Fabrication

4.2.1 Dry Film Resist

Photopatternable resists for printed circuit board fabrication have typically been applied by spray coating, but dry film resists are often more convenient to use as they can be applied to the substrate by hot-rolling in a simple lamination machine. Such films can also be used as a structural material for microfabrication, and some materials are suitable for microfluidic use as they can be compression bonded to form a sealed channel. An example is the epoxy-based polymer film SY300 supplied by Elgar Europe Ltd. The material is cross-linked by exposure to UV radiation, so must be exposed through a dark-field mask. Regions that are not exposed remain soft and can be removed by

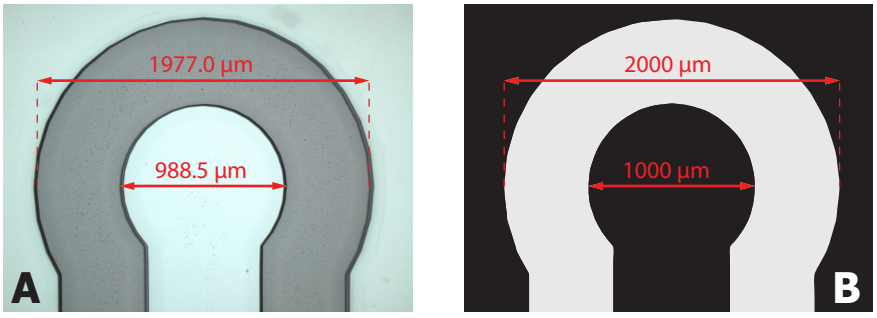

FIGURE 4.1: Microscopy image of a section of microfluidic channel fabricated from a photo-patterned dry film resist (a), with an image of the mask from which it was produced (b). The resist was exposed to a columnated light source through a contact mask, so the developed structures show a close dimensional tolerance to the features in the mask.

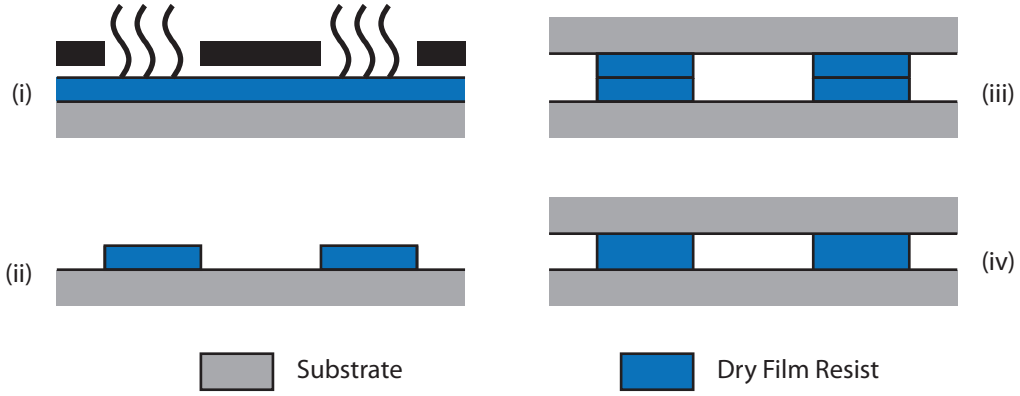

FIGURE 4.2: Fabrication of a microfluidic device using dry film resist: the substrate is laminated with the resist and exposed to UV radiation through a contact mask (i), exposed regions of the polymer cross-link, and so do not dissolve when the substrate is developed in solvent (ii). Symmetrical features on two opposing substrates are aligned (iii), and the two layers coalesce under elevated temperature and pressure to form a closed channel.

dissolution in an organic solvent (BMR, Elgar). Figure 4.1 shows a microfluidic channel fabricated in dry film resist, and the mask with which it was patterned.

A closed microfluidic channel can be created between two glass substrates by compression bonding two patterned dry film resist layers at elevated temperature. The patterned layers are typically mirror images of each other (or are symmetrical along at least one axis) so that they overlap when placed in contact. Features in the two patterned resist layers must be aligned - this can be performed either by hand or by microscopic observation with micromanipulators, depending on the feature size and the level of alignment required for optimal performance. Access holes must be drilled through one of the substrates to open the channel (see Section 4.3). Figure 4.2 shows the fabrication sequence used to produce a closed microfluidic channel.

Features with dimensions of 20 μm have been reliably reproduced in DFR (Vulto et al.,

2005). Generally a contact mask is used, and a columnated light source must be used for production of the smallest features. It is also possible to process DFR using rudimentary laboratory equipment, outside a clean-room environment. A non-columnated light source can be used, such as a UV 'light box' - the patterned resist will generally have features slightly larger than in the mask, with sloping side walls, due to exposure under the edges of the mask. This does not usually cause many problems if the angle of the sidewalls is anticipated and the features to be produced are significantly larger than the thickness of the resist. The DFR features shown in Figure 4.4(b) were produced using a non-columnated light source, and have correspondingly large, non-vertical sidewalls.

Dry film resists are particularly suitable for fabrication of microfluidic devices that require electrodes on opposing faces of the channel (examples include dielectrophoretic barriers and octopole traps, see Figure 4.3). The material is sufficiently thin to provide the correct separation between the two substrates, yet is still able to be applied to the substrate efficiently. Such devices require the electrodes on each substrate to be aligned before bonding.

The production of bonded microfluidic devices using dry film resists has reached maturity, and it is now possible to reliably produce large batches of devices. Nevertheless, a large number of parameters required optimisation before this stage was reached. The bonding pressure of the two DFR layers must be controlled sufficiently so they coalesce, without producing significant compression of the channel material. Similarly, pressure must be applied evenly across the surface of the substrates, or the glass may crack or otherwise be damaged.

4.2.2 PDMS Molding

PDMS (polydimethylsiloxane) is a silicone polymer that is commercially available as a two-part self-curing material supplied in liquid form (such as Sylgard, Dow Corning).

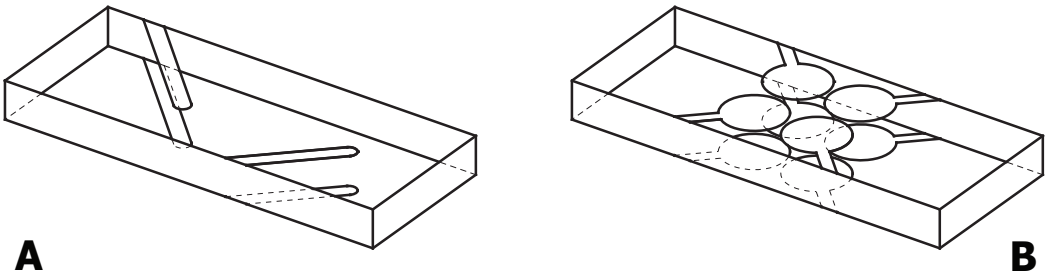

FIGURE 4.3: DEP devices that require electrodes on opposing faces of the microfluidic channel include (a) barriers and (b) the octopole trap.

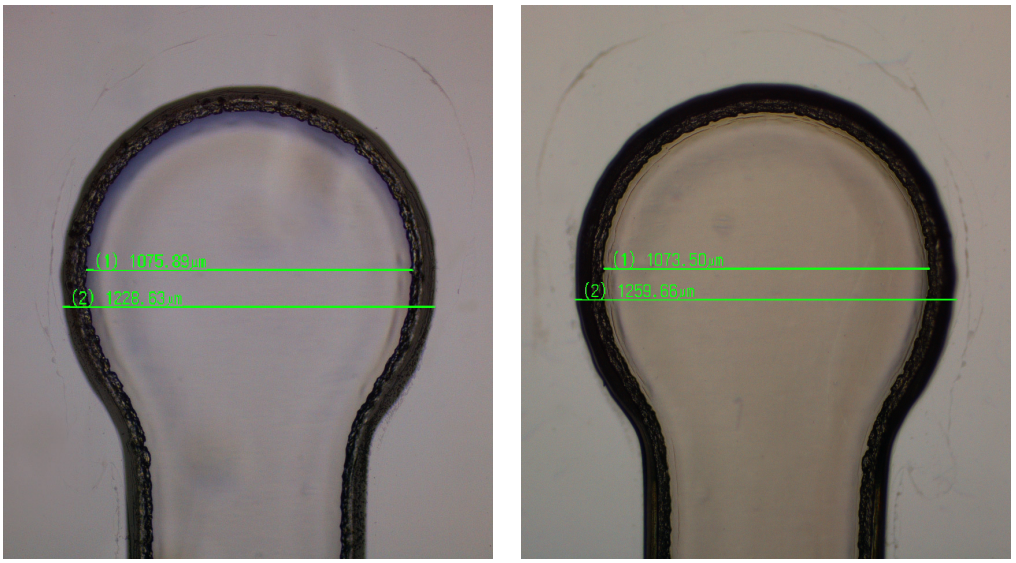

(a) Moulded PDMS channel (b) Dry film resist master

FIGURE 4.4: Microscopy image of a microfluidic channel moulded in PDMS around a DFR master.

The material is highly suitable for use in microfabrication as a structural material as it is transparent, tough, self-sealing and easy to mould and cut.

Microfluidic channels are typically formed by moulding polymeric materials around a master substrate. Features in the master can be produced using photolithography, such as by etching a silicon wafer, or in dry film resist (see above). Channels moulded in this fashion are suitable only for devices that require electrodes on a single surface of the channel (or do not require electrodes at all), so are suitable for use with the ring electrodes used in Chapters 5 and 6 but not the sorting gate used in Chapter 7 as that required electrodes on two opposing faces of the channel.

The protocol for fabrication of a PDMS mould from a pre-prepared master is quite simple:

1. The master is cleaned and prepared: ultrasonic cleaning in water with a mild detergent is sufficient, followed by air drying.
2. PDMS pre-polymer is mixed with the curing agent in a ratio of 10:1.
3. The master is placed within a suitable container, and the liquid PDMS mixture is poured on top.
4. Air bubbles within the liquid PDMS are removed by degassing in a vacuum chamber for approximately 20 minutes.
5. The PDMS will cure and be fully solidified after about 10 hours at room temperature, or 1 hour at 60°C.

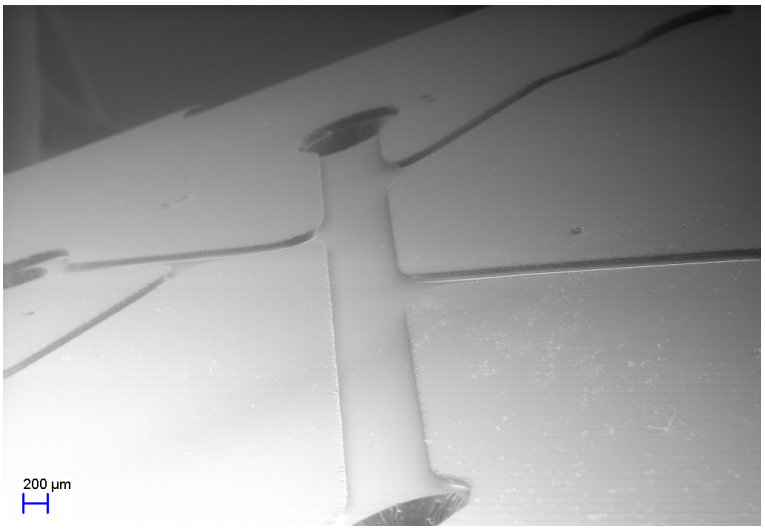

FIGURE 4.5: SEM image of a moulded PDMS microfluidic channel, similar to the design used in Chapter 6. Holes have been punched using a hollow corer to provide fluid inlets and outlets. Image taken by Diego Morganti.

6. The moulded region can be cut from the surrounding PDMS with a scalpel, and peeled from the master.

After polymerisation and cross-linking, the PDMS surface is hydrophobic. Adsorption of hydrophobic contaminants can be a problem for PDMS microchannels, particularly protein adsorption. Plasma oxidation or chemical functionalisation has been shown to be useful in limiting surface adsorption (McDonald et al., 2000; Hillborg et al., 2000).

Figure 4.4 shows a microfluidic channel moulded in PDMS around a DFR master. Dimensions of the fabricated channel correspond well with the master - within 2.5%. The microfluidic channel used with the ring trap arrays in Chapter 6 were fabricated by moulding PDMS. Although not necessary to seal the channel, a glass lid was used on top of the moulded PDMS to improve compatability with the fluid manifold, as the o-rings that seal the fluid channel between the manifold and the glass device were found to compress the PDMS and occasionally block the free passage of fluid. Figure 4.5 shows a scanning electron microscopy (SEM) image of a microfluidic channel moulded in PDMS from a DFR master. The master was exposed using a non-columnated light source, producing non-vertical sidewalls in both the master and the moulded channel.

4.3 Fluid Interfacing

Although it has been shown possible to achieve a high level of integration within a microfluidic device, such as with integrated fluid pumping, cell culture, or analysis stages, all of the devices in this work relied upon external sources of flow control and sample

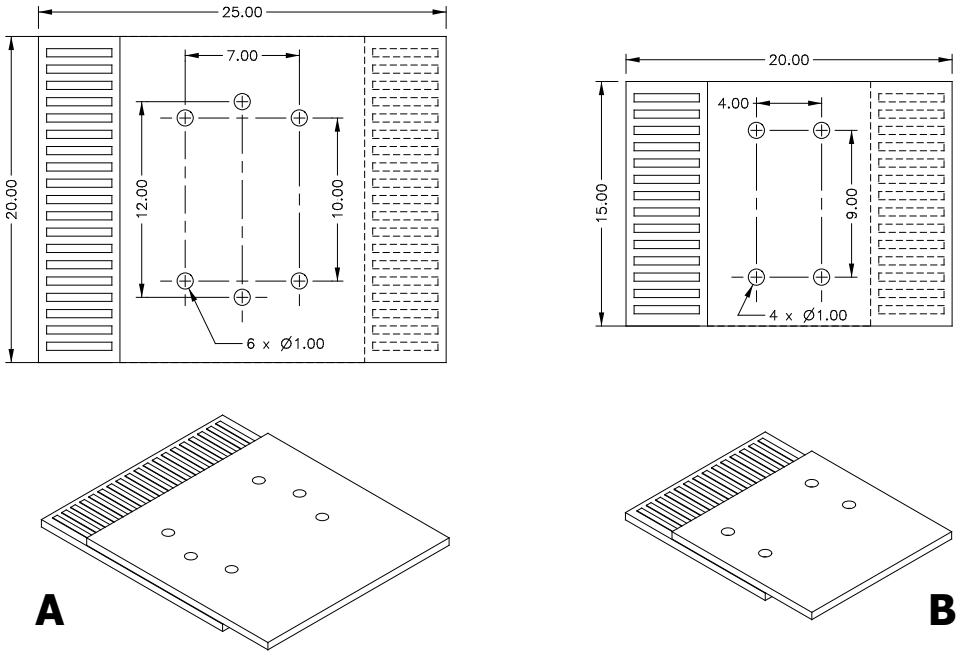

FIGURE 4.6: Access port geometry on (a) 25 x 20 mm devices and (b) 20 x 15 mm devices.

injection and recovery. Hence, it was necessary to interface external macrofluidic technologies to the microfluidic device. Although this interface could be as simple as adhesive bonding of tubes to the device, the more developed solution of a clamped fluid manifold was employed as it enabled the microfluidic device to be rapidly changed without re-bonding.

The microfluidic device was clamped against the fluid manifold, with a pliable membrane in between to seal the fluid channels. Tubing was then connected to the manifold with screw connectors, and to macrofluidic components at other end. The manifold was designed to permit microscopic observation of the active area of the channel, and to enable electric connection to the device.

A standardised hole layout was used for the majority of the devices used in this work, with substrates diced into 25 x 20 mm regions - Figure 4.6 (a). An alternative hole layout was used for the simpler, smaller devices that required substrates diced into 20 x 15 mm regions - Figure 4.6 (b). Figures 4.7, 4.8 and 4.9 show exploded schematics of three generations of the fluid manifold as it was developed and improved between designs.

It was also necessary to develop techniques to produce the fluid access ports in microfluidic devices. The microfluidic channels were produced at the interface between two substrates, so it was required to produce ports through one of the substrates for fluid to enter and exit the device.

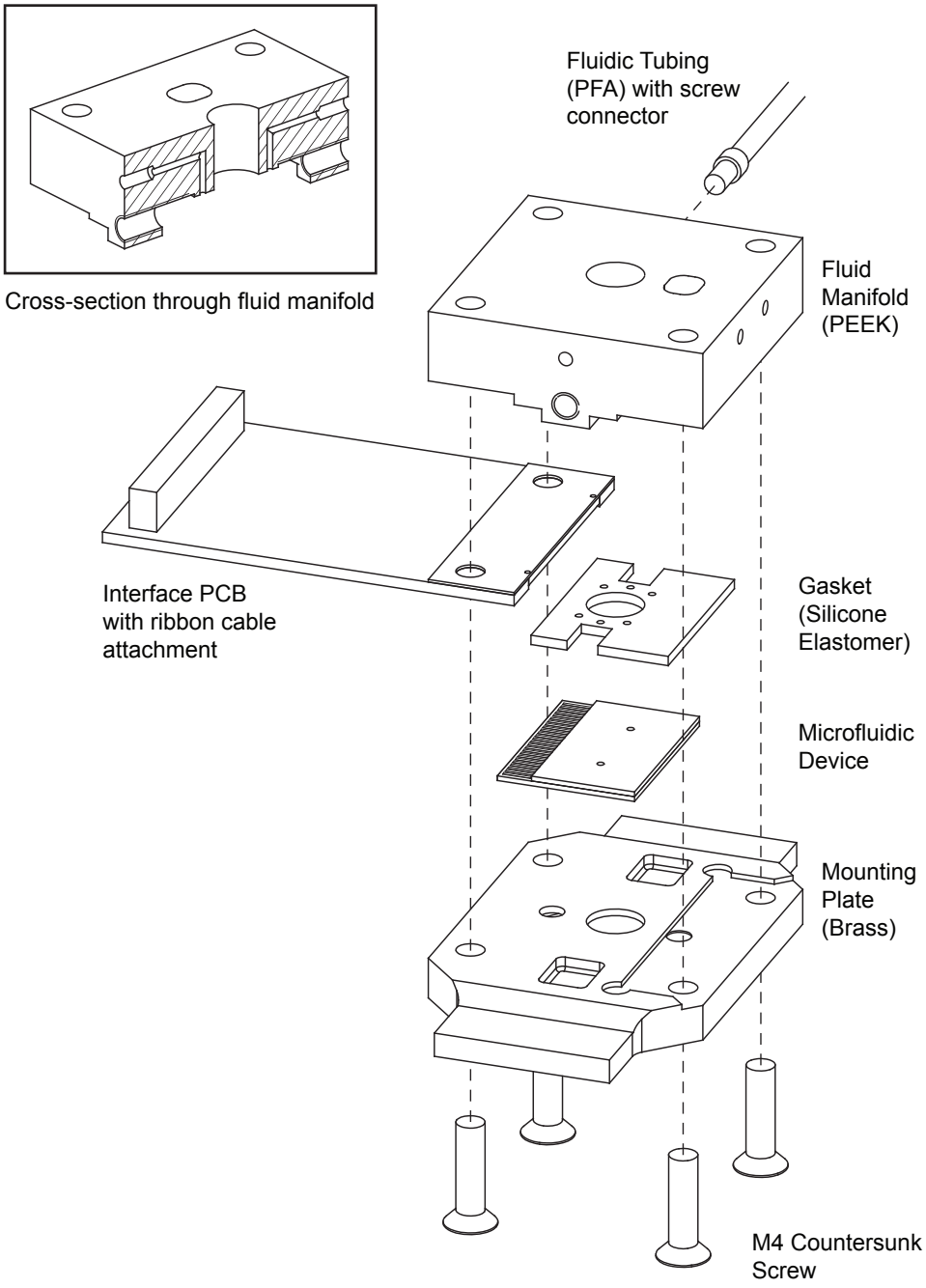

FIGURE 4.7: An exploded schematic of the first generation of the fluid manifold, designed to hold devices ranging in size from 25 x 15 mm to 25 x 25mm. A laser-cut silicone rubber gasket sealed the microfluidic device to the manifold. Integrated PCBs with spring contacts were included for electrical connections.

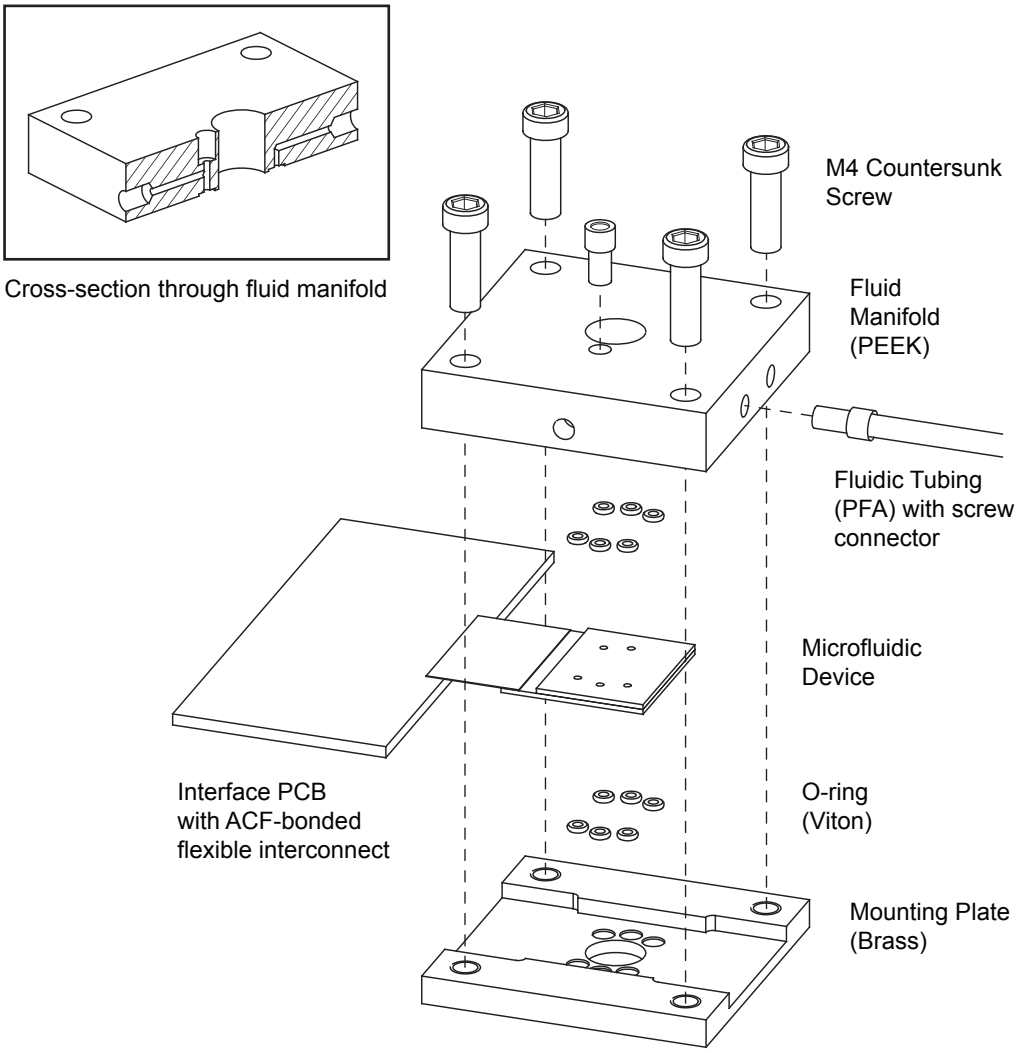

FIGURE 4.8: An exploded schematic of the second generation of the fluid manifold. Electrical connections were provided by separate flexible circuit boards, ACF bonded to each device. Polymer o-rings, made from the chemically resistant material viton, were used to seal the microfluidic device to the manifold. The same o-rings were also used underneath the microfluidic device to aid alignment of the fluid channels, and to provide a compliant but load bearing surface so that compressive forces were only applied to the device in a direction normal to its surface.

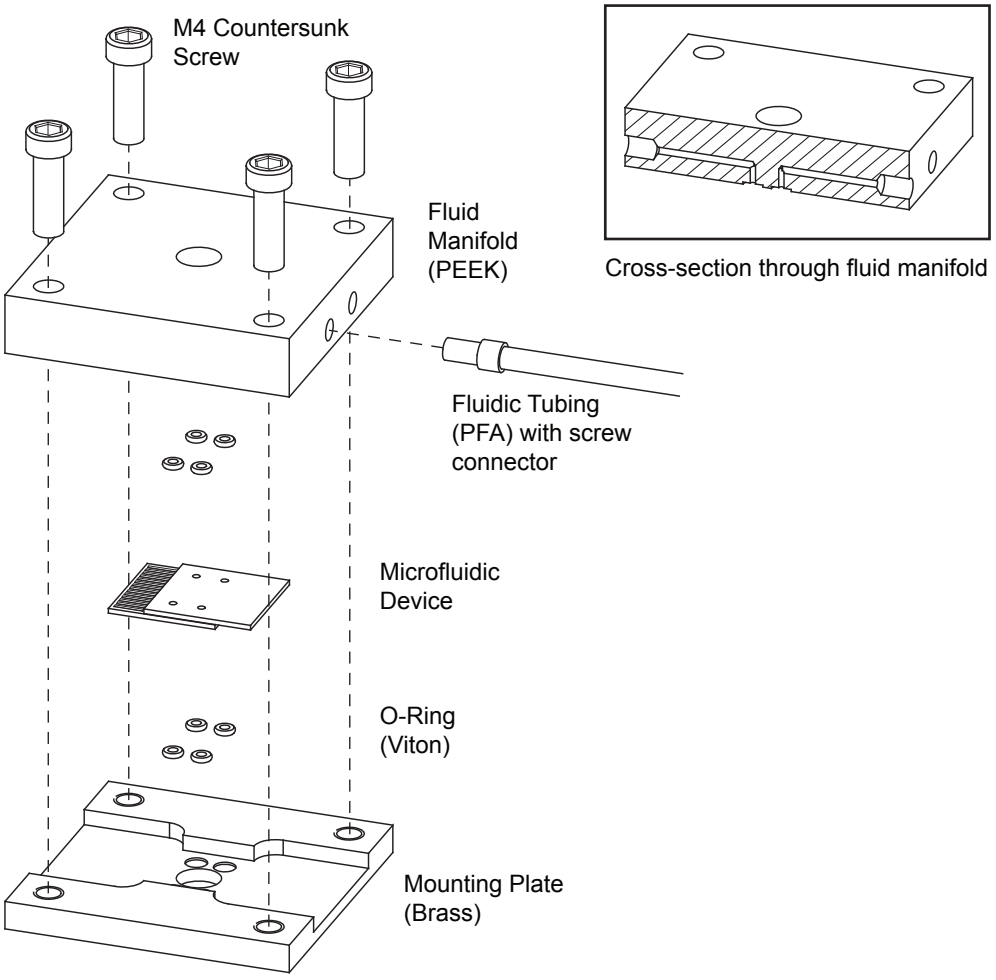

FIGURE 4.9: An exploded schematic of the third generation of the fluid manifold, very similar to the previous generation but designed for the smaller 20 x 15 mm devices with four external fluid connections. Electrical connections were soldered directly to each device.

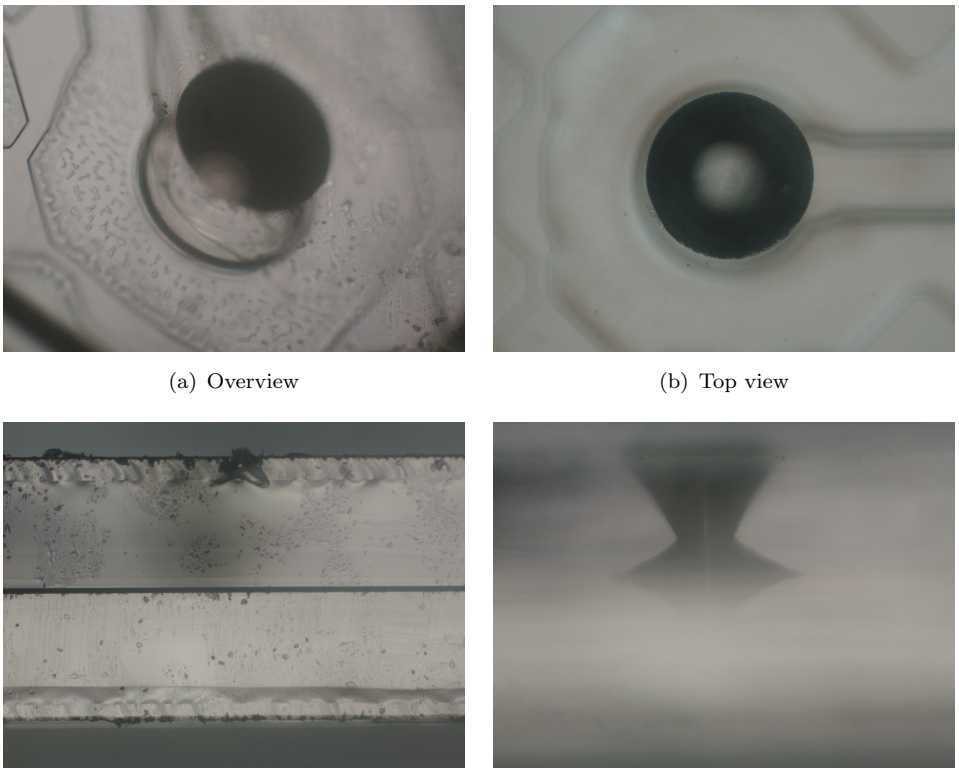

(a) Overview (b) Top view

(c) Side view of bonded microfluidic device (d) Hole profile

FIGURE 4.10: Hole drilled by tungsten carbide spade drill (60° tip angle), through one half of a microfluidic device - formed from two 700 μm borosilicate glass wafers. 875 μm maximum diameter.

4.3.1 Mechanical Drilling

Mechanical twist drill bits can be used to drill access holes through harder substrates. Care must be taken to avoid damage to the substrate through excess heating or mechanical pressure. When drilling a glass substrate, development of cracks through the substrate (on the macroscale) or 'chipping' on the reverse side of the substrate (generally on the microscale) are both symptomatic of over-pressure or over-temperature. Figure 4.10 shows a hole drilled through a 700 μm glass wafer with a 1 mm diameter tungsten carbide spade drill.

4.3.2 Punching

A sharpened needle may be used to punch holes in softer substrates such as PDMS, by removing a 'core' of material. Holes may be produced very quickly and cleanly, as the materials are much less prone to fracture than glass or silicon. Figure 4.11 shows a hole punched through a moulded PDMS sheet. Compression of the substrate produces sidewalls with a flared profile.

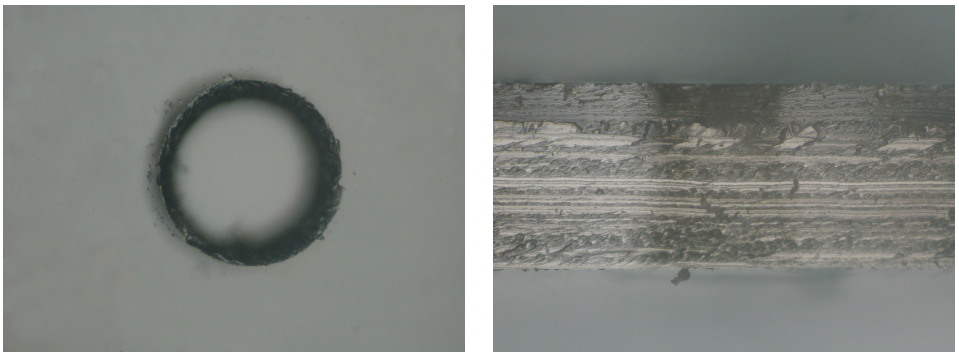

(a) Top view

(b) Side of PDMS sheet

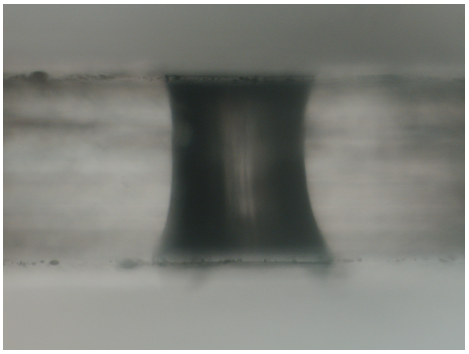

(c) Hole profile

FIGURE 4.11: Hole punched through a 975 μm thick PDMS sheet by hollow corer. Compression of the substrate produces a characteristic flared profile - diameter varies from 696-982 μm.

4.3.3 ECDM

Electrochemical discharge machining (ECDM) involves the removal of material from the substrate in a chemical reaction with the electrolyte in the presence of an electrical discharge. Originally pioneered by Kurafugi and Suda (1968), the technique is particularly suitable for producing small apertures through a glass substrate, such as for fluidic interconnections on a microfluidic device.

The substrate is immersed in an alkaline electrolyte (30% NaOH is commonly used) with a tool electrode and (larger) counter electrode. A DC voltage across the electrodes causes the electrolytic decomposition of water and gas evolution at either electrode. Above a critical voltage, the gas bubbles coalesce into a film, insulating the electrode. Electrical discharge across the gas film and Joule heating produce intense local heating at the tip of the tool electrode. The tip of the electrode is brought into close proximity to the glass substrate, heating it above the material softening temperature (∼1190 K) leading to material removal by reaction with the Na+ ions in the electrolyte (West and Jadhav, 2007):

$$2Na^{+}_{(aq)} + SiO_{2(s)} + 2OH^{-}_{(aq)} \rightarrow Na_2SiO_{3(aq)} + H_2O.$$

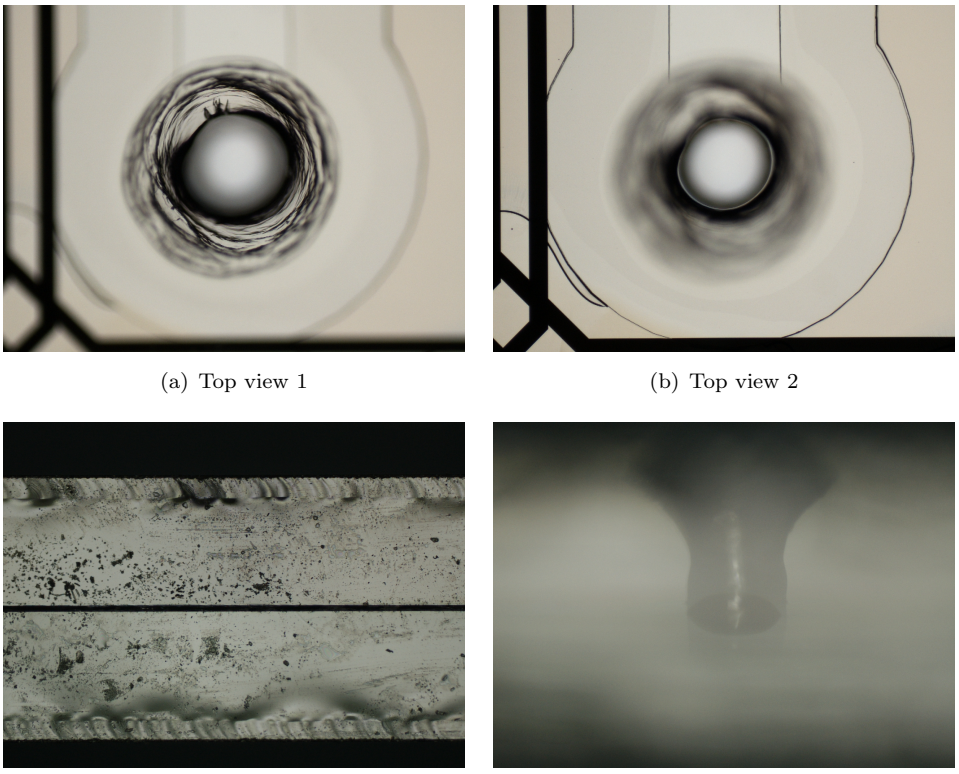

(a) Top view 1

(b) Top view 2

(c) Side view of bonded microfluidic device

(d) Hole profile

FIGURE 4.12: Hole produced by electro-chemical discharge machining (spark erosion) through one half of a microfluidic device - formed from two 700 μm borosilicate glass wafers.

A simple laboratory setup was used to drill fluid interconnections in glass microfluidic devices using ECDM. A platinum tool electrode was carried by a computer-controlled motorised micro-manipulator, and driven with a DC voltage switched at 10 Hz. The main parameters of the machining process are shown in Table 4.1. Figure 4.12 shows a sequence of images of a hole produced in a 700 μm borosilicate glass wafer by ECDM.

Process Parameter	Value
Voltage	40V dc
Switching Frequency	10 Hz
Current	20 mA typically
Electrode	Platinum wire
Diameter	400 μm approximately
Feed rate	2 μm sec^{-1}
Electrolyte	NaOH 30% aqueous

TABLE 4.1: Summary of the main parameters used during ECDM of borosilicate glass wafers.

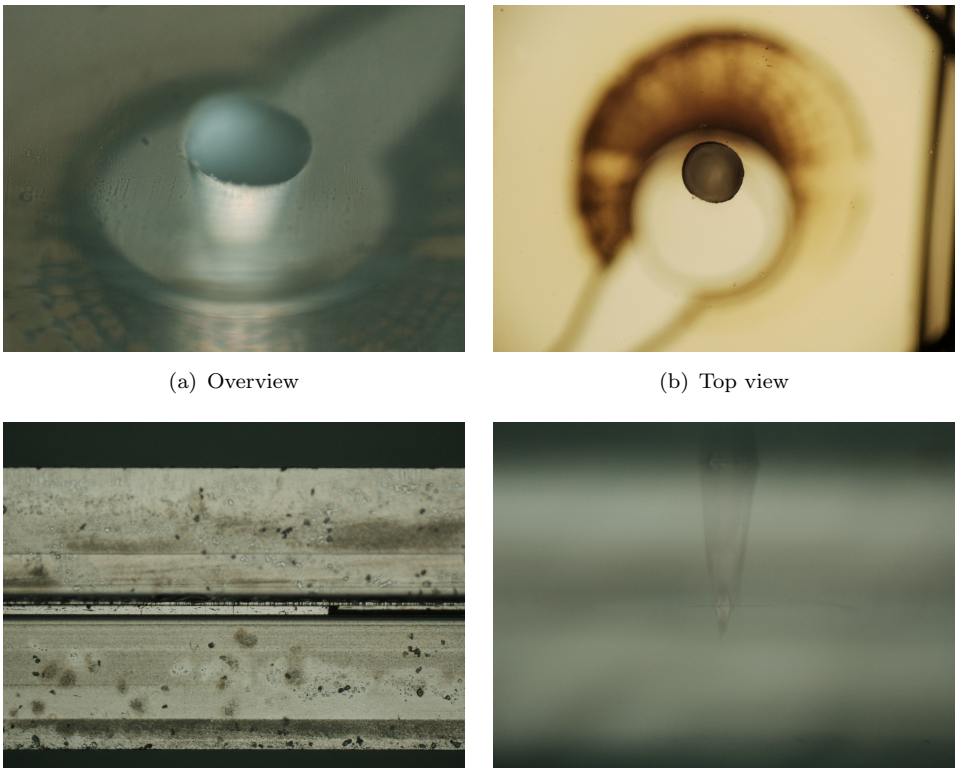

(a) Overview (b) Top view

(c) Side view of bonded microfluidic device (d) Hole profile

FIGURE 4.13: Hole produced by laser ablation through one half of a microfluidic device - formed from two 700 μm borosilicate glass wafers.

4.3.4 Laser Ablation

Intense light, typically from a laser source, may be used for the targeted removal of material from a substrate. As with ECDM, mechanical contact with the substrate is not required, although heating of the substrate may be an issue that limits the rate at which material may be removed. Figure 4.13 shows a hole produced in a 700 μm glass wafer by laser ablation. Some damage to the dry film resist that forms the microfluidic channel is visible.

4.4 Electrode Fabrication

A broad range of techniques exist for the production of microelectrode structures, although they can generally be surmised as a two step process: (i) a surface is coated in a metallic layer, and (ii) material is removed from certain areas to leave behind the patterned electrodes. Metal deposition and patterning is a difficult and technically demanding process, so all the electrodes used in this work were prepared by professional staff in a clean-room environment.

Micro-electrodes are generally constructed with thin-film deposition techniques (as opposed to thick-film techniques such as screen printing), evaporation and sputtering being the most common. Briefly, metal atoms from the source are driven into vapour phase by heating (evaporation) or by a plasma stream (sputtering), within a vacuum chamber, and deposit on the surface of the substrate to be coated. Electrodes of 100 nm thickness were used in this work; early designs used a 3-layer structure of titanium-gold-titanium (titanium for its excellent adhesion to glass at the bottom layer and for its hardness as the top layer, and gold for its high electrical conductivity in between) although subsequently a dual layer titanium-platinum structure was used as this proved more resilient in an aqueous environment.

Metallised substrates are typically patterned by photolithography, by exposure to light through a high-resolution mask. A photopatternable resist can be applied on to the metallised surface, patterned by photolithography, and subsequently used as an etch mask to pattern the metal layer below - this process is shown schematically in Figure 4.14 (a). Alternatively, a photopatternable resist of similar material can be applied to the substrate and patterned prior to metal deposition. Metal above the resist layer is 'lifted off' when the resist is dissolved, leaving only the metal that has deposited on to the exposed substrate. This is shown in Figure 4.14 (b).

4.4.1 Single Metal Layer Devices

The microelectrodes constructed with a single metal layer (used in Chapter 7) were fabricated by Katie Chamberlain at the Southampton Nanofabrication Centre, University of Southampton. Metallised glass wafers (700 μm thickness, sputter coated - 20 nm titanium, 200 nm platinum) were purchased from EPFL (Lausanne, Switzerland). A positive resist (S1813 from Shipley, US) was applied by spin coating, and was developed by UV exposure through a high-resolution glass/chrome contact mask (JD Photo-Tools, UK) and hard baked. The exposed metal was removed by ion-beam milling (Oxford Instruments Ionfab 300+). Finally, the resist was removed in fuming nitric acid.

4.4.2 Two Metal Layer Devices

Complex electrode designs such as the ring trap electrodes used in Chapters 5 and 6 could not be produced using a single metal layer, as the electrical connections cross and overlap, so a multi-layer structure was used with two metal layers separated by an insulating dielectric. The dielectric layer was patterned to produce electrical connections between the metal layers. The first generation of electrodes used a 1 μm thick layer of benzocyclobutene (BCB) as a dielectric, although this was subsequently changed to a 700 nm layer of silicon nitride as this proved less susceptible to degradation in an aqueous environment. All two-metal layer microelectrodes were fabricated by Nico Kooyman

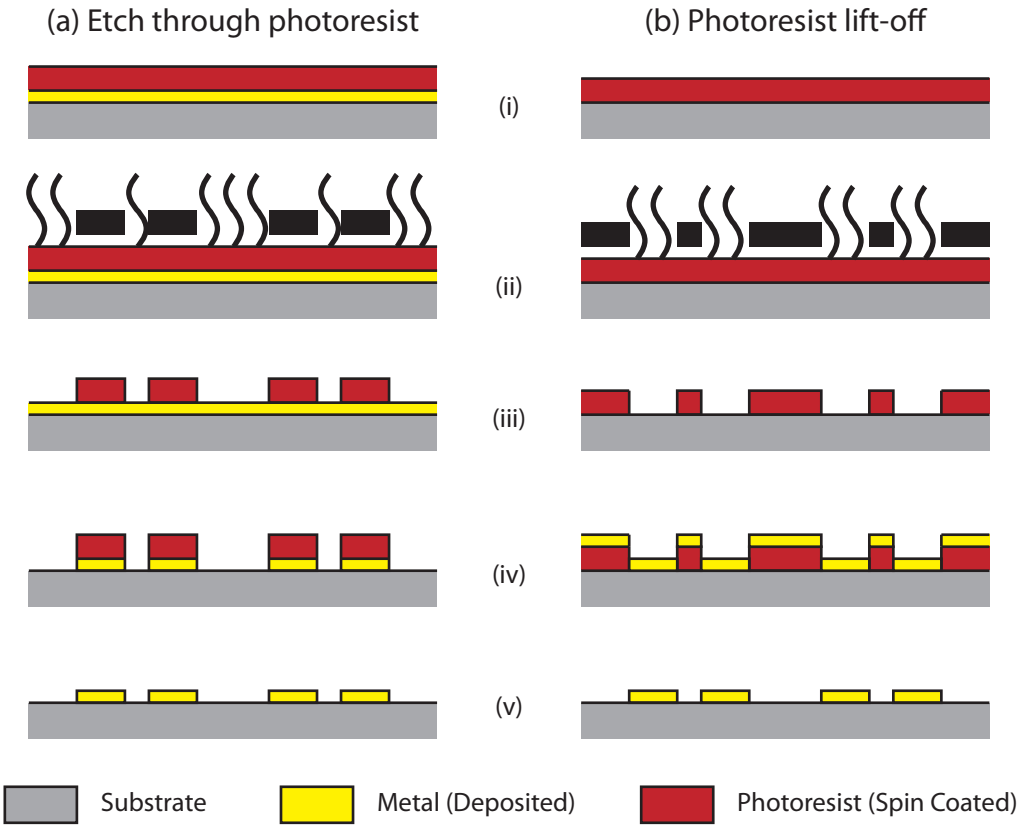

FIGURE 4.14: Process schematics of steps in the patterning of thin metal films. Photopatternable resists can be used as an etch mask (a): the substrate is metallised and spin-coated with a positive photoresist (i), and is exposed to light through a mask (ii). The exposed regions of the photoresist are soluble in the developing solvent, and can be removed (iii), exposing regions of the metal layer that can also be removed by etching (iv). The remaining resist can be stripped, leaving the patterned metal (v). An alternative process is 'lift-off' (b): the substrate is spin-coated with photoresist (i), which is patterned by exposure (ii) and development (iii) (Note that for this process the mask design has been inverted.) The substrate is metallised (iv), and metal above the patterned photoresist is removed by stripping the resist (v).

at Mi Plaza, Philips Research Laboratories, Eindhoven, The Netherlands using similar techniques to that used for the single metal layer devices. BCB was deposited by spin coating, silicon nitride by PECVD.

4.5 Device Integration

Although it is possible to integrate a wide variety of electronic components on to a metalised glass substrate, the expense of producing microelectrode structures means that they are normally manufactured in small quantities and integrated into a larger electrical system. Techniques for producing electrical connections can be as simple as standard soldering techniques, or include computer-aligned multi-way bonding.

The first generation of fluid manifold (Figure 4.7) used gold-plated spring terminals mounted on a PCB to make electrical contact with the microfluidic device. Clamping the microfluidic device to the fluid manifold simultaneously compressed the spring terminals against exposed electrode contact pads, providing electrical connection. The pads are typically 1 x 5 mm, with a pitch of 2 mm. The spring terminals must be aligned to the contact pads each time the microfluidic device is removed from the manifold; if this is performed with the unaided eye, a pitch of 1 mm is usually the minimum feasible.

It is also possible to use solder or conductive epoxy to directly connect wires to contact pads on the electrodes. This negates the requirement to realign the contact pads each time the fluid manifold is removed, although requires each new device to be connected before it can be used. A pitch of 1 mm is usually the minimum feasible if unaided techniques are used, although this can be reduced be an order of magnitude if micromanipulation is used, particularly automated wire-bonding machinery.

4.5.1 Anisotropic Conductive Film Bonding

The ring trap array electrodes (used for cell separation experiments described in Chapter 6) were connected using anisotropic conductive film (ACF) bonding. ACF is a nanostructured material that, when in its bonded state, exhibits much increased electrical conduction in one axis. Hence, ACF can be used to create multiple parallel electrical connections simultaneously.

Figure 4.15 shows the components of a complete device before bonding - the patterned microelectrodes on glass substrate, flexible foil interconnect (gold coated copper patterned on polyamide film, Hallmark Electronics, UK), and rigid PCB. Although the glass substrate could be bonded directly to a rigid PCB, it is generally more suitable to connect the two through a flexible interconnect as this negates the need to simultaneously align other connections and relieves bending stresses on the ACF bonds. The square symbols in the vicinity of the bonding pads are alignment marks that overlap when the flexible interconnect is correctly orientated above the electrodes. ACF tape was purchased from Hitachi Chemical Company; Table 4.2 shows a summary of the parameters used for producing the bonded connections. An assembled device is shown in Figure 4.16.

Bond	ACF Tape	Stage	Temperature	Pressure	Time
Glass/Foil	AC-7206U-18	Pre-bond	108°C	0.4 kgf cm^{-2}	10 s
		Final	237°C	2.2 kgf cm^{-2}	37 s
Foil/PCB	AC-2052P-45	Pre-bond	108°C	0.4 kgf cm^{-2}	8 s
		Final	250°C	1.3 kgf cm^{-2}	30 s

Table 4.2: Summary of the bonding parameters used with the ACF tape.

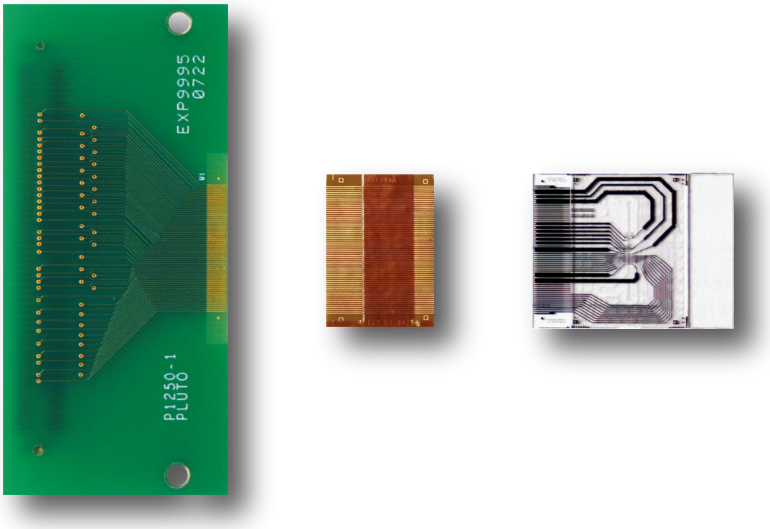

FIGURE 4.15: Photograph of a glass substrate with microelectrodes, the flexible interconnect, and the rigid PCB that will be bonded together using ACF bonding. The flexible interconnect has been inverted to show the gold/copper tracks on its underside.

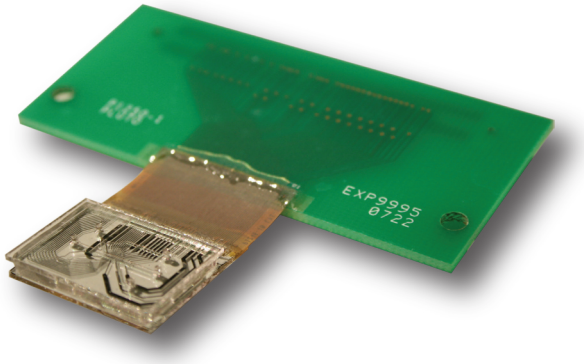

FIGURE 4.16: Photograph of an ACF-bonded microfluidic device with attached PCB. A PDMS microchannel has been fitted over the electrodes, with a glass lid on top. Silicone sealant has been applied around the ACF bonds to add mechanical stability.

4.5.2 Summary of Fabrication Techniques

A broad range of techniques have been developed for the fabrication of microfluidic electrokinetic devices, with several techniques usually required on a single device to produce electrode structures, fluidic channels, and to provide the relevant connectivity. Consideration must be given to the order in which processes are carried out, particularly with regard to the ability of each material to withstand the subsequent processing conditions. An alignment stage is required at key points during fabrication, typically involving the alignment of a photolithographic mask to the substrate for each layer of electrodes, dielectric, or microfluidic channel. This is often a laborious and time-consuming task requiring specialised equipment, and the use of equivalent alternative processes that

require fewer alignment stages often results in an overall streamlining of the microfabrication protocol. An example would be the use of PDMS to construct a microfluidic channel rather than DFR, as this would require only a single alignment stage to be performed rather than the two that would be required using DFR. If electrodes are only required on one side of the microfluidic channel, this would likely be a prudent decision.

Over the next three chapters, the use of microfabricated devices for single cell and particle manipulation and sorting is explored. The choice of fabrication technology for each section of work is slightly different, as requirements for the placement of electrodes and the number of electrical connections develops.

Chapter 5

Single Particle Dielectrophoretic Traps

5.1 Introduction

Dielectrophoresis is particularly suited for trapping and immobilising particles within a microfluidic device, as it is able to manipulate the particles with minimal disturbance to the suspending medium. Isolation of cells by confinement within a particle trap is one route towards single cell manipulation and analysis. There are also applications for cell patterning, an important step in the production of biosensors, and cell processing such as co-culture. The ability to trap single cells as required can also be used to separate rare or important cells from a heterogeneous population. Target cells can be immobilised in an array of traps, while unwanted cells are removed by fluid flow.

A condition of cell viability and proliferation is the presence of ionic solutes, that render the surrounding environment isotonic. These conditions are found both *in vivo* and *in vitro* physiological solutions such as for cell culture. Due to the high electrical conductivity of physiological medium, positive DEP does not occur. Hence, dielectrophoretic devices that operate in these conditions must utilise negative DEP. Concern must also be given to the power dissipation within the device, as thermal energy will be distributed within the medium in direct proportion to the electric field strength and the medium conductivity, as shown in Equation 2.12.

From these requirements, we can postulate that an ideal dielectrophoretic cell trap should have the following characteristics:

- Operate in (high conductivity) physiological media.
- Have minimum power dissipation (avoid fluid heating).

- Limit the exposure of cells to high electric fields
- Operate at high frequencies to minimise induced transmembrane potentials.
- Capture a single cell in a closed cage.
- Be scalable to an array, ideally with a single wire connection per trap.

The ring trap electrodes are a novel design of dielectrophoretic particle trap that potentially meets all of these requirements. The electric field between a ring electrode and a surrounding ground plane curves above the electrodes to create a closed DEP trap against the substrate. The ground plane can be shared between many traps, so only a single electrical connection is necessary to control the trap. As cells are trapped in the centre of the ring, they are kept away from the high field regions at the electrode edges. The central ring is completely surrounded by the ground plane. This means that the trapping force is equal in every direction, but necessitates a multiple metal layer fabrication process to provide electrical connection to the ring and bypassing the ground plane.

5.1.1 Forces on a Trapped Particle

Figure 5.1 shows forces on a particle in a DEP trap - if the particle is immobilised then a force equilibrium will exist in the horizontal plane:

$$F_{DEP-x} = F_{HD-x} \tag{5.1}$$

$$mg + F_{DEP-y} = F_B + F_L + F_N \tag{5.2}$$

where the force (F) subscripts correspond to: DEP - dielectrophoretic, HD - hydrodynamic (Stokes) drag, B - buoyancy, L - hydrodynamic lift, N - normal surface reaction.

As was shown in Section 3.3, the electric field strength varies greatly across the centre of the ring array, with a zero value in the centre and maximum at the electrode edges in the gap between the electrodes. At any given height above the substrate, the lateral DEP force $F_{DEP,x}$ is zero in the centre, and increases to a maximum over the ring electrode. Hence, a trapped particle in a fluid flow is displaced a certain distance from the centre of the ring. This position is given by the balance of the Stokes drag force and the DEP trapping force. The hydrodynamic drag on a spherical particle in a uniform flow field can be calculated by Stokes law:

$$F_{HD} = -6\pi a\eta\mathbf{v} \tag{5.3}$$

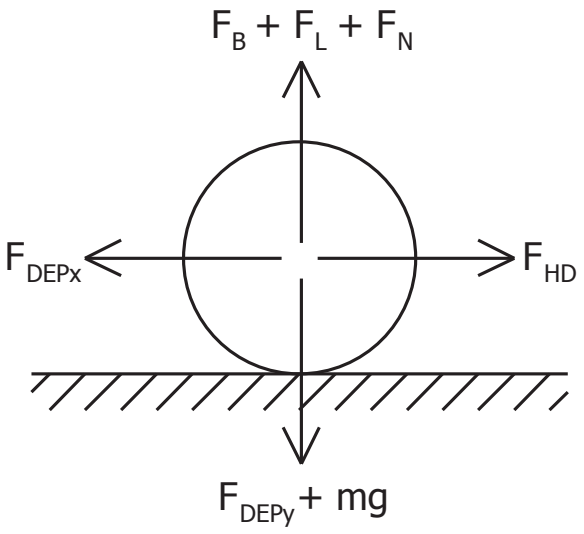

FIGURE 5.1: Forces on a particle immobilised in a DEP trap against a fluid flow.

In the case of a particle within a shearing flow, Stokes Law can be modified to incorporate the shear rate:

$$F_{HD} = -6\pi a\eta hS \tag{5.4}$$

where h is the height of the particle within the shear field (distance from the zero point at the channel wall) and S is the shear rate within the flow. Such a calculation assumes that the flow around the particle is unrestricted, however, and becomes unreliable for a particle near to a plane wall. Goldman et al. (1967) found that wall effects increased the hydrodynamic drag on a spherical particle in a laminar shear flow, and the effect could be modelled by a non-dimensional coefficient that is proportional to the distance of the particle from the wall:

$$F_{HD} = -6\pi a\eta hSK \tag{5.5}$$

where K is a coefficient that incorporates wall effects, and for the case where the particle is in contact with the wall ($h/a = 1$), this coefficient has a value of 1.7005.

5.2 Materials and Methods

5.2.1 Electrode Fabrication

The electrodes were fabricated on 150mm diameter, 700 μm thick glass wafers by Nico Kooyman at Philips Research Laboratories, Eindhoven. Electrode layers were made

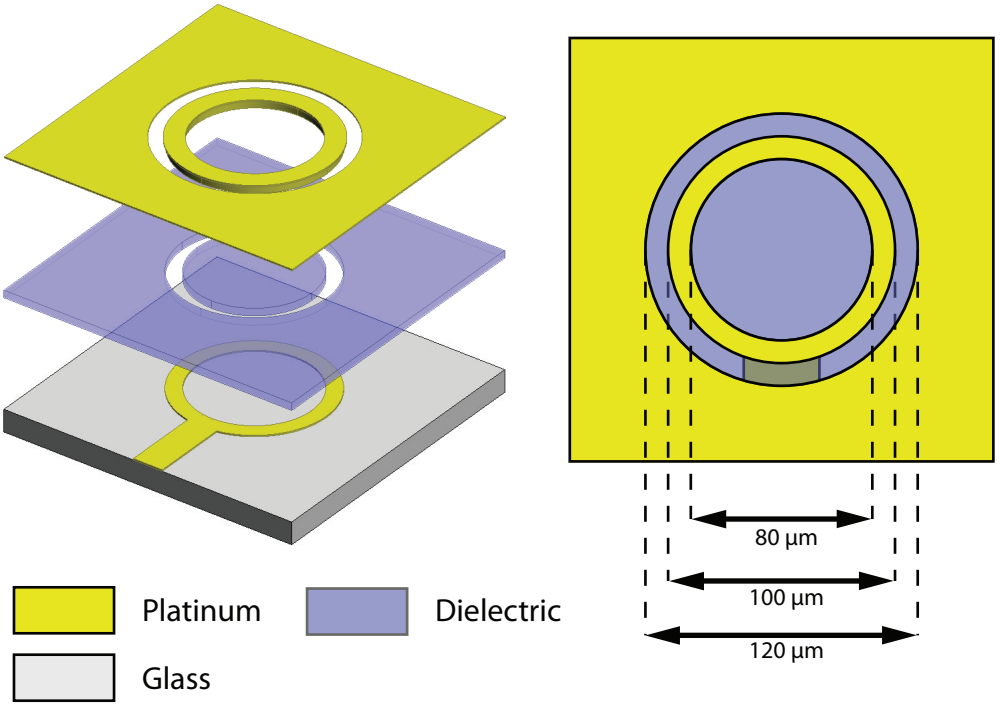

FIGURE 5.2: Overview of the fabrication of the multi-layer electrodes. A dielectric layer of benzocyclobutene separated and insulated the two metal layers, enabling a more complex interconnection strategy than would be possible with a single metal layer.

from layers of titanium (for adhesion) and platinum, patterned using photolithography and ion beam milling. To fabricate a ring electrode in the ground plane, two metal layers separated by a dielectric insulator were required. The dielectric was a 1 μm thick layer of benzocyclobutene (BCB) patterned using reactive ion etching. Wafers were diced into individual chips, 20 mm square. The ring electrodes were fabricated with internal diameters of 40 and 80 μm, the width of the ring electrode was 10 μm and the gap between the ring and the ground plane was 10 μm - as shown in Figure 5.2.

5.2.2 Microfluidic Channel

The microfluidic channel was fabricated separately on each chip, from a layer of Ordyl SY355 dry film resist (Elga Europe), bonded between the chip and a glass lid. One layer of resist was laminated on to each of the two surfaces (chip and glass lid) by hot-rolling at 100°C. The laminate was patterned by exposure to UV radiation through a negative contact mask and developed in BMR developer (Elga Europe) using a process similar to that described by Vulto et al. (2005). A closed microfluidic channel was produced by bonding the two resist layers together at 200°C. Inlet and outlet holes (1 mm diameter) were drilled in the glass lid after bonding using a tungsten carbide spade drill bit (Drill Service, Horley, UK).

5.2.3 Macrofluidic Equipment

A fluidic manifold was used to interface macroscale fluidic connections to the microdevice and also provided electrical contact via spring contacts mounted on a printed circuit board. Bead suspension was driven through the device using a Cole-Palmer 79000 syringe pump with flow rates in the range 0.25 to 20 μL min^{-1}.

5.2.4 Ancillary Electronics

Sinusoidal voltages produced by a TTI TG2000 signal generator were split across 20 channels of a custom produced switch board into the normally open (NO) terminal. The ring electrode from each ring trap was independently switched between connection to ground (normally closed, NC) or the sinusoidal voltage. Voltages at the board were confirmed using an oscilloscope (Agilent 54641D) prior to each experiment, to ensure the voltage on each channel was close to the specified value.

5.2.5 Microscopic Observations

Particles were imaged and tracked using a custom-built fluorescence microscope, using around a Nikon 10x Plan Fluor objective lens and a Panasonic AW-E600E colour camera. A blue LED (Lumiled Luxeon, peak output 470nm) provided illumination for (FITC/GFP compatible) fluorescence observations, while broadband illumination from a 'white' LED (5500K CCT) mounted underneath the target was used for transmitted-light measurements.

5.2.6 Cells and Microparticles

Latex test particles were suspended in a solution of 0.1 mM KCl containing 0.02 % (v/v) TWEEN-20, prepared in deionised water. The conductivity was measured at 1.9 mS m^{-1} (25°C) using a (Hanna EC215) conductivity meter. Polystyrene microspheres (Polybeads, Polysciences Ltd) were purchased from Park Scientific Inc, with a mean diameter of 15.61 μm (CV $\leq$ 15%, density 1.05.). For trap characterisation, a 100 μL aliquot of bead suspension (1.35 x 10^7 beads mL^{-1}, or 2.5% solids) was washed three times in the 0.1 mM KCl/TWEEN solution by centrifugation and resuspension. Bead solutions were passed through a 41 μm filter (Whatman) prior to use. Figure 5.3 shows a plot of the Claussius-Mossotti factor for the beads suspended in the 0.1 mM KCl/TWEEN solution, calculated using Equation 2.4.

GFP-modified HeLa (Human epithelial carcinoma) emit green fluorescence when illuminated with light in the 450-500 nm region. Cells were cultured in DMEM (Dulbecco's Modified Eagle's Medium - 4mM L-glutamine, Hepes buffer, no Pyruvate) with

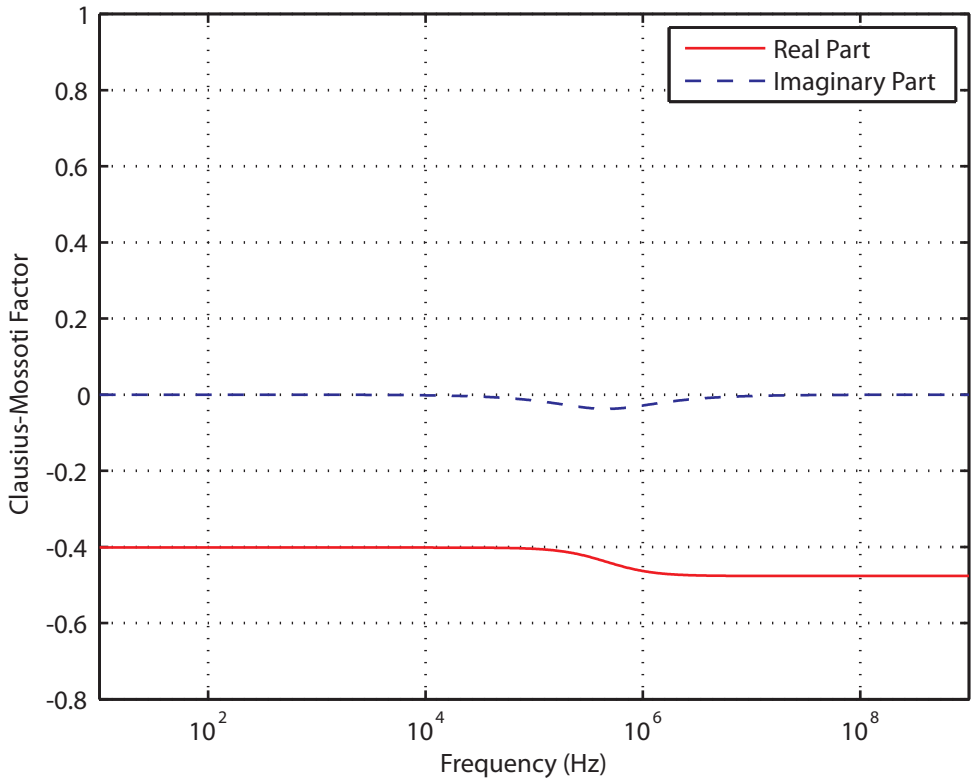

FIGURE 5.3: Plot of the real and imaginary parts of the Clausius-Mossotti factor for 15.61 μm polystyrene spheres ($\epsilon_{r,p}$ = 2.5, K_s = 1 x 10^{-9} S) in aqueous solution ($\epsilon_{r,m}$ = 78, σ_m = 1.9 mS m^{-1})

10% foetal calf serum and 100 μg mL^{-1} Penicillin/Streptomycin, at 37°C. To maintain growth, the cultures were split every 3rd or 4th day by trypsinisation, and fresh culture medium added. For experiments, the cells were removed from culture, incubated at 37°C and used within 3 hours. The cells were concentrated by centrifugation in culture medium to a density of 10^6 cells mL^{-1}. Prior to use, the chip was flushed through with DMEM, and a sample of HeLa cell suspension injected at a flow rate of 10 μL min^{-1}.

5.2.7 Characterisation of Trapping Force

A bead suspension was pumped through the channel, and a single bead immobilised in a ring trap using a signal of 1 MHz at 5 Vpp. With a bead trapped, the flow rate was increased in steps from 0 to 5.5 μL min^{-1}, and the position of the bead recorded. Data was recorded for 10 seconds for each flow rate, and 20 frames from each clip at 0.5 second intervals were analysed. Bead position relative to the centre of the trap was measured (in pixels, and converted to μm) for each frame, and an average value for all 20 frames was obtained. This experiment was repeated four times.

For comparison with experimental data, the force on a 15.61 μm diameter polystyrene particle was calculated using Equation 2.3 and the simulated electric field, setting

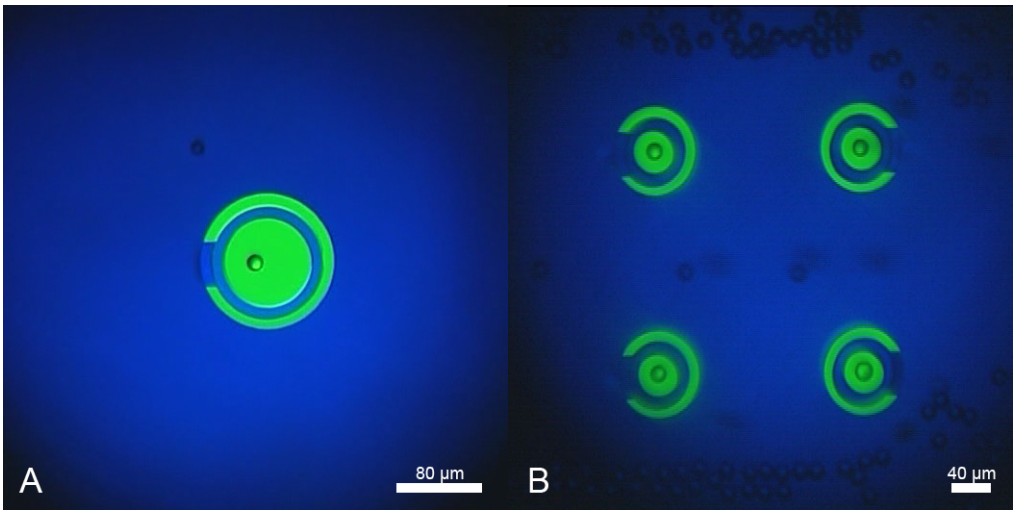

FIGURE 5.4: (a) A single 15.61 μm polystyrene microparticle trapped within an 80 μm diameter ring trap. (b) An array of four 40 μm diameter ring traps each with a single polystyrene microparticle trapped inside. Metallised regions reflect episcopic illumination, so appear blue. Transparent regions appear green due to white diascopic illumination through the fluorescence filter set.

$Re(f_{CM})$ = -0.475 (with ϵ_r =2.5, σ_p=0.27 mS m^{-1}, V = 5 Vpp and f = 1 MHz). Only the horizontal component of the DEP force is considered, as this is the only component that can be determined directly from the hydrodynamic drag force.

5.3 Results

Single 15.61 μm polystyrene microparticles were immobilised from a fluid flow and trapped in the 80 μm diameter ring traps - Figure 5.4 (a). Once energised, the trap was closed and surrounding particles were deflected around or over the trap. Particles could be held within the trap at flow rates of up to 5.5 μL min^{-1} (with electrical excitation of 5 Vpp, 1 MHz), above which they were displaced from the trap by hydrodynamic drag. The particles were also held in an array of eight 40 μm diameter traps - Figure 5.4 (b). The smaller size of the electrodes produced stronger DEP forces, and particles could be held within the trap at flow rates of up to 20 μL min^{-1}.

Measurements of the trapping force were made by gradually increasing the fluid flow rate from 0.25 μL min^{-1} until the particle was removed from the trap by fluid flow. Video of the particle position was analysed using custom-produced image processing/feature recognition algorithms written in the Matlab environment (Mathworks). Figure 5.5 shows three frames from the recorded video, and their subsequent analysis. The data is plotted in Figure 5.6, showing bead displacement against volumetric flow rate. The displacement from the centre of the array increases with increasing flow rate, but the rate of increase slows as the particle approaches the ring due to the rapidly increasing

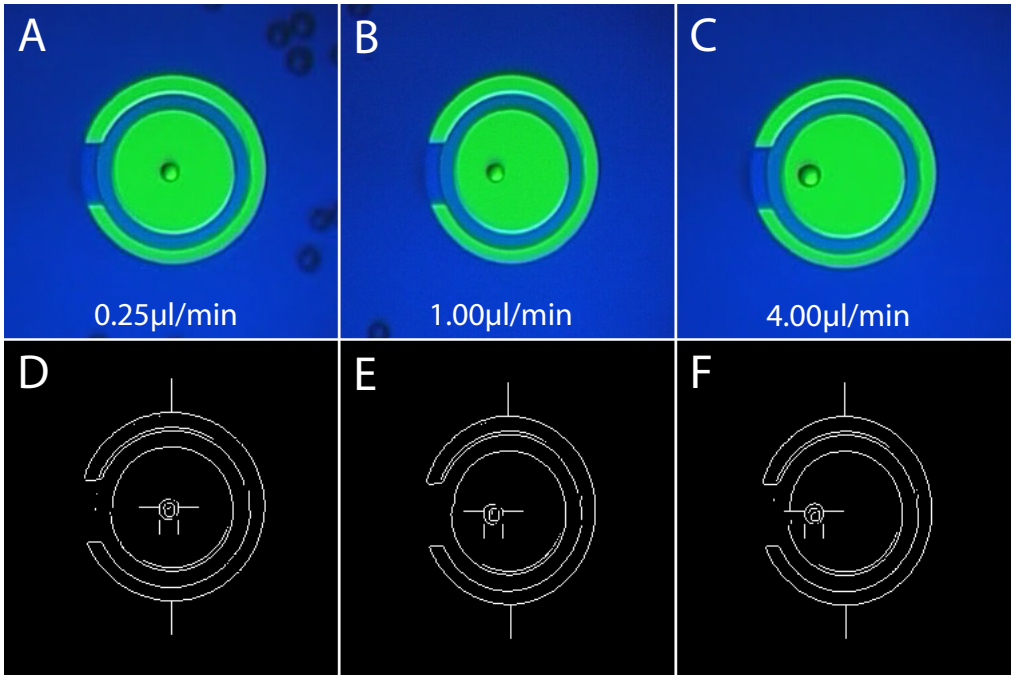

FIGURE 5.5: Hydrodynamic drag displaced 15.61 μm polystyrene particles trapped in the ring electrodes, until an equilibrium was reached with the DEP force closer to the edge of the electrodes. Automated image recognition software was used to track the location of the particle with reference to the static features of the electrode edges.

DEP force. At an applied voltage of 5 Vpp, the beads escaped from the trap when the flow rate exceeded 5.5 μL min^{-1}.

The fluid flow velocity profile within the microchannel was calculated from the volumetric flow rate using a Fourier series approximation of the Navier-Stokes law in 2-dimensions for each of the flow rates used in the experimental tests. The results of the calculation for one of the flow rates (5.5 μL min^{-1}) are plotted in Figure 3.11. Due to the aspect ratio of the channel being very small (much wider than deep) the lateral position within the channel (x-axis) does not have a significant effect (<0.05%) on the fluid velocity within the the central 90% of the channel width. Hence, the fluid velocity is almost entirely a function of the vertical position within the channel. An approximation of the flow with variation in one dimension only (the y-axis) is shown in Figure 5.7 with a 15.61 μm diameter particle to scale.

To estimate the hydrodynamic drag on a particle immobilised in a ring electrode using Stokes law, it was necessary to approximate the flow field to a linearly shearing flow. The fluid velocity field was averaged over the surface of the particle by splitting the particle into a 0.5 μm square grid, and calculating the average of the fluid velocity at each grid intersection. The shear rate for each volumetric flow rate (0.25-5.5 μL min^{-1}) was then calculated. This was used to calculate the hydrodynamic drag force on a particle for each flow rate using Equation 5.5. Figure 5.8 shows the hydrodynamic drag data cross-referenced with the measurements of particle displacement. The velocity of

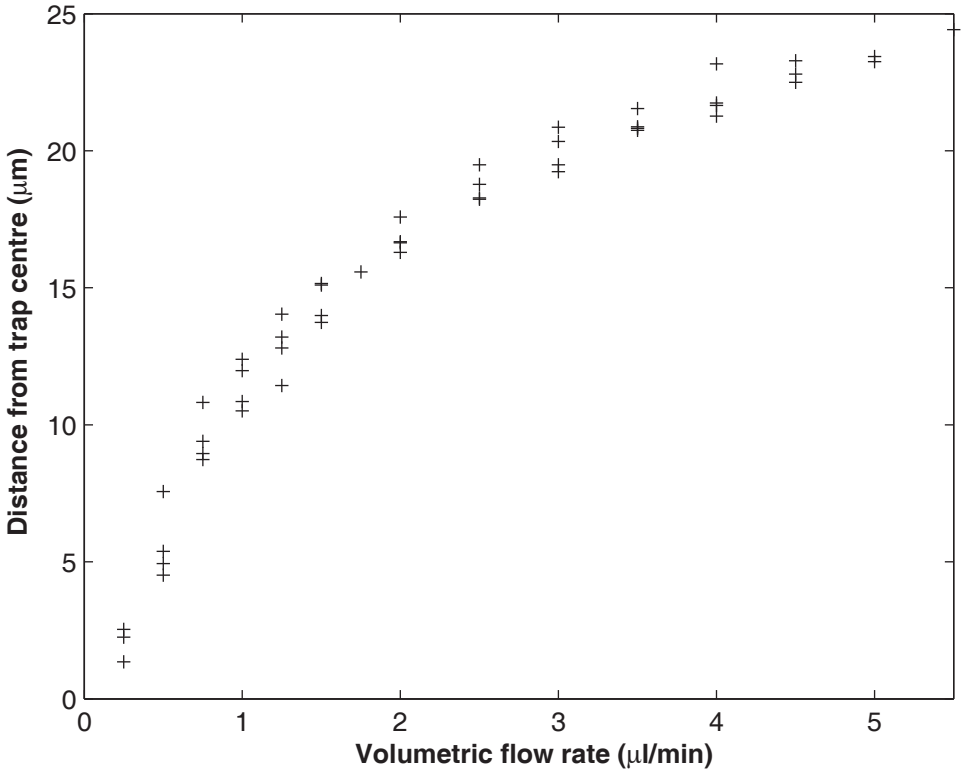

FIGURE 5.6: 15.61 μm diameter polystyrene particles were trapped in the centre of a ring trap (electrical excitation 5 Vpp, 1 MHz) but were increasingly displaced by hydrodynamic drag as the volumetric flow rate of the fluid was increased.

the fluid is shown on the opposite axis; as the particle is in a shear flow this is the velocity impinging on the centre of the particle.

Single HeLa cells (suspended in DMEM, σ_m = 1.6 S m^{-1}) were also trapped in the ring traps - Figure 5.9 (a) shows a single GFP-positive HeLa cell immobilised in a 40μm diameter ring trap. Figure 5.9 (b) shows a development of the original ring trap electrode design, with the ground plane replaced with a ground ring. The ring-ring electrode traps could hold 15.61 μm polystyrene particles against flow rates of up to 2.06 μL min^{-1} (mean value, s.d. = 0.15, with electrical excitation of 5 Vpp, 1 MHz), and HeLa cells against flow rates of up to 1.03 μL min^{-1} (mean value, s.d. = 0.11, with electrical excitation of 5 Vpp, 20 MHz). The microfluidic channel on the ring-ring device was smaller than on the ring-plane device, with dimensions of 1600 x 100 μm, so a given volumetric flow rate produced a higher flow velocity and hydrodynamic drag force. The average peak trapping force produced was 27.5 pN for the polystyrene microparticles and 13.8 pN for the HeLa cells (given an average diameter of 15.9 μm, s.d. = 1.2). The use of this electrode design is explored further in Chapter 6.

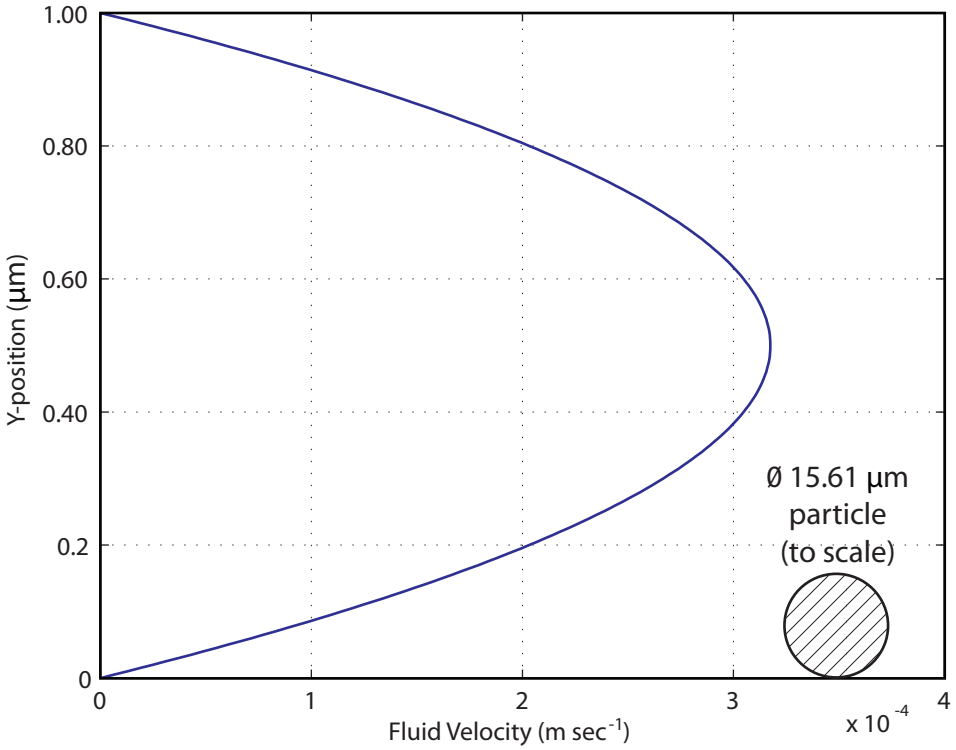

FIGURE 5.7: Approximation of the fluid flow velocity through the microchannel at 5 μL min^{-1}.

5.4 Discussion

Single particles have been trapped within the ring electrodes, with up to 8 particles trapped in separate traps simultaneously. The requirement for a single electrical connection (and shared ground plane) per trap means that only one control line was required for each trap. This means that the design can be scaled to larger arrays of traps quite simply, and would be suitable for arrayed operation if driven from a transistor matrix such as a TFT device.

In the absence of fluid flow, trapped particles are directed towards the centre of the ring electrodes by the dielectrophoretic force. Motion of fluid around the trapped particle produces a hydrodynamic drag force that displaces the particle from the central position. The displacement from the centre of the trap increases with flow rate, but the rate of increase slows as the particle approaches the edge of the ring electrode due to the rapidly increasing DEP force. The displacement of the particle was measured as the fluid flow rate was adjusted, the results are plotted as a line in Figure 5.8.

Comparison of the experimental data with the simulated force (FEA) shows excellent agreement, with small deviations in the centre and edge of the trap. The discrepancy at small displacements may be due to errors in measurement of small displacements and the difficulty in controlling low flow rates. At the edge of the trap the error may be due to the limitations of the dipole approximation used to calculate the force. Assumptions

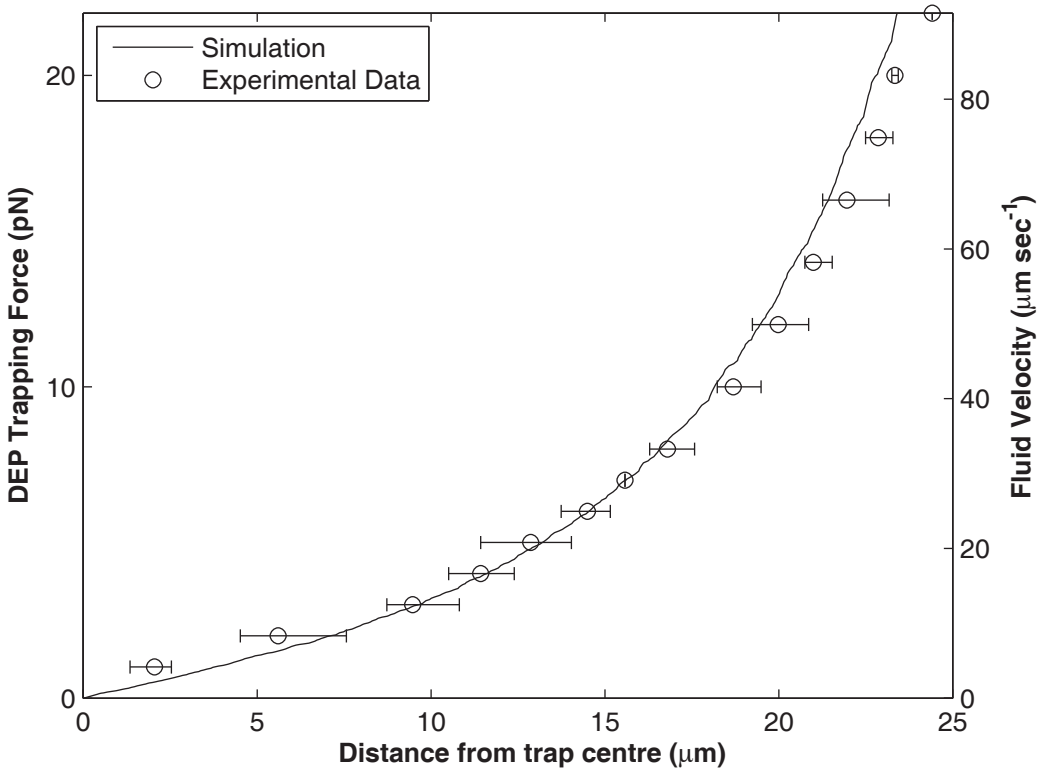

FIGURE 5.8: The trapping force developed by the ring traps on 15.61 μm diameter polystyrene beads was calculated from models of the fluid velocity profile, and was found to be similar to values derived from FEA simulations of the electric field distribution. The fluid velocity, at a distance from the channel wall equal to the particle radius, is shown on the alternate axis.

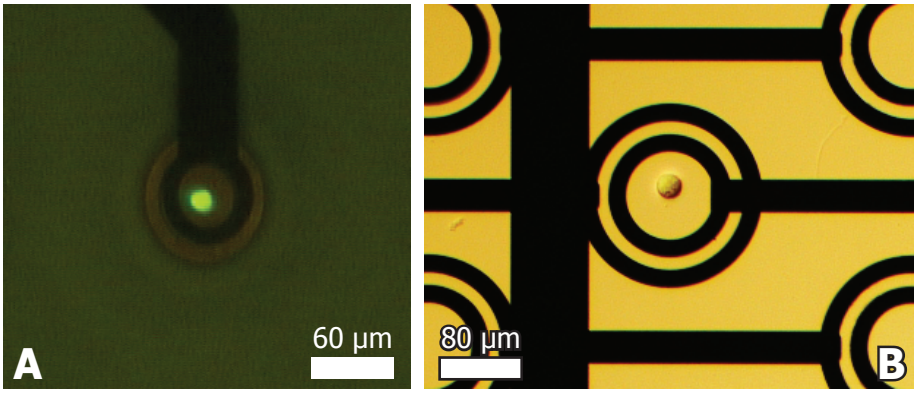

FIGURE 5.9: A single HeLa cell (Cervical cancer, GFP-modified) suspended in DMEM culture medium immobilised in (a) a ring trap with ground plane (electrical excitation 20 Vpp, 20 MHz) and (b) a ring trap with ground ring (electrical excitation 5 Vpp, 20 MHz).

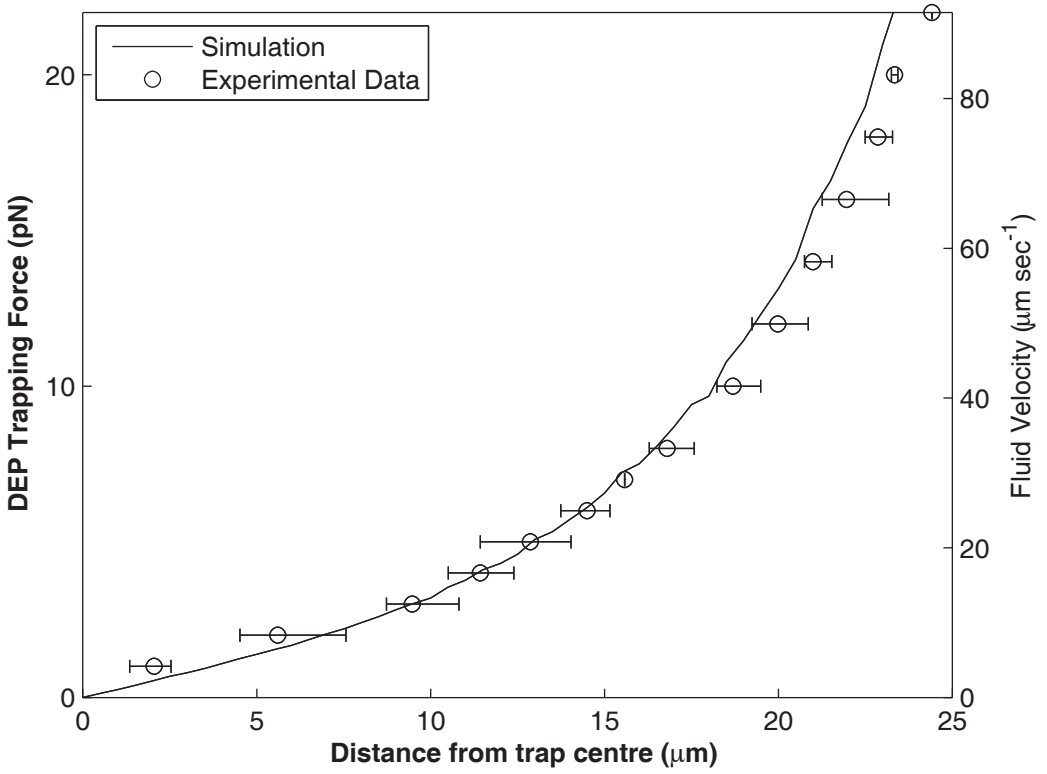

FIGURE 5.10: Data from numerical simulations fits closely with experimental results (R^2=0.9958) is obtained if the applied voltage used in the simulation is reduced to 4.8 Vpp, suggesting that a small voltage drop could have occurred along the interconnects.

regarding the distribution of charge around the particle being equivalent to a dipole become less accurate if the particle is located in the highly divergent field close to the edges of the electrodes. A near perfect agreement (R^2=0.9958) is obtained if the applied voltage used in the simulation is reduced to 4.8 Vpp, suggesting that a small voltage drop could have occurred along the interconnects - Figure 5.10.

The maximum trapping force developed on a 15.61 μm polystyrene microparticle was 23 pN, sufficient to immobilise the particle against a flow of 5.5 μL min^1. To put this into context, this exceeds the particle's weight force of 20.51 pN (assuming density = 1.05 g ml^{-3}, particle mass = 2.09 x 10^{-12} kg). In aqueous solution, the particle would also receive a buoyancy force of approximately 19.5 pN. Hence, in the absence of a flow, the particle would remain trapped if the trap array were to be held vertically. The DEP trapping force scales with the third power of particle radius (a^3, Equation 2.3), while the hydrodynamic drag scales with the first power of radius (a, Equation 5.5). This means that larger particles can be trapped at higher flow rates than smaller particles, for a given value of applied voltage and trap size.

The DEP forces produced by the ring-ring electrodes are similar to the ring-plane electrodes (up to 27.5 pN on a 15.61 μm diameter latex particle with 5 Vpp, 1 MHz, compared with 23 pN for the ring-plane design). The dimensions of the microfluidic channel were smaller, leading to higher fluid velocities for a given volumetric flow rate. The ring-ring electrode traps could hold the HeLa cells against a fluid flow of 1.03 μL min^{-1} (mean value, s.d. = 0.11) with an applied signal of 5 Vpp at 20 MHz. This corresponds to a trapping force of 13.8 pN for a 15.9 μm diameter cell (mean value, s.d. = 1.2 μm). The maximum flow rate against which biological cells can be held is generally lower than for similarly sized polystyrene particles, because the Clausius Mossotti factor for cells suspended in physiological media is lower than for polystyrene particles at frequencies suitable for nDEP.

Numerical simulation of the electric field - Figure 3.4 - shows the location of the region of field gradient minimum (the trapping location) in the centre of the ring electrodes. A second minimum can be seen above the electrodes at the top water-glass interface. Comparison of the two trapping locations indicates that the upper trap is at least two orders of magnitude weaker than the lower trap within the ring electrodes. As can be seen from the arrow plot in Figure 3.4, the DEP force around the minimum at the top of the channel acts in a substantially vertical direction. The lack of a horizontal component to the DEP force suggests that hydrodynamic flow will carry particles through this location and they will not be trapped. No particles were observed to trap in the upper trap location during operation of the ring electrodes.

The ring electrodes form a closed dielectrophoretic trap when driven with a sinusoidal voltage. This is very different to quadrapole electrode traps (see Section 1.3.1 - DEP Trapping) which form a 'force funnel' and must be confined with another electrode set to form an octopole set if the particle position is to be accurately defined. Particles that are not trapped within the electrodes are repelled by the field, passing around or over the top of the trap. The trajectories of particles around the trap is simulated in Figure 3.12. Because the trap is closed, particles must be located within the trapping region before the trap is activated, or they will be repelled from the vicinity of the trap. Hence, the ring traps are unlike designs such as the 'horseshoe' electrodes - Figure 1.15 - which are self-filling. A control system (automated of manual) is required to fill the traps with particles, by activating the traps when a particle is directly above the trapping region.

HeLa cells suspended in physiological medium (DMEM) were trapped using voltages of 5 Vpp, 20 MHz. Higher frequencies were used as damage to the electrodes was observed when the device contained DMEM and the traps were driven with signals in the region of 1 MHz at 5 Vpp. Figure 5.11 shows two images of the ring electrodes are used in DMEM media. The damage to the electrodes was believed to related to the ionic content of the medium and the frequency of the applied electric fields. At 20 MHz, the rate of damage to the electrodes was much slower, and cells could be manipulated for over one hour before noticeable damage to the ring electrodes was observed. The developed design of

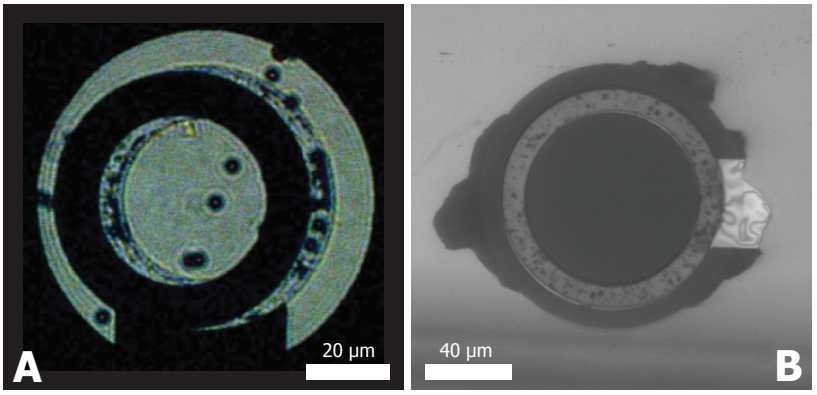

FIGURE 5.11: Damage to electrode structures as a result of electrokinetic manipulation, illustrating two modes of failure: (a) delamination of the metal layers has led to the entire ring electrode detaching from the substrate, and (b) electrochemical attack with degradation of the metal layer around the edges.

ring electrodes with a double ring structure were fabricated from titanium-platinum with a silicon nitride dielectric (see Chapter 4), rather than titanium-gold-titanium with a BCB dielectric, and these appeared far more resilient, although this could be as a result of better metal adhesion rather than a better choice of materials.

5.5 Conclusions

Dielectrophoretic ring electrodes have been shown suitable for the trapping and immobilisation of single particles and cells within a microfluidic device. Values for the trapping forces calculated from numerical simulation of the electric field agree closely with the measured results. This validates both the use of numerical simulation of the electric field to determine DEP forces, and the calculation of hydrodynamic drag through velocity flow profile analysis. With knowledge of the electrical parameters or dimensions of a particle, either of these methods can be used to determine the flow rates at which the particle can be trapped.

The trapping of multiple single cells is an exciting concept, as it opens up the possibility of new ways of working with cells. Rather than treating cells as a bulk population that must be described by statistical terms, single cells can be isolated and analysed. The ability to isolate single cells is of interest in its own right, but has many more possibilities when it is combined with other components into an integrated system. An array of ring traps can be used as a particle concentrator, to position cells for culture, or to isolate cells within a cell-based assay. Particle immobilisation can also be used as a separation technique. By trapping particles of interest, the remaining particles can be washed away with fluid flow to leave a purified population. This method of separation is explored in the next chapter.

Chapter 6

Automated Control of Dielectrophoretic Traps for Cell Separation

6.1 Introduction

The ability to separate cells is key step in many biomedical, analytical and therapeutic processes, and requires two key competences: the ability to recognise and distinguish between cells of different types, and the ability to differentially manipulate cells so that they can be isolated. The identification of sufficient cell surface markers can permit a particular cell type to be identified, and it is common practice to use fluorescently labelled antibodies to determine the presence of surface markers within a population of cells. Fluorescence-activated cell sorting (FACS) is an established technique for the separation of cells with fluorescent labels, generally by deflection of cells within a fluid stream into one of a number of different outputs. Electrostatic deflection of small droplets (each containing a single cell) is commonly used to separate cells in commercially available FACS machines, typically operating in the range of several thousand cells per second, although the viability of recovered populations can be affected by the manipulation techniques used.

Cells can also be separated by differential attachment to magnetic microparticles, such as by immunological coupling. The cellular conditions encountered during magnetic-activated cell sorting (MACS - see Chapter 2) generally have less impact on cell health, as cells are separated by passing through a magnetic mesh, and are not exposed to high-voltage electric fields or aerosolised by passing at high velocity through a nozzle. The introduction of MACS revolutionised laboratory preparation of purified cell samples, as it permits large numbers of cells to be separated with relative ease, with purities in excess of 90% being commonplace (Willasch et al., 2009). The inability to recover a

100% pure sample places some limitations on the extent of its use, however, such as the selection of stem cells from donor samples for tissue regeneration therapies.

A number of cell sorting systems have also been developed within a microfluidic environment. Methods for directing the motion of particles include controlling the flow of the carrier fluid by electro-osmotic switching (Fu et al., 1999), flow switching with external solenoid valves (Wolff et al., 2003) or on-chip pressure-driven valves (Fu et al., 2002), and manipulation of particles using dielectrophoresis (Holmes et al., 2005). The ability to manipulate single cells has potential for the separation of particles with particularly high purity. Isolation of cells by immobilisation of target cells within a microfluidic device has advantages over conventional cell sorters that separate cells from a particle stream into multiple outputs, particularly if cells are to be maintained on chip for further culture or analysis. Such a device can also act as a concentrator, increasing the number of cells within a given volume of liquid.

In the previous chapter, ring electrodes were used to trap and isolate single HeLa cells suspended in physiological medium. Here, similar electrodes are used to separate and purify osteosarcoma cells (MG63) by automated detection of fluorescent labelling. Cells with a particular fluorescent label are identified by optical detection and are trapped within the ring electrodes. Non-target cells are then washed away by fluid flow, leaving a purified population of cells that can be recovered or maintained on chip for further analysis.

6.2 Materials and Methods

6.2.1 Electrode Fabrication

Multi-layer electrode structures were fabricated on 700 μm borosilicate glass wafers using established techniques as described in Section 4.4. 700 nm silicon nitride was used as an inter-layer dielectric. All fabrication of electrode structures was performed by Nico Kooyman at Philips Research Laboratories, Eindhoven. Figure 6.1 shows an overview of the electrode geometry.

Anisotropic conductive film was used to make electrical connections between the glass electrodes, a flexible interconnect, and a PCB daughterboard - as described in Section 4.5.1. An assembled device is shown in Figure 6.2. Two designs of microfluidic channel and associated macrofluidic systems were developed to handle cells as they were introduced into the dielectrophoretic traps.

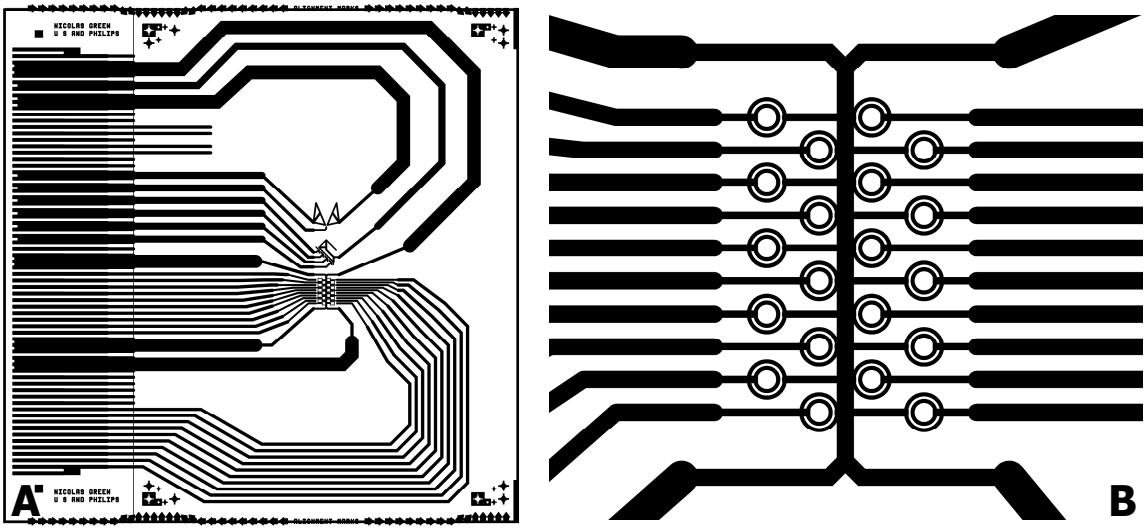

FIGURE 6.1: An overview of the electrode geometry on the ring trap devices (a), and an enlarged view of the array of ring electrodes themselves (b).

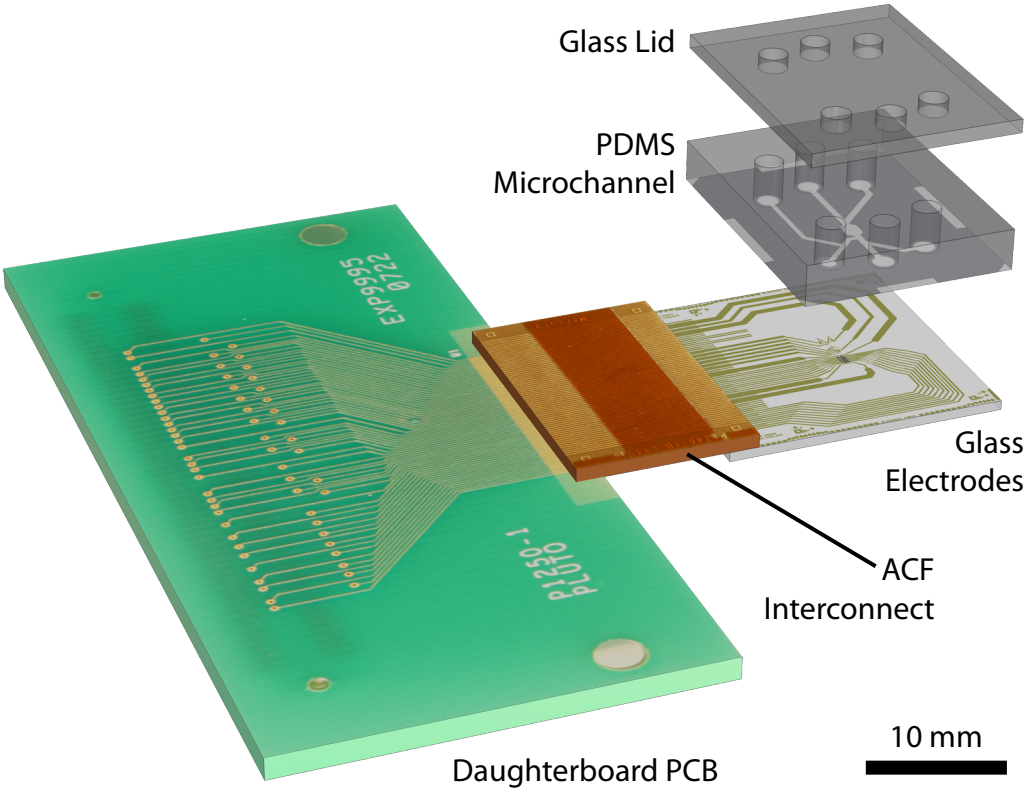

FIGURE 6.2: A completed device incorporating anisotropic conductive film connections between PCB daughterboard, flexible interconnect, and the glass electrodes.

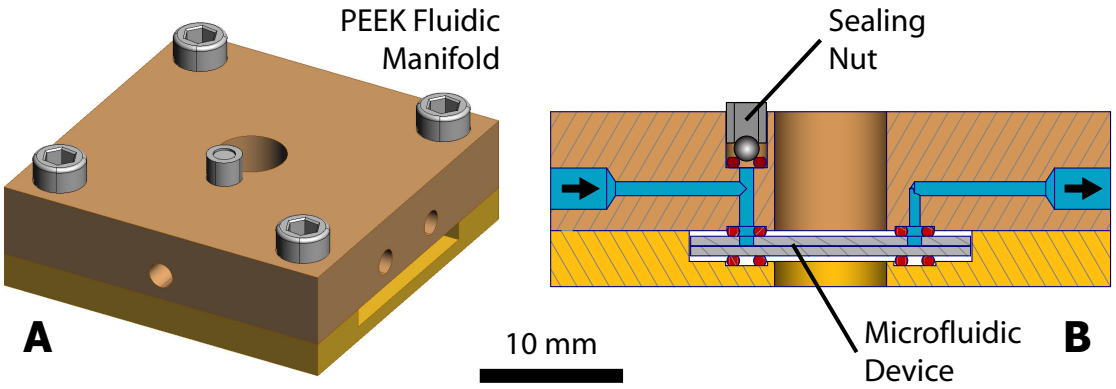

FIGURE 6.3: A cross-section through the manifold used to provide fluidic connections to the microfluidic device.

6.2.2 Design A: Dry Film Resist Channel with Sample Injection

6.2.2.1 Sample Injection

Although microfluidic systems are ideal for handling small samples, challenges exist when such samples must be introduced and moved around the system. The volume of liquid in surrounding macrofluidic equipment such as valves and pumps can easily dwarf the useful sample. As described previously, the flow within microfluidic channels (and also tubing with micron-sized diameters, commonly used for interconnections) is within the laminar regime. There is a fluid velocity profile across the channel cross-section, with fluid flowing faster at the centre of the channel. This acts to disperse the sample, reducing its concentration.

A modified microfluidic manifold (Figure 6.3) was developed with a sample injection port. This meant that very small volumes (typically 1 μL) could be injected directly at the inlet of the microfluidic device. A sealing nut kept the port closed when it was not in use. To introduce cells into the system, the sealing nut was unscrewed so that the needle of a 10 μL syringe (Hamilton) could be inserted towards the inlet of the microfluidic device. A sample was injected, and the nut replaced. An exploded schematic of the fluid manifold assembly is shown in Figure 4.8.

6.2.2.2 Microfluidic Channel

The microfluidic channel shown in Figure 6.4 was fabricated in dry film resist using techniques described previously by Katie Chamberlain at Southampton Nanofabrication Centre. A single inlet is used, with a sample of cell suspension injected at this point directly on to the device. Suspending medium flowing into the device at this point carried the cells through the device. Two outlets were provided: a general outlet for unsorted 'waste' cells, and a dedicated 'recovery' outlet for sorted 'target' cells. Macrofluidic

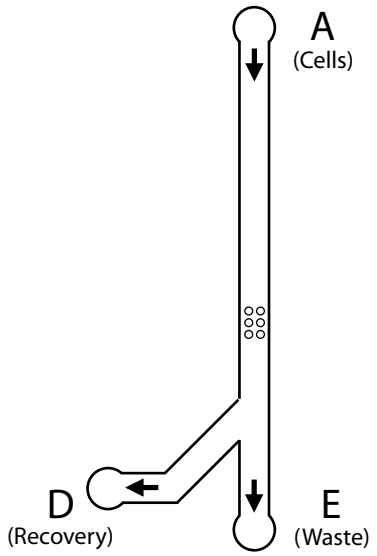

FIGURE 6.4: Overview of the microfluidic channel used with the ring arrays.

valves on the tubing connected to each outlet controlled the fluid flow through each outlet.

6.2.2.3 Macrofluidic Equipment

The microfluidic chip was clamped within the fluidic manifold, and connections to external tubing were made via threaded connectors. Six inputs and outputs were available, although only three were required for this work. A syringe pump (Cole Palmer 79000) was used to control fluid flow through the device. Two sizes of syringe were used, to permit a range of fluid velocities to be used. A 10ml plastic syringe (BD) was used to clean and flush through the device with large volumes of liquid during setup and cell recovery. A 25 μL glass syringe (Hamilton) was used during trapping operations, as the smaller diameter permitted flow rates of less than 0.1 μL to be used without introducing significant pulsations into the flow from the pump. A 3-way valve (Omnifit) at the input to the microfluidic device permitted the flow to be switched between the syringes. An overview of the fluidic equipment used with the system is shown in Figure 6.5.

An on-off valve (Omnifit) was used on each of the outputs to isolate the flow. Suspending medium and untrapped cells were collected from the 'waste' outlet into a collection jar. A similar container was used on the 'recovery' outlet to collect fluid during cleaning and preparation, but during the recovery of sorted cell populations the tube was removed from the container and droplets were dispensed directly into a 384-well microplate (Corning CellBind).

The fluidic manifold was mounted on a custom-built stage with Peltier thermoelectric elements and water cooling. This enabled approximately 10 W of cooling power or 20 W

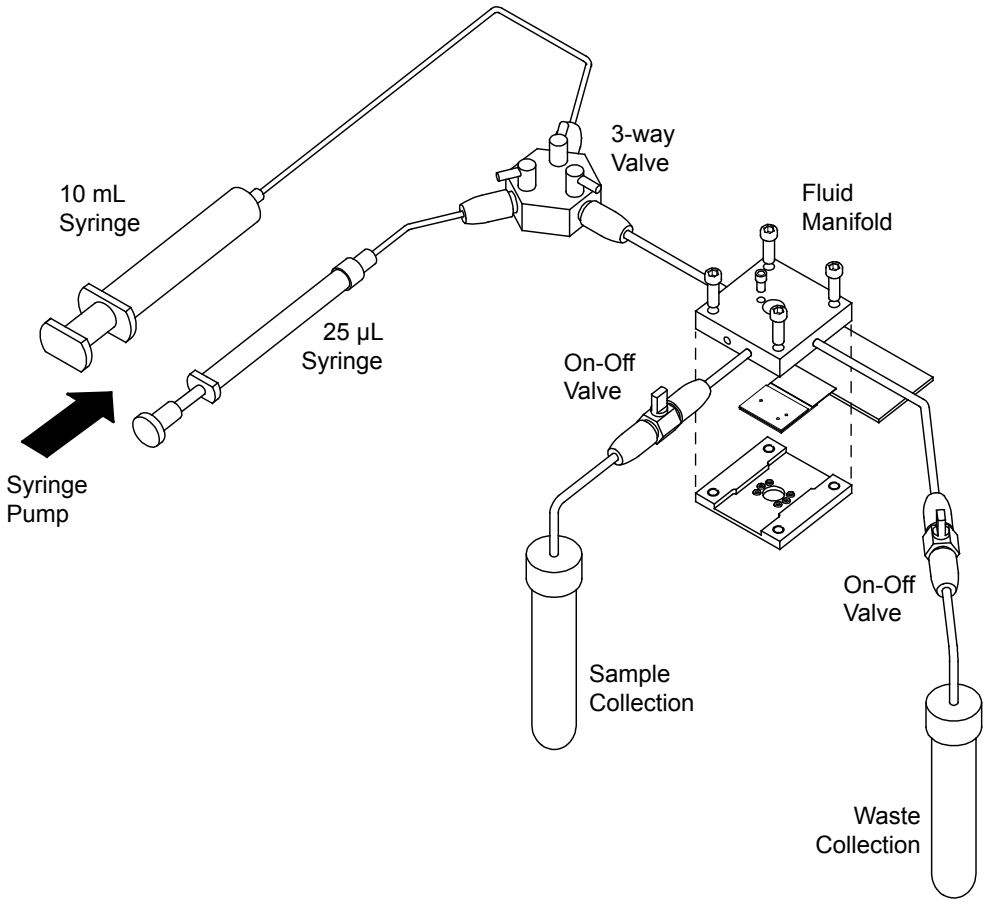

FIGURE 6.5: Schematic of the macrofluidic connections surrounding the microfluidic device.

of heating power to be applied to the manifold by adjusting the voltage on the Peltier elements from a DC power supply. A thermocouple (J-type, insulated junction) was placed within the fluidic manifold, and the stage and manifold covered in insulating wadding. A digital readout of the temperature of the manifold was obtained by a voltmeter through an interface box. This permitted the temperature of the manifold to be controlled over a range of approximately 2-45°C.

6.2.2.4 Operation

Red and green labelled cells (see below) were mixed to achieve a final ratio of red to green of approximately 4:1, suspended in DMEM + 4% Dextran-70 at a concentration of approximately 5 x 10^5 cells per mL. 1 μL samples of cell solution (approximately 500 cells) were dispensed at the inlet to the microfluidic channel, and the system resealed. The sequence of operation was:

1. Suspending medium flowed through the inlet at 0.1 μL/min, carrying cells through the device.
2. Green cells were trapped in the ring electrodes; untrapped cells carried away through the 'waste' output.
3. After at least 20 minutes, all the cells suspended in medium had been carried through the device.
4. The valve on the 'waste' output was closed, and the 'recovery' channel opened. Cells were released from the traps (the voltage is turned off), and flushed towards the 'recovery' outlet.
5. Cells were recovered onto a microplate in 40 μL droplets at 1 mL min^{-1}.

40 μL DMEM + 20% FCS + Penicillin/Streptomycin (1x) was added to each well, and the microplate placed in a cell culture incubator.

6.2.3 Design B: Moulded PDMS Channel with Bulk Sample Handling

6.2.3.1 Microfluidic Channel

Work on the previous design of microfluidic channel highlighted a number of limitations in its operation. The single inlet was used for both cells and plain medium, so it was difficult to perform a washing step to remove untrapped cells from the device, as it was not possible to be sure that all the cells that had been injected at the inlet had already passed through. The channel was redesigned to provide separate inlets for cells and medium. A second inlet was added so that the 'recovery' outlet could be washed with suspending medium to prevent cells entering that channel during normal use, and so that target cells could be flowed down the recovery outlet with little risk of drawing other cells from the main 'cells' inlet.

Microfluidic channels were molded in PDMS (Sylgard 184, Dow Corning) using established techniques as described in Section 4.2.2. Two layers of 55 μm dry film resist were patterned to form the master, producing channels of 95 μm depth after processing.

6.2.3.2 Macrofluidic Equipment

A similar set of external fluidic equipment was used, with a syringe pump driving fluid around the system and the same fluid manifold. A sample loop was added to the 'cells' inlet and a number of valves incorporated, so that the pump could drive fluid through any of the the three inputs. As described above, the fluidic manifold was mounted on a temperature controlled stage, adjustable through the range of approximately 2-45°C. An overview of the system is shown in Figure 6.7.

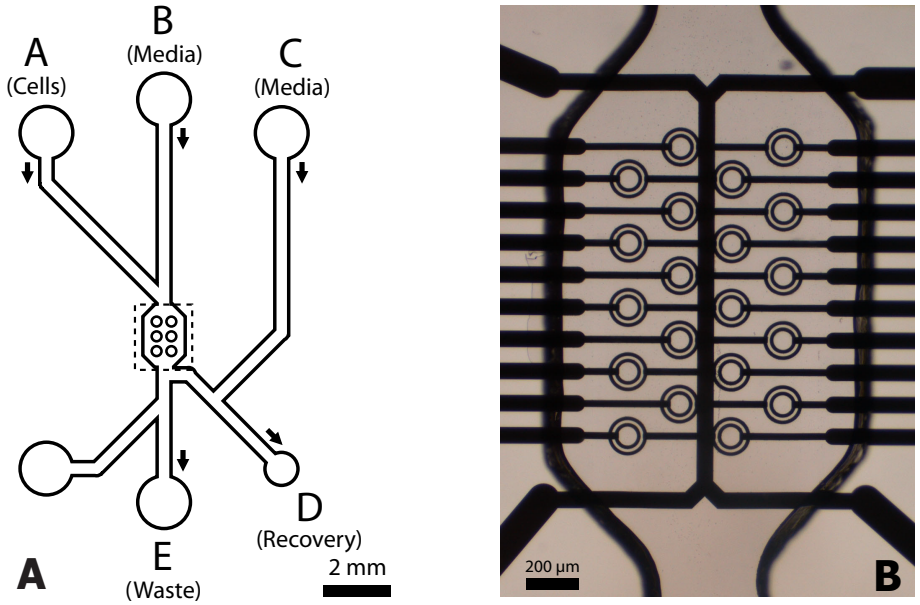

FIGURE 6.6: Overview of the microfluidic channel layout (a) and a microphotograph of the device area around the ring electrodes (b) used in Design B.

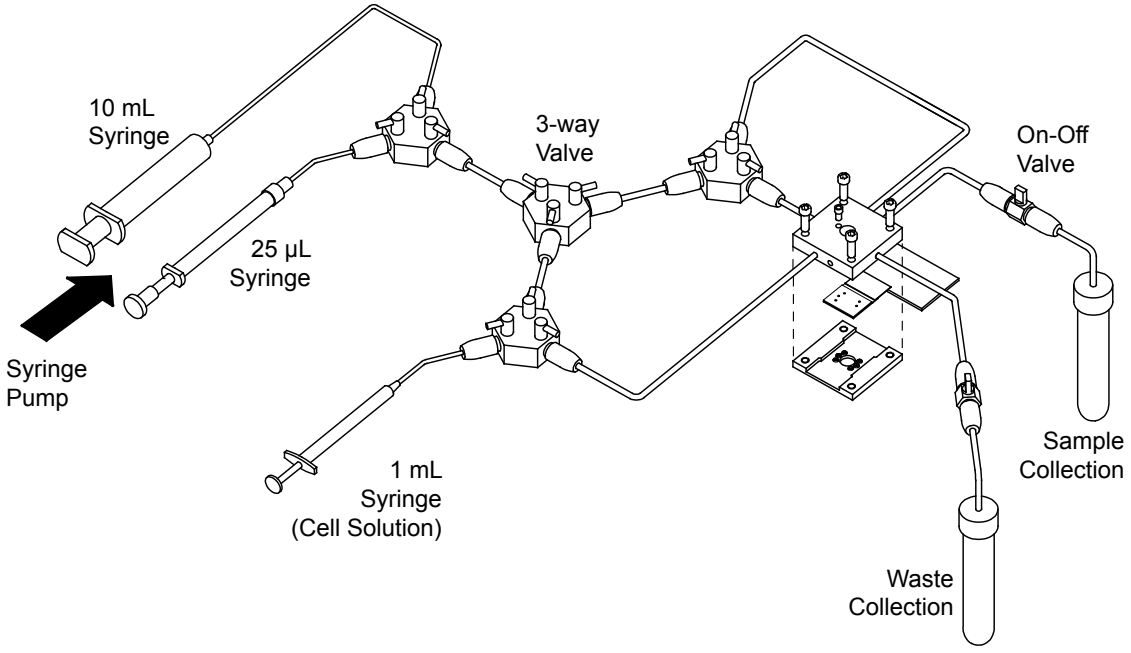

FIGURE 6.7: Schematic of the macrofluidic connections surrounding the microfluidic device.

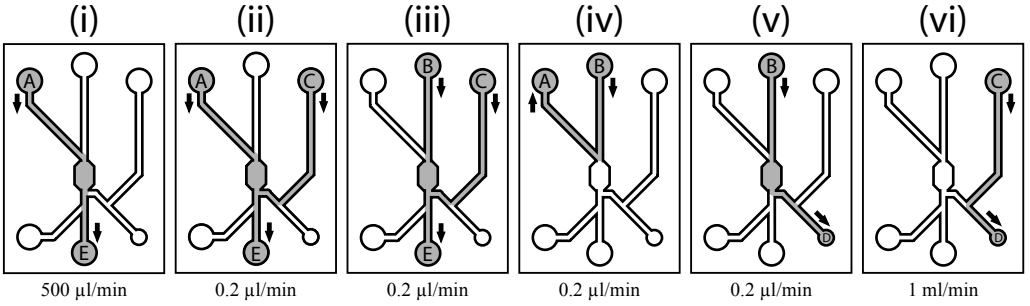

FIGURE 6.8: Valve operation sequence during the sorting (i-ii), washing (iii-iv) and recovery (v-vi) stages.

6.2.3.3 Operation

Red and green labelled cells (see below) were mixed to achieve a final ratio of red to green of approximately 4:1. Cells suspended in DMEM + 4% Dextran-70) were introduced into the device at a concentration of 5 x 10^5 cells per mL. A cell injection protocol was developed to maximise the recovery of the trapped cells and minimise the potential for contamination with unwanted cells. Fluid valves were connected to each inlet/outlet to control the flow of fluid, the sequence of operation is depicted in Figure 6.8:

i. Cells were introduced into the system through A.

ii. Cells were pumped through the system at a constant rate and trapped in the ring electrodes. At the same time the 'recovery' channel was washed (C to E) with cell-free medium.

iii. Untrapped cells were flushed through the device from B.

iv. Cells remaining in the inlet channel were removed by flushing medium back towards A.

v. Cells were released from the traps (the voltage was turned off), and flushed towards the recovery outlet (D).

vi. Cells were recovered onto a microplate by flushing fluid from C.

40 μL DMEM + 20% FCS + Penicillin/Streptomycin (1x) was added to each well, and the microplate placed in a cell culture incubator.

6.2.4 Automated Control Systems and Electronics

To trap a cell in a trap, it was necessary to switch the trap on as the cell was passing over the top of the trap. Traps were controlled by an automated system using custom

scripts written in the Matlab (Mathworks) environment, using the image acquisition and image processing toolboxes.

The trapping system is setup and initiated using a graphical user interface created by an application called 'labelRegions'. A screenshot of the interface is shown in Figure 6.9. The main functions of this application are to:

- Set a reference image (background) for the image processing algorithms.
- Mark the centre and extents of each trap.
- Produce a trap hierarchy, so that traps would be filled in a particular order.
- Set values for the target colour and minimum size for a cell.
- Start a log file to record the experimental conditions.
- Test the entered values through the image processing algorithms.

It was necessary to fill traps in a particular order, as the traps are arranged in an array, and the filling of one trap would deflect cells away from all the other traps downstream. Hence, the downstream traps were filled first, and the software maintained a list of each trap and its place in the hierarchy.

Real-time processing and control algorithms are contained in an application called 'Trapper', along with video display and record features. The application does not enable any user interaction, to avoid the processing overhead associated with a graphical user interface (GUI). A screenshot of the running of the application is shown in Figure 6.10. A flow chart of the program sequence of operation is depicted in Figure 6.11.

A set of decision algorithms was used to control the electrodes using the information presented concerning the cells detected. Crucially, the detection of a single green cell would trigger the trap to be switched on, with the intention of trapping the cell. The trap would not be activated if a red cell was detected. Traps would be checked every cycle for the following 30 seconds to determine if the cell had been correctly trapped and was still trapped - if a cell had escaped the trap would be switched off. After the 30 seconds, the cell was considered successfully trapped, and the trap 'locked'. This time limit for checking was imposed to compensate for photobleaching of the fluorescent cell stains, which after an extended period of time could cause the fluorescent intensity of the cells to drop below the detection threshold.

Sinusoidal voltages produced by a TTI TG2000 signal generator were split across 20 channels of a relay board (Omega ERB-48), into the normally open (NO) terminal. The ring electrode from each ring trap was independently switched between connection to ground (normally closed, NC) or the sinusoidal voltage. Software control of the relay

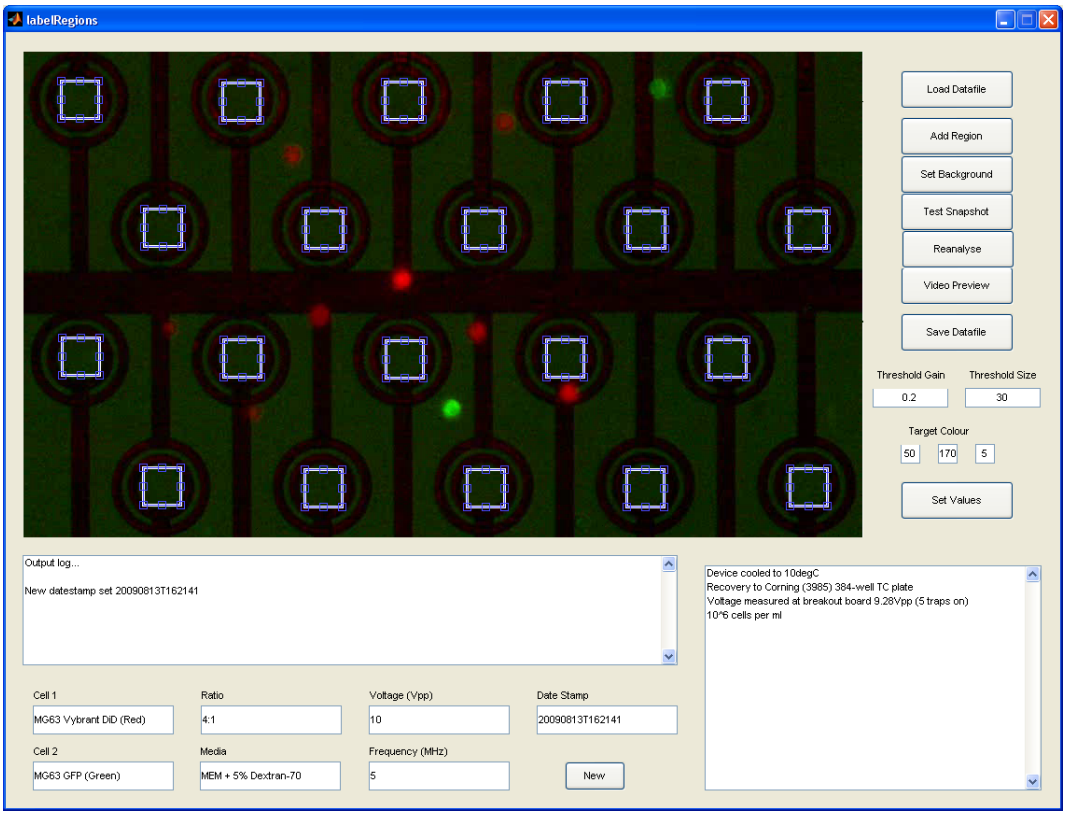

FIGURE 6.9: The graphical user interface of the 'labelRegions' application permits trap locations to be entered, as well as adjustment of parameters for the image processing algorithms.

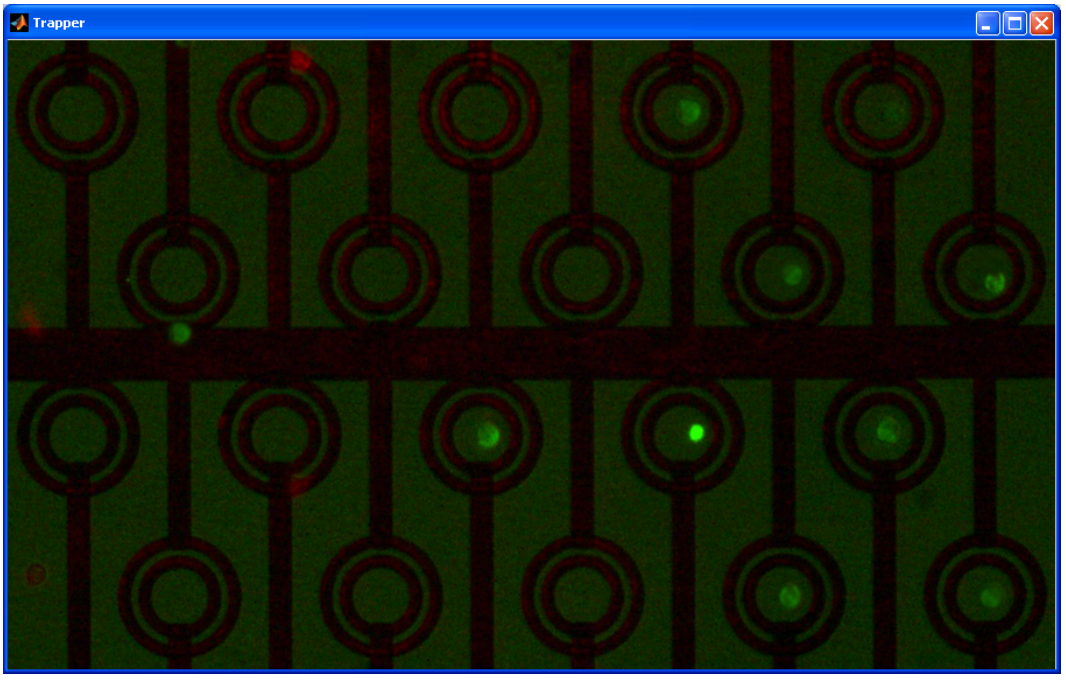

FIGURE 6.10: The live video feed is the only visual interface produced by the 'trapper' script, so that maximal processing time is available for the real-time image processing algorithms.

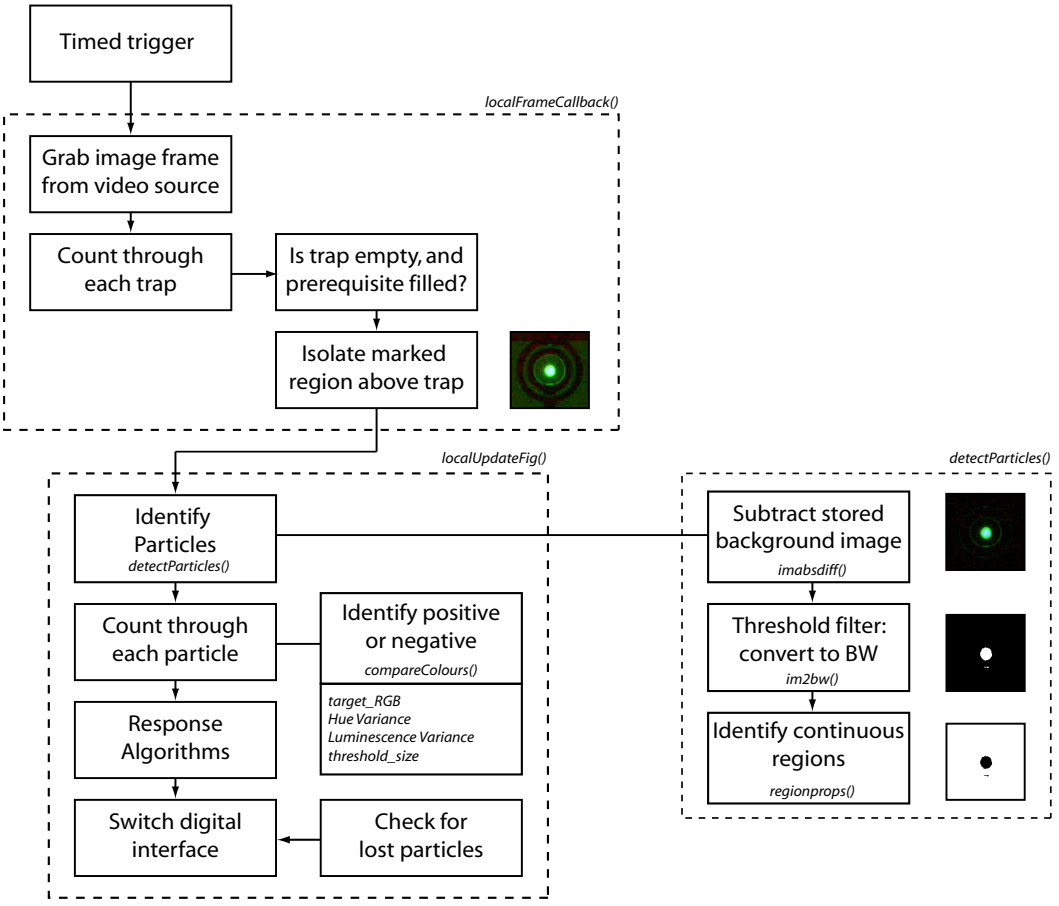

FIGURE 6.11: The program operation sequence of the 'Trapper' application, represented as a flow chart. A timed trigger passes video frames into the image processing algorithms every 0.1 seconds. Regions of the image that have been previously marked as trap locations (using labelRegions) are compared against a stored background image to identify discontinuities. A threshold function is applied, and continuous regions of the image are identified. Each region is compared against size, colour and luminosity targets, and if it is within a specified range it is identified as either a target or negative cell.

board was through a USB interface box (National Instruments USB-6009). A breakout board connected to the microfluidic device provided separate connections for each channel. Voltages at the board were confirmed using an oscilloscope (Agilent 54641D) prior to each experiment, to ensure the voltage on each channel was close to the specified value. An electrical schematic of a single channel of the equipment is depicted in Figure 6.12.

A cell in an alternating electric field experiences a potential induced across its cellular membrane (see Section 6.4.3). Calculations of cellular transmembrane potential indicate that the induced potential is inversely proportional to the frequency of the applied field, so it is advantageous to use as high a frequency as is feasible to avoid damaging the trapped cells. The cabling and switching elements that are present between the function

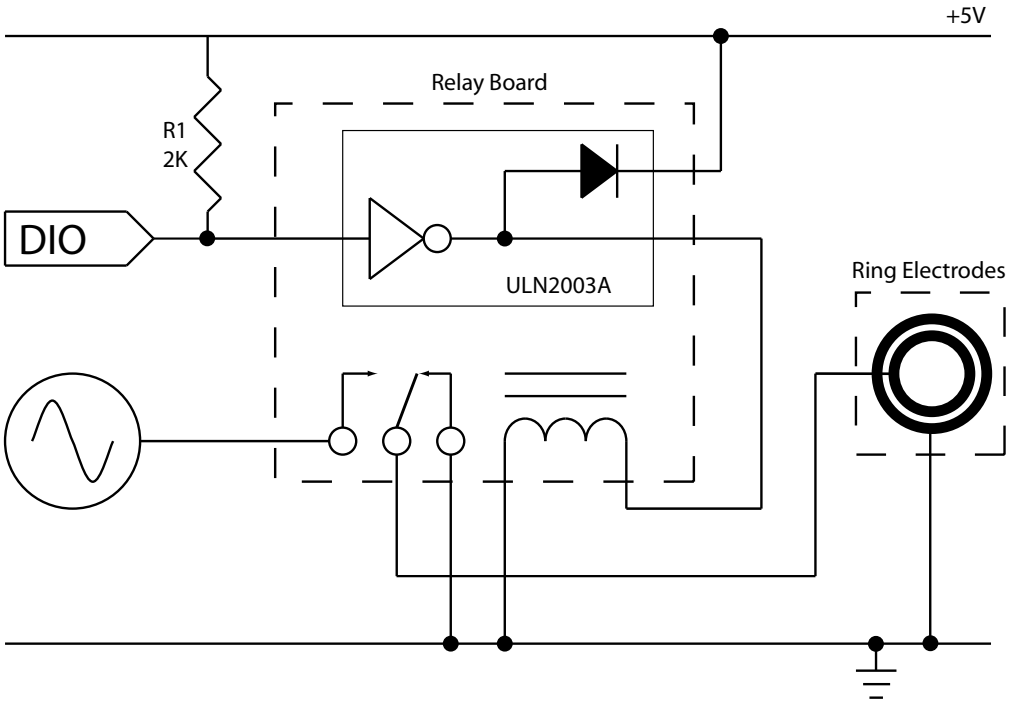

FIGURE 6.12: Schematic of the electrical circuit for a single channel of the ring trap device.

generator and the electrodes have a certain capacitive coupling to ground, which causes increasingly large signal losses as higher frequencies are used.

Figure 6.13 is a graph of the voltage measured close to the electrodes as the source frequency is changed and the number of traps used is increased. The source is set at a constant 5.0 Vpp, and the voltage is measured at the circuit board to which the microfluidic device is connected via a flexible interconnect. The measured voltage was observed to drop significantly below the set level when multiple traps were used simultaneously with a frequency set above 5 MHz. Therefore, the frequency used in all cell trapping experiments was 5 MHz.

6.2.5 Cell culture

MG63 (osteosarcoma) cells were cultured in tissue culture flasks in DMEM (Dulbecco's Modified Eagle's Medium - 4 mM L-glutamine, Hepes buffer, no Pyruvate) at 37°C, 5% CO_2. To maintain growth, the cultures were split every 3rd or 4th day by trypsinisation, and fresh culture medium added. Cultures were kept at below approximately 80% confluence, as cells harvested from fully confluent cultures were observed to be more prone to coagulate into small groups of cells when in suspension; the device was designed to handle monodisperse cell solutions, and the recovered populations were more likely to be pure if such a population was used.

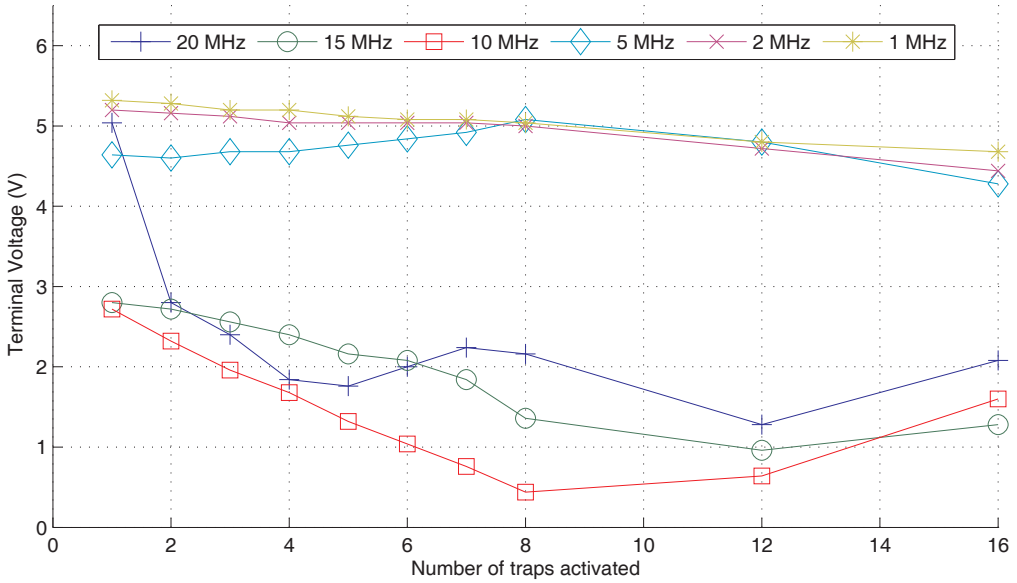

FIGURE 6.13: Plot of the voltage present on the ring electrodes as different frequencies and numbers of traps are used.

6.2.5.1 Labelling procedure

A number of commercial cell staining products were used to fluorescently label the cells. Stains were analysed to determine their staining efficiency and effect on cell viability. Target cells were labelled with a green colour: CellTracker Green, Vybrant DiO and Alexa GFP transfection were used. Negative (non-target) cells were labelled with a red colour: CellTrace Far-Red and Vybrant DiD were used.

Labelling solutions of each dye were prepared by suspending the dry powder in 20 μL DMSO, and adding to 20 mL DMEM (serum-free). The medium was aspirated from cell cultures in T75 flasks, which were then washed in PBS, and one labelling solution added to each flask. Flasks were incubated at 37°C for 45 minutes (CellTracker/CellTrace) or 10 minutes (Vybrant), the medium replaced with fresh DMEM (with 10% FCS), and incubated for a further 30 minutes. A dual-band (FITC and Cy-5 compatible) fluorescence filter set (dichroic mirror and emission filter) was used for simultaneous observation of both target and negative cells, with lasers of 473 nm and 635 nm for excitation.

Label	Manufacturer	Colour	Abs (nm)	Em (nm)	Equivalent Filter
CellTracker CMFDA	Invitrogen, US	Green	490	517	FITC
Vybrant DiO	Invitrogen, US	Green	484	501	FITC
pmaxGFP	Amaxa	Green	489	508	FITC
CellTrace DDAO	Invitrogen, US	Red	647	657	Cy-5
Vybrant DiD	Invitrogen, US	Red	644	665	Cy-5

TABLE 6.1: Summary of cell labelling products and their fluorescent properties: Abs - peak absorption, Em - peak fluorescent emission.

6.2.5.2 Harvesting and Sample Preparation

After labelling, cells were removed from culture by trypsinisation, resuspended in DMEM (with 10% FCS and incubated at 37°C. Samples from each population were counted, and their concentrations adjusted to 5 x 10^5 cells mL^{-1}. 200 μL of the green-labelled cells were combined with 800 μL of the red-labelled cells to form a mixed population of ratio 1:4. Cells were used within 3 hours of harvesting.

6.2.6 Experimental

6.2.6.1 System Preparation

Prior to use, a 0.2 μm filter device was fitted to the main fluidic inlet, and the entire microfluidic system was sterilised by flushing with 10% sodium hypochlorite solution, followed by distilled water and ethanol, to remove any residual gas bubbles. PBS was then flowed through the system at a rate of 400 μL min^{-1} for 10 minutes to remove the cleaning agents.

During preliminary experiments, cells were found to spontaneously attach to surfaces within the device. These cells could be positive or negatively-stained, and were prone to detaching during recovery of target cells when the fluid flow rate was increased, leading to contamination of the recovered population. To reduce this non-specific attachment, three methods were employed simultaneously:

i. BSA was flushed through the device at 400 μL min^{-1} for 10 minutes and incubated for 30 minutes.

ii. Dextran-70 was added to the medium (4%) to increase its buoyancy, thereby increasing the time taken for cells to sediment out of solution and contact the glass substrates. Dextran-70 is a large molecular weight polysaccharide, unable to be metabolised by the MG63 cells.

iii. The fluid manifold was cooled to approximately 10°C using the temperature-controlled stage. Macroscale tests using glass slides refrigerated to 4°C showed that this significantly reduced cell attachment to glass surfaces in comparison with slides maintained at room temperature.

The system was filled with DMEM + 4% Dextran-70 by flushing through at 400 μL min^{-1} for 10 minutes before cells were introduced.

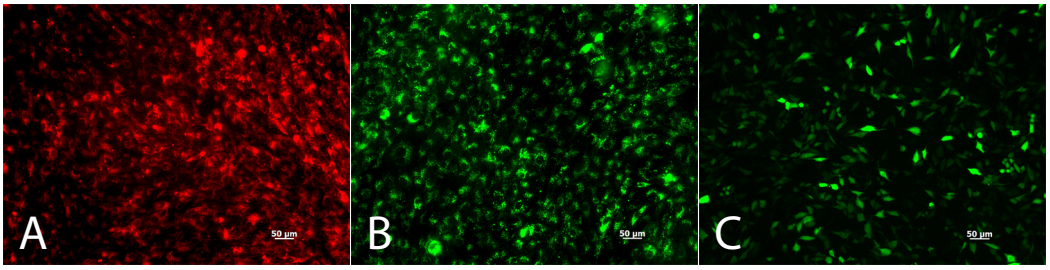

FIGURE 6.14: Fluorescent microphotographs of (a) Vybrant DiD (Red) stained (b) Vybrant DiO (Green) stained and (c) GFP-transfected cells after 24 hours in culture

6.3 Results

The CellTracker CMFDA and CellTrace DDAO products demonstrated a staining efficiency > 90%, although the receiving cells exhibited poor viability when returned to culture after staining. Cells retained spherical morphology, and did not appear to spread out on the surface of a tissue-culture treated microplate or under go further cell division.

Cell stained using Vybrant DiO or DiD typically had a > 90% staining efficiency (Figures 6.14 a, b). GFP transfection was 60-70 % efficient as determined by the percentage of cells expressing GFP (Figure 6.14c). All the populations exhibited viability and proliferation.

The ring electrodes were able to trap and isolate cells from a suspension flowing at up to 0.3 μL min^{-1}. The flow was maintained at 0.2 μL min^{-1} so that cells of a range of sized could be trapped, and so that cells were not displaced by the fluid flow close to the edge of the electrodes. Figure 6.15 shows a sequence of images of the trap array during its operation.

In a typical experiment, up to ten cells were captured from a mixed population of 4:1 red to green cells. Using Design A, it was possible to recover the trapped cells, although more cells were recovered than originally trapped, with a high number of impurities. Using Design B, 100% pure populations of green cells were recovered in 8 separate experiments, with only one experiment containing a single red cell. This data is summarised in Table 6.2. On average 70% of the cells trapped were recovered into the tissue-culture microplate. Cells stained with Vybrant DiO Green stain failed to readhere to the microplate surface or demonstrate further cell division. Cells transfected with GFP readhered to the microplate surface, but failed to demonstrate significant cell divison. Figure 6.16 shows photographs of two GFP+ cells that have readhered to the microplate and spread across the surface, (a) 24 hours after sorting and (b) 72 hours after sorting.

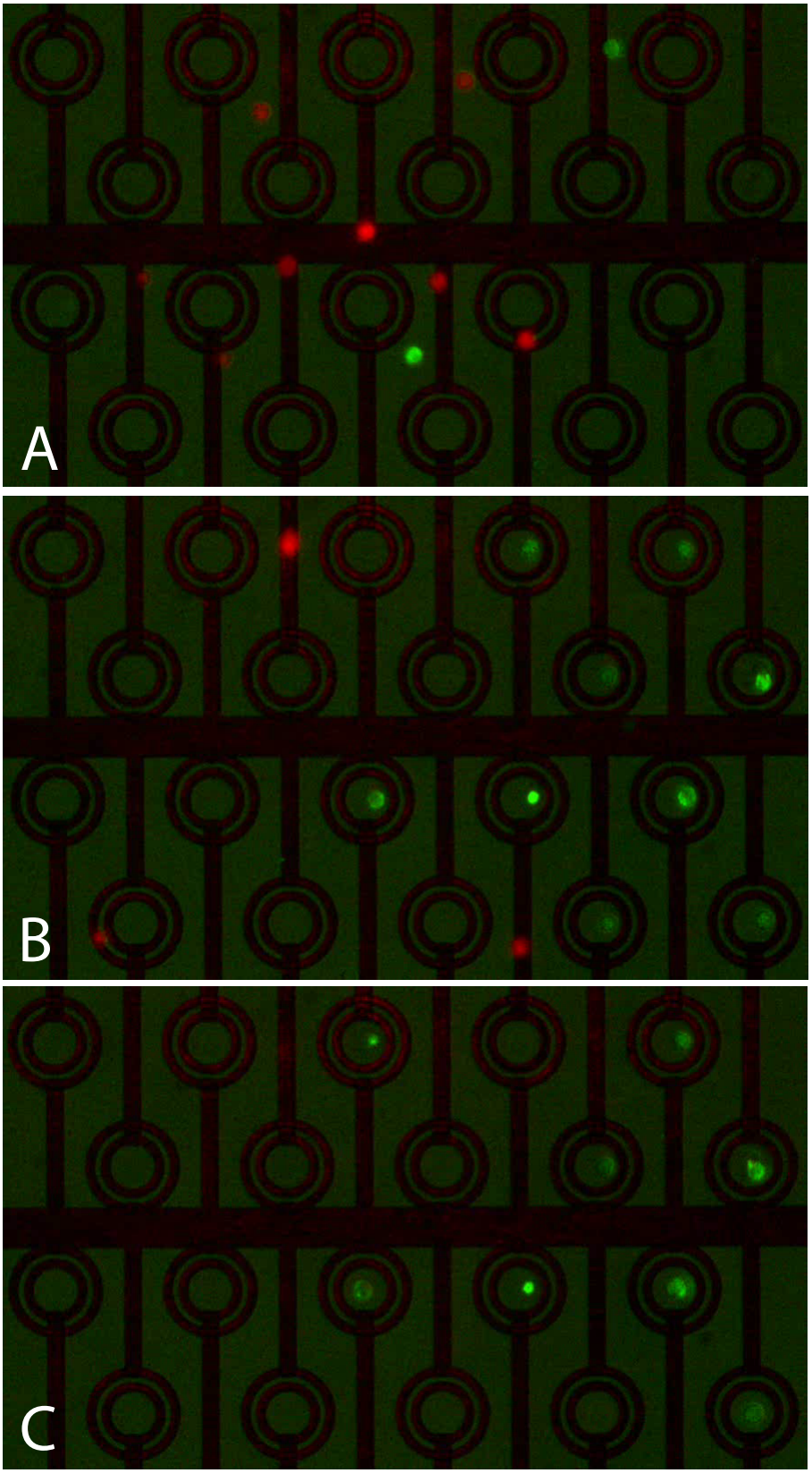

FIGURE 6.15: A sequence of photographs showing (a) red and green fluorescently-labelled MG63 cells flowing over the traps, (b) green fluorescently-labelled MG63 cells trapped within the ring electrodes while the red cells are repelled and (c) the green fluorescently-labelled MG63 remain trapped in the ring electrodes as the red cells are washed away.

Run no.	Channel design	Green cells trapped	Red stain	Red recovered	Green stain	Green recovered	Green purity %	Red adhered	Green adhered	Green adhered after 72 hours
1	Design A	9	DiD	12	DiO	15	56	0	0	0
2	Design A	5	DiD	6	DiO	9	60	0	0	0
3	Design B	4	DiD	0	DiO	4	100	0	0	0
4	Design B	2	DiD	1	DiO	2	67	0	0	0
5	Design B	5	DiD	0	DiO	2	100	0	0	0
6	Design B	5	DiD	0	DiO	3	100	0	0	0
7	Design B	3	DiD	0	DiO	3	100	0	0	0
8	Design B	4	DiD	0	GFP	4	100	0	2	2
9	Design B	6	DiD	0	GFP	5	100	0	4	5
10	Design B	7	DiD	0	GFP	3	100	0	1	0
11	Design B	4	DiD	0	GFP	2	100	0	1	1

TABLE 6.2: Summary of recovered populations after 24 and 72 hours. Key: DiD, Vybrant DiD; DiO, Vybrant DiO.

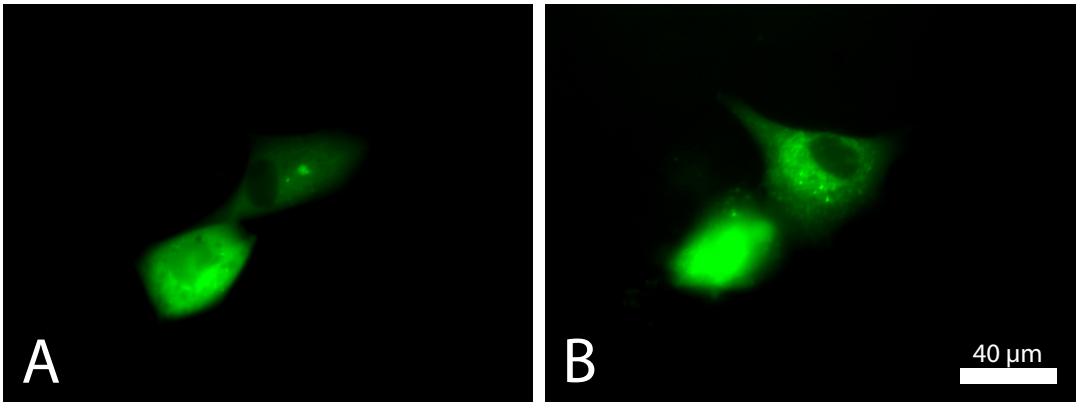

FIGURE 6.16: Photographs of GFP-transfected MG63 cells taken (a) 24 hours and (b) 72 hours after sorting, that have been recovered into a microplate. The cells have re-adhered to the surface of the plate.

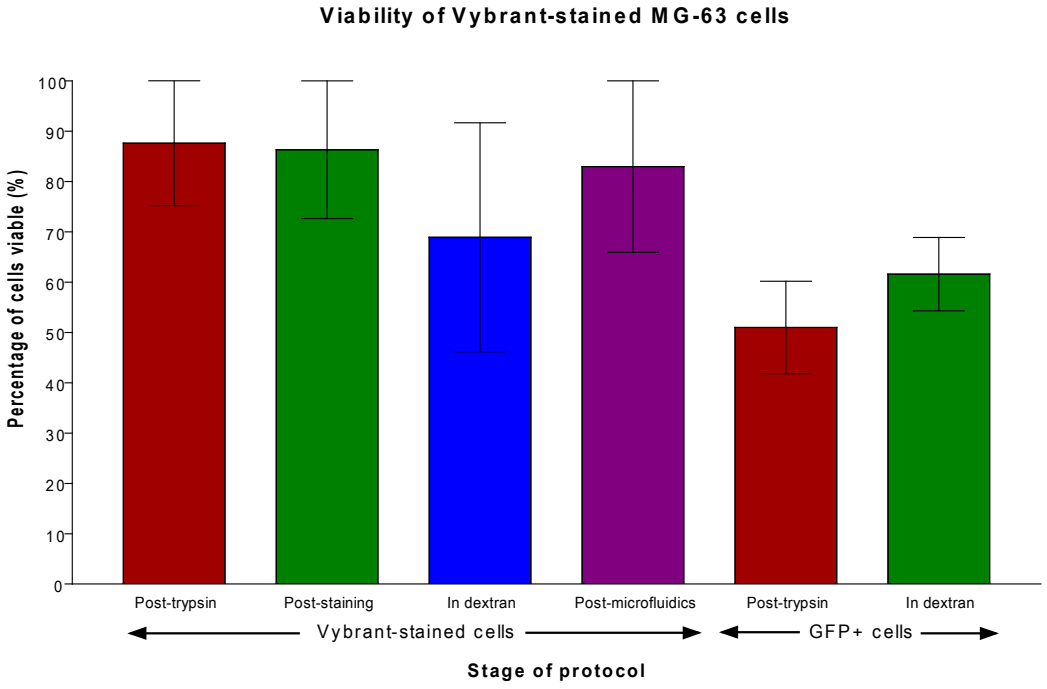

FIGURE 6.17: Cell viability from Vybrant-stained and GFP-transfected populations at various stages of the microfluidic process when seeded at approximately 10 cells/well, samples were viewed 24 hours after seeding. The error bars show the range of viability recorded.

6.3.1 Cell Health and Viability

Figure 6.17 is a graph of cell viability of control samples taken at points throughout the experiment. Samples were diluted and dispensed into a 384-well plate at approximately 10 cells per well. 40 μL DMEM + 20% FCS + Penicillin/Streptomycin (1x) was added to each well, and the microplate placed in a cell culture incubator.

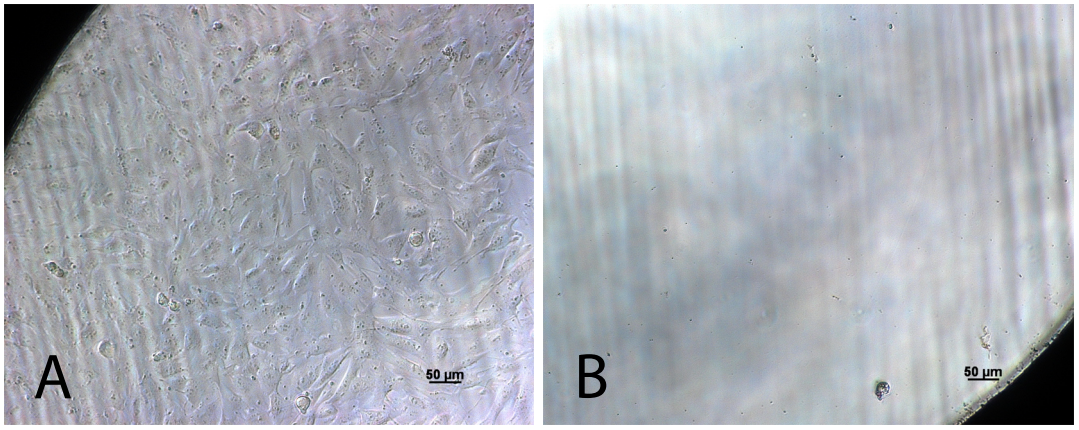

FIGURE 6.18: Photographs of MG-63 control populations after 12 days, demonstrating (a) proliferation in wells seeded at >10 cells/well and (b) lack of proliferation, resulting in cell death and detachment in wells seeded at <10 cells/well.

6.4 Discussion

6.4.1 Design A: Dry Film Resist Channel with Sample Injection

The sample injection system permitted sub-microlitre volumes of cell suspension to be injected directly at the entrance to the microfluidic device. In the experiments performed, 1 μL samples containing approximately 500 cells were used. Initially, the inlet contains a mixture of cells and medium, and as the cells are carried through and out of the device the inlet reverts to supplying plain medium. Such a system has the limitation, however, that it cannot be said with certainty if the medium flowing in the inlet contains cells or otherwise is plain medium. It was found that as trapped (target) cells were being released and recovered with a corresponding increase in fluid velocity, a number of non-target cells that were present in the microfluidic channel were recovered with the target cells, reducing the purity of the recovered population. The fluid path constricts strongly around the inlet to the microfluidic device, so it is likely that cells had become lodged around the entrance to the microfluidic channel, and were subsequently released into the flow. As Table 6.2 shows, the purity of green target cells could be increased from 20% at the input to 60% in the recovered population, but it was not possible to recover a pure population using this device. Such a system, could still be useful however, if it was required to trap a particular population of cells and maintain them on chip for further analysis and culture.

6.4.2 Design B: Moulded PDMS Channel with Bulk Sample Handling

The modified design of microfluidic channel used in Design B enabled the recovery of a purified population of sorted cells. As shown in Table 6.2, from a total of 9 separate experiments, 8 had 100% pure populations.

6.4.2.1 Cell Health and Viability

After trapping experiments were performed it was discovered that in all cases, recovered cells stained with Vybrant DiO failed to adhere to tissue culture plastic, whilst most GFP-transfected cells remained viable and adhered after trapping.

Cell viability control data (Figure 6.17) was taken at each stage of the protocol; 10 samples of the cell solution (40 μL) were aliquoted into a microplate at a density of approximately 10 cells/well. There was no difference in viability between unstained cells and cells stained with the Vybrant DiO (green) stain. Cell viability was slightly lower for cells resuspended in the medium containing 4% Dextran-70 (to control the buoyancy), but this reduction in viability was not observed for cells resuspended in the DMEM/Dextran medium and passed through the microfluidic system, so is probably not significant. It is likely that the failure of the cells stained with the Vybrant DiO stain to readhere in culture was not due to any one process, but rather the combined effects of multiple stimuli.

MG63 cells were transfected with GFP while adhered to a tissue culture flask, and remained in culture for a further 24 hours. The viability of cells when removed from culture was 50-60%, which is in line with typical results from GFP transfection. Recovered populations showed similar viability (57%) after trapping and sorting, suggesting that the electrokinetic/microfluidic system had little effect on cell health.

Control tests (see Table 6.3) identified an issue with MG63 cell proliferation at low seeding densities. Using 384-well plates (80 μL per well) cell populations with less that 10 cells per well failed to proliferate. Trapped GFP+ cells were recovered into a microplate by aliquoting 40 μL of the collection medium per well, with an additional 40 μL DMEM + 20% FCS added. This resulted in cell densities of approximately 1-3

Well	Initial adhered cell count	Adhered cell count after 12 days
A	11	0
B	16	>50
C	8	0
D	7	0
E	15	>50
F	11	>20
G	4	3
H	10	0
I	9	0
J	14	>50
K	9	0
L	6	0

TABLE 6.3: Summary of cell growth and proliferation in control cultures of MG-63 cells.

cells per well, too low to maintain a healthy population. Although GFP-transfected cells readhered to the surface of the microplate after recovery, further growth and proliferation was not observed.

6.4.2.2 Device Operation

A number of technical issues remain to be addressed if the technology is to be useful. For example, actuation of the flow control valves during washing stages introduced a small displacement of the fluid, often sufficient to dislodge trapped cells. Hence, a certain proportion of the trapped cells could not be recovered as they dislodged from the traps. It was also not possible to fill all 20 ring traps in a reasonable time (e.g. 10-15 minutes), so the number of recovered cells for each sorting operation represents less than 25% trap occupancy. Increasing the length of time cells remained in the device (at 10°C) would inevitably lead to lower cell viability. Greater numbers of cells could be recovered by increasing the number of traps on the device, and by distributing the traps to ensure greater coverage across the microfluidic channel.

Separate inlets were used for injection of cells and medium, so that non-target cells could be flushed away effectively. Additionally, separate outlets were used for recovery of target cells and waste (non-target cells). An additional washing inlet was provided to flow medium into the device along the recovery outlet, preventing cells entering the recovery outlet until non-target cells had been sufficiently flushed out (Figure 6.8).

6.4.2.3 Cell/Surface Attachment

Cells in contact with, or moving near a surface occasionally became attached. These cells could detach at a later time when the flow rate was increased and contaminate the sample, leading to non-target cells being recovered. The microfluidic network and flushing procedure implemented in Design B was designed to minimise contamination with unwanted cells. To limit cell-surface interactions, the microfluidic channel was designed so that it is constricted in areas away from the ring electrodes, increasing fluid velocity and reducing the likelihood of cell attachment. The techniques discussed in Section 6.2.6 in conjunction with the redesign of the microfluidic channel appear to have been successful, and subsequent attachment of cells to the channel was not a significant problem.

6.4.3 Transmembrane Potential

The dielectrophoretic traps produce a large gradient in the electric field in the region surrounding the traps, which will alter the electrical potential across the membrane of a

cell. The membrane has a natural 'resting' potential across it of approximately 70 mV. Application of a significant potential across the membrane can lead to temporary or permanent poration of the cell membrane, the later causing cell lysis. Equation 6.1 was derived by Grosse and Schwan (1992) using a model of a cell with partially insulating membrane:

$$\Delta U = \frac{3/2Ea\cos\theta}{1 + a(G_m + i\omega C_m)\left[\rho_i + \frac{\rho_m}{2}\right]} \tag{6.1}$$

ΔU is the potential generated across the cellular membrane, E is the magnitude of the electric field, θ is the polar angle, measured with respect to the direction of the field, ω is the angular frequency of the electric field, G_m is the membrane conductance, C_m is the membrane capacitance, ρ_i is the resistivity of the interior of the cell and ρ_a is the resistivity of the electrolyte.

As detailed values for the electrical properties of MG63 cells were not available, typical values for the membrane capacitance and conductance of HeLa cells were used - another adherent, immortalised carcinoma cell derived from a human source. The parameters are listed in Table 6.4.

Figure 6.19 is a plot of the approximate transmembrane potential induced on MG63 cells immobilised in the ring electrodes. At 5 MHz, the magnitude of the potential is 20 mV. Such a value is generally considered to have little effect on cell viability: Glasser and Fuhr (1998) found mouse fibroblast cells continued to proliferate at induced transmembrane potentials up to 130 mV.

Characteristic	Symbol	Value	Note
Cell Radius	a	9.75 μm	1
Membrane Capacitance	C_m	19 mF m^{-2}	2
Membrane Conductance	G_m	0.95 S m^{-2}	2
Electric Field	E	44314 V m^{-1}	3
Field Angle (polar)	θ	0 rad	4
Angular Frequency of Electric Field	ω	31415926 rad s^{-1}	5
Resistivity of the Cell Interior	ρ_i	5 Ω m	6
Resistivity of the medium	ρ_m	1.25 Ω m	7

TABLE 6.4: Parameters used for the calculation of transmembrane potential on cells immobilised within the ring trap electrodes.

Notes:

1: Measurement of 20 MG63 cells in DMEM, average value using Nikon Digital Sight instrument. Range 15.6-23.8 μm, St. dev 1.68 μm.
2: Taken from Asami et al. (1990), value for HeLa cells.
3: Numerical simulation (FEA) using Comsol Multiphysics 3.4
4: Worst case value, where $\cos\theta = 1$, when field is perpendicular to the membrane.
5: Value for $f = 5$ MHz, $\omega = 2\pi f$.
6: Taken from Kotnik et al. (1997), calculated from typical value of $\sigma_m = 0.2$ S m^{-1}.
7: Measurement using Hanna EC215 Conductivity, $\sigma_m = 0.81$ S m^{-1} at 10°C

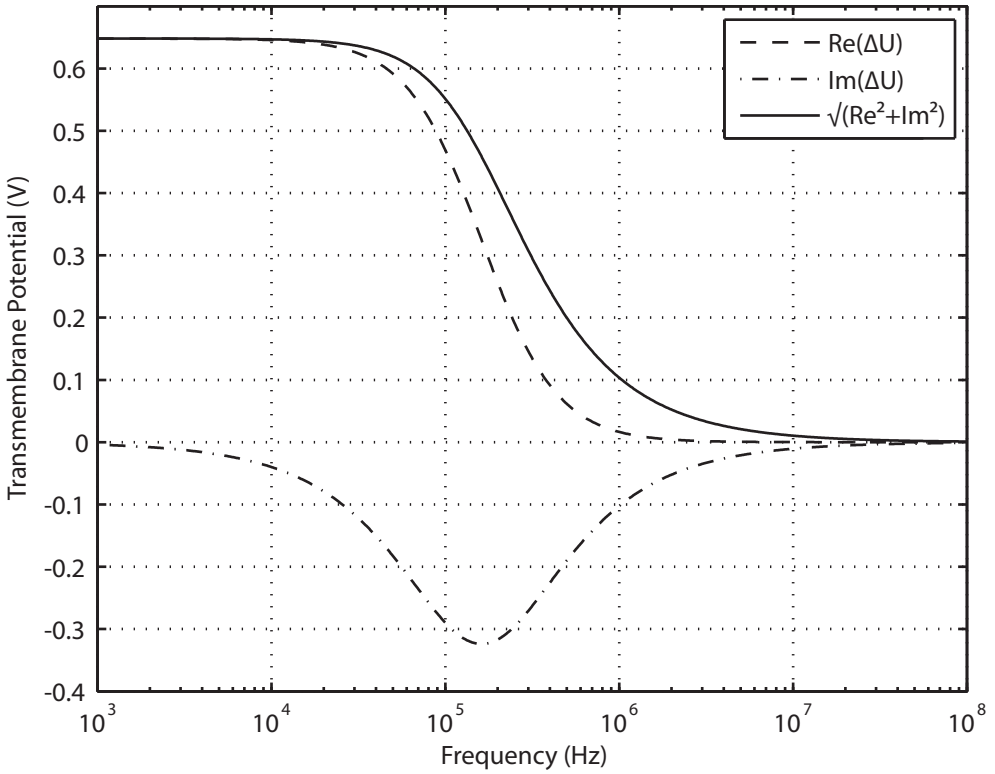

FIGURE 6.19: Plot of the approximate transmembrane potential induced on MG63 cells immobilised in the ring electrodes, calculated using Equation 6.1 and the parameters in Table 6.4.

Although parameters for membrane capacitance and conductance are taken from a different cell line, this approximation serves to give an indication of the size of the transmembrane potential likely to be induced on the cells. Kotnik et al. (1997) showed that for high frequency electric fields with cells suspended in physiological media, variations in the the values of membrane and media conductivity had small effects. The conductivity of the media was reduced from a typical value of 1.65 S m^{-1} for DMEM at room temperature to 0.81 S m^{-1} as the device was cooled to $10°C$, but the overall effect of this was a reduction in the transmembrane potential of 1 mV. The membrane conductance was found to have little effect on the calculated value of the transmembrane potential, and could be neglected without having a significant impact. The membrane capacitance and radius of the cell have significant impact on the induced transmembrane potential, the latter being simple to accurately determine using microscopic imaging. Membrane capacitance can be measured using the patch clamp technique, or by electrorotaion, both long and involved processes. The induced transmembrane potential would reach levels believed to be harmful if the membrane capacitance was ten times smaller than the estimate used here.

6.4.4 Thermal Effects

Localised heating of the medium around the cell may also occur. The high electrical conductivity of physiological media means that Joule heating in the vicinity of the ring electrodes may raise the temperature sufficiently that cell viability may be affected due to thermal effects. The thermal environment was modelled by finite element analysis using Equation 3.8.

Figure 3.10 is a plot of the simulation of the temperature in the vicinity of the ring electrodes, performed in the FlexPDE software package using the geometry shown in Figure 3.9. With the device cooled to approximately 10°C, the temperature in the centre of the ring was 19.9°C, and the maximum temperature was 21.9°C, above the electrodes. These temperatures are unlikely to cause significant changes to the viability of the cells.

6.4.5 Comparison with Alternative Technologies

A whole industry has developed around producing equipment for the separation of cells, so any new technology must meet a demanding set of criteria if it is to be useful. The key metrics that cell separation devices are measured against are: speed (often measured in thousands of cells per second for high throughput devices), purity of the recovered populations (or degree of enrichment over the original sample), and viability of the recovered cells.

Of the 11 sorting operations conducted using the ring trap electrodes, 5 cells were trapped on average per run, with each run taking approximately 15 minutes. As this equates to approximately 3 minutes per cell, it can be seen that the ring trap devices are not suitable for high throughput cell sorting. There are few examples in the literature of similar devices that sort cells by trapping, the most significant being the work of Kovac and Voldman (2007) that uses optical forces to sort cells from microwells. This study was also one of the first uses of 'image-based' sorting. Slightly higher sorting rates were produced (70 cells per hour), although a much larger array was used, containing 10,000 trapping locations. In comparison, the rate at which particles can be sorted with the ring electrodes scales favourably with the number of traps available, as each individual trap can operate independently. It would be difficult to control such a similarly large number with the current technology, however. Populations of sorted cells were recovered with purities of up to 89%, and this was believed to be as a result of limited control of non-specific cell adhesion to the inner surfaces of the microdevice.

Care must be taken to understand the particular conditions under which a device has been operated before a comparison can be drawn. The device produced by Fu et al. (1999) sorted cells at a rate of 20 per second, producing enriched populations of GFP E.

coli cells at a purity of 30.8%. Hence, for every individual target cell that was sorted, 2 of the non-target cells were also recovered. The concentration of cells passing through the sorting device was sufficient that it was not possible to sort individual cells. It would be possible to reduce the concentration of particles by a factor of 10, and the purity of the recovered population would be closer to 100%, but the rate at which cells were recovered would then be much lower. The value in the ring trap electrodes is that they typically recover 100% pure populations, and allow individual cells to be selected from a hetergeneous population. Table 1.1 (Chapter 1) lists performance characteristics from several cell sorting devices published in the literature.

6.4.6 Alternative Uses

6.4.6.1 Particle Concentration

Another useful advantage of the ring trap electrodes is that they concentrate cells during sorting. As an example, a fully populated array would have 20 cells within an 80 nL volume - equivalent to a density of 2.5 x 10^8 cells mL^{-1}. If cells were injected at a density of 5 x 10^5 cells mL^{-1} as used in these experiments, this would be a concentration of 500 times. This is analogous to concentration by centrifugation, often performed on cells and particles on the macroscale. Of course, it is difficult to recover the concentrated cells from the device without diluting them, so this is most useful if cells are to be maintained within the microfluidic device, such as for use in a cell-based assay.

6.4.6.2 Image-based Fluorescence Measurements

Conventional cytometers perform fluorescence measurements at a single time point only. Although a population of cells can be measured again at a later point, it is not possible to associate a particular measurement with a particular cell. Only large scale changes that affect the general population can be detected. The ability to fix the spatial location of multiple single cells (such as with an array of ring traps) within a cytometer would permit fluorescence measurements to be repeatedly made on a single cell with a wide temporal distribution. This technique has been discussed by Voldman et al. (2002); Kovac and Voldman (2007) in the concept of a 'dynamic array cytometer' using a number of different electrokinetic and hydrodynamic trapping technologies, and used to measure dynamic calcein loading in HL60 cells.

6.5 Conclusions

The device demonstrates that isolation and recovery of specific cell types is possible using dielectrophoretic ring traps. Sorted populations remained viable, but did not

exhibit further proliferation. Control tests indicate that the numbers of cells recovered were below the threshold needed to restart a population of MG63 cells in culture, and simulations indicate that the thermal and electrophysiological conditions produced by the ring electrodes were unlikely to affect the viability of cells trapped by the device. This would suggest that the sorted cells did not proliferate as insufficient cells were recovered, but this could only be confirmed by repeating the experiments with a larger or more densely populated array of cell traps so that greater numbers of cells could be recovered.

Whilst the low numbers of recovered cells prevented re-establishment of somatic cell populations, this device offers potential for the isolation and recovery of stem cells because they maintain viability and proliferation even when cultured as single cells. The determination of sufficient markers to fluorescently label a stem cell could enable the system to be used to isolate and recover such a cell. This technology is also a potentially useful component of an integrated cell analysis platform, as cells can be sorted, concentrated and maintained within a microfluidic device, removing the need for external processing steps.

Chapter 7

Automated Particle Separation by a Dielectrophoretic Sorting Gate

7.1 Introduction

An alternative strategy to cell separation by trapping is to deflect cells laterally within a fluid stream, and then split the fluid stream into a number of separate outlet channels. This chapter details a number of devices and strategies for separation of cells and particles as they move through a microfluidic device in a fluid stream.

Figure 7.1 shows streamlines in a fluid as it splits into three separate output channels. Neglecting other forces (such as gravity, or electrokinetic forces), particles suspended in the fluid will follow the streamlines. The channel through which they exit the system will depend on their original lateral position in the channel. Metal electrodes on the top and bottom surfaces of the channel can be used to create a number of different DEP barriers, gates and focusing devices that can deflect particles laterally across the fluid stream.

An important characteristic of a particular sorting electrode geometry is the rate at which it can sort particles. As can be seen from Equation 7.1, the rate (R) at which particles flow through the device is dependent on two factors: the fluid volumetric flow rate (Q), and the concentration of particles in the fluid (C).

$$R_{particles} = Q_{fluid} * C_{particles} \tag{7.1}$$

The sorter designs developed in this chapter all require the particles to be focused into a narrow stream, before entering the active region of the sorting gate. This creates an

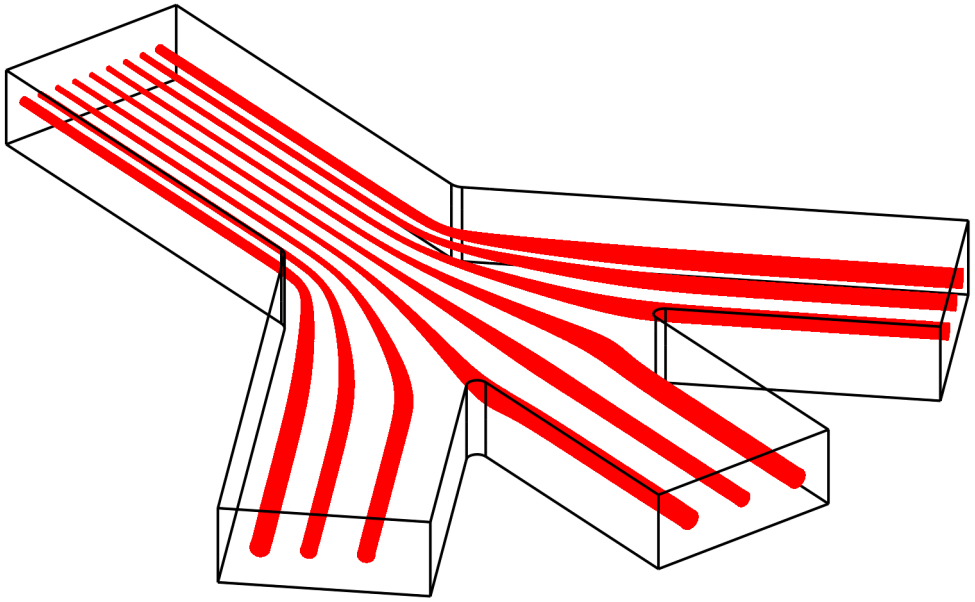

FIGURE 7.1: Streamlines in a fluid stream splitting into three outlets. The laminar flow in a microfluidic environment ensures that there is little inter-mixing normal to the direction of fluid flow.

upper limit on the fluid flow rate, because particles must spend sufficient time in the focusing region to be adequately focused. Although dielectrophoresis does not need to be the dominant force on the particle (particles are still carried through the device by hydrodynamic drag forces), it must still be sufficient to provide the spatial displacement necessary to move particles between the fluid streamlines.

7.2 Materials and Methods

7.2.1 Design A: The Sorting Gate

A primary application for a particle sorting device is the recovery of a purified sample from a mixed population. Two outputs are required, a 'recovery' output for the purified sample, and a 'waste' output for everything else. The sorting gate electrodes deflect cells and particles laterally between the two outputs by creating a negative DEP 'tunnel', as shown in Chapter 3. Figure 7.2 shows the concept of a sorting gate at a microfluidic junction. The polarity of the electrodes is switched when a 'target' particle approaches the junction to deflect it into the 'recovery' output, otherwise the electrodes deflect all the particles towards the 'waste' output. Optical measurements (such as fluorescent intensity) are often used to differentiate between 'target' and 'negative' particles, and it is easy to integrate the planar structure commonly used to fabricate microfluidic devices into external optical components; impedance spectroscopy could also be used.

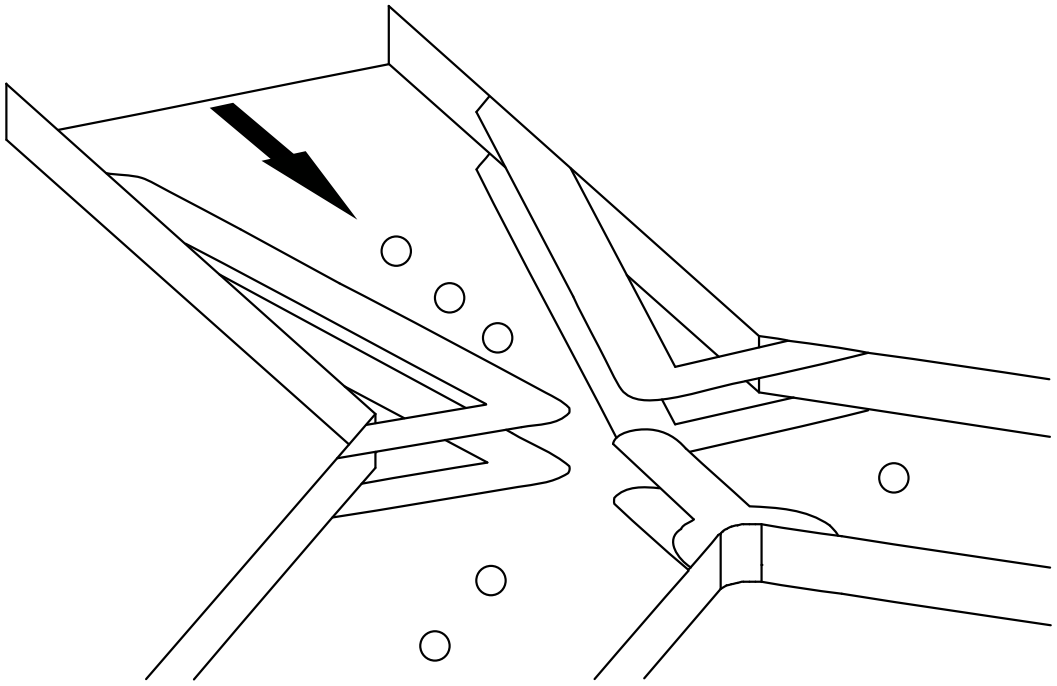

FIGURE 7.2: Electrodes at a microfluidic junction are switched to actively separate a population of particles as the flow is split between two outputs.

7.2.1.1 Microfluidic Device

Figure 7.3 shows the microfluidic channel with electrodes on the top and bottom surface for the sorting of particles between two output streams. Figure 7.4 is an enlargement of the focusing and sorting electrodes respectively. In the centre are two pairs of overlapping electrodes for impedance spectroscopy of particles and cells, which were not used in this work.

The electrodes were fabricated by depositing a single (composite) layer of titanium-platinum as described in Section 4.4.1. The microfluidic channel was produced by laminating each substrate with SY320 dry film resist (Elgar Europe, Italy), patterning by development in BMR Developer/Rinse, and compression bonding at elevated temperature, as described in Chapter 4. The channel had a depth of 26 μm after bonding. Devices were of the 20 x 15 mm form factor (see Section 4.3, and so were diced accordingly. All fabrication work was performed by Katie Chamberlain at the Southampton Nanofabrication Centre, University of Southampton.

7.2.1.2 Macrofluidic Equipment

The microfluidic device was mounted in an appropriately sized fluid manifold (see Figure 4.9). A pressure controller (Fluigent MFCS-4C) was used to control the gas pressure in three sample containers and hence the fluid flow through the particle inlet and the

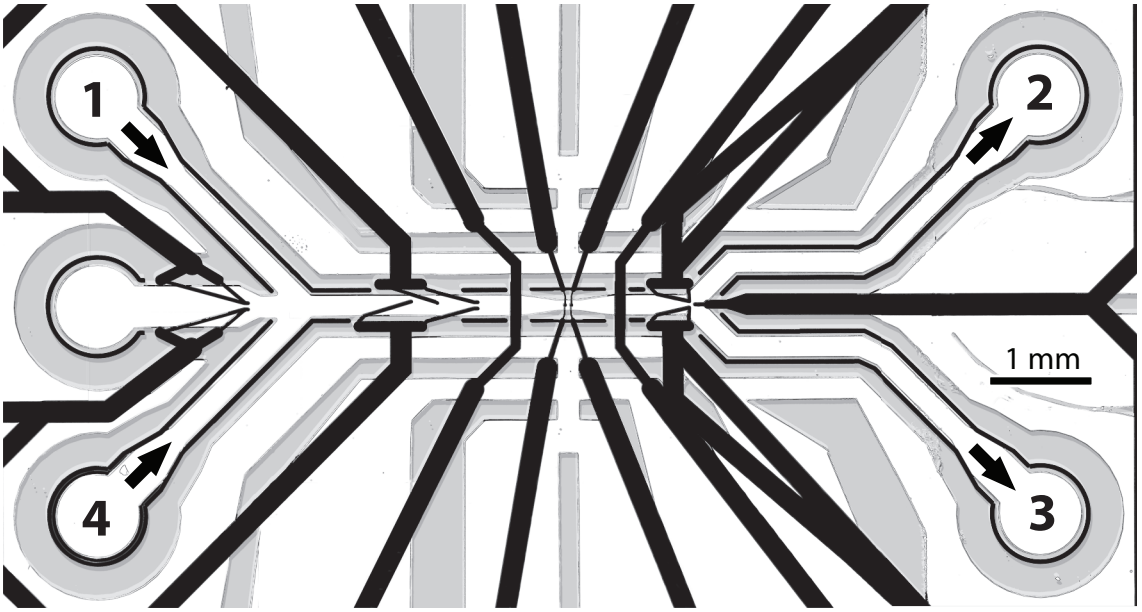

FIGURE 7.3: Composite photograph of the microfluidic channel (grey regions) and associated electrodes (black) of the sorter device. The channel is 200 μm wide, except at a constriction in the centre where it narrows to 100 μm. The fluid inlets and outlets were as follows:
1: Inlet for the suspending medium (no particles) for washing particles from the channel and recovery of sorted populations.
2: 'Recovery' outlet for sorted target particles.
3: 'Waste' outlet for all unsorted target and negative particles.
4: Inlet for particles in their suspending medium.

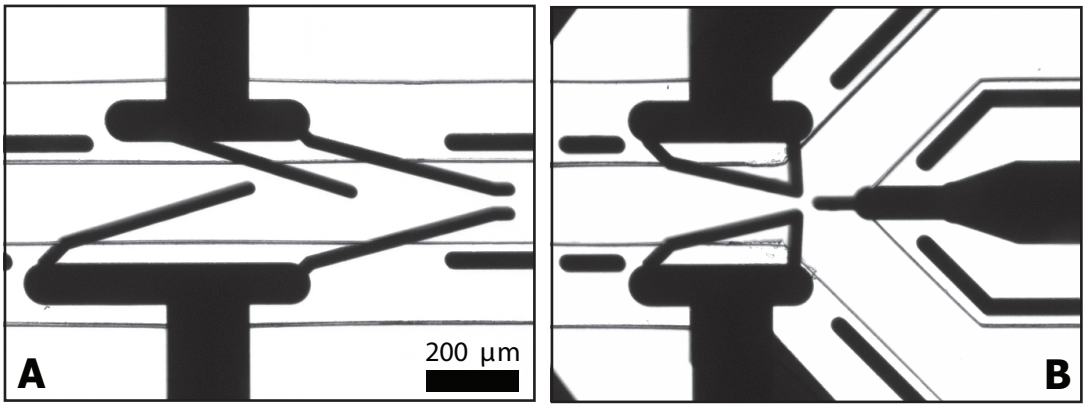

FIGURE 7.4: Photographs of (a) the focusing electrodes and (b) the sorting electrodes. Particles are carried through the device from left to right by fluid flow. The channel is 200 μm wide.

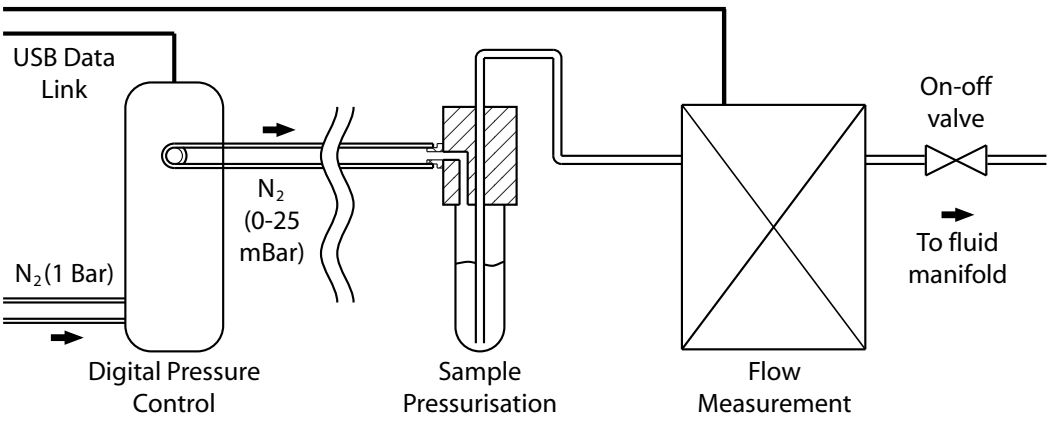

FIGURE 7.5: The digital pressure controller controls fluid flow out of the sample container by adjusting the pressure of nitrogen gas above the fluid. The flow rate in each channel is also measured, and the values displayed on the computer through a USB link.

'recovery' and 'waste' outlets of the microfluidic channel. The pressure in each channel could be independently varied in increments of 0.25 mBar, which corresponded to adjustments in the fluid flow of approximately 2.5 nL/min with the fluidic configuration used. The volumetric flow rate through each channel was measured (Fluigent Flow-ell) and a digital readout displayed on the computer. Figure 7.5 shows the principle of operation of a single channel of the pressure-controlled system. The other inlet was connected to a 10 mL syringe containing the plain buffer, without any particles. The syringe was mounted in a syringe pump (Cole Palmer 79000) and used to drive fluid through the device before sorting - to clean the device - and after sorting - to recover the sorted populations. An on-off valve (Omnifit) was fitted to each inlet and outlet of the fluid manifold so that the flow could be shut off if required.

7.2.1.3 Automated Control Systems

Automated control software was written in the Matlab (Mathworks) environment based on the scripts used to control the ring trap electrodes. The operation of the 'Sorter' application is fundamentally similar to the 'Trapper' application described in Chapter 6. The modular architecture means that a slightly different set of decision algorithms can be substituted into the framework, without substantial modifications to the program operation. The core routines such as processing an image from a video source, removing background noise, identifying particles and comparing colours are identical. Improvements include the addition of maximum particle size threshold to positively identify a particle as a 'target' particle, to improve the identification of cell aggregates that could contain a negative cell trapped within. Figure 7.6 shows the 'labelRegions' application being configured for sorting red and green beads; a detection region has been marked out close to the centre of the electrodes. Figure 7.7 shows a screen-shot of the 'Sorter'

application during the sorting of red and green beads. The video feed is simultaneously displayed and recorded to hard disk.

Decision algorithms were based around a conservative strategy, with the aim of maximising the purity of the recovered population. Some 'target' particles would be rejected to the 'waste' outlet in order to preserve the purity of the recovered population. This might be necessary if, for example, a 'target' particle and a 'negative' particle approach the sorting gate in close proximity, and recovering the 'target' particle would risk also recovering the 'negative' particle. The *detectParticles()* function returns a value to the inquisitive function based on its interpretation of the image from the video source - see Table 7.1.

The sorting gate by default directs all particles down the waste outlet - this is defined as the 'closed' condition. The gate is opened (particles diverted to the recovery outlet) in response to values returned from the *detectParticles()* function. The action taken in response to the returned values may differ depending on the sorting priorities:

i. The usual response would be to open the gate, or keep it open if it is already. All of the identified objects in the detection region fit within the parameters specified for a 'target' particle.

ii. The gate should be closed if open, or kept closed. Any 'target' particles that may have triggered the opening of the gate have moved out of the detection region, and the gate should be closed in preparation for a subsequent 'negative' particle.

iii. The gate should be closed if open, or kept closed. An object has been identified with attributes matching a 'negative' particle. A more conservative response (that could boost the purity of the recovered population, with a possible reduction in quantity) might be to keep the gate closed for a specified time period. This would negate the possibility of the fluorescent signal fluctuating below the detection threshold for a 'negative' particle, which could permit an adjacent 'positive' cell triggering the gate to open. This is a possibility, as the illumination is not completely spatially uniform, but was not found to significantly boost the purity of the recovered population when sorting brightly coloured fluorescent beads. A more effective strategy was to enlarge the area of the detection region - see below.

Returned Value	Summary
1	One or more 'target' particles have been detected.
2	No particles have been detected
3	At least one 'negative' particle has been detected.

TABLE 7.1: Response values from the *detectParticles()* function.

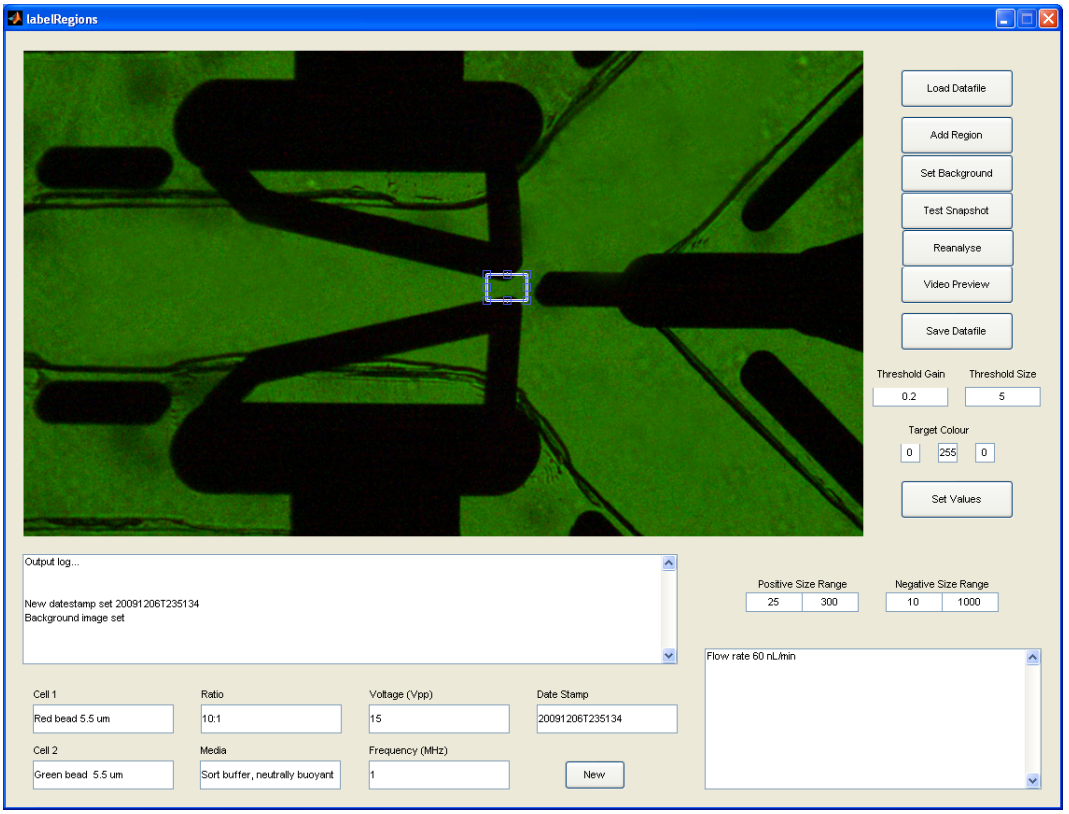

FIGURE 7.6: The graphical user interface of the 'labelRegions' application permits the detection region location to be defined, as well as adjustment of parameters for the image processing algorithms.

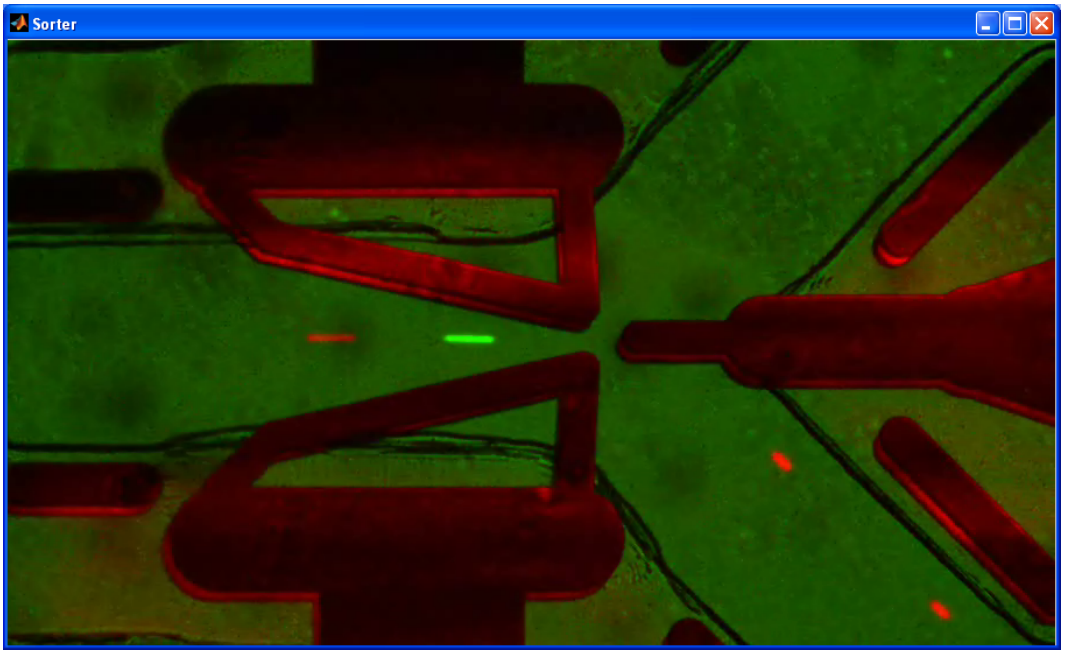

FIGURE 7.7: Screenshot of the 'Sorter' application during operation. As with the 'Trapper' application, the live video feed is the only visual interface produced, so that maximal processing time is available for the real-time image processing algorithms.

7.2.1.4 Operation

The fluid flow through the microfluidic device was controlled using the valves on each port and the syringe pump and pressure controller to ensure that the 'recovery' outlet was not contaminated with unsorted cells during loading. Figure 7.8 shows an overview of the fluid flow during the device during preparation, sorting and recovery of the particles. The syringe pump was used to deliver large volumes of fluid as its maximum flow rate was much higher than what could be achieved using the pressure controller. The pressure controller was required during particle sorting, as it permitted the flow rates in and out of the device to be finely adjusted. It was necessary for the flow to divide evenly between the two outlets for the electrodes to deflect the particles sufficiently, so the pressure on each outlet was independently adjusted.

7.2.2 Designs B and C: Multi-stage Sorting Devices

A logical extension of the sorting gate concept is the addition of multiple outputs so that more particle sub-types or cell populations can be recovered. Figure 7.9 shows four designs of sorting devices that incorporate negative DEP barriers. All the sorter designs are intended for a common mode of operation (lateral deflection of a focused particle stream) but achieve it by different methods. Design B (the 'multi-gate sorting device') effectively combines four sorting gates into a single, more compact five-output sorter. Design C (the 'particle router' device) is a further development, intended to more accurately define the path that sorted particles follow, and to increase the separation distance between outputs, combining three sorting gates for four outputs. The remaining two designs develop the single sorting gate concept, by combining three gates sequentially to deflect particles between one of four outputs. All four devices were fabricated within a single microfluidic device, although only Designs B and C were developed for analysis.

7.2.2.1 Microfluidic Device

The four designs of sorter shown in Figure 7.9 were fabricated on a single device, as shown in Figure 7.10. Multi-layer electrode structures were fabricated in titanium/platinum on two 700 μm borosilicate glass wafers using established techniques as described in Section 4.4. 700 nm silicon nitride was used as an inter-layer dielectric. All fabrication of electrode structures was performed by Nico Kooyman, Mi Plaza, Philips Research Laboratories, Eindhoven, The Netherlands. The microfluidic channel was fabricated by Katie Chamberlain at the Southampton Nanofabrication Centre by laminating each substrate with SY3355 dry film resist (Elgar Europe, Italy), patterning by development in BMR Developer/Rinse, and compression bonding at elevated temperature as described

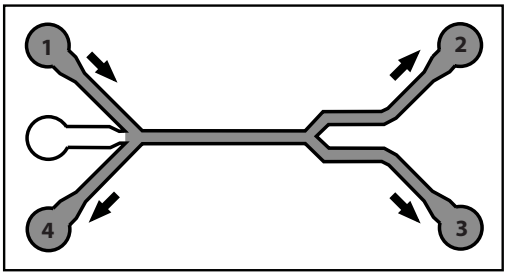

(i) Syringe pump: 4 mL,1 mL / min
Buffer flows through the microfluidic device

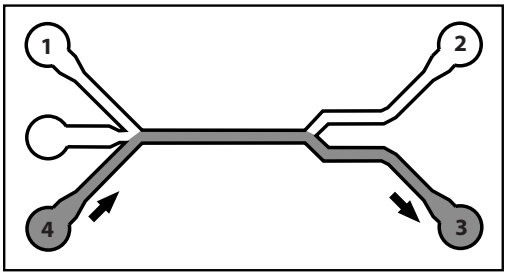

(ii) Pressure control: 200 µL, 100 µL / min
Particles are introduced into the system

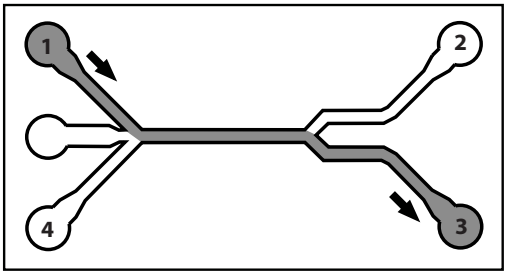

(iii) Syringe pump: 1 mL, 1 mL / min
The 'waste' output is flushed clean with buffer

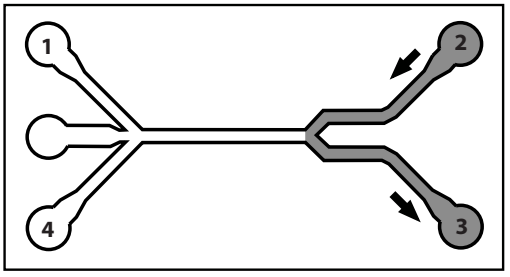

(iv) Pressure control: 200 nL, 100 nL / min
The 'recovery' outlet is flushed clean by flowing buffer back along the channel

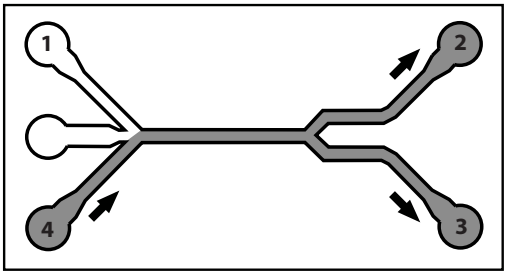

(v) Pressure control: 1-100 nL / min
Particles are sorted between the two outputs

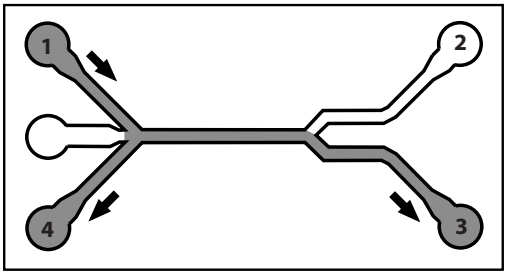

(vi) Syringe pump: 1 mL, 1 mL / min
Particles are flushed from the channel and the 'waste' output collected

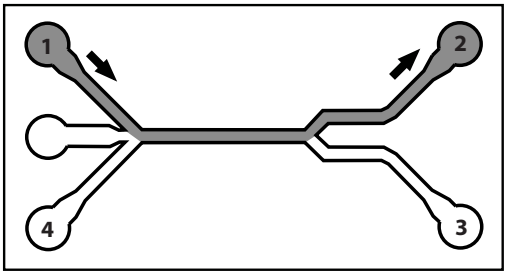

(vii) Syringe pump: 1 mL, 1 mL / min
The sorted 'target' particles are collected from the 'recovery' outlet

Key:
1: Plain buffer, no particles
2: 'Recovery' outlet
3: 'Waste; outlet
4: Particle inlet

FIGURE 7.8: Valve operation sequence used with the sorting gate device during preparation, sorting particles and recovery of the sorted populations.

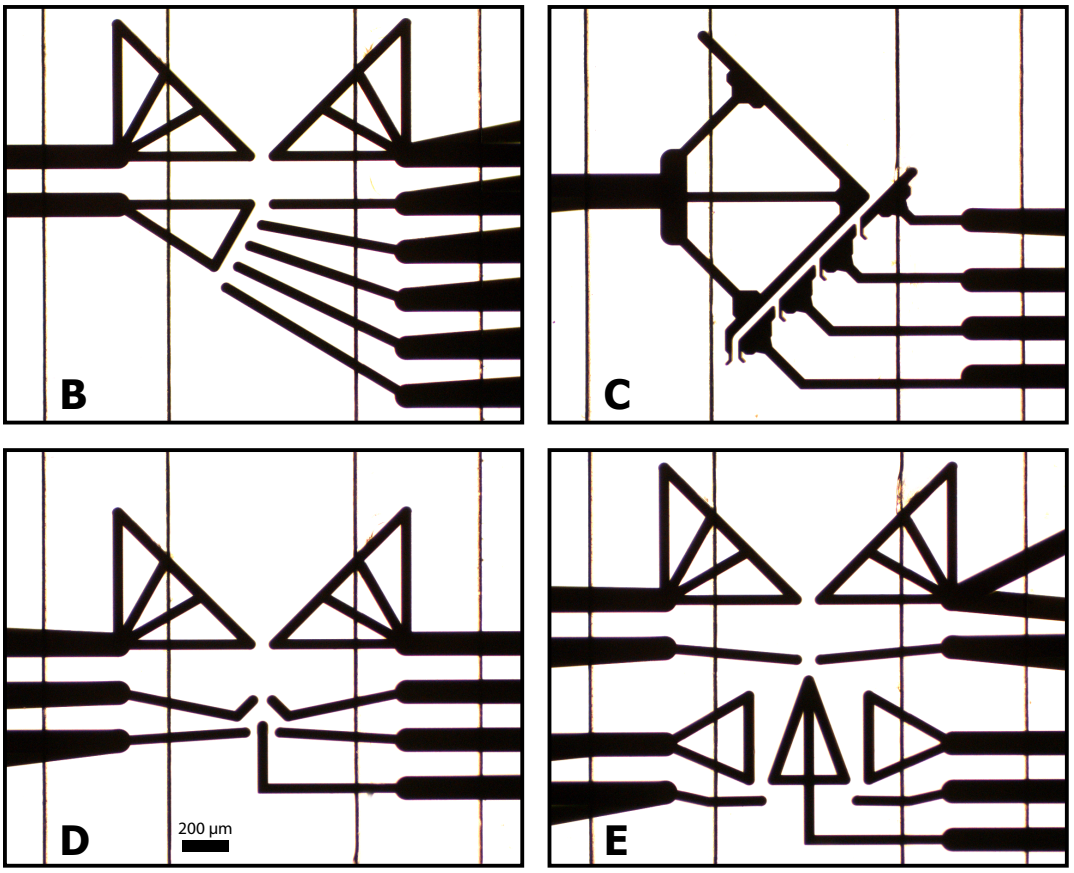

FIGURE 7.9: Close-up views of the mask designs used to fabricate the channel and four different sorting gate electrodes.

in Chapter 4. The channel had a depth of 100 μm after bonding. Anisotropic conductive film was used to make electrical connections between the glass electrodes, a flexible interconnect, and a PCB daughterboard - as described in Section 4.5.1.

7.2.2.2 Macrofluidic Equipment

The microfluidic chip was clamped within a manifold block, as used in the previous experiments with the ring electrodes, and two of the six access ports were used. A syringe pump (Cole Palmer 79000) was used to control fluid flow through the device. Two syringes were used, to permit a range of fluid velocities to be used. A 10 mL plastic syringe was used to clean and flush through the device with large volumes of liquid during setup and cell recovery. A 25 μL glass syringe (Hamilton) was used during dielectrophoretic particle manipulation, as the smaller diameter permitted flow rates of less than 0.1 μL min^{-1} to be used without introducing significant pulsations into the flow from the pump. A 3-way valve (Omnifit) at the input to the microfluidic device permitted the flow to be switched between the syringes. An overview of the fluidic equipment used with the system is shown in Figure 7.11.

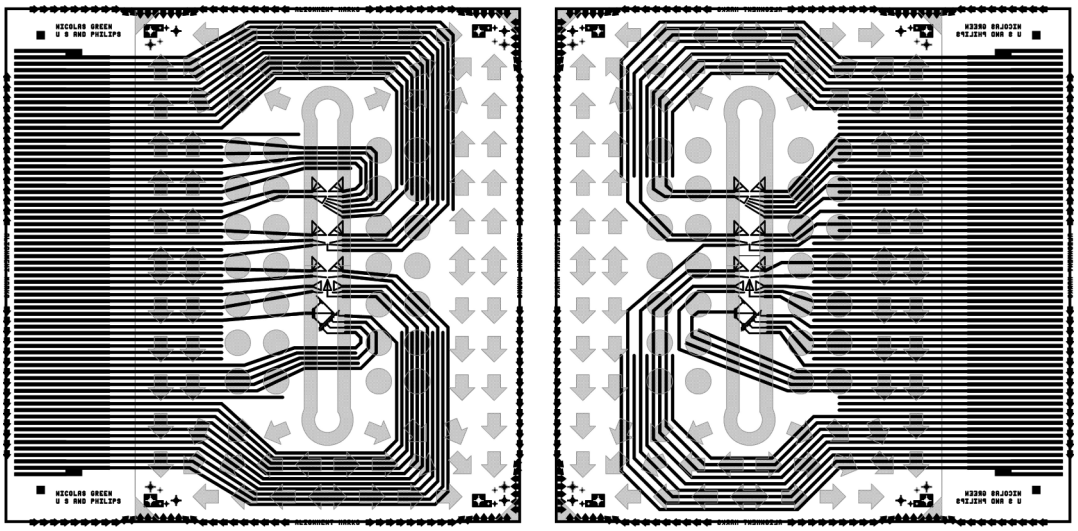

FIGURE 7.10: Plan view of the microfluidic device showing the channel and electrodes on the top (left) and bottom (right) glass substrates, created from the mask design files. Gray regions are the dry film resist that forms the walls of the microfluidic channel and supporting structures, black regions are the platinum electrodes. The channel and electrodes on the top glass would be on the underside of the substrate, as viewed in the figure. Each substrate is of dimensions 20 x 20 mm, with thickness 700 μm.

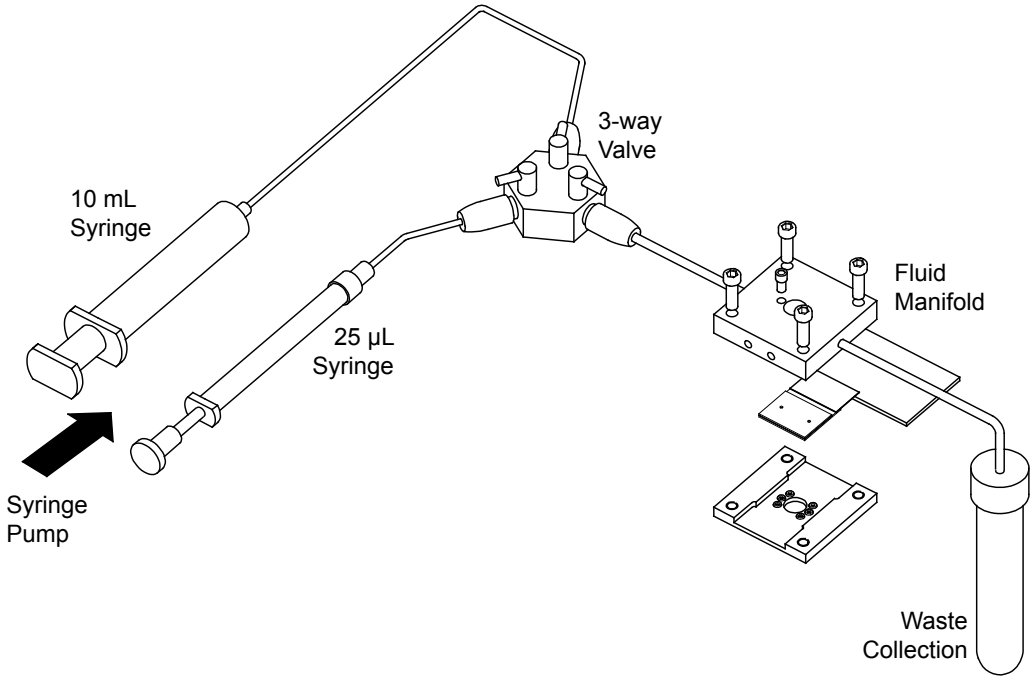

FIGURE 7.11: Schematic of the macrofluidic connections surrounding the microfluidic device.

7.2.2.3 Experimental

The microfluidic device was loaded with a solution of 15 μm diameter fluorescent green microspheres (see below). The electrical excitation was set at 12 Vpp, 1 MHz, and the electrodes were configured to focus the particles into a narrow stream as they were carried by the fluid flow (1 μL min^{-1}) through the device. The polarity of the sorting electrodes was reconfigured to drive the particle stream through each stage of the sorting device in turn. Video data was recorded throughout, and subsequently analysed using particle-image velocimetry (see below).

The DEP force is proportional to the cube of the particle radius ($a^3_{particle}$), while the hydrodynamic drag that carries particles through the system is proportional to the particle radius only ($a_{particle}$). As the fluid flow rate increases, smaller particles (due to minor variations within the manufacturing tolerance) will break through the DEP barrier first because the DEP force they experience is less than that experienced by larger particles. Measurement of the speed at which particles break through the DEP barrier permits quantification of the sorter performance and places an upper limit on the fluid flow rate at which it may be operated for a particular particle and size.

The sorting electrodes were again configured to focus the particles into a stream, and direct them through the first output of the gate. The fluid flow was adjusted so that all the particles were correctly sorted, then was gradually increased until 50% of the particles were breaking through the DEP barriers and were not being sorted correctly. Video footage of the particles was recorded directly on to computer and saved in video files for analysis.

Custom scripts were written in Matlab 2008a (Mathworks) to interpret the video files and take measurements of particle velocity (particle image velocimetry - PIV). To measure the breakthrough velocity of the particles, a region downstream from the focusing electrodes (that particles would only pass through if they had broken through the DEP barrier) was selected for processing, and all particles passing through this region were identified (by size and colour) on a frame-by-frame basis. Particles were subsequently tracked between frames, and measurements of their displacement were combined with the video timebase and averaged across several frames to calculate their average velocity. Figure 7.12 shows the PIV software tracking two particles that have broken-through the focusing barrier.

7.2.3 Microparticles and Solutions

Fluorescent polystyrene microparticles were purchased from Bangs Laboratories (Indiana, USA) - see Table 7.2. Green and red fluorescent 5.5 μm beads were mixed to create a heterogeneous population for processing through the sorter device (Design A).

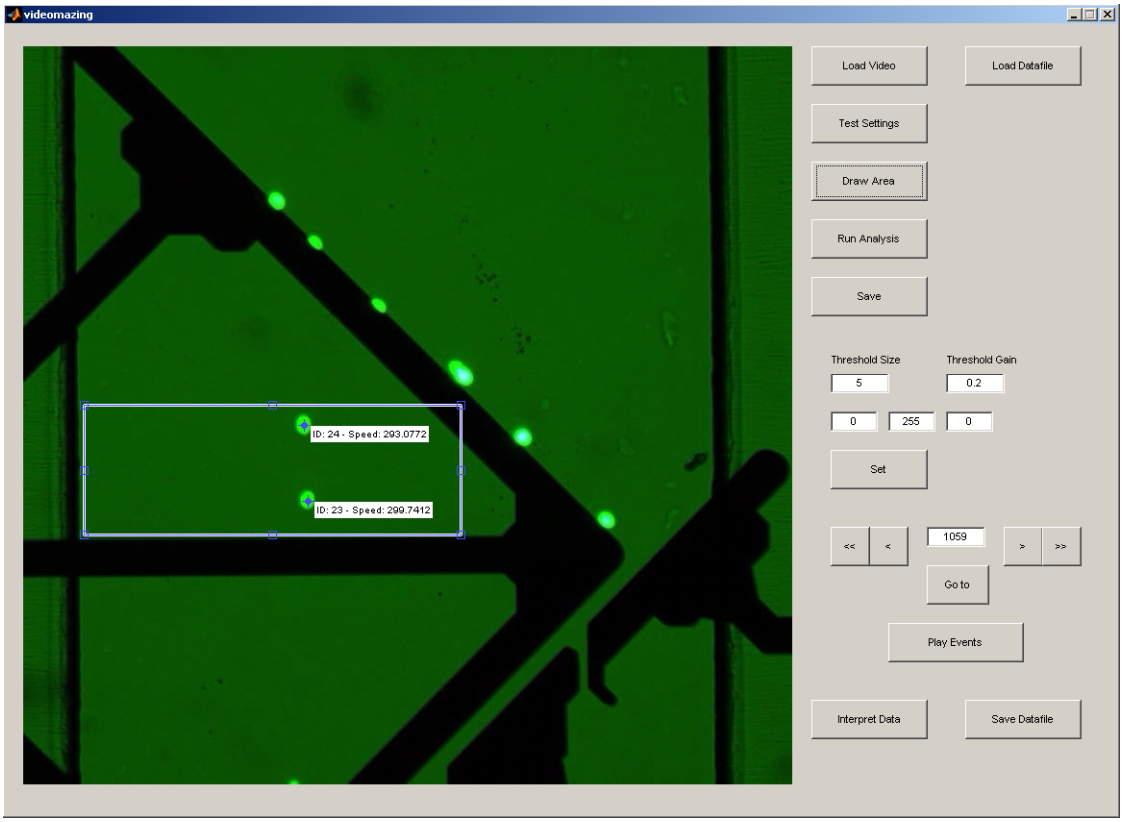

FIGURE 7.12: A screen image of the PIV software, showing deflected particles moving along the DEP barrier, and particles that have broken through the barrier being tracked through the detection region.

Bead solutions were mixed with the ratio of red to green beads of 10:1, at a concentration of 2.26 x 10^6 mL^{-1}. The final ratio of beads was determined by flow cytometry (BD FACSAria) as the bead concentrations in the supplied solutions were not identical. Bead mixtures were resuspended in a sorting buffer of 0.02% TWEEN-20, 0.1% PBS in aqueous solution with sucrose added at approximately 12.8% to adjust the density of the solution to $(\rho_{medium}) = 1.0533$ g cm^{-3}. A sample tube containing the bead solution in sorting buffer was placed in the centrifuge for 2 minutes at 10,000g, after which the beads were clearly still present in suspension, indicating the solution was neutrally buoyant. The conductivity of the solution was measured as $(\sigma_{medium}) = 0.18$ mS m^{-1}. Green fluorescent 15.61 μm beads were prepared in a similar solution for use in the particle routing device (Design B). Equation 2.4 was used to model the polarisability of the microparticles in the above solutions, and the Clausius-Mossotti factor was calculated - see Figure 7.13(b).

Colour	Diameter	St. Deviation	Peak Absorption	Peak Emission
Flash Red	5.5 μm	0.53 μm	660 nm	690 nm
Dragon Green	5.5 μm	0.53 μm	480 nm	520 nm
Dragon Green	15.61 μm	1.52 μm	480 nm	520 nm

TABLE 7.2: Fluorescently labelled beads purchased from Bangs Laboratories.

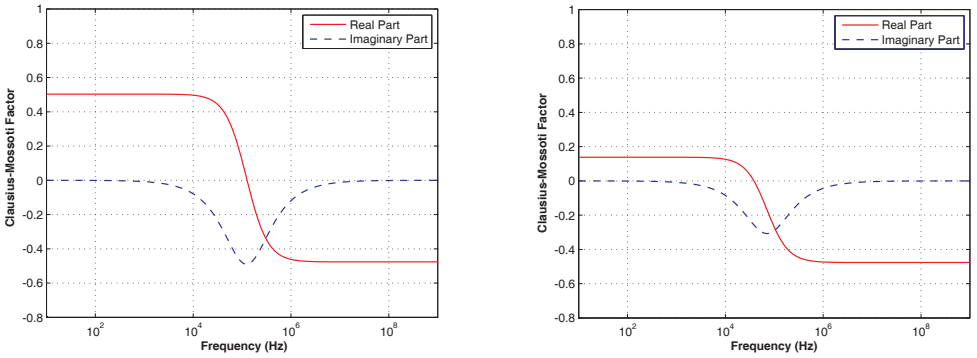

(a) 5.5 μm Diameter

(b) 15.61 μm Diameter

FIGURE 7.13: Plot of the Clausius-Mossotti factor for 5.5 μm and 15.61 μm polystyrene spheres ($\epsilon_{r,p} = 2.5$, $K_s = 1$ x 10^{-9}) in aqueous solution ($\epsilon_{r,m} = 78$, σ_m=0.18 mS m^{-1})

7.2.4 Electrode Control and Signal Generation

Electrical signals were supplied to the electrodes using a set of equipment similar to that used in the previous chapter. Sinusoidal voltages from a TTI TG2000 signal generator were split between 10 channels of an Omega ERB-48 relay board and connected to the electrodes, so that each channel could be switched between the alternating voltage or ground. The relay board was controlled by custom scripts written in the Matlab (Mathworks) environment through a NI USB-6009 interface. Circuit schematics are shown in Section 6.2.4.

7.3 Results

7.3.1 Design A: The Sorting Gate

Figure 7.14 shows flow cytometry data for separate (unsorted) samples of the red and green beads. Fluorescent intensity in both the FITC band (530/30 nm) and the APC band (660/20 nm) is analysed. The regions 'P1' and 'P2' are representative of particular ranges of fluorescent intensity in each band, and are chosen to completely cover measurements for the red and green beads respectively. The red and green populations are separated by approximately two orders of magnitude in both the FITC and APC band. The plots show 5000 measurements for each bead colour, with no beads being detected in the opposite region.

Figure 7.15 shows flow cytometry data for the mixed sample of red and green beads used for sorting experiments. The sample was produced from a 10:1 (v/v) mixture of red and green beads in solution; as the figure shows, the actual ratio of red to green beads (ratio of the number of particles) is 10.77:1. A small number of events were detected (0.8% of the total) with intensities outside of the P1 and P2 ranges. These are not shown.

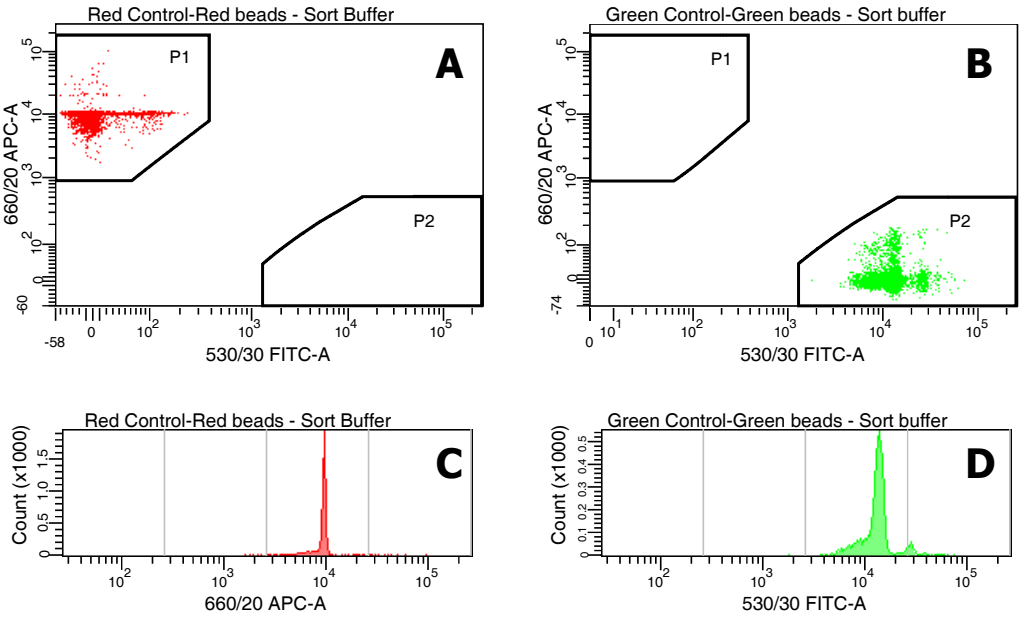

FIGURE 7.14: Plots of flow cytometry results showing fluorescent intensity in the FITC and APC-A bands (wavelengths 530 and 660 nm respectively), performed on separate samples of fluorescently labelled red and green beads (5.5 μm diameter). Populations were defined by labelling particular regions of the plot (particular ranges of fluorescent intensity) with 'gates' (P1 and P2).

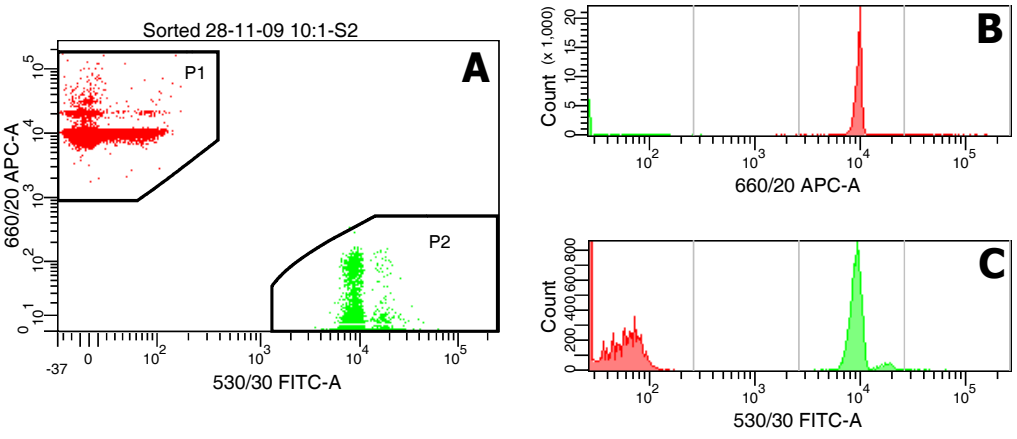

Tube: S2

Population	#Events	%Parent	%Total
All Events	79,702		100.0
P1	72,353	90.8	90.8
P2	6,719	8.4	8.4

FIGURE 7.15: Plots of flow cytometry results showing fluorescent intensity in the FITC and APC-A bands, performed on the mixture of fluorescently labelled red and green beads (5.5 μm diameter) at a ratio of 10:1. The actual ratio of red to green beads (number of particles) is 10.77:1.

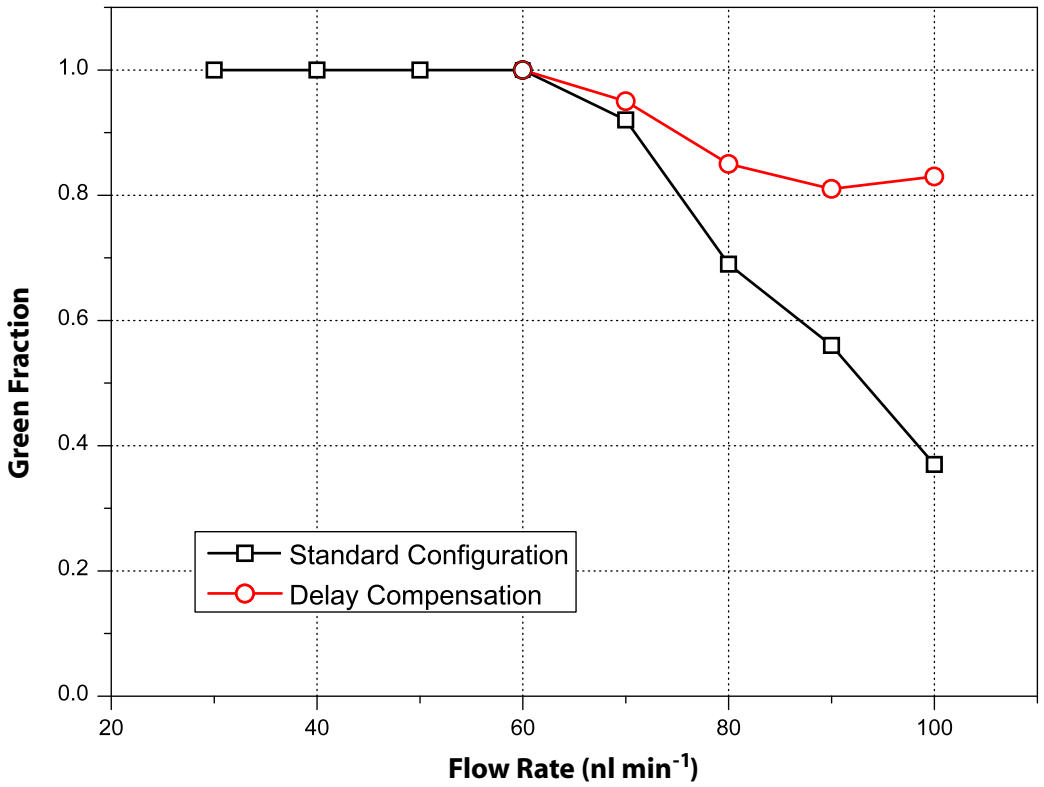

FIGURE 7.16: Plot of the purity of samples (green fraction) recovered after sorting. Data taken from FACS analysis.

Mixtures of fluorescently labelled red and green beads (5.5 μm diameter) at a ratio of 10:1 were sorted, and the contents of the recovery and waste outlets collected, each in 1 mL of the sorting buffer. An additional sample of 1 mL was taken from each of the outlets as a check that all of the beads had been collected. 500 μL PBS was added to each sample (to decrease the buoyancy) and the samples concentrated down to 100 μL by centrifugation at 10,000g for 2 minutes and removal of the majority of the supernatant. Samples were then analysed by flow cytometry (BD FACSAria) to obtain counts of the number of red and green beads in each sample.

Figure 7.16 is a plot of the green fraction - the fraction of the beads from the recovery outlet that are green ('target') beads - for sorting operations over a range of fluid flow rates. Data was calculated from the results of flow cytometry analysis on samples recovered from the microfluidic device. A value of 1 represents a sample that contained 100% green beads. Pure samples (100% green) were obtained for flow rates up to 60 nL min^{-1}.

Figure 7.17 shows the rate at which particles were sorted through the microfluidic device over a range of fluid flow rates. Data was obtained by counting the number of particles that passed through the sorting gate from analysis of recorded video logs. Figure 7.18 is a graph of the proportion of green ('target') beads that were not sorted to the recovery outlet, out of the total number of green beads that passed through the sorting gate. The

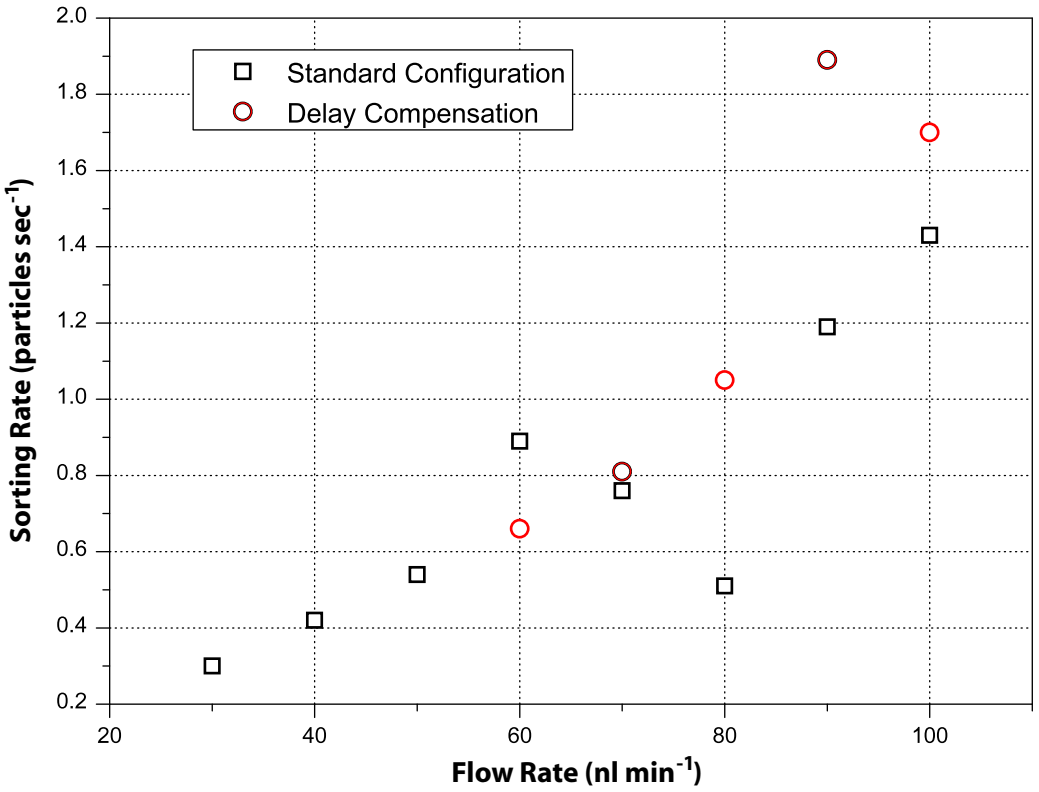

FIGURE 7.17: Plot of the average rate at which particles were sorted through the device. Data taken from video analysis.

data was obtained by counting the number of particles that entered the recovery and waste outlets from analysis of recorded video logs.

7.3.2 Design B and C: Multi-Stage Sorting Devices

Both of the multiple-stage sorting devices were able to sort particles between all of their outlets over a range of voltages and flow rates. Figure 7.19 shows a sequence of images taken as 15 μm diameter fluorescent green beads are focused into a stream and sorted by the multi-gate sorter device into each of the output streams. The flow rate is 1 μL min^{-1} and the electrodes are driven with a 12 Vpp signal at 1 MHz. Figure 7.20 shows a sequence of images under similar conditions for the particle router device.

The particle router device was designed to direct particles out of the trap along a predetermined path, set by the electrode geometry. This path should be ideally independent of parameters such as the particle size, the Clausius-Mossotti factor of the system, or the voltage on the electrodes (assuming the DEP force is of sufficient magnitude to correctly deflect the particles). Video data of the operation of both sorting devices was processed using the particle-image velocimetry software, to determine the trajectory of each particle as it passed through and out of the sorting devices. Each video frame was processed to identify bright, moving objects, and the coordinates of the geometric centre of each

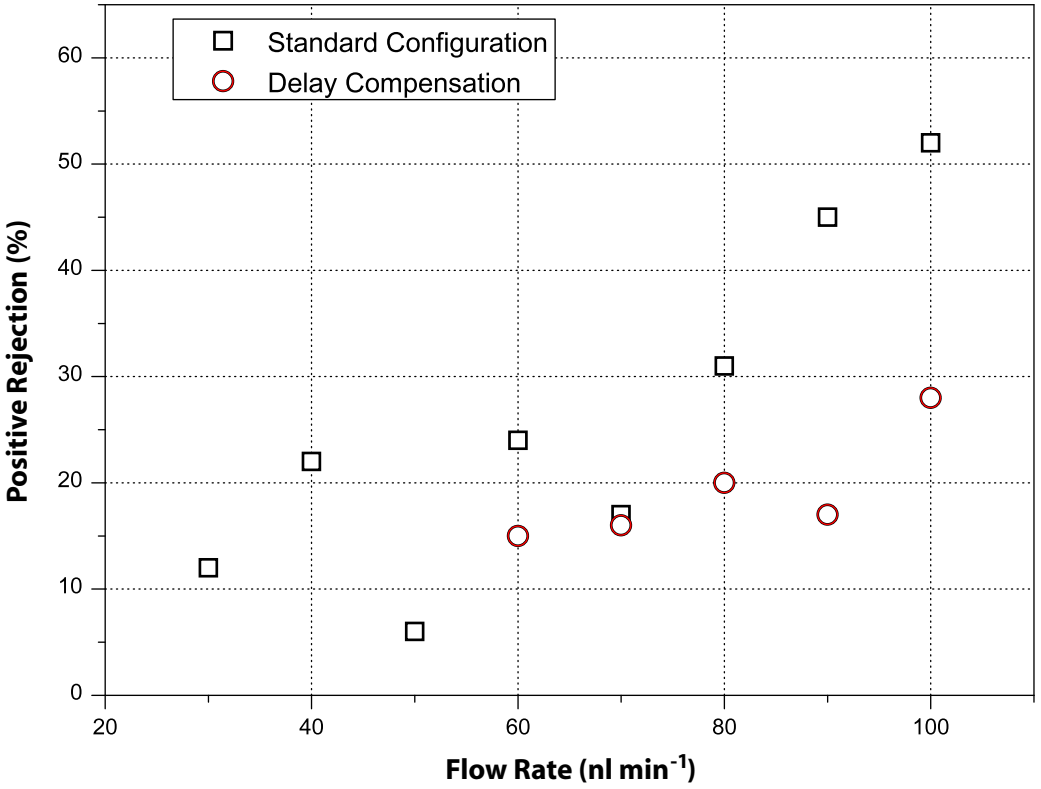

FIGURE 7.18: Plot of the percentage of positive (green) particles that were not recovered. Data taken from video analysis.

object was recorded. Each coordinate was plotted as a single point, and an image of the electrode geometry was superimposed. The results of the analysis for the multi-gate sorter device is shown in Figure 7.21 and for the particle router device in Figure 7.22.

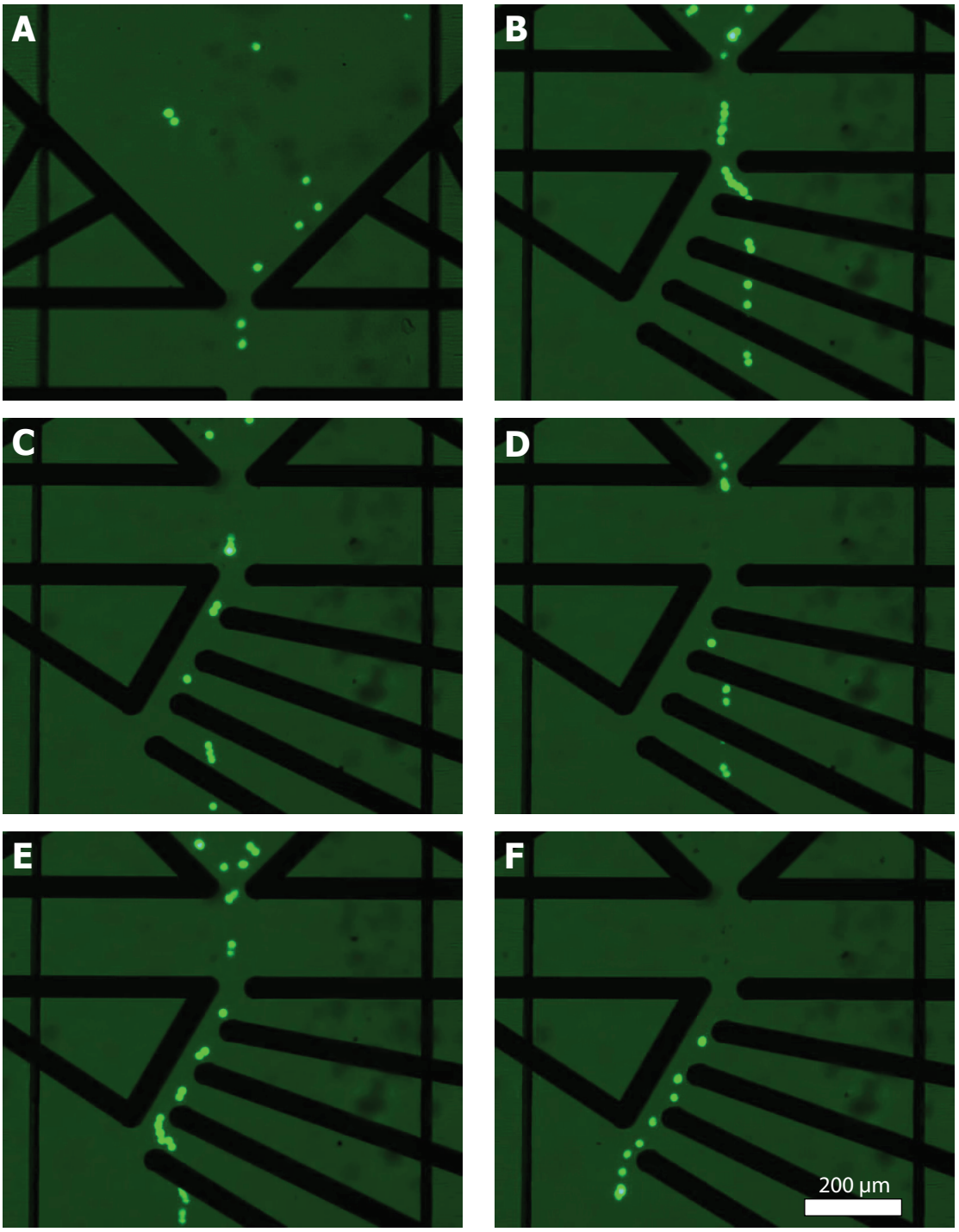

FIGURE 7.19: Sequence of photographs taken during operation of the multi-gate sorter device (Design B). 15 μm diameter fluorescent green microspheres in suspension flow through the microfluidic device at 1 μL min^{-1}, and are focused into a narrow stream and deflected by DEP between one of five output streams. Electrical excitation is 12 Vpp, 1 MHz. Channel dimensions 900 x 100 μm.

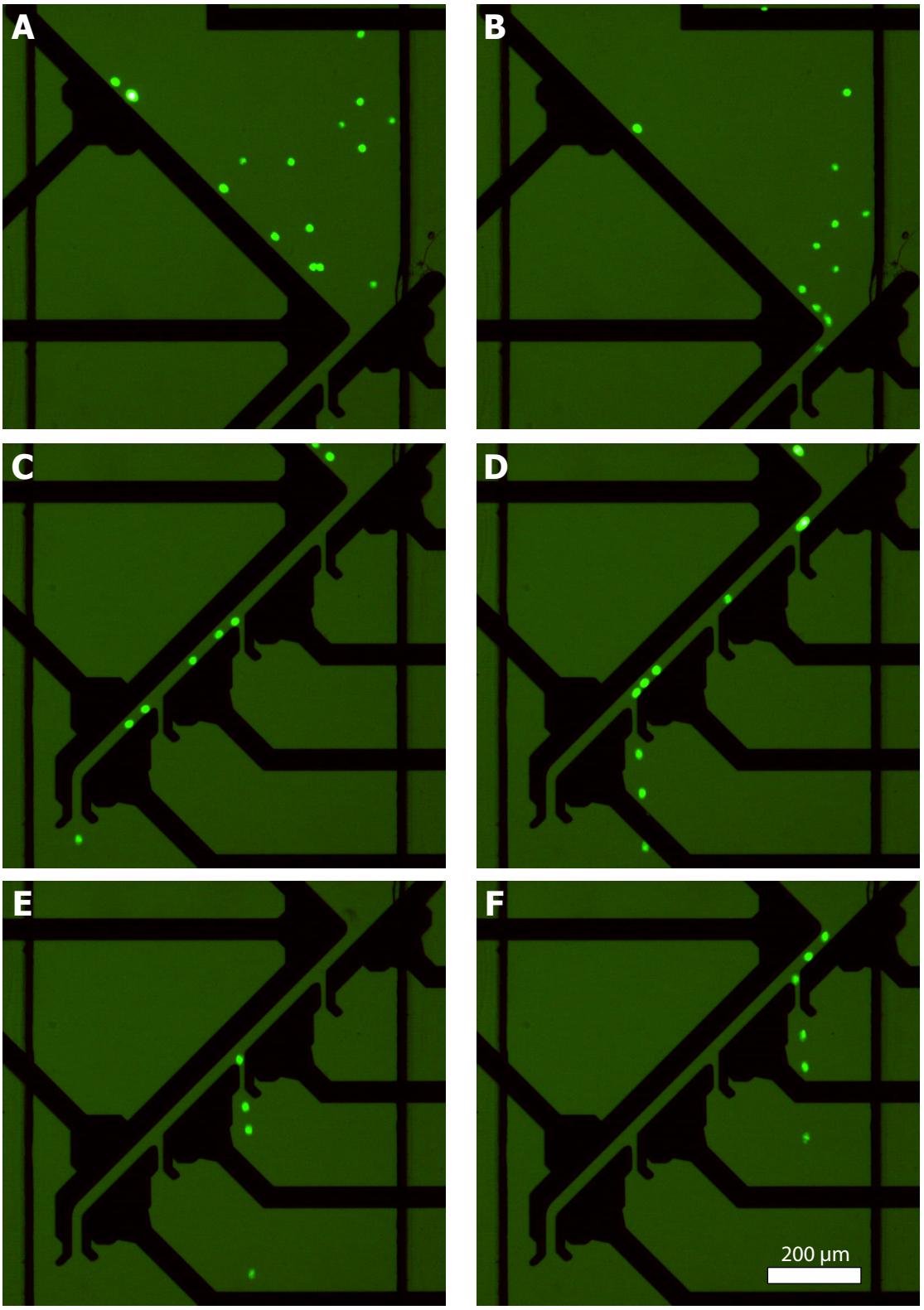

FIGURE 7.20: Sequence of photographs taken during operation of the particle router (Design C). 15 μm diameter fluorescent green microspheres in suspension flow through the microfluidic device at 1 μL min^{-1}, and are focused into a narrow stream and deflected by DEP between one of four output streams. Electrical excitation is 12 Vpp, 1 MHz. Channel dimensions 900 x 100 μm.

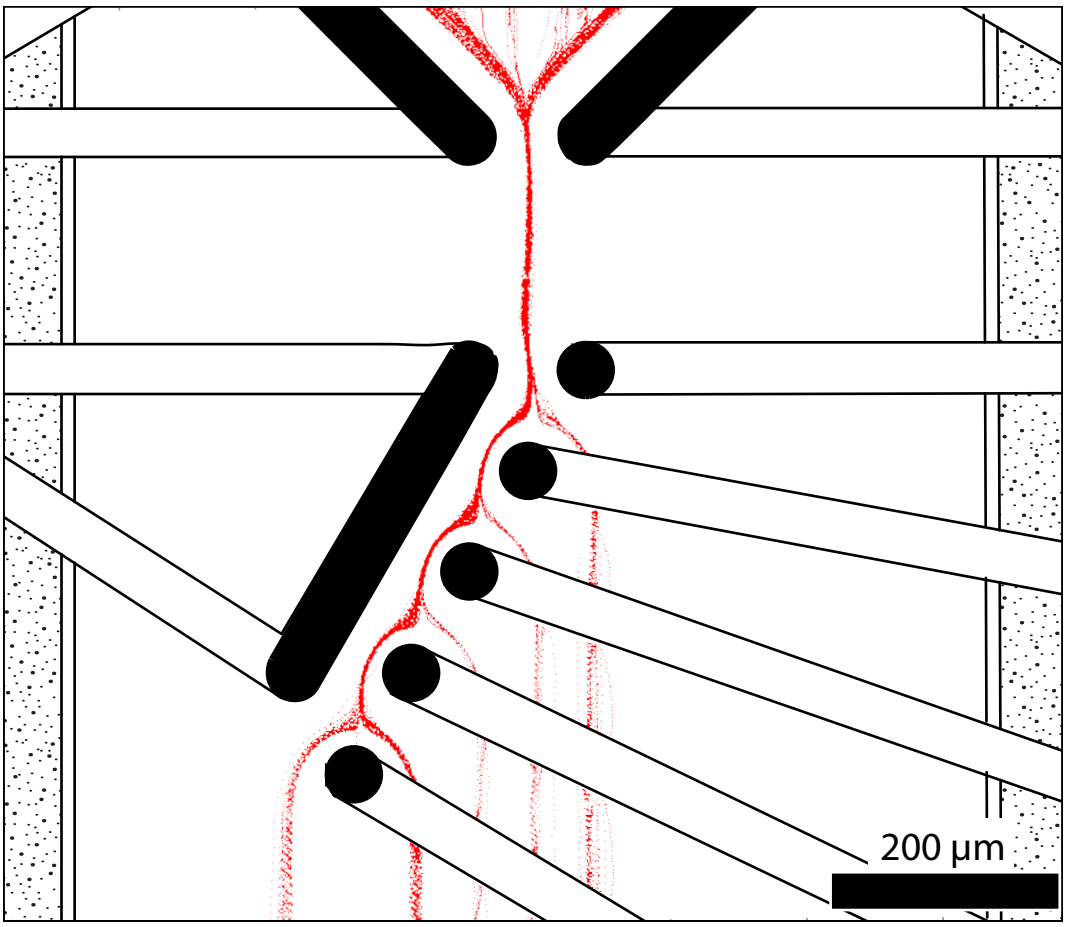

FIGURE 7.21: Plot of the bead trajectories through the multi-gate sorter device. Particle position was measured by analysis of pre-recorded video sequences. Each point represents the geometric centre of a single particle in a single frame. An image of the electrodes and channel wall is superimposed, with the top metal layer (from which the DEP force originates) coloured in solid black. Recorded at 40 fps, flow rate 1 μL min^{-1}, electrode voltage 12 Vpp, 1 MHz.

Outlet:	1	2	3	4	5
Stream Width (μm)	16	11	10	17	24
Stream Separation (μm)	96	47	46	41	

TABLE 7.3: Measurements of the output streams leaving the multi-gate sorter device.

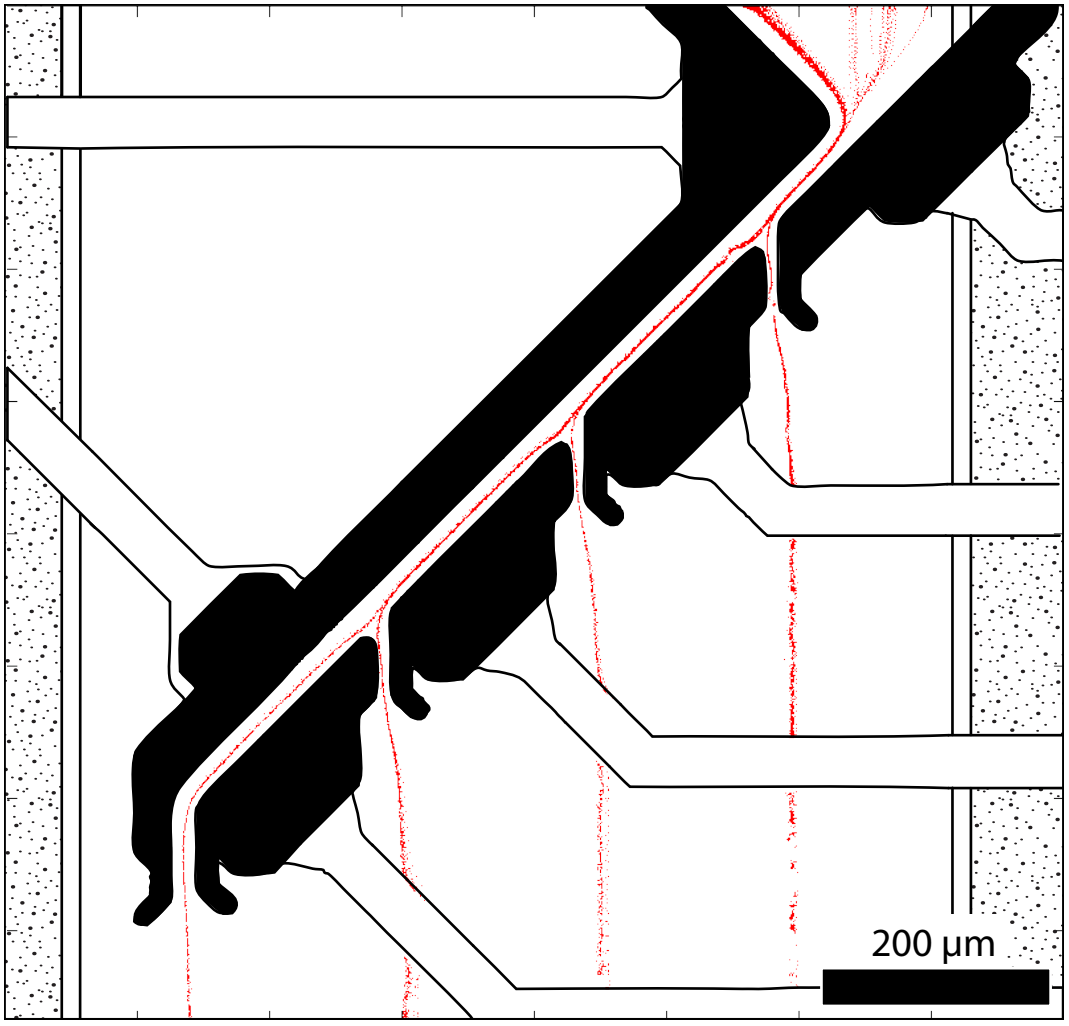

FIGURE 7.22: Plot of the bead trajectories through the particle router device. Particle position was measured by analysis of pre-recorded video sequences. Each point represents the geometric centre of a single particle in a single frame. An image of the electrodes and channel wall is superimposed, with the top metal layer (from which the DEP force originates) coloured in solid black. Recorded at 40 fps, flow rate 1 μL min^{-1}, electrode voltage 12 Vpp, 1MHz.

Outlet:	1	2	3	4
Stream Width (μm)	4	7	4	5
Centre Offset (μm)	4.5	12	11	12
Stream Separation (μm)		170	147	146

TABLE 7.4: Measurements of the output streams leaving the particle router device. As it was intended for particles to leave the device along a defined path, the lateral distance of the centre of the stream from the centre of the outlet (centre offset) is also calculated.

For each output stream, the width was measured after a point 70 μm from the exit of the sorter. Similarly, the distance between the centre-lines of each adjacent stream (separation) was measured. As the particle router device was designed to direct particles along a predetermined path (the centre-line of the outlet) the offset between the particle stream centre-line and the outlet was also measured for this device. These measurements are presented in Table 7.3 and Table 7.4 for the multi-gate sorter and particle router device respectively.

As the fluid flow rate was increased (or the electrode voltage decreased) particles started to break through the DEP barrier imposed by the focusing electrodes. Particles must be focused into a narrow stream before they enter the sorting gate, so this imposes an upper limit on the rate at which particles can be sorted by the device. The electrode voltage on the focusing electrodes of the particle router device were adjusted from 6.00 - 18.00 Vpp, and for each voltage level the fluid flow was adjusted until 50% of the particles were breaking through the DEP barrier. Video data was recorded, and subsequently analysed with the particle-image velocimetry software. Figure 7.23 shows a plot of the break-through velocities of particles over a range of excitation voltages. The equivalent data was also calculated from numerical simulation of the electric field (Figure 3.14), for a 15.61 μm diameter particle in aqueous medium ($\epsilon_m = 78$) experiencing negative DEP ($Re(f_{CM})$ = -0.47). A summary of the measurement data is shown in Table 7.5.

7.4 Discussion

7.4.1 Design A: The Sorting Gate

The sorting gate was able to sort particles at flow rates of up to 60 nL per minute and produce a recovered sample with 100% purity (comprised of 100% green target particles with no non-target particles). As the flow rate was increased, the green fraction made up an increasingly small part of the recovered population as more negative particles were also recovered.

Voltage (Vpp)	Total number of particles	Average particle (μm sec^{-1})	Min. velocity (μm sec^{-1})	Max. velocity (μm sec^{-1})	St. Deviation (μm sec^{-1})
6.00	16	129.2	123.1	135.1	4.0
9.44	69	346.2	317.8	393.9	11.7
11.63	23	567.5	459.0	608.5	29.9
15.06	40	854.5	815.3	940.4	23.7
18.00	22	1234.0	1193.1	1323.4	34.1

TABLE 7.5: Summary of the measurements on particles breaking through the DEP focusing barrier for each voltage level.

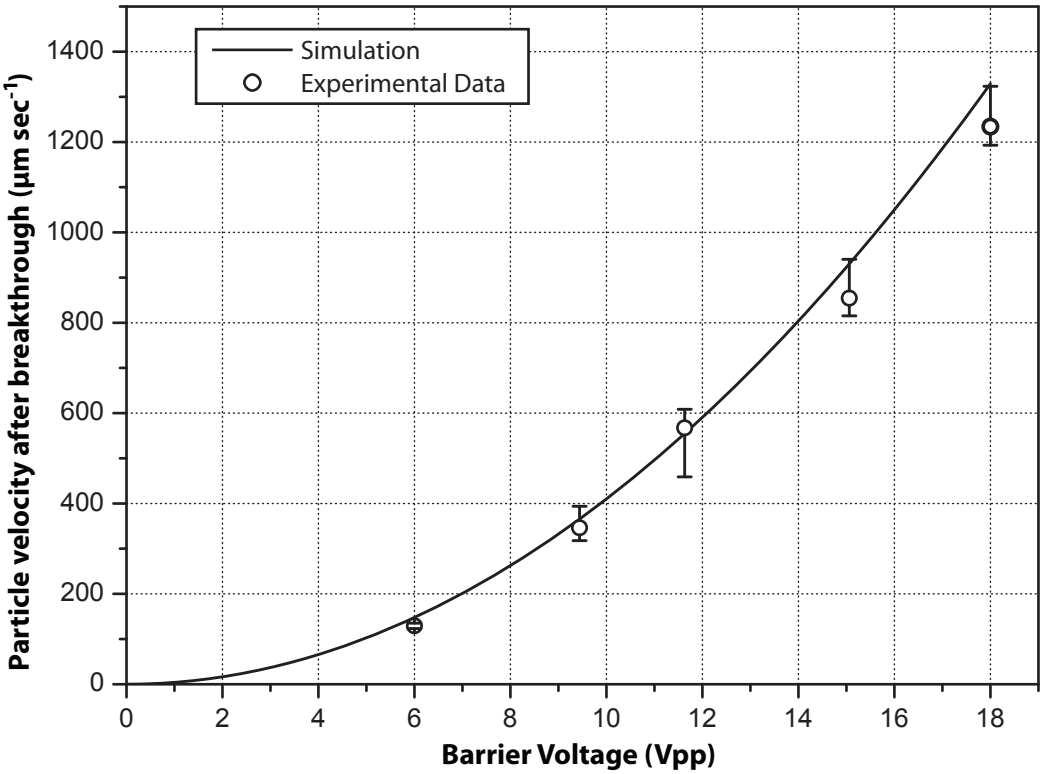

FIGURE 7.23: Plot of the velocity of particles measured after breaking through the DEP barriers of the particle router device, and equivalent data calculated from numerical simulation of the electric field (Figure 3.14). The error bars show the range of the experimental measurements.

Analysis of the video files indicated that at higher flow rates (70-100 nL min^{-1}) a 'target' particle would frequently trigger the gate to open but would instead flow down the waste outlet, and a succeeding 'negative' particle would be directed down the recovery outlet. This suggests that the voltage on the electrodes may not be being switched sufficiently quickly to sort the particles correctly. A switching delay is likely to originate within the control software: the 'Sorter' application is scripted rather than compiled, and a number of processor-intensive image manipulation tasks must be performed on each frame before a particle can be identified. The maximum rate at which the 'Sorter' application could run was 10 frames per second, if simultaneous video display and recording was required. On average, this leads to a delay of 50 ms between the time that a particle enters the detection region and the time at which the software *begins* processing the next frame.

One solution to this problem is to introduce a delay compensation. In practice, this can be achieved by offsetting the detection region slightly upstream of the sorting gate, so that the voltage on the electrodes is switched earlier. As Figure 7.16 shows, offsetting the detection region to introduce a delay compensation significantly increases the purity of the recovered populations (an increase from 37% to 83% at 100 nL per minute, for example). Figure 7.24 shows the sorting electrodes with the detection region in its standard configuration, and with delay compensation. An alternative would be to

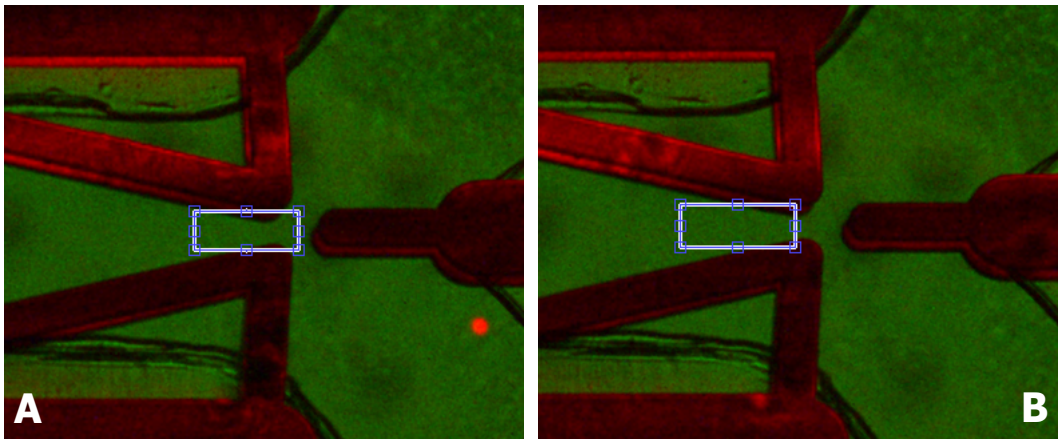

FIGURE 7.24: Image of the sorting electrodes with the detection region overlaid in (a) standard configuration and (b) with delay compensation - the region is offset approximately 25 μm upstream.

change the control system to reduce the processing time, such as by using a compiled program or a lower level language, or to use a hardware solution such as an application specific integrated circuit (ASIC). Changing the switching elements from mechanical relays to solid state electronics would also help to reduce the delay.

At higher flow rates (80-100 nL per minute), it was observed that particles were not being deflected correctly by the sorting electrodes, and were instead coming to a near standstill in front of the central sorting electrode before being slowly pushed down one channel or the other. This is most likely because particles did not spend adequate time in the region in the centre of the sorting electrodes to be sufficiently deflected by the DEP force when being carried by the fluid at high flow rates. This could lead to an accumulation of particles within the active area of the sorting gate, causing multiple 'negative' particles to enter the recovery channel. This effect was mitigated by reducing the flow rate, or increasing the gate voltage, suggesting that a higher gate voltage would be more appropriate for these flow rates.

Figure 7.18 shows the a positive correlation between the positive rejection (a measure of the proportion of 'target' particles that were not sorted into the recovery outlet) and the flow rate. Although the particles approach the sorting gate at higher velocities when higher flow rates are used, the average spatial separation distance should remain unchanged for a given concentration of particles. Hence, a mixture of particles should not become more difficult to separate if it is sorted at higher flow rates. This increase in the positive rejection is likely due to particle distortion in each video frame at higher flow rates. The fixed exposure time of the video camera means that particles appear closer together as they are elongated by motion blur at increasing flow rates. The conservative decision algorithms will reject particles to 'waste' as soon as negative particles are detected, and this becomes more common as the particles appear closer together at high flow rates.

Figure 7.17 shows, as expected from Equation 7.1, a general trend between the fluid flow rate and the rate at which particles were sorted through the device. Any solution of particles is, by its nature, a random and chaotic mixture, and so when a solution is flowing through a microfluidic device only probabilistic methods can indicate when the particles will arrive at the electrodes. The particle rate equation (Equation 7.1) provides an indication of the average number of particles flowing through the sorter in unit time, but the actual distribution will be Gaussian with the average value at this rate. Hence, the likelihood of two (or more) particles being within the active area at the same time, and one of them being deflected towards the incorrect output, increases with the concentration of particles ($C_{particles}$).

Comparison with data on alternative sorting technologies (Table 1.1 - Chapter 6) shows the sorting gate device compares similarly to other published microfluidic sorting devices. It is notable that few groups working on cell and particle separation have chosen to publish data on attempts to recover pure populations from sorting devices - the majority of data concerns achieving enrichment of low purity samples at high rate, with quite significant levels of impurities remaining in the recovered samples. The work of Dittrich and Schwille (2003) is significant, as they have produced recovered populations of several thousand particles (red and green fluorescent beads) with purities of 99.1%, sorted at 0.68 particles per second.

7.4.2 Design B and C: Multi-stage Sorting Devices

All of the sorting devices in this chapter are intended to produce particle separation by lateral displacement of sub-populations into two or more discrete streams within the fluid flow. If the fluid flow can be divided evenly at the correct point, these streams can be recovered as separate samples. The larger the degree of separation, the more likely that the particle will leave the microfluidic device by the correct outlet. Alternatively, further processing may be required on chip, the degree of separation provided by the sorting device will determine the likelihood that a particle enters the correct analysis unit. As an example, a sorting device or design similar to the particle router was provided on the ring trap electrodes used in Chapter 6 - although this was not used as electrodes were only fabricated on the bottom substrate, the design was intended to direct a particular cell into a particular trap. The output streams of the sorting device were aligned with each column of ring electrodes, so it would be necessary to produce a separation of the streams equal to the pitch of the ring electrodes (190 μm) with the streams offset by a distance less than the radius of the traps (40 μm).

Asymmetry in the electrode geometry around the outlets of the sorting devices produced a lateral DEP force on particles as they left the vicinity of the sorting device, deflecting the particles within the fluid flow. As is known from Equation 2.3, this force is proportional to the particle radius, its electrical characteristics, and the voltage on

the electrodes. A distribution of particle sizes, for example, will produce a distribution in the magnitude by which particles are deflected as they leave the sorting device, and hence the particle stream will be distributed across the width of the channel. Similarly, a reduction in the fluid flow rate will lead to an increase in the amount by which each particle is deflected. A redesign of the sorting electrodes with a more symmetrical output geometry would be likely to reduce the offset displacement of the output streams. Although it is not possible to make the electrodes completely symmetrical about every outlet, as every element in the electrodes will have some influence over each particles trajectory, the geometry closest to the outlet has the most effect on the particle trajectory.

Tables 7.3 and 7.4 show that the particle router design both confines the output stream more closely and provides significantly more stream separation than the multi-gate sorter design at the expense of requiring more substrate area. The particle router design could be extended simply to provide any degree of separation required. Both designs could be extended to provide additional outputs, limited by the substrate area and requirement for electrical connectivity.

As can be seen from Equation 3.14, the magnitude of the hydrodynamic force acting to push a particle through a DEP barrier is proportional to the sine of the angle between the barrier and the direction of fluid flow. Electrodes that cross the channel at a shallow angle produce a barrier able to deflect particles at higher flow rates, at the expense of the electrodes requiring a greater proportion of the channel length.

Figure 7.23 and Table 7.5 show experimental data for particle breakthrough velocity as the electrode voltage is adjusted. The results of numerical simulation (extracted from Figure 3.14) are also presented. This data was produced by scaling the maximum value of the gradient of the electric field ($\nabla |\mathbf{E}|^2$) - produced by simulation with electrode voltages of 1 V - in proportion to the square of the electrode voltage. Hence, the line of simulated data is a quadratic. Values for the breakthrough velocity calculated from numerical simulation are in close agreement with experimental measurements.

7.5 Conclusions

Dielectrophoresis has been proven as a suitable technology for the manipulation and sorting of single particles within a microfluidic device. The recovery of 100% pure populations is an exciting prospect, and if this can be translated to the sorting of viable cells it would enable isolation of rare cells from a mixed population. With the identification of sufficient cell surface markers, this could be used for the isolation of stem cells from an ex vivo sample.

Image-based particle sorting has been shown to be a practical method for sorting fluorescent particles at relatively low rates, of around one particle per second. The method is advantageous as it negates some of the requirement for the more advanced optical equipment used in many sorting devices, such as photomultiplier tubes, and lessens the required alignment tolerances of the optical system. The device used in this work could also be operated on a standard fluorescence microscope. The use of image-based sorting (rather than threshold detection, as commonly used in commercial FACS machines) means that sophisticated decision algorithms can be used to distinguish 'target' from 'negative' particles, incorporating factors such as particle size, shape or colour by simple changes to the control software.

All of the hardware used (most specifically the video camera and laser illumination) would be capable of operating at up to 90 frames per second - nine times more than currently used. With a redesign of the control software, and an increase in the gate voltage, the system could be operated with much higher throughput. The technique of image-based sorting is unlikely to reach the throughput possible by other methods such as FACS, however, with the current technology.

Manipulation of particles at comparatively low flow rates within a microfluidic device may have advantages for cell sorting. Many high throughput FACS machines produce sorted population with reduced viability (Seidl et al. (1999) reported a reduction in viability of up to 25% following FACS); shear stresses from hydrodynamic flow and aerosolisation can be sufficient to rupture the cell membrane. FACS machines can compensate for this, however, by sorting many thousands of cells. Although the microfluidic/electrokinetic environment is not without its own cellular stresses - shear stress is still an issue at high flow rates, as are induced transmembrane potentials and thermal effects - there is potential for recovery of pure populations with high viability.

Chapter 8

Conclusions

Microfluidic electrokinetic devices have been used to separate cells and particles in heterogeneous populations using fluorescent signals and image-based sorting. Two methods of separation have been developed: trapping target cells within dielectrophoretic ring traps so that they can be held as other cells are removed in the fluid flow, or deflecting target particles within a fluid stream so that they are carried by the flow towards a particular outlet. Both technologies have been used to recover small sorted populations with 100% purity.

8.1 Technological Achievements

8.1.1 Image-based Particle Sorting

Image-based particle detection significantly reduces the complexity of the optical equipment needed to collect data for cell sorting, by using a single sensor (a colour CCD camera) and moving the task of data separation into software algorithms. Conventional fluorescence-activated cell sorters interpret the signal from photomultiplier tubes as a cell passes through a detection region. Modern devices incorporate multiple lasers for illumination at different wavelengths, and obtain intensity data across a range of different wavelength bands, each with an individual sensor. Scattered light is also measured in the forward and side axes, which provides a measure of the approximate cell size and granularity respectively. We have demonstrated the simultaneous measurement of fluorescence information in two bands, and it would be simple to extend this to three or four bands with the appropriate filter set. It would be difficult to obtain as much data as is possible with a modern FACS machine using a single sensor, although it is unlikely that all of the bands would need to be used simultaneously. The use of video data permits a range of measurements to be taken, such as particle colour, size and shape, although it

does place a limitation on the rate at which particles can be sorted as it cannot exceed the camera frame rate without potential loss of accuracy.

While conventional fluorescence-based sorting devices seek to minimise the detection volume in order to increase sensitivity, with image-based sorting the detection volume can be defined dynamically. The image processing algorithms use a feature recognition and threshold function to isolate regions of the image that contain particles, so the detection region is optimised individually for each particle. While it is not possible to equal the sensitivity of a photomultiplier tube using only a video camera, this method goes some way to improving the results.

For particle detection and analysis over a large area, such as to control a large array of trapping electrodes, image-based detection is one of the few feasible choices. It would rapidly become impractical to provide a single sensor for each trap for even moderately sized arrays if standard photomultiplier tubes were used. Some success has been had integrating photosensors into DEP manipulation arrays on to silicon substrates (Manaresi et al., 2003); alternatively a multiplexed sensor could be used.

Generation of droplets in a conventional FACS machine simplifies the sorting operation as droplets pass through the sorting electrodes at regular intervals and their spacing can be controlled. This limits the possibility of two cells entering the sorting region in close succession, and one being sorted incorrectly. It is still possible for two cells to be placed in the same droplet, however, although they will be detected simultaneously and the appropriate action taken. With the microfluidic system used in this study, particles approach the electrodes in a random, probabilistic manner. The average spacing between particles can be adjusted by controlling the particle concentration in solution, but it is still possible for two or more different particles to enter the sorting region separated by a distance that is insufficient for both to be sorted correctly. Fortunately, by using image-based sorting a large region of the microchannel can be monitored for particles without sacrificing sensitivity, and multiple particles tracked. This permits conservative sorting strategies to be implemented, and both particles can be rejected to a 'waste' output to preserve the purity of the sorted population.

Image-based particle manipulation and sorting is only likely to be the preferred option for particular and specialised applications, as it is unable to match the sensitivity and speed possible with other optical detectors. This is particularly the case in the cell sorting arena, where high throughput enables the separation of even smaller minority groups. The burgeoning interest in stem cell therapies highlights the sorting problem: although it is relatively simple to isolate the mononuclear fraction of an ex vivo sample before sorting, stem cells may still make up less than 1 in 10,000 of these cells (Pittenger et al., 1999). Unless such numbers of cells can be sorted in a reasonable length of time, it is unlikely that even a single target cell will be detected.

8.1.2 Microfluidics and Electrokinetics

Dielectrophoretic particle manipulation has been shown suitable for both trapping particles and deflecting particles at a sorting junction. Although the DEP force can be scaled up for higher throughput by increasing the electrode voltage, limitations are imposed by the onset of electrolysis in the fluid and electrothermal heating - the later being a particular problem if cells are suspended in high conductivity physiological media.

Trapping single particles within a microfluidic device has many potential applications, not least as a sorting technique. It is a useful step in cell patterning, for cell culture, or as a cell concentration stage. The method also provides a means to bypass the limitation on the sorting rate imposed by the camera frame rate during image-based sorting, as multiple cells can be trapped simultaneously. The technique is most useful for applications that require cells to remain 'on-chip', such as when an integrated analysis or culture stage is used, as such devices typically require small numbers of cells to be sorted or processed and the ability to concentrate cells within the microfluidic system is most useful.

Deflection of particles as they flow through a microfluidic channel has been demonstrated as suitable for the sorting of fluorescent synthetic particles, and work is underway on the sorting of cells. Although the principle of operation is identical for the sorting of cells or synthetic particles, some optimisation must be performed if useful levels of purity are to be obtained when sorting cells, as they are a less 'ideal' population, with significant variations in fluorescent intensity and size, and are more prone to the formation of aggregates. There are also some applications that would benefit from the ability to manipulate synthetic particles, such as the increasing number of chemical processes that are performed on the surface of microparticles, including DNA sequencing (Hultman et al., 1989).

8.2 Future Potential

Cell and particle sorting is likely to remain an important laboratory process, and equipment is likely to gradually become faster and more accurate. The paucity of techniques and markers to identify some cell types places a constraint on the manner and accuracy in which cells can be sorted. Immunological tagging methods such as fluorescently-tagged monoclonal antibodies or magnetic nanoparticles remain the most popular choice, although label-free methods are receiving particular attention as research aims to avoid the use of potentially toxic markers that may limit subsequent use. Electrical impedance spectroscopy has been demonstrated as a cell analysis tool, able to differentiate between leukocytes on size and electrical properties (Holmes et al., 2007), although as yet has not been integrated into a sorting device. A dielectrophoretic sorting gate triggered by an

impedance analysis system could form a well integrated all-electric system, and would be a natural progression.

There is potential to increase the sorting rate of both the ring trap and the sorting gate systems, although neither are likely to reach the high throughput of modern commercial FACS machines. The maximum sorting rate limit imposed by the video hardware could potentially be increased by up to nine times by increasing the frame rate to the hardware maximum (90 fps). The control software would also need to be improved to match the increased speed of operation, although this would not be difficult if a lower-level programming language were used. Although even faster camera equipment is available, the photosensitivity would start to be a concern as the decreasing exposure time reduces the image intensity. More sensitive optical equipment could be used, such as a photomultiplier tube, although that would negate the advantages of using image-based sorting. The sorting rate could be increased by increasing either the concentration of particles within the device or the fluid flow rate through the device; the later would also require a proportional increase in the DEP force acting on the particles, typically achieved by increasing the electrode voltage. The ring trap design is highly scalable, and it would be a simple matter to increase the number of traps triggered from a single camera. This would increase both the particle sorting rate and the number of cells that could be sorted before the array was fully populated.

Ultimately, as with all incremental technological development, a new technology will be adopted if it offers a clear advantage over the current state of the art. In the field of cell and particle sorting the key performance indicators are sorting rate, purity, and viability of recovered populations. As was shown in Chapter 1, however, care must be taken to examine the operating conditions under which a sorting device reaches its peak performance before an informed decision can be made. Novel technologies may be well exploited if they can find their niche application. Dielectrophoretic particle manipulation technology is capable of sorting small numbers of cells with high purity and requires little ancillary equipment, so is particularly suited to use as a preparatory stage within an integrated microfluidic system.

8.3 Publications arising from this work

Rupert S. Thomas, Hywel Morgan and Nicolas G. Green. Negative DEP traps for single cell immobilisation. *Lab on a Chip*, 9:1534-1540, 2009.

Rupert S. Thomas, Peter D. Mitchell, Richard O.C. Oreffo and Hywel Morgan. Trapping single osteoblast-like human cells from a heterogeneous population using a dielectrophoretic microfluidic device. *Biomicrofluidics*, submitted.

Rupert S. Thomas, Peter D. Mitchell, Richard O.C. Oreffo and Hywel Morgan. Dielectrophoretic sorting gates for fluorescence-activated cell isolation, manuscript in preparation.

Appendix A

Solution to the Navier-Stokes Equation using Fourier Series

As discussed in Chapter 2, fluid within a microchannel exhibits laminar flow, and the interaction between the fluid and the walls of the channel produces a variation in the fluid velocity across the channel cross-section. The fluid velocity profile can be determined by solving the Navier-Stokes equation. If the aspect ratio of the channel is near to 1, however, the fluid velocity varies across two dimensions, and the boundary conditions alone do not sufficiently constrain the solution to solve the equation by integration. The equation can be solved by introducing a Fourier series, and a full derivation of this method is presented below, which was produced with the assistance of Dr Nicolas Green at the University of Southampton. Figure A.1 shows a cross-section through a microfluidic channel, with the dimensions and coordinate system used during calculation of the fluid velocity profile.

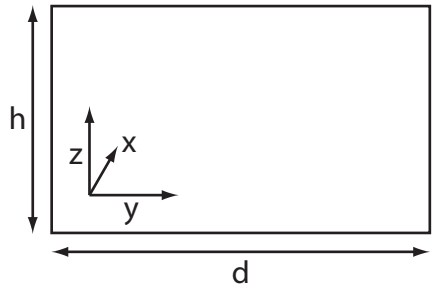

FIGURE A.1: Schematic of a cross-section across the microfluidic channel, showing dimensions and coordinate system used during analysis of the flow profile. Fluid flow is solely along the x-axis.

A continuous Newtonian fluid flowing under low Reynolds number conditions can be modelled using the equation:

$$\rho_m \frac{\partial \mathbf{u}}{\partial t} + \rho_m(\mathbf{u} \cdot \nabla)\mathbf{u} = -\nabla p + \eta \nabla^2 \mathbf{u} + f \tag{A.1}$$

Under steady-state conditions, with no external force acting on the fluid, Equation A.1 reduces to:

$$\rho_m(\mathbf{u} \cdot \nabla)\mathbf{u} = -\nabla p + \eta \nabla^2 \mathbf{u} \tag{A.2}$$

The fluid flow is unidirecional along the x axis ($\mathbf{u} = (u, 0, 0)$), and varies as a function of the position in the y and z axes ($\mathbf{u}(y, z)$).

Continuity Equation:

$$\frac{\partial u}{\partial x} + \frac{\partial\,(0)}{\partial y} + \frac{\partial\,(0)}{\partial z} = 0 \Rightarrow \frac{\partial \mathbf{u}}{\partial x} = 0 \tag{A.3}$$

From Equation A.2:

$$\rho_m(\mathbf{u}\frac{\partial \mathbf{u}}{\partial x}) = \frac{\partial p}{\partial x} + \eta \nabla^2 \mathbf{u} \tag{A.4}$$

$$\Rightarrow \nabla^2 \mathbf{u} = \frac{1}{\eta}\frac{\partial p}{\partial x} \tag{A.5}$$

$$\text{With boundary conditions:} \quad \begin{cases} u = 0 \ @ \ y = 0, d \\ u = 0 \ @ \ z = 0, h \end{cases} \tag{A.6}$$

Hence, the equation to solve is the diffusion equation:

$$\frac{\partial^2 \mathbf{u}}{\partial y^2} + \frac{\partial^2 \mathbf{u}}{\partial z^2} = \Omega = \frac{1}{\eta}\frac{\partial p}{\partial x} \tag{A.7}$$

The fluid velocity profile ($\mathbf{u}$) can be equated to a two-dimensional Fourier series:

$$\mathbf{u} = \sum_{n=1}^{\infty}\sum_{m=1}^{\infty} a_{nm}(\sin ny + \cos ny)(\sin mz + \cos mz) \tag{A.8}$$

Applying the boundary conditions (Equation A.6), Equation A.8 reduces to:

$$\mathbf{u} = \sum_{n=1}^{\infty}\sum_{m=1}^{\infty} a_{nm}(\sin ny)(\sin mz) \tag{A.9}$$

$$u = 0 \ @ \ y = d \Rightarrow nd = k\pi \text{ where } k = 1, 2, 3... \Rightarrow n = \frac{k\pi}{d}$$
$$u = 0 \ @ \ z = h \Rightarrow mh = l\pi \text{ where } l = 1, 2, 3... \Rightarrow m = \frac{l\pi}{h} \tag{A.10}$$

$$\Rightarrow \mathbf{u} = \sum_{n=1}^{\infty}\sum_{m=1}^{\infty} a_{kl}\left(\sin\frac{k\pi}{d}y\right)\left(\sin\frac{l\pi}{h}z\right) \tag{A.11}$$

The coefficients can be determined by integration to check for orthogonality:

$$\int_0^d\int_0^h \mathbf{u}\sin\frac{p\pi y}{d}\sin\frac{q\pi z}{h}dydz = \sum_{k=1}^{\infty}\sum_{l=1}^{\infty}\int_0^d\int_0^h a_{kl}\sin\frac{k\pi y}{d}\sin\frac{p\pi y}{d}\sin\frac{l\pi z}{h}\sin\frac{q\pi z}{h}dydz \tag{A.12}$$

LHS:

$$\begin{cases} \frac{2d}{p\pi}\frac{2h}{q\pi}\mathbf{u} & \text{if p,q odd} \\ 0 & \text{if p,q even} \end{cases}$$

$$\Rightarrow \frac{4dh}{pq\pi^2}\mathbf{u} \text{ if p,q odd} \tag{A.13}$$

RHS:

$$\begin{cases} 0 & \text{if p} \neq \text{k or q} \neq \text{l} \\ a_{kl}\frac{d}{2}\frac{h}{2} & \text{if p} = \text{k \& q} = \text{l} \end{cases}$$

$$\Rightarrow \frac{dh}{4}a_{kl} \text{ if p} = \text{k \& q} = \text{l} \tag{A.14}$$

$$\therefore \frac{4dh}{pq\pi^2}\mathbf{u} = \frac{dh}{4}a_{kl} \text{ if p} = \text{k, q} = \text{l and all odd} \tag{A.15}$$

$$\Rightarrow a_{kl} = \frac{4dh}{kl\pi^2}\frac{4}{dh}\mathbf{u} = \frac{16}{kl\pi^2}\mathbf{u} \tag{A.16}$$

From Equation A.6:

$$\frac{\partial^2\mathbf{u}}{\partial y^2} + \frac{\partial^2\mathbf{u}}{\partial z^2} = \Omega = -\left[\left(\frac{k\pi}{d}\right)^2 + \left(\frac{l\pi}{h}\right)^2\right]\mathbf{u} \tag{A.17}$$

$$\mathbf{u} = \frac{-\Omega}{\left[\left(\frac{k\pi}{d}^2\right) + \left(\frac{l\pi}{h}^2\right)\right]} \tag{A.18}$$

From Equation A.16:

$$a_{kl} = \frac{16}{kl\pi^2}\mathbf{u} = \frac{16}{kl\pi^2}\frac{-\Omega}{\left[\left(\frac{k\pi}{d}^2\right) + \left(\frac{l\pi}{h}^2\right)\right]} \tag{A.19}$$

From Equation A.11:

$$\Rightarrow \mathbf{u} = \sum_{n=1,3\ldots}^{\infty}\sum_{m=1,3\ldots}^{\infty} a_{kl}\sin\left(\frac{k\pi}{d}y\right)\sin\left(\frac{l\pi}{h}z\right) \tag{A.20}$$

The volumetric flow rate can be determined by a surface integral across the fluid velocity profile:

$$\begin{aligned} Q &= \sum_{n=1,3\ldots}^{\infty}\sum_{m=1,3\ldots}^{\infty} a_{kl}\int_0^d\int_0^h \sin\left(\frac{k\pi}{d}y\right)\sin\left(\frac{l\pi}{h}z\right) \\ &= \sum_{n=1,3\ldots}^{\infty}\sum_{m=1,3\ldots}^{\infty} a_{kl}\frac{2d}{k\pi}\frac{2h}{l\pi} \\ &= \sum_{n=1,3\ldots}^{\infty}\sum_{m=1,3\ldots}^{\infty} a_{kl}\frac{4dh}{kl\pi^2} \end{aligned} \tag{A.21}$$

Bibliography

J.D. Adams, U. Kim, and H.T. Soh. Multitarget magnetic activated cell sorter. *Proc Natl Acad Sci USA*, 105(47):1816570, 2008.

M. Agirregabiria, F.J. Blanco, J. Berganzo, M.T. Arroyo, A. Fullaondo, and K. Mayora. Fabrication of su-8 multilayer microstructures based on successive cmos compatible adhesive bonding and releasing steps. *Lab on A Chip*, 5:545–552, 2005.

S. Archer, T. Li, A. Tudor Evans, S.T. Britland, and H. Morgan. Cell reactions to dielectrophoretic manipulation. *Biochemical and Biophysical Research Communications*, 257:687–98, 1999.

K. Asami, Y. Takahashi, and S. Takashima. Frequency domain analysis of membrane capacitance of cultured cells (hela and myeloma) using the micropipette technique. *Biophysical Journal*, 58:143–8, 1990.

A. Ashkin. Acceleration and trapping of particles by radiation pressure. *Physical Review Letters*, 24:156, 1970.

A. Ashkin and J.M. Dziedzic. Optical trapping and manipulation of viruses and bacteria. *Science*, 235:1517–1520, 1987.

A. Ashkin, J.M. Dziedzic, and T. Yamane. Optical trapping and manipulation of single cells using infrared-laser beams. *Nature*, 330:769–771, 1987.

E.S. Asmolov. The inertial lift on a spherical particle in a plane poiseuille flow at large channel reynolds number. *Journal of Fluid Mechanics*, 381:63–87, 1999.

Jean-Christophe Baret, Oliver J. Miller, Valerie Taly, Michal Ryckelynck, Abdeslam El-Harrak, Lucas Frenz, Christian Rick, Michael L. Samuels, J. Brian Hutchison, Jeremy J. Agresti, Darren R. Link, David A. Weitz, and Andrew D. Griffiths. Fluorescence-activated droplet sorting (fads): efficient microfluidic cell sorting based on enzymatic activity. *Lab on a Chip*, pages 1850 – 1858, 2009.

F.F. Becker, X.B. Wang, Y. Huang, R. Pethig, J. Vykoukal, and P.R.C. Gascoyne. The removal of human leukemia-cells from blood using interdigitated microelectrodes. *Journal of Physics D - Applied Physics*, 27:2659–62, 1994.

F.F. Becker, X.B. Wang, Y. Huang, R. Pethig, J. Vykoukal, and P.R.C. Gascoyne. Separation of human breast-cancer cells from blood by differential dielectric affinity. *Proceedings of the National Academy of Sciences of the United States of America*, 92: 860–64, 1995.

A. B. D. Brown, C. G. Smith, and A. R. Rennie. Pumping of water with ac electric fields applied to asymmetric pairs of microelectrodes. *Physical Review E*, 63(1):016305, Dec 2000.

D. Di Carlo, D. Irimia, R.G. Tompkins, and M. Toner. Continuous inertial focusing, ordering, and separation of particles in microchannels. *Proceedings of the National Academy of Sciences of the United States of America*, 104(48):1889218897, 2007.

D. Di Carlo, L.Y. Wu, and L.P. Lee. Dynamic single cell culture array. *Lab on a Chip*, 6:1445–9, 2006.

A. Castellanos. *Electrohydrodynamics*. Springer Verlag, 1998.

M. Chalfie, Y. Tu, G. Euskirchen, W.W. Ward, and D.C. Prasher. Green fluorescent protein as a marker for gene expression. *Science*, 263(5148):802–5, 1994.

K.L. Chan, P.R.C. Gascoyne, and F.F. Becker R. Pethig. Electrorotation of liposomes: verification of dielectric multi-shell model for cells. *Biochimica et Biophysica Acta - Lipids and Lipid Metabolism*, 1349:182–96, 1997.

D.F. Chen and H. Du. Simulation studies on electrothermal fluid flow induced in a dielectrophoretic microelectrode system. *J. Micromech. Microeng.*, 16:241119, 2006.

J. Cheng, E.L. Sheldon, L. Wu, M.J. Heller, and J.P. O'Connell. Isolation of cultured cervical carcinoma cells mixed with peripheral blood cells on a bioelectronic chip. *Analytical Chemistry*, 70:2321–26, 1998.

P.Y. Chiou, A.T. Ohta, and M.C. Wu. Massively parallel manipulation of single cells and microparticles using optical images. *Nature*, 436:370–372, 2005.

E.B. Cummings. Streaming dielectrophoresis for continuous-flow microfluidic devices. *IEEE Engineering in Medicine and Biology Magazine*, 22:75–84, 2003.

M.B. Dainiak, A. Kumar, I.Y. Galaev, and B. Mattiasson. Methods in cell separations. *Adv Biochem Eng Biotechnol*, 106:1–18, 2007.

Petra S. Dittrich and Petra Schwille. An integrated microfluidic system for reaction, high-sensitivity detection, and sorting of fluorescent cells and particles. *Analytical Chemistry*, 75:5767–74, 2003.

M. Eisenstein. Cell sorting: divide and conquer. *Nature*, 441:11791185, 2006.

S. Fiedler, S.G. Shirley, T. Schnelle, and G. Fuhr. Dielectrophoretic sorting of particles and cells in a microsystem. *Analytical Chemistry*, 70:1909–15, 1998.

A.Y Fu, H.P. Chou, C. Spence, F.H. Arnold, and S.R. Quake. An integrated microfabricated cell sorter. *Analytical Chemistry*, 74:2451–57, 2002.

A.Y Fu, C. Spence, A. Scherer, F.H. Arnold, and S.R. Quake. A microfabricated fluorescence-activated cell sorter. *Nature Biotechnology*, 17:1109–11, 1999.

P.R.C. Gascoyne and J. Vykoukal. Particle separation by dielectrophoresis. *Electrophoresis*, 23:1973–1983, 2002.

S. Gawad, L. Schild, and P. Renaud. Micromachined impedance spectroscopy flow cytometer for cell analysis and particle sizing. *Lab on a Chip*, 1:76–82, 2001.

P. Gerardo. A fluidic motherboard including fluidic and optical interconnections having modular functionality for optical analysis in microfluidic systems. In *Proceedings of Micro-TAS 2006 Conference*, pages 1549–1551, 2006.

J.C. Giddings, F.J. Yang, and M.N. Myers. Flow-field-flow fractionation: a versatile new separation method. *Science*, 193(4259):1244–45, 1976.

J. Gimsa. Particle characterization by ac-electrokinetic phenomena: 1. a short introduction to dielectrophoresis (dp) and electrorotation (er). *Colloids and Surfaces A - Physicochemical and Engineering Aspects*, 149:451–9, 1999.

H. Glasser and G. Fuhr. Cultivation of cells under strong ac-electric field: differentiation between heating and trans-membrane potential effects. *Bioelectrochemistry and Bioenergetics*, 47:301–10, 1998.

A.J. Goldman, R.G. Cox, and H. Brenner. Slow viscous motion of a sphere parallel to a plane wallii couette flow. *Chemical Engineering Science*, 22(4):65360, 1967.

D.S. Gray, J.L. Tan, J. Voldman, and C.S. Chen. Dielectrophoretic registration of living cells to a microelectrode array. *Biosensors and Bioelectronics*, 19:771–80, 2004.

N.G. Green, H. Morgan, and J.J. Milner. Dielectrophoresis of tobacco mosaic virus. *Biophysical Journal*, 72:448, 1997.

N.G. Green, A. Ramos, and H. Morgan. Solid-state ac electric field driven micropumps. In *15th MicroMechanics Europe Workshop*, pages 187–190, 2004.

J.A. Grimbergen, K. Visscher, D.S.G. Demesquita, and G.J. Brakenhoff. Isolation of single yeast-cells by optical trapping. *Yeast*, 9:723–732, 1993.

C. Grosse and H.P. Schwan. Cellular membrane potentials induced by alternating fields. *Biophysical Journal*, 63:1632–42, 1992.

D.J. Harrison, A. Manz, Z. Fan, H. Ludi, and Widmers H.M. Capillary electrophoresis and sample injection systems integrated on a planar glass chip. *Analytical Chemistry*, 64:1928–32, 1992.

L.F. Hartley, K.V.I.S. Kaler, and R. Paul. Quadrupole levitation of microscopic dielectric particles. *Journal of Electrostatics*, 46:233–46, 1999.

L.A. Herzenberg, D. Parks, B. Sahaf, O. Perez, M. Roederer, and L.A. Herzenberg. The history and future of the fluorescence activated cell sorter and flow cytometry: A view from stanford. *Clinical Chemistry*, 48(10):1819–1827, 2002.

L.A Herzenberg, R.G. Sweet, and L.A. Herzenberg. Fluorescence-activated cell sorting. *Scientific American*, 234(3):108–117, 1976.

H. Hillborg, J.F. Ankner, U.W. Gedde, G.D. Smith, H.K. Yasuda, and K. Wikstrom. Crosslinked polydimethylsiloxane exposed to oxygen plasma studied by neutron reflectometry and other surface specific techniques. *Polymer*, 41(18):6851–63, 2000.

D. Holmes, J. Cakebread, J. Holloway, D. Davies, and H. Morgan. Impedance spectroscopy for label-free differential leukocyte counts. In *Proc. MICROTAS 2007*, 2007.

D. Holmes, N.G. Green, and H. Morgan. Microdevices for dielectrophoretic flowthrough cell separation. *IEEE Engineering in Medicine and Biology Magazine*, 22:85–90, 2003.

D. Holmes, H. Morgan, and N.G. Green. The potential of dielectrophoresis for single-cell experiments. *Biosensors and Bioelectronics*, 21:1621–30, 2006.

D. Holmes, M.E. Sandison, N.G. Green, , and H. Morgan. On-chip high-speed sorting of micron-sized particles for high-throughput analysis. *Iee Proceedings-Nanobiotechnology*, 152:129–135, 2005.

R. Holzel. Single particle characterization and manipulation by opposite field dielectrophoresis. *Journal of Electrostatics*, 56:435–447, 2002.

Y. Huang, R. Holzel, R. Pethig, and X.B. Wang. Differences in the ac electrodynamics of viable and non-viable yeast cells determined through combined dielectrophoresis and electrorotation studies. *Phys Med Biol*, 37:1499–517, 1992.

Y. Huang and R. Pethig. Electrode design for negative dielectrophoresis. *Measurement Science and Technology*, 2:1142–46, 1991.

Y. Huang, X.B. Wang, F.F. Becker, and P.R. Gascoyne. Introducing dielectrophoresis as a new force field for field- flow fractionation. *Biophysical Journal*, 73(2):1118–29, 1997.

M.P. Hughes, H. Morgan, F.J. Rixon, J.P.H. Burt, and R. Pethig. Manipulation of herpes simplex virus type 1 by dielectrophoresis. *Biochimica et Biophysica Acta*, 1425:119–26, 1998.

T. Hultman, S. Stahl, E. Hornes, and M. Uhln. Direct solid phase sequencing of genomic and plasmid dna using magnetic beads as solid support. *Nucleic Acids Res*, 17(13): 4937–46, 1989.

T.B. Jones and J.P. Kraybill. Active feedback-controlled dielectrophoretic levitation. *Journal of Applied Physics*, 60:1247–52, 1986.

James W. Jorgenson and Krynn DeArman Lukacs. Zone electrophoresis in open-tubular glass capillaries. *Analytical Chemistry*, 53:1298–302, 1981.

James W. Jorgenson and Krynn DeArman Lukacs. Capillary zone electrophoresis. *Science*, 222(4621):266–72, 1983. ISSN 00368075.

J. Khandurina, T.E. McKnight, S.C. Jacobson, L.C. Waters, R.S. Foote, and J.M. Ramsey. Integrated system for rapid pcr-based dna analysis in microfluidic devices. *Analytical Chemistry*, 72:2995–3000, 2000.

U. Kim, J. Qian, S.A. Kenrick, P.S. Daugherty, and H.T. Soh. Multitarget dielectrophoresis activated cell sorter. *Analytical Chemistry*, 80:865661, 2008.

T. Kotnik, F. Bobanovic, and D. Miklavcic. Sensitivity of transmembrane voltage induced by applied electric fields a theoretical analysis. *Bioelectrochemistry and Bioenergetics*, 43:285–91, 1997.

J.R. Kovac and J. Voldman. Intuitive, image-based cell sorting using opto-fluidic cell sorting. *Analytical Chemistry*, 79:932130, 2007.

M. Kriegmaier, M. Zimmermann, K. Wolf, U. Zimmermann, and V.L. Sukhorukov. Dielectric spectroscopy of schizosaccharomyces pombe using electrorotation and electroorientation. *Biochim Biophys Acta*, 1568:135–46, 2001.

H. Kurafugi and K. Suda. Electrical discharge drilling of glass. *Ann. CIRP*, 16:415–9, 1968.

Jrg P. Kutter. Current developments in electrophoretic and chromatographic separation methods on microfabricated devices. *Trends in Analytical Chemistry*, 19(6):352–63, 2000. ISSN 0165-9936.

E.T. Lagally, I. Medintz, and R.A. Mathies. Single-molecule dna amplification and analysis in an integrated microfluidic device. *Analytical Chemistry*, 73:565–570, 2001.

I.R. Lauks. Microfabricated biosensors and microanalytical systems for blood analysis. *Accounts of Chemical Research*, 31:317–324, 1998.

M.P. MacDonald, S. Neale, L. Paterson, A. Richies, K. Dholakia, and G.C. Spalding. Cell cytometry with a light touch: Sorting microscopic matter with an optical lattice. *Journal of Biological Regulators and Homeostatic Agents*, 18(2):200–5, 2004.

M.P. MacDonald, G.C. Spalding, and K. Dholakia. Microfluidic sorting in an optical lattice. *Nature*, 426:421–24, 2003.

N. Manaresi, A. Romani, G. Medoro, L. Altomare, A. Leonardi, M. Tartagni, and R. Guerrieri. A cmos chip for individual cell manipulation and detection. *Ieee Journal of Solid-State Circuits*, 38:2297–2305, 2003.

A. Manz, N. Graber, and H.M. Widmer. Miniaturized total chemical analysis systems: a novel concept for chemical sensing. *Sensors and Actuators B*, 1:244–248, 1990.

G.H. Markx, P.A. Dyda, and R. Pethig. Dielectrophoretic separation of bacteria using a conductivity gradient. *Journal of Biotechnology*, 51:175–80, 1996.

G.H. Markx, Y. Huang, X.F. Zhou, and R. Pethig. Dielectrophoretic characterization and separation of microorganisms. *Microbiology*, 140:585–591, 1994.

J. C. McDonald, D. C. Duffy, J. R. Anderson, D. T. Chiu, H. Wu, O. J. A. Schueller, and G. M. Whitesides. Fabrication of microfluidic systems in poly(dimethylsiloxane). *Electrophoresis*, 21(1):27–40, 2000.

G. Medoro, C. Nastruzzi, and R. Guerrieri R. Gambari N. Manaresi. Lab on a chip for live-cell manipulation. *IEEE Design and Test of Computers*, 24:26–36, 2007.

F.E.P. Mikkers, F.M. Everaerts, and T.P.E.M. Verheggen. High-performance zone electrophoresis. *Journal of Chromatography*, 169:11–20, 1979.

S. Miltenyi, W. Muller, W. Weichel, and A. Radbruch. High-gradient magnetic cell-separation with macs. *Cytometry*, 11:231–8, 1990.

M.R.N. Monton and S. Terabe. Recent developments in capillary electrophoresis-mass spectrometry of proteins and peptides. *Analytical Science*, 21(1):5–13, 2005.

H. Morgan and N.G. Green. *AC Electrokinetics: colloids and nanoparticles*. Research Studies Press, 2003.

H. Morgan, N.G. Green, M.P. Hughes, W. Monaghan, and T.C. Tan. Large-area travelling-wave dielectrophoresis particle separator. *Journal of Micromechanics and Microengineering*, 7:65–70, 1997.

H. Morgan, M.P. Hughes, and N.G. Green. Separation of submicron bioparticles by dielectrophoresis. *Biophysical Journal*, 77:516–525, 1999.

Hywel Morgan, Tao Sun, David Holmes, Shady Gawad, and Nicolas G Green. Single cell dielectric spectroscopy. *Journal of Physics D: Applied Physics*, 40(1):61–70, 2007.

T. Muller, G. Gradl, S. Howitz, S. Shirley, T. Schnelle, and G. Fuhr G. A 3-d microelectrode system for handling and caging single cells and particles. *Biosensors and Bioelectronics*, 14:247–56, 1999.

T. Muller, A. Pfennig, P. Klein, G. Gradl, M. Jager, and T. Schnelle. The potential of dielectrophoresis for single-cell experiments. *IEEE Engineering in Medicine and Biology Magazine*, 22:51–61, 2003.

A. Orfao and A. Ruiz-Arguelles. General concepts about cell sorting techniques. *Clin Biochem.*, 29:5–9, 1996.

R. Pethig, Y. Huang, X.B. Wang, and J.P.H. Burt JPH. Positive and negative dielectrophoretic collection of colloidal particles using interdigitated castellated microelectrodes. *Journal of Physics D - Applied Physics*, 25:881–888, 1992.

Mark F. Pittenger, Alastair M. Mackay, Stephen C. Beck, Rama K. Jaiswal, Robin Douglas, Joseph D. Mosca, Mark A. Moorman, Donald W. Simonetti, Stewart Craig, and Daniel R. Marshak. Multilineage potential of adult human mesenchymal stem cells. *Science*, 284:143–147, 1999.

H.A. Pohl. The motion and precipitation of suspensoids in divergent electric fields. *Journal of Applied Physics*, 22:869–71, 1951.

H.A. Pohl. A new technique for studying cells and organelles. *Bulletin of the American Physical Society*, 15:1362, 1970.

H.A. Pohl and J.S. Crane. Dielectrophoresis of cells. *Biophysical Journal*, 11:711, 1971.

J.A.R. Price, J.P.H. Burt, and R. Pethig. Applications of a new optical technique for measuring the dielectrophoretic behaviour of micro-organisms. *Biochimica et Biophysica Acta*, 964:221–230, 1988.

L. Qian, M. Scott, K.V.I.S. Kaler, and R. Paul. Integrated planar concentric ring dielectrophoretic (dep) levitator. *Journal of Electrostatics*, 55:65–79, 2002.

A. Ramos, A. Gonzalez, A. Castellanos, N.G. Green, and H. Morgan. Pumping of liquids with ac voltages applied to asymmetric pairs of microelectrodes. *Physical Review E*, 67(1):056302, 2003.

A. Ramos, H. Morgan, N.G. Green, and A. Castellanos. Ac electrokinetics: a review of forces in microelectrode structures. *J. Phys. D: Appl. Phys*, 31:233853, 1998.

C. Reichle, T. Muller, T. Schnelle, and G. Fuhr. Electro-rotation in octopole micro cages. *Journal of Physics D-Applied Physics*, 32:2128–35, 1999.

A. Rosenthal and J. Voldman. Dielectrophoretic traps for single-particle patterning. *Biophysical Journal*, 88:2193–205, 2005.

J. Ruzicka and E.H. Hansen. Integrated microconduits for flow-injection analysis. *Analytica Chimica Acta*, 161:1–25, 1984.

N. Sasaki, T. Kitamori, and H.B Kim. Ac electroosmotic micromixer for chemical processing in a microchannel. *Lab on A Chip*, 6:550–554, 2006.

S. Sato and H. Inaba. Optical trapping and manipulation of microscopic particles and biological cells by laser beams. *Optical and Quantum Electronics*, 28:1–16, 1996.

T. Schnelle, R. Hagedorn, G. Fuhr, S. Fiedler, and T. Muller. 3-dimensional electric-field traps for manipulation of cells - calculation and experimental verification. *Biochimica et Biophysica Acta*, 1157:127–40, 1993.

Thomas Schnelle, Torsten Mller, G. Gradl, S. G. Shirley, and G. Fuhr. Paired microelectrode system: dielectrophoretic particle sorting and force calibration. *Journal of Electrostatics*, 47(3):121 – 132, 1999. ISSN 0304-3886.

U. Seger, S. Gawad, R. Johann, A. Bertsch, and P. Renaud. Cell immersion and cell dipping in microfluidic devices. *Lab on A Chip*, 4:148–51, 2004.

J. Seidl, R. Knuechel, and L.A. Kunz-Schughart. Evaluation of membrane physiology following fluorescence activated or magnetic cell separation. *Cytometry*, 36:10211, 1999.

O. Shimomura, F.H. Johnson, and Y. Saiga. Extraction, purification and properties of aequorin, a bioluminescent protein from the luminous hydromedusan, aequorea. *J Cell Comp Physiol.*, 59:223–39, 1962.

S. Shoji, M. Esashi, and T. Matsuo. Prototype miniature blood-gas analyzer fabricated on a silicon-wafer. *Sensors and Actuators*, 14:101–107, 1988.

B.M. Taff and J. Voldman. A scalable addressable positive-dielectrophoretic cell sorting array. *Analytical Chemistry*, 77:7976–83, 2005.

M.S. Talary, J.P.H. Burt, J.A. Tame, and R. Pethig. Electromanipulation and separation of cells using travelling electric fields. *Journal of Physics D - Applied Physics*, 29: 2198–2203, 1996.

A.J. Tdos, G.A.J. Besselink, and R.B.M. Schasfoort. Trends in miniaturized total analysis systems for point-of-care testing in clinical chemistry. *Lab on a Chip*, 1:83–95, 2001.

S.C. Terry. *A gas chromatography system fabricated on a silicon wafer using integrated circuit technology.* PhD thesis, Department of Electrical Engineering, Stanford University, Stanford, California, 1975.

R.S. Thomas, H. Morgan, and N.G. Green. Negative dep traps for single cell immobilisation. *Lab on a Chip*, 9:1534–40, 2009.

T. Thorsen, S.J. Maerkl, and S.R. Quake. Microfluidic large-scale integration. *Science*, 298:580–584, 2002.

R.Y. Tsien. The green fluorescent protein. *Annual Review of Biochemistry*, 67:509–44, 1998.

S. Tuukkanen, A. Kuzyk, J.J. Toppari, H. Hakkinen, V.P. Hytonen, E. Niskanen, M. Rinkio, and P. Torma. Trapping of 27 bp-8 kbp dna and immobilization of thiol-modified dna using dielectrophoresis. *Nanotechnology*, 18, 2007.

H.T.G. Vanlintel, F.C.M. Vandepol, and S. Bouwstra. A piezoelectric micropump based on micromachining of silicon. *Sensors and Actuators*, 15:153–167, 1988.

E. Verpoorte. Microfluidic chips for clinical and forensic analysis. *Electrophoresis*, 23: 677–712, 2002.

J. Voldman, R.A Braff, M. Toner, M.L. Gray, and M.A. Schmidt. Holding forces of single-particle dielectrophoretic traps. *Biophysical Journal*, 80:531–41, 2001.

J. Voldman, M .L. Gray, M. Toner, and M.A. Schmidt. A microfabrication-based dynamic array cytometer. *Analytical Chemistry*, 74:3984–90, 2002.

J. Voldman, M. Toner, M.L. Gray, and M.A. Schmidt. Design and analysis of extruded quadrupolar dielectrophoretic traps. *Journal of Electrostatics*, 57:69–90, 2003.

P. Vulto, N. Glade, L. Altomare, J. Bablet, L. Del Tin, G. Medoro, I. Chartier, N. Manaresi, M. Tartagnia, and R. Guerrieria. Microfluidic channel fabrication in dry film resist for production and prototyping of hybrid chips. *Lab on a Chip*, 5:158–62, 2005.

M.M. Wang, E. Tu, D.E. Raymond, J.M. Yang, H.C. Zhang, N. Hagen, B. Dees, E.M. Mercer, A.H. Forster, I. Kariv, P.J. Marchand, and W.F. Butler. Microfluidic sorting of mammalian cells by optical force switching. *Nature Biotechnology*, 23(1):83–7, 2005.

X.B. Wang, Y. Huang, J.P.H. Burt, G.H. Markx, and R. Pethig. Selective dielectrophoretic confinement of bioparticles in potential-energy wells. *Journal of Physics D - Applied Physics*, 26:1278–85, 1993.

X.B. Wang, J. Yang, Y. Huang, J. Vykoukal, F.F. Becker, and P.R.C. Gascoyne. Cell separation by dielectrophoretic field-flow-fractionation. *Analytical Chemistry*, 72:832–9, 2000.

Jonathan West and Amol Jadhav. Ecdm methods for fluidic interfacing through thin glass substrates and the formation of spherical microcavities. *Journal of Micromechanics and Microengineering*, 17(2):403–409, 2007.

A. Willasch, S. Eing, G. Weber, S. Kui, G. Schneider, J. Soerensen, A. Jarisch, E. Rettinger, U. Koehl, T. Klingebiel, H. Kreyenberg, and P. Bader. Enrichment of cell subpopulations applying automated macs technique: purity, recovery and applicability for pcr-based chimerism analysis. *Bone Marrow Transplant*, 2009.

A. Wolff, I.R. Perch-Nielsen, U.D. Larsen, P. Friis, G. Goranovic, C.R. Poulsen, J.P. Kutter, and P. Telleman. Integrating advanced functionality in a microfabricated high-throughput fluorescent-activated cell sorter. *Lab on A Chip*, 3:22–7, 2003.

J.M. Yang, J. Bell, Y. Huang, M. Tirado, D. Thomas, A.H. Forster, R.W. Haigis, P.D. Swanson, R.B. Wallace, B. Martinsons, and M. Krihak. An integrated, stacked microlaboratory for biological agent detection with dna and immunoassays. *Biosensors and Bioelectronics*, 17:605–18, 2002.

X.F. Zhou, G.H. Markx, and R. Pethig. Effect of biocide concentration on electrorotation spectra of yeast cells. *Biochimica et Biophysica Acta - Biomembranes*, 1281:60–64, 1996.